Università degli Studi Di Ferrara

Research Doctorate in Physics – XXXIV Cycle

Exploiting ^{40}K radioactivity to probe the Earth and the environment

Supervisor:
Prof. Fabio Mantovani

Candidate:
Andrea Serafini

Academic Year 2020-2021

Andrea Serafini

Exploiting ^{40}K radioactivity to probe the Earth and the environment

Observing the world from a different perspective

Table of Contents

INTRODUCTION

I firmly believe that every choice I have made in my life has always been driven by curiosity. And I think it was curiosity that pushed me more than 3 years ago to accept the challenge thrown to me by who was to become my future supervisor: how could we exploit the physical properties of potassium to explore the Earth and the environment? A peculiar and unusual question, at least until you consider the importance of this element for life on Earth and its exceptional peculiarities which make it an invaluable probe in the remote study of what surrounds us.

Potassium, in addition to being the 8th most abundant elements on Earth's crust, has chemical and physical characteristics that are difficult to find in any other element. It is siderophile, moderately volatile, but above all, it has among its natural isotopes a radionuclide, potassium-40 (^{40}K), which has a half-life of more than a billion years. This long lifespan made it a constant presence in the evolution of our planet and not only as a travel companion, but also as an active part in its development. Indeed, while decaying, ^{40}K generates heat, and not just a little. Together with uranium-238 (^{238}U) and thorium-232 (^{232}Th), it is estimated that these radionuclides still produce half of the heat available to the internal processes that regulate the dynamics of our inner planet. During its decays, ^{40}K produces electrons, positrons, photons, neutrinos, and antineutrinos through electron captures, plus and minus beta decays and gamma transitions. A so abundant radionuclide with such a varied decay dynamics offers the possibility to probe the Earth on different spatial scales (Figure 1).

The photons emitted in ^{40}K gamma transitions can travel for tens of centimeters and meters in matter and air, respectively. Interacting with the medium they cross, they retain precious information on the environment which surround us. They thus find wide use in applied physics and in the characterization of field-scale radioactivity by means of proximal remote sensing techniques, particularly in precision agriculture. The photons produced in the underground decays of ^{40}K are attenuated proportionally to soil density and are consequently sensitive to its physical characteristic, particularly to the amount of water stored in the soil. This feature makes gamma spectroscopy possibly effective as a decision support system for irrigation. A rational and responsible management of water resources is a priority for efficient and meaningful climate action and is crucial for achieving all the four official goals of the Climate Change Conference COP26. Agriculture accounts by itself for

more than half of global water withdrawals. Improvement of farming practices is thus imperative to ensure availability and sustainable management of water in the future. Proximal gamma ray spectroscopy has the ambition to represent an effective tool for estimating the soil water content at field scale (~10 m) in real time. In this context, this technique would place itself between punctual sensors (probing soil moisture at the ~dm scale) and satellites (~km), filling a still unbridged spatial gap.

Two other decay products of ^{40}K are instead more elusive. Neutrinos and antineutrinos (with the latter produced to a larger extent), can travel undisturbed for millions of kilometers, making them valuable messengers in the study of the inner Earth. The study of these so-called "geoneutrinos", produced inside the Earth in the decays of ^{40}K and in the decay chains of ^{238}U and ^{232}Th, allow us to recover information on the composition of our planet and on the energy budget of Earth's mantle. While ^{238}U and ^{232}Th geoneutrinos have already been detected, ^{40}K geoneutrinos remains unobserved due to experimental challenges foreseen for their detection. The shadow covering this low part of the geoneutrino energy spectrum currently limits a comprehensive understanding of planetary composition and thermal evolution.

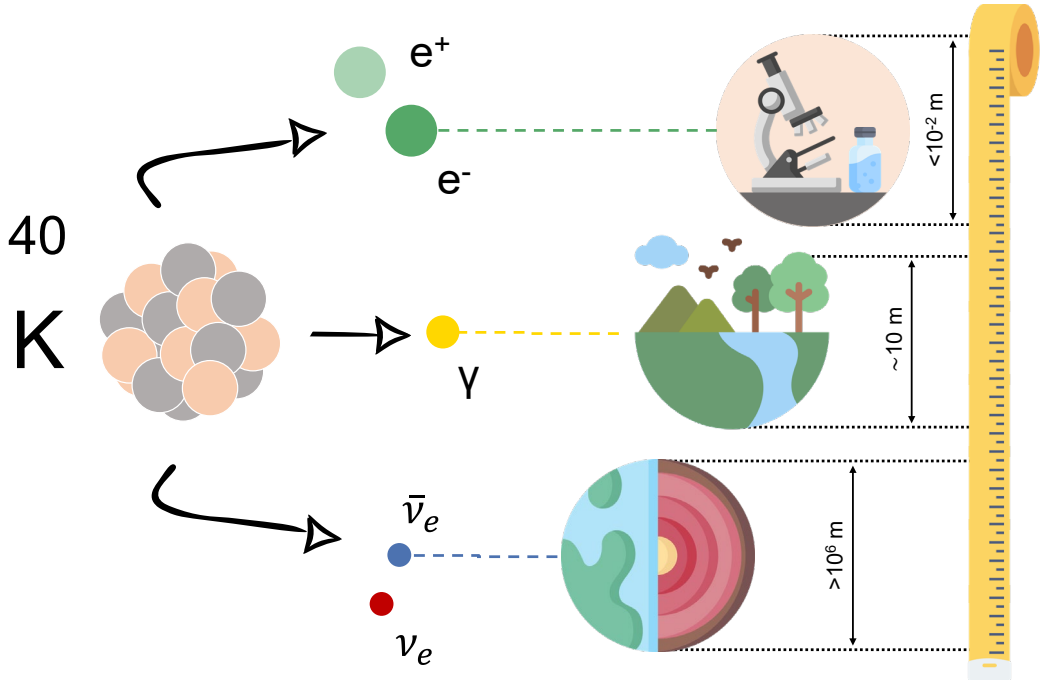

With these considerations in mind, the challenges I have set myself are two:

- What information can be recovered from the current experimental measurements of geoneutrinos? Is it possible to identify a detection technique that will finally allow us to measure ^{40}K geoneutrinos?
- Is it possible to exploit ^{40}K radioactivity to continuously estimate in real-time the soil water content at field scale?

These questions have accompanied me for the past 3 years and have led me to undertake a path of professional and personal growth to which I owe a lot. A path that I will try to expose and deepen in 3 chapters: a first chapter (Chapter 1) presenting the decay properties of ^{40}K, a second chapter (Chapter 2) dedicated to the study of the Earth through geoneutrinos and to possible detection techniques for ^{40}K antineutrinos, and a third chapter (Chapter 3) devoted to the application of ^{40}K gamma spectroscopy to precision agriculture.

Andrea Serafini

Exploiting ^{40}K radioactivity to probe the Earth and the environment

Observing the world from a different perspective

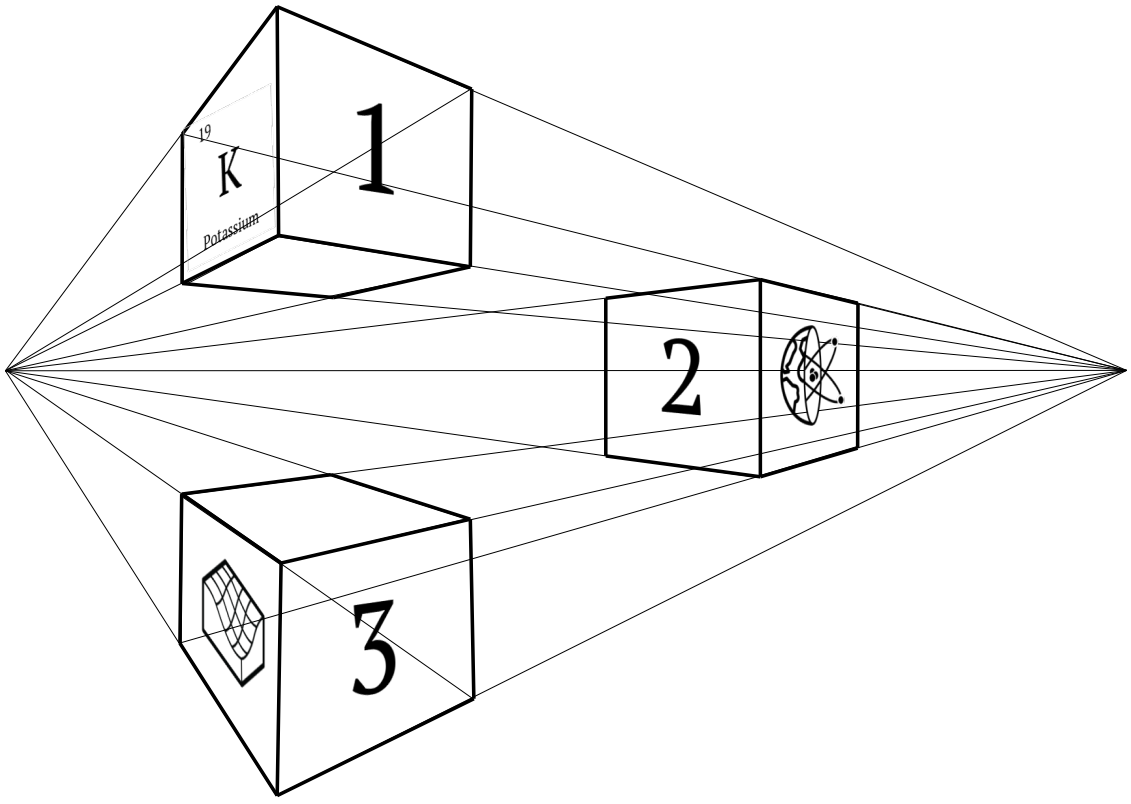

1.

PHYSICS OF ^{40}K

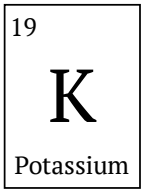

Potassium is a chemical element with the symbol K and atomic number 19. It is the eighth most abundant element on Earth, comprising about 2% of the Earth's crust and thought to represent from ~0.01% to ~0.02% of Earth's mass.

Pure potassium is a soft and waxy metal. However, it is a very reactive element and is rarely found free in nature. In the periodic table, potassium is one of the alkali metals, all of which have a single valence electron in the outer electron shell, that is easily removed to create a cation, that combines with anions to form ionic salts. Potassium reacts with oxygen to form potassium superoxide (KO_2) and with water to form potassium hydroxide (KOH). It is contained in several common minerals including sylvite (KCl), carnallite ($KCl{\cdot}MgCl_2{\cdot}6H_2O$), langbeinite ($K_2Mg_2(SO_4)_3$) and polyhalite ($K_2Ca_2Mg(SO_4)_4{\cdot}2H_2O$), with potassium chloride (KCl) being its most common compound. The latter, together with the potassium nitrate (KNO_3) is commonly used in agriculture as fertilizer. Potassium is therefore ubiquitous in soils, rocks and in Earth's crust in general. It is contained in Earth's mantle, and it is thought to be possibly included in small portions even in Earth's core (Chapter 2.2.3).

There are 25 known isotopes of potassium, with only three occurring naturally: ^{39}K (93.3%), ^{40}K (0.0117%), and ^{41}K (6.7%). Among these, ^{40}K is not stable. It can decay to ^{40}Ar and ^{40}Ca and represents one of the natural radioisotopes with largest abundance on Earth.

1.1 ^{40}K: decay properties

Potassium-40 (^{40}K) is a naturally occurring radioactive isotope of potassium. It is relatively abundant in nature, representing 0.0117% of the total amount of potassium. It has a long half-life of 1.248×10^9 years comparable to the age of the Earth (4.54×10^9 years), which makes it ideal to recover information on Earth's evolution, at the same time allowing to consider its abundance as constant on human timescales. Thanks to these properties, it represents an excellent tool to probe our planet and the environment around us.

^{40}K offers a wide variety of channels allowing its study, being a rare example of an isotope possibly undergoing both types of β decays and electron capture ε. With an 89.28% Branching Ratio (B.R.), ^{40}K undergoes β^- decay to ^{40}Ca ground state, emitting an electron (e^-) and an antineutrino ($\bar{\nu}_e$) (having maximal energy of E_{max}=1.311 MeV) [1]. On the other hand, 10.72% of the times, ^{40}K emits a neutrino (ν_e) while decaying to ^{40}Ar in one of the following processes: i) electron capture ε to ^{40}Ar ground state (0.046% B.R.) with the emission of a 1.5 MeV monoenergetic ν_e, ii) electron capture ε to ^{40}Ar excited state (10.67% B.R.) with the emission of a 43.6 keV monoenergetic ν_e and a deexcitation 1461 keV gamma photon (γ) and iii) β^+ decay to ^{40}Ar ground state (0.001% B.R.) with the emission of a positron (e^+) and a ν_e (E_{max} = 0.5 MeV) (Figure 2).

^{40}K	
Mass [AMU]	39.96399817(6)*
I.A. [%]	0.0117(1)
I.A. [%wt]	0.0197(9)
$T_{1/2}$ [10^9 y]	1.248(3)
Q^- [keV]	1310.91(6)
Q^+ [keV]	1504.40(6)

*number in brackets reports the uncertainty on the last digit

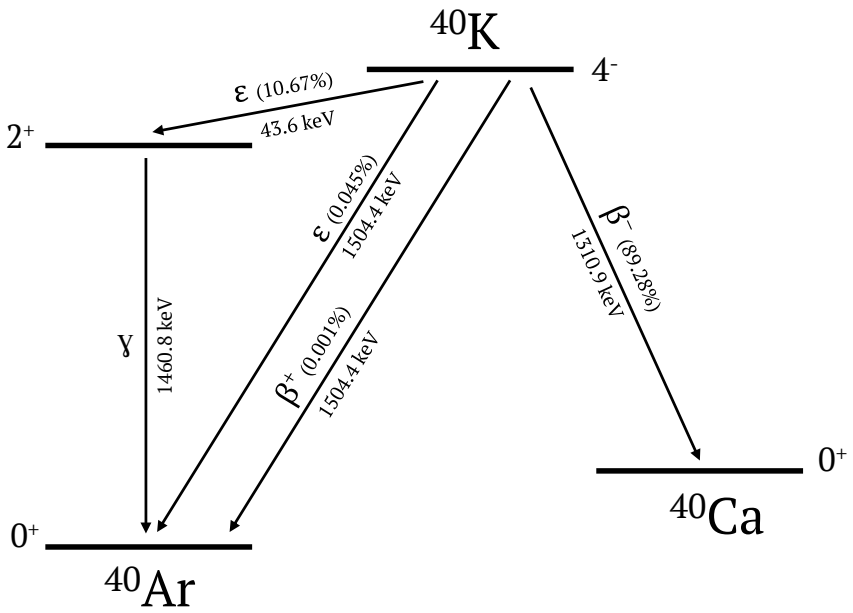

Figure 2. Decay scheme of ^{40}K. For each decay branch, the decay mode (electron capture ε, beta minus and beta plus decays $\beta^{-/+}$, gamma transition γ), its Branching Ratio (B.R.) (in brackets) and the associated decay energy (in keV) are reported. Decay data are taken from [1]. Spin and parity values (J^π) for each nuclear state are also reported alongside the corresponding level.

The resulting energy spectra of its diverse decay products (Figure 3) allows the use of various detection techniques probing different energy windows up to 1.5 MeV to investigate the presence and the abundance of ^{40}K in our planet and in the environment (Chapter 1.2).

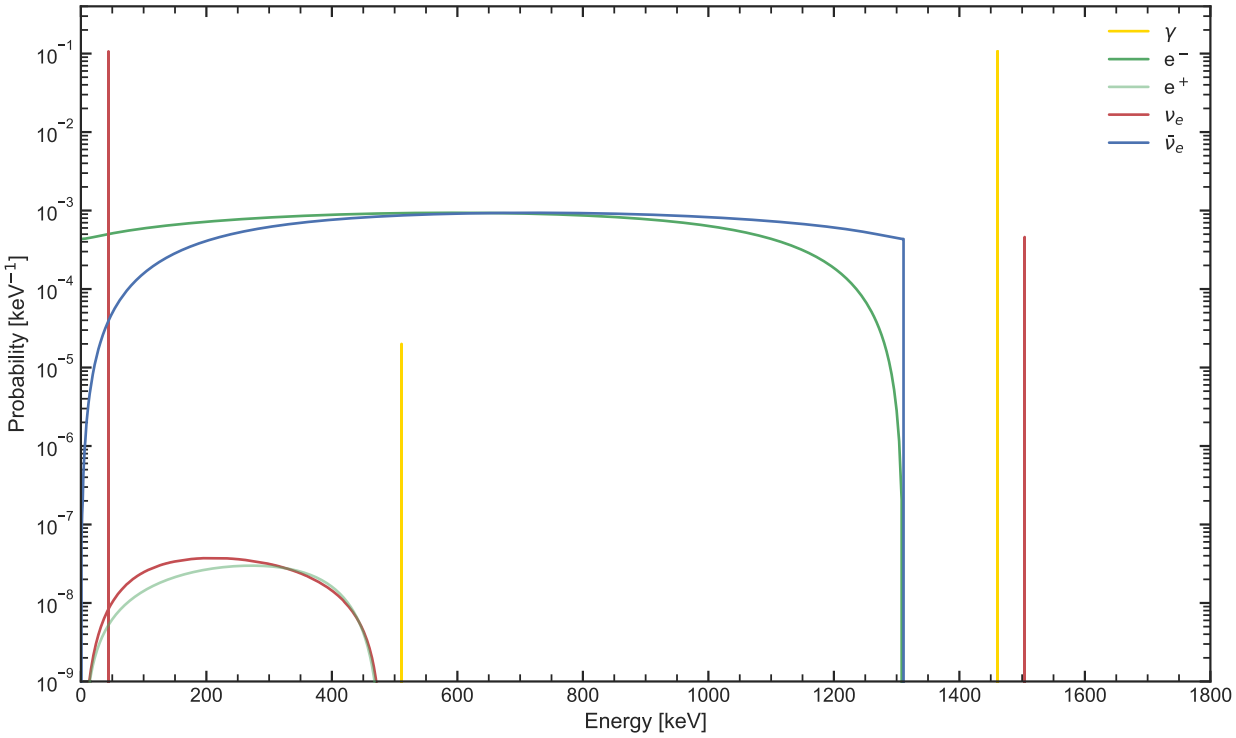

Figure 3. Energy spectra of ^{40}K decay products. Spectra are reported in red and blue when associated to the emission of a neutrino or an antineutrino respectively, in dark or light green when referring to electrons and positrons and in yellow for gamma photons. All continuous spectra were calculated via the Betashape utility [2].

1.1.1 β⁻ decay

The predominant decay channel of ^{40}K is via β⁻. With a branching ratio of 89.28%, ^{40}K decays to ^{40}Ca ground state by emitting an electron (e⁻) and an antineutrino ($\bar{\nu}_e$).

Decay	B.R. [%]
$^{40}\text{K} \rightarrow {}^{40}\text{Ca} + \text{e}^- + \bar{\nu}_e$	89.28(13)

Being a three-body decay, the total energy at disposal ($Q^- = 1310.9$ keV) is shared by the three outgoing particles as kinetic energy. However, because of the much higher mass of ^{40}Ca atom with respect to the other decay products, almost all of the energy is divided between the e⁻ and the $\bar{\nu}_e$, which present continuous energy spectra (Figure 4) ending at

1310.9 keV. On average, these two particles carry kinetic energies of $\langle E_{e^-} \rangle$ = 583.6 keV and $\langle E_{\bar{\nu}} \rangle$ = 727.3 keV, respectively.

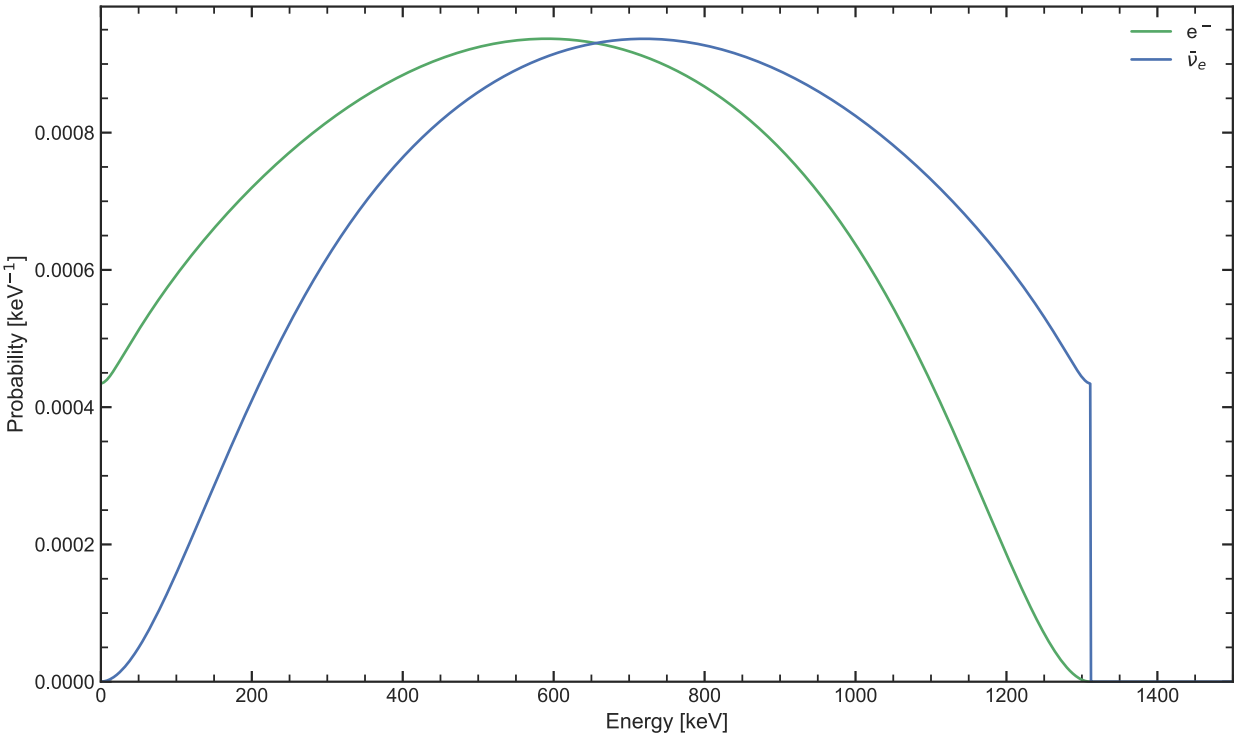

Figure 4. Energy spectra of ^{40}K β^- decay products. Spectra are reported in green and blue for electrons and antineutrinos, respectively. All spectra were calculated via the Betashape utility [2].

1.1.2 Electron capture and β⁺ decay

With a probability of 10.72%, ^{40}K decays to ^{40}Ar in one of the following processes: i) electron capture ε to ^{40}Ar ground state (0.046%), ii) electron capture ε to ^{40}Ar* excited state (10.67%) and iii) β^+ decay to ^{40}Ar ground state (0.001%).

Decay	B.R. [%]
$^{40}K + e^- \rightarrow {}^{40}Ar^* + \nu_e$	10.67(11)
$^{40}K + e^- \rightarrow {}^{40}Ar + \nu_e$	0.045(6)
$^{40}K \rightarrow {}^{40}Ar + \nu_e + e^+$	0.00100(13)

In its electron capture processes, ^{40}K absorbs one of its inner atomic electrons, producing ^{40}Ar and an electron neutrino (ν_e). Being a two-body decay, the outgoing products share the total energy at disposal (Q^+) in a ratio well defined by their masses. Because of the much higher mass of ^{40}Ar, the entire Q^+ is converted in kinetic energy for the outgoing ν_e, visible

as a monoenergetic line in the energy spectrum. Depending on the energy level of the final ^{40}Ar state, the net energy available to the ν_e is Q^+ = 1504.4 keV when decaying to ^{40}Ar ground state and Q^+ - E(^{40}Ar*) = 43.6 keV when decaying to ^{40}Ar* excited state. The resulting energy spectrum is thus characterized by two monoenergetic lines having energies and intensities defined by their Q^+ and branching ratios, respectively (Figure 5).

With a very small probability (0.001%), ^{40}K can decay directly to ^{40}Ar ground state via β^+, emitting a positron (e^+) and a ν_e. It is worth noting that in this decay, ^{40}Ar must shed an orbital e^- to balance charge. Thus, when calculating the energy at disposal of the decay products, two electron masses should be subtracted from the Q^+, leaving a total of $Q^+ - 2m_e$ = 482.4 keV available as kinetic energy for the outgoing particles. As in the case of β^-, almost all of the energy is divided between the e^+ and the ν_e, which present continuous energy spectra (Figure 5) ending at 482.4 keV. On average, these two particles carry kinetic energies of $\langle E_{e^+} \rangle$ = 251.8 keV and $\langle E_\nu \rangle$ = 231.2 keV. The emitted e^+ further slows down and annihilates, producing two back-to-back 511 keV gamma rays.

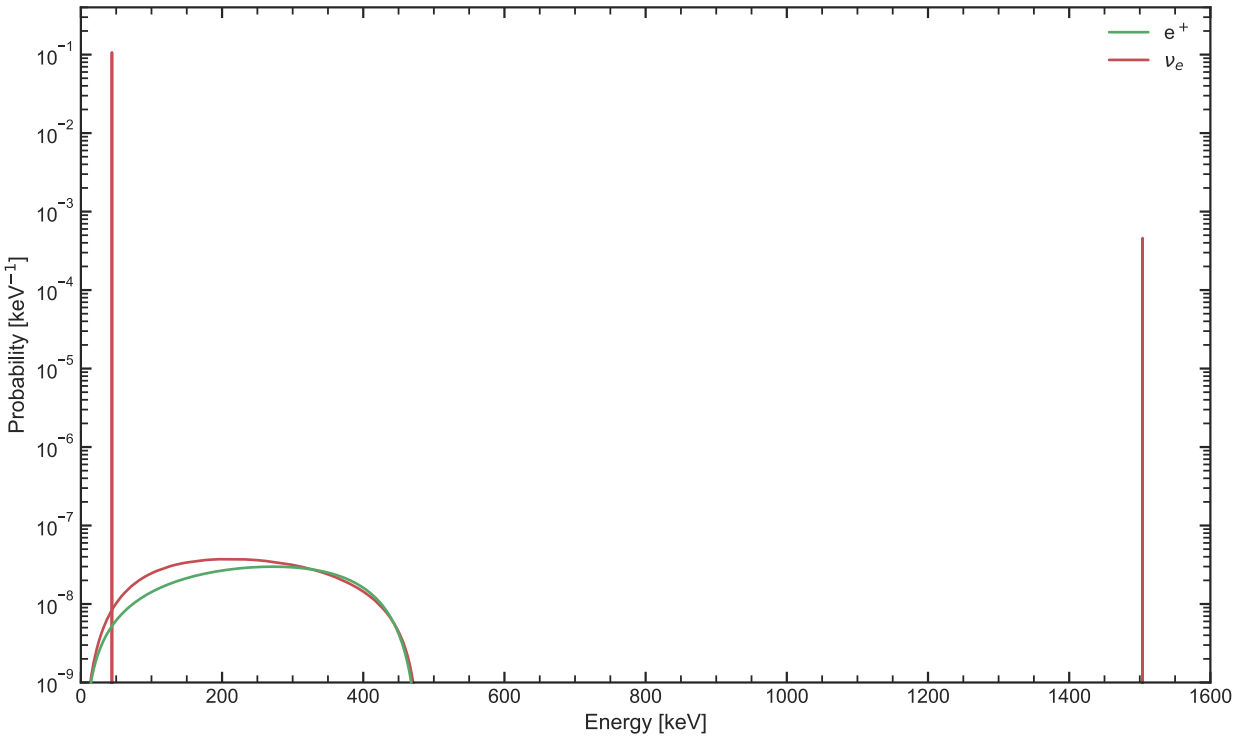

Figure 5. Energy spectra of ^{40}K ε/β^+ decay products. Spectra are reported in green and red for positrons and neutrinos, respectively. Continuous spectra were calculated via the Betashape utility [2].

1.1.3 γ transition

As we saw in the previous chapter, 10.67% of the times ^{40}K decays to ^{40}Ar* excited state via electron capture. The resulting ^{40}Ar* atom then reaches its stable configuration ^{40}Ar via a gamma (γ) transition (occurring 100% of the times) with a half-life of 1.15 ps.

Decay	B.R. [%]
$^{40}Ar^* \rightarrow {}^{40}Ar + \gamma$	10.66(13)[1]

The resulting gamma spectrum (Figure 6) thus present a monoenergetic line at 1460.8 keV, with a nearly invisible peak (having a branching ratio of 0.002%) at 511 keV caused by the emission of the two gamma photons following e^+ annihilation in β^+ decay.

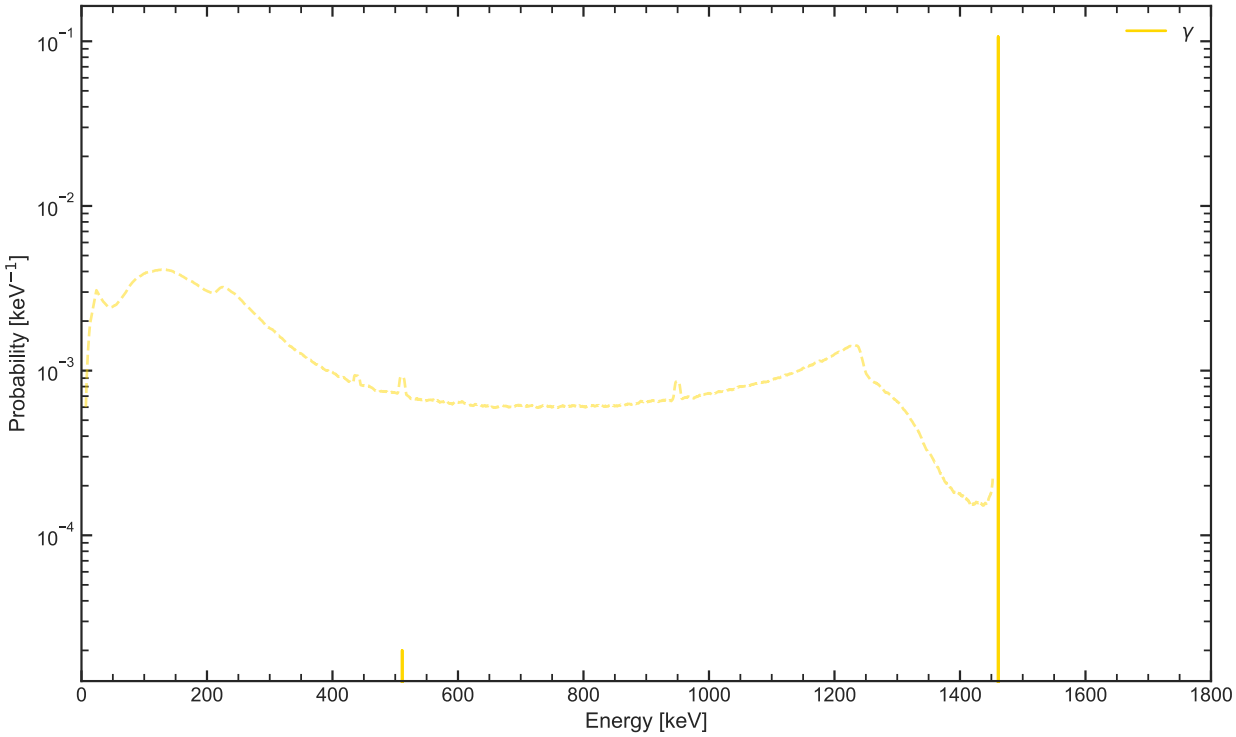

Figure 6. Energy spectra of the gamma emissions following a ^{40}K decay. Solid lines represent the gamma lines associated to ^{40}Ar* transition to ground state (1461 keV) and to the positron annihilation **(**511 keV**)** following a β^+ decay. The dashed line reports an experimental gamma spectrum measured via a HPGe detector, with photopeak (1461 keV) intensity normalized to the theoretical B.R. (10.66%). At energies below the photopeak, it is possible to observe the so-called Compton continuum caused by the scattering of photons on electrons, the single- and double-escape peaks (at (1461-511 keV and 1461-2 · 511 keV, respectively), and the peak associated to photons' pair production **(**511 keV**)**.

[1] Derived from the β^- B.R. and corrected for the measured γ/β^- ratio.

1.2 Exploiting ^{40}K to sense our world

The rich variety of products offered by ^{40}K decays presents a wide range of channels allowing the detection of this radioisotope. The different interactions of its products with matter provide a way to indirectly probe the presence and the abundance of ^{40}K in the Earth and in the environment. Each of these particles has different peculiarities and in general a different probability for its interaction with matter to occur.

The measure of the probability that a specific process will take place is usually quantified via the cross section (σ). Besides ruling the interaction probability in the detection process, the cross section indirectly regulates the distance that a particle of energy E can cover before scattering via the linear attenuation coefficient μ:

$$\mu(E) = n\,\sigma(E)$$

where n is the density of the target (in targets cm^{-3}) and σ is the interaction cross section (in cm^2) on that target. The intensity I of an unscattered particle beam crossing a homogeneous material having linear attenuation coefficient μ is reduced during its path of length L according to the exponential law:

$$I(E, L) = I(E, 0)\, e^{-\mu L}$$

The cross section thus provides a rough estimate of the spatial scale that is possible to investigate by using that specific particle as a probe (Figure 7).

As we saw in the previous subchapters, ^{40}K decay products consists of electrons, positrons, gamma photons, neutrinos, and antineutrinos. The interaction of electrons and positrons with matter is mediated by the electromagnetic force. At MeV scale, these massive and charged particle hardly travel more than a cm in matter [3], hence making them useful only to probe small-scale phenomena. They are used for instance in the treatment of superficial tumors like cancer of skin regions, diseases of the limbs or nodal irradiation [4].

Gamma photons electromagnetically interact with matter, but being massless and neutrally-charged, the cross section for their interaction is several orders of magnitude lower than electrons' one. Consequently, they can travel from tens of centimeters (when travelling in rocks and soil) up to hundreds of meters (when traveling in the air). They can thus be used as probes to study and understand the environment around us and to characterize natural radioactivity at field-scale (~10 m, Chapter 3).

Neutrinos and antineutrinos weakly interact with matter. Their cross section is typically lower than 10^{-42} cm^2 per target and they can thus travel billions of kilometers without being stopped or attenuated. Their small cross section makes them elusive and challenging particles to detect, but at the same time it makes them precious messengers that allow to recover information on the unexplored parts of the inner Earth, inaccessible to other probes (Chapter 2).

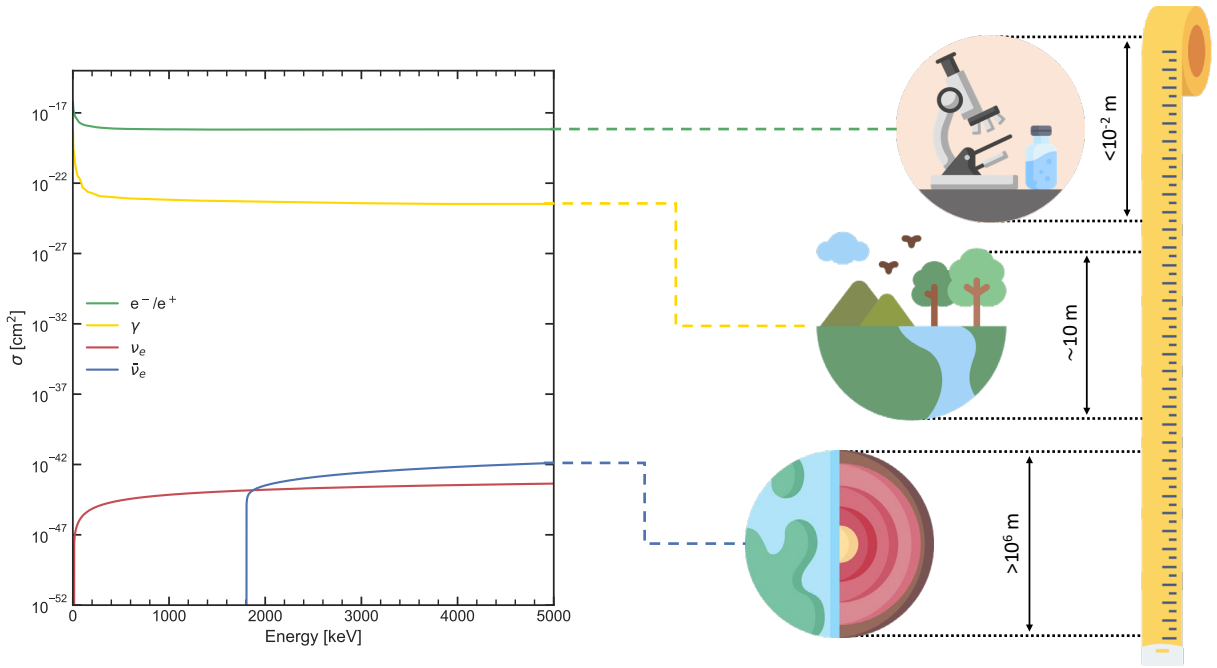

Figure 7. Sketch of the cross sections for unit target for electrons, positrons (in green), gamma photons (in yellow), neutrinos (in red) and antineutrinos (in blue) as a function of their energy. Electron cross section is adapted from [5]'s estimates on water targets, positron cross section is here considered as equal to electron's one, gamma cross section is taken from [6] and neutrino and antineutrino cross sections are calculated according to the elastic scattering on electrons and Inverse Beta Decay on protons formulas discussed in Chapter 2.9.1, respectively. For each cross section a rough estimate of the spatial scale that is possible to investigate by using that particle as a probe is reported on the right.

2.

CHALLENGES IN PARTICLE PHYSICS

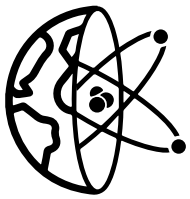

The ephemeral proprieties of neutrinos have always been the blessing and the curse for their employment in the comprehension of the Universe. Their weak interaction with matter makes them particularly elusive particles to detect, but also precious probes for exploring the most remote parts of the Earth, Sun and stars. The use of neutrinos for the real-time monitoring of the thermonuclear fusion processes occurring in the Sun's core has represented a major astrophysics milestone of the past fifty years. Concurrently, starting from the mid-twentieth century, the electron antineutrinos originating from β^- emitters inside our planet (^{238}U, ^{232}Th and ^{40}K), geoneutrinos, were proposed as a precious tool for exploring the inner Earth. Since from the first formulation of this hypothesis, it was clear to everyone that the low expected flux and the small cross section would have represented an arduous technological challenge for future experiments. The lack of stringent constraints on the radiogenic contribution to terrestrial heat power and the impossibility of having direct geochemical insights of the deep Earth, make neutrino geoscience a particularly multifaceted and convoluted discipline.

After the claims of the first uranium-238 (^{238}U) and thorium-232 (^{232}Th) geoneutrino observations by the KamLAND collaboration in 2005 [7] followed by the Borexino collaboration in 2010 [8, 9], the results published with greater statistical significance in the second decade of the 21st century highlighted an unavoidable necessity of geophysical and

geological models for understanding geoneutrino signals. The next decade will open the era of "multi-site detection" of geoneutrinos. By 2030, humanity would collect the results from four experiments spread over three different continents: KamLAND and JUNO in Asia, Borexino in Europe and SNO + in America.

All these direct measurements of antineutrinos produced by U and Th decay chains in the bowels of the Earth will pose stringent constraints to fundamental questions about the formation, thermal history, dynamics, and composition of our planet. This monumental experimental effort will be in vain unless followed by an equally enormous joint effort between particle physicists and Earth scientists in understanding each other's paradigms and methods (Figure 8). The study of uncertainties and their correlations is the new frontiers of geoneutrino science: no experimental data will be fully understood without the development of a common ground among different disciplines.

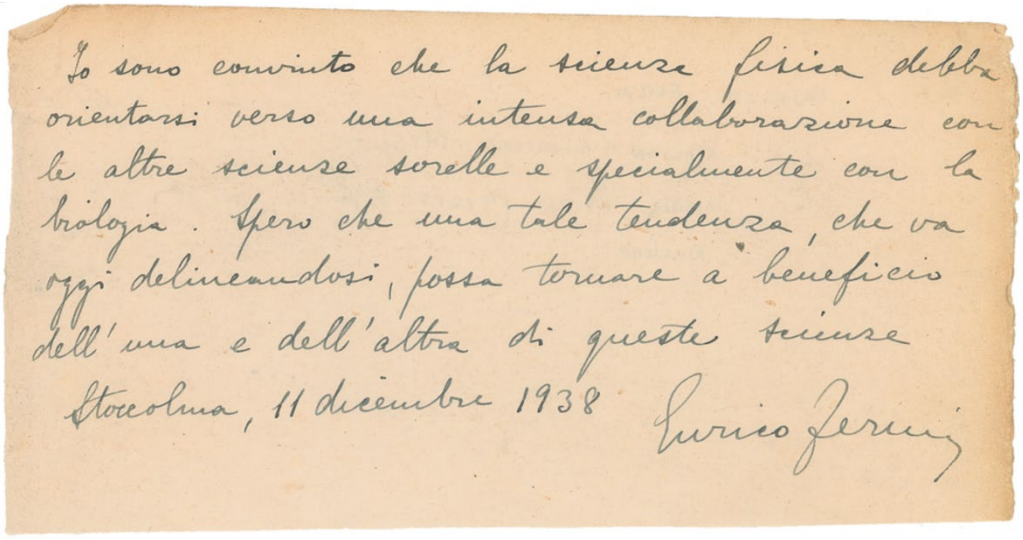
Io sono convinto che la scienza fisica debba orientarsi verso una intensa collaborazione con le altre scienze sorelle e specialmente con la biologia. Spero che una tale tendenza, che va oggi delineandosi, possa tornare a beneficio dell'una e dell'altra di queste scienze
Stoccolma, 11 dicembre 1938 Enrico Fermi

Figure 8. A handwritten note from Enrico Fermi on the importance of interdisciplinarity. The document is preserved at Museo Storico della Fisica e Centro Studi e Ricerche Enrico Fermi (CREF). Translation is available at https://cref.it/en/the-institute/.

In this perspective, after reviewing the present state-of-the-art understanding on Earth structure and main composition, I combined KamLAND and Borexino experimental data in view of present geophysical and geochemical models to gather insights on mantle radioactivity.

While current geoneutrino measurements can already provide precious information on mantle's heat power, they currently rely on a model dependent K/U ratio. Because of their low energy (<1.311 MeV) and the threshold (1.806 MeV) of the currently employed

detection technique, the measurement of ^{40}K geoneutrinos still remains an unattended goal. A direct measurement of the ^{40}K heat power would provide an experimental constraint to the radiogenic fraction of the Earth's internal heat budget and critical information about the behaviour of volatile elements during Earth's early stage formation [10]. Measuring ^{40}K geoneutrinos would also be crucial to shed light on the "missing K" hypothesis and in turn provide insights into Earth's composition, structure, and thermal evolution; thus, this may stand as the most important quest and challenge for geoneutrino research in the near future.

To explore this low energy region of the geoneutrino spectrum, considered today as being practically undetectable, I discuss a set of new reactions with an energy threshold lower than 1.311 MeV, together with a possible experimental approach.

2.1 A picture of the Earth

2.1.1 The structure of the Earth

The major divisions of the Earth's interior in crust, mantle and core have been known from seismology for about 80 years. This knowledge is based on the reflection and refraction of primary (P) and secondary (S) body waves emitted by earthquakes and traveling through the interior of the Earth. Thanks to the linear relation between compressional P-wave velocity (v_P) and the density (ρ) of rocks and minerals [11], it was possible to accurately establish a density profile for our planet [12, 13]. The obtained Earth's density profile can be further tested and constrained through the measurement of the terrestrial moment of inertia, which notoriously differs from that of a homogeneous sphere (Table 1). The picture that emerges is of a concentrically layered planet, characterized by a density increasing monotonically with depth, subdividable in a solid inner core (IC), a liquid outer core (OC) consistent with the absence of shear waves, a highly viscous mantle and an outer solid shell called lithosphere (LS).

Each Earth reservoir is separated from the others by sharp changes in density (Figure 9). These seismic discontinuities are the result of compositional boundaries or mineralogical phase changes and are often associated with the presence of transition zones. The most significant compositional boundary in the Earth is the core–mantle boundary (CMB), which is surmounted by a ~200 km thermal boundary layer called D'' zone, whose inhomogeneities determine some properties of hotspots and mantle convection (Chapter 2.1.3). Instead, the

410-660 km transition zone is a well-documented thermally controlled boundary layer which defines an Upper Mantle (UM) and a Lower Mantle (LM), possibly distinct in composition. Finally, the boundary between the crust and the mantle is called the Mohorovicic discontinuity (MOHO) and it may be a chemical change or a phase change or both. In its uppermost part, the UM is further subdivided by the Lithosphere-Asthenosphere Boundary (LAB), a seismic and electromagnetic transition whose depth (typically at ~175 km) is still a topic of debate. The solid and rigid UM underlying the continents contained between the LAB and the MOHO is usually referred to as Continental Lithospheric Mantle (CLM). The ductile mantle below the LAB is often called sublithospheric mantle, hereafter referred to simply as mantle (M). The silicate portion of our planet, corresponding to M and LS, is known as Bulk Silicate Earth (BSE).

The IC extends from Earth's center up to ~1220 km. It is solid and represents only 5% of the core's mass. The remaining portion of the core, the OC, is instead liquid and extends from 1220 km up to the CMB, situated at ~3480 km. Having a mass of $1.8 \cdot 10^{24}$ kg, the OC is the second main reservoir of our planet after the mantle. The mantle extends from the CMB up to the MOHO for a total mass of $4.01 \cdot 10^{24}$ kg. Most of this mass ($3.911 \cdot 10^{24}$ kg) is attributed to the sublithospheric mantle, which extends from the CMB to the LAB for a total of ~2800 km. The CLM, together with the rest of the oceanic crust (OCC) and continental crust (CC), forms the LS, the outer rocky shell of our planet.

Table 1. Average thickness, bulk masses [14], factor of inertia [15] of different Earth's reservoirs. Columns 5-7 list the average density (ρ) and the velocities of P (v_p) and S (v_s) seismic waves obtained from the seismic profile of the Earth [12]. Columns 8-10 report the order of magnitude of the expected abundances of U (a(U)) and Th (a(Th)) together with the main four elements composing the reservoir.

Reservoir	Thickness [km]	Mass [kg]	Inertia factor	ρ [kg/m^3]	v_p [km/s]	v_s [km/s]	a(U) [µg/g]	a(Th) [µg/g]	Main elements
Oceans	3.7	$1.36 \cdot 10^{21}$	-	1025	-	-	~0.001	~0.000001	O, H, Cl, Na
Athmosphere	16 (480)	$5.15 \cdot 10^{18}$	-	<1.2	-	-	0	0	N, O, Ar, C
CC	35-40	$20.6 \cdot 10^{21}$	-	2861	5.7	3.1	~1	~1	O, Si, Al, Fe
OCC	7-10	$6.6 \cdot 10^{21}$	-	2826			~0.1	~0.1	
CLM	140	$97 \cdot 10^{21}$	-	3370	-	-	~0.01	~0.1	O, Mg, Si, Fe
M	2800	$3.911 \cdot 10^{24}$	0.29215	4776	10.2	5.5	~0.01	~0.01	O, Mg, Si, Fe
OC	2260	$1.835 \cdot 10^{24}$	0.03757	10832	9.5	0.14	0	0	Fe, Si, Ni, S
IC	1220	$9.675 \cdot 10^{22}$	0.000235	12720	11.2	3.6	0	0	
BSE	2891	$4.035 \cdot 10^{24}$	0.29217	4420	9.4	5.1	~0.01	~0.01	O, Mg, Si, Fe
Earth	6371	$5.972 \cdot 10^{24}$	0.3299765	5510	9.5	4.4	~0.01	~0.01	Fe, O, Si, Mg

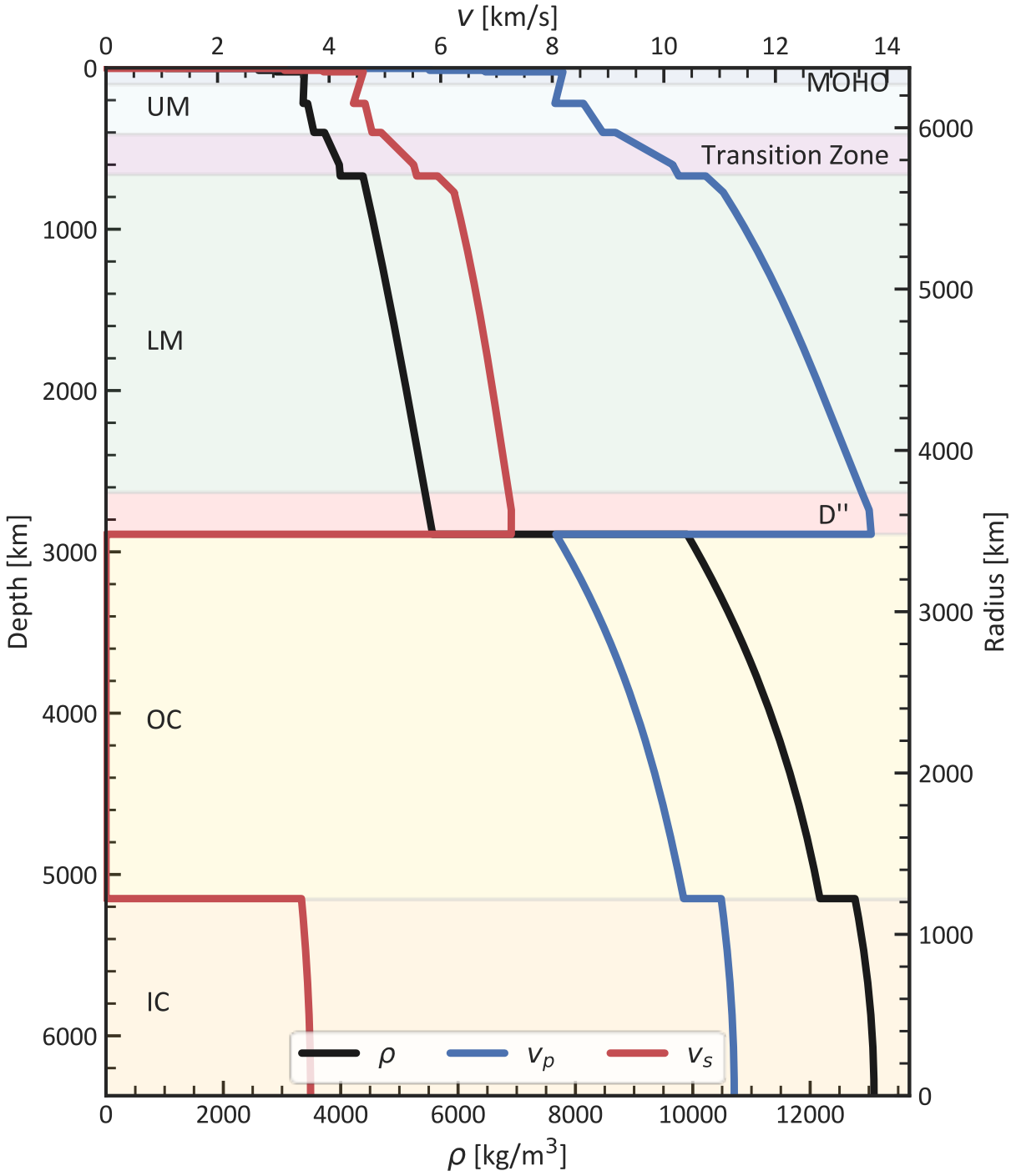

Figure 9. Profile of Earth's density (in black) and of primary and secondary seismic velocities (in blue and red, respectively) as a function of depth [12]. The density profile clearly highlights the main Earth's seismic discontinuities (MOHO, D'' and the Transition Zone) which delimit different reservoir of our planet: Upper Mantle (UM), Lower Mantle (LM), Outer Core (OC), Inner Core (IC).

2.1.2 The composition of the Earth

Despite Earth's internal structure is relatively well established, its deep interior remains inaccessible, making its bulk composition impossible to measure directly. However, there is broad agreement among Earth scientists in stating that Earth is mainly made out of Fe (32%wt), O (30%wt), Si (16%wt), Mg (15%wt), Ca (2%wt), Al (2%wt) and S (1%wt), which together account for ~97% of our planet's mass [16, 17]. All other elements are present in smaller fractions and the assessment of their abundances requires the formulation of compositional models, which are still under great debate (Chapter 2.3).

The peculiar structure of the Earth is a consequence of the physical and chemical processes that occurred in Earth's early history. The fundamental result of planetary differentiation is that elements are not uniformly distributed in the Earth, but rather controlled by their combination of chemical and physical affinities. According to their preferred host phases (Figure 10), elements are generally grouped following the Goldsmith geochemical classification, into:

(i) lithophile elements which tend to occur with oxygen in oxides and silicates;
(ii) siderophile elements which tend to be metallic and readily dissolve in iron either as solid solutions or in molten state;
(iii) chalcophile elements which tend to concentrate as sulphides combining readily with sulfur and other chalcogen other than oxygen;
(iv) atmophile elements which tend to not form stable compounds (e.g. noble gases) and occur in liquids and/or gases (H, C, N) at temperatures and pressures found on the surface of the planet.

According to their condensation temperature[2] (T_C) elements are further categorized in refractory (T_C > 1300 K) and volatile (T_C < 1300 K).

[2] The condensation temperatures are the temperatures at which 50% of the element will be in the form of a solid (rock) under a pressure of 10^{-4} bar.

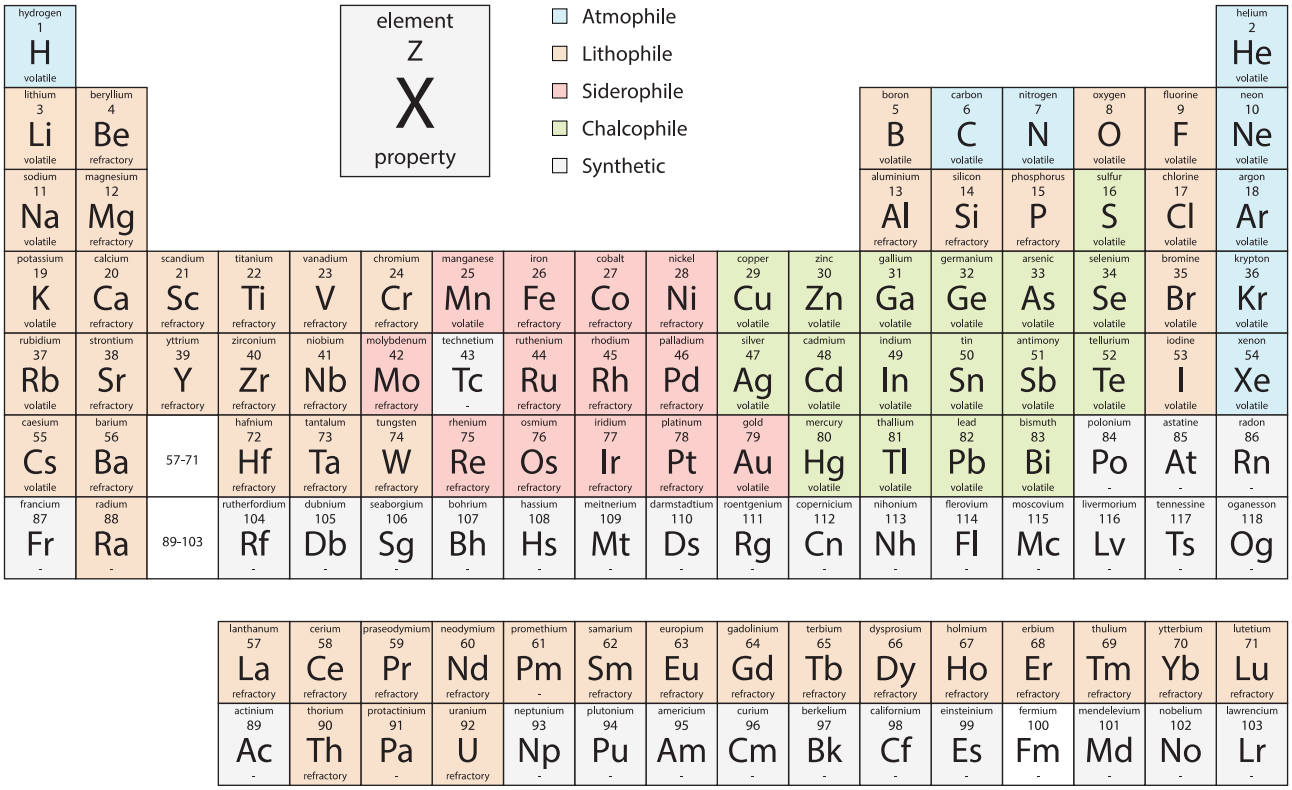

Figure 10. Chemical affinities (denoted by colors) and tendency to volatize (described in the element property) for the different elements of the periodic table.

In this complicated scenario, the only elements reliably accessible to Earth science are the refractory lithophile elements (RLEs). These elements followed the same behavior in the early Solar System, as demonstrated by the fact that they share the same abundance ratios in all types of chondritic meteorites known [18]. Considering that lithophile elements are not likely to be incorporated in the core, measuring the RLE content of M and LS, translates into assessing the RLE's content for the bulk Earth. Instead, since refractory siderophile elements are so concentrated in the core, these are known for their rarity in the Earth's crust. However, they are believed to be present in the bulk Earth according to their solar abundances.

On the other hand, volatiles appear heavily depleted on Earth when compared to meteorites and other undifferentiated bodies of the Solar System. The volatile lithophile elements show a coherent depletion pattern as a function of their T_C [19-21], hinting to depletion mechanisms at the basis of our planet accretion and evolution [21, 22]. For elements that are both volatile and siderophile, the complexities of the volatile-element depletion add to our lack of knowledge on how much of an element's loss is due to volatility and how much is due to partitioning into the core [19].

The present picture of the Earth sees a core mainly composed of Fe and a fraction of siderophile elements, which have sunk into the core because of their chemical affinity with iron. At inner core pressure and temperature conditions, it is predicted that a pure iron core should be solid, but its density would exceed the known density of the core by approximately 3%. This requires the presence of a light component in the IC (e.g. O, Si, S in the form of oxides or sulfides, accounting for 2-3%wt), in addition to the probable presence of Ni (up to 10%wt) [23]. The OC is instead liquid (as testified by the absence of S-waves propagation, Figure 9), it shares the same main composition of the IC, but it is expected to have about twice the fraction of light elements envisaged for the IC and to contain 8-13% of O [23, 24]. Recent studies investigated the possibility of HPEs inclusion in the core, finding that only small amounts could be potentially included (up to 10 ng/g of U, 21 ng/g of Th, 250 µg/g of K) [25-30] (Chapter 2.2.3). Even so, this possibility cannot be completed ruled out yet and the debate is still open within the scientific community.

The remaining portion of the Earth, the so-called BSE, is instead rich in chalcophile and lithophile elements. These elements readily combined with chalcogens remaining close to the surface and not sinking into the Earth's core. Cooling and crystallization of mantle over timescales of millions of years resulted in its chemical differentiation according to density. This differentiation could have left most of the Earth’s mantle different in composition from the uppermost sampled part of it [31], opening a debate as to whether the rest of the mantle has the same bulk composition. The outer portion of the mantle, slowly solidified in the now-called LS, which consequently ended up being highly enriched in incompatible elements (such as U and Th), unsuitable in size or charge to the cation sites of the surrounding minerals.

The mantle is the largest Earth’s reservoir, and therefore it dominates any attempt to perform major-element mass balance calculations. Most estimates of its composition are based on rocks that sample only the uppermost mantle. The mantle is thought to be mainly made of O, Mg, Si, Fe and other chalcophile elements.

Instead, the lithosphere is the smallest solid Earth’s subdivision (2% wt), but it contains a large fraction of the terrestrial inventory of many elements. The present surface crust represents 0.4% of the Earth’s mass and 0.6% of the silicate Earth, but contains a very large proportion (20-70%, depending on the element) of incompatible elements, such as the two HPEs, U and Th. Thus, the crust factors prominently in any mass balance calculation for the Earth as a whole and in estimates of the thermal structure of the Earth.

2.1.3 A dynamic Mantle

Starting with the formulation of continental drift theory and plate tectonics, during the last century the idea of a dynamic Earth started to persuade geoscientists. Although initially it was thought that the mantle was too rigid to allow movements, later measurements (mantle viscosity by postglacial rebound) established that the mantle behaves as a fluid on long time scales. In the current understanding of our planet, continental motion and seafloor spreading are driven by convective motions of the mantle. Thanks to the advances in computing power over the 2000s decade, the field of mantle dynamics came a long way through the use of numerical simulations. The modern knowledge of mantle convection can rely on a multitude of inputs as (i) paleomagnetic studies which prove the relative continental motion and seafloor spreading, (ii) seismology which provides the delineation and locations of plate boundaries and subducting slabs along Wadati–Benioff zones (i.e. planar zones where the oceanic crust sinks under the continental lithosphere), and (iii) geodetic measurements of Earth's gravity field which ensure important constraints about the density structure of the mantle associated with convection [32]. Heat flow and bathymetry measurements show that lithospheric plates move from hot ridges to cold trenches, testifying that these structures are the expression of upwellings and downwellings. These plates spreading and subduction at ridges and slabs, demand vertical transfer of material from the mantle into the surface and vice versa. The material exchange is largely proven as shown by tomographic images of down-going slabs of oceanic lithosphere penetrating into the lower mantle [33], leaving little doubts that the mantle convects. The current debate is about "how" it convects.

Indeed, an additional and independent source of information comes from mantle geochemistry. The disparity between the concentration of incompatible elements in composition of mid-ocean ridge basalts (MORBs) representative of the upper portion of the mantle and ocean island basalts (OIBs) thought to come from the lower mantle was one of the driving motivations for supposing the preservation of isolated reservoirs and, thus, a layered mantle. Additional evidence come from geochemical arguments involving noble gas isotopes, volatiles abundances and elemental ratios. However, these geochemical observations seem to conflict with geophysical evidence for whole mantle convection and this has engendered a long-standing debate about the details of mantle convection. High-pressure mineral physics experiments indicated that mantle discontinuities are most likely associated with solid–solid phase transitions, not compositional changes. The major upper mantle component olivine was shown to undergo a change to a spinel structure called

wadsleyite at 410 km depth; wadsleyite itself undergoes a less dramatic transition to a ringwoodite at around 510 km and then, at 660 km depth, ringwoodite changes to a combination of perovskite and magnesiowustite. Studies of convection in the presence of such phase changes indicated that they might impede convection temporarily but not indefinitely. Seismic tomographic studies using body waves showed that many slabs do indeed penetrate this boundary and sink well into the lower mantle [34, 35].

In the last years, various complexities were discovered in the deep lower mantle that was previously considered as rather homogeneous. At small scale, a laterally intermittent layer at the base of D" ultralow-velocity zone (ULVZ) (Figure 11), with a maximum thickness near 40 km and a strong decrease of v_p, is most simply explained as the result of partial melt at this depth [36]. A pair of seismic discontinuities observed in some fast (cold) regions of D" could be the result of a double-crossing of the postperovskite phase boundary by the geotherm at two different depths [37]. Two deep slow velocity anomalies under West Pacific and Africa (roughly underneath the two maxima of the geoid) have unusual seismic properties. They have an anomalously large ratio of compressional to shear velocity ratio, v_P/v_s [38], and an anticorrelation between ρ and seismic velocities [39] and between v_P and v_s [40]. These anomalous regions have very sharp boundaries [41] and depending on the authors have been named megaplumes, thermochemical piles, or large low-shear-velocity provinces (LLSVPs) [42]. These LLSVPs only cover part of the CMB surface (Figure 11), which is itself four times smaller than the Earth's surface, and as they only extend up to a few hundred kilometers, their total volume is three times larger that of the continental crustal volume [43]. These observations of the deep mantle heterogeneity cannot easily be explained by temperature variations. They seem to require lateral variations of Fe or Si contents in the mantle and, more in general, compositional inhomogeneities [44, 45], although some authors interpret these observations in the framework of pure thermal models [46]. The LLSVP should be intrinsically denser to resist entrainment by convection. These compositional pyramids may anchor the hot spots [47]. The presence of a petrologically dense component of the source of hot spots also seems necessary to explain their excess surface temperature [48]. These abyssal heterogeneities help to bridge the gap between geochemical observations and convection modeling [49, 50].

The current leading hypothesis for the LLSVPs is the accumulation of subducted oceanic slabs. This corresponds with the locations of known slab graveyards surrounding the Pacific LLSVP. These graveyards are thought to be the reason for the high velocity zone anomalies surrounding the Pacific LLSVP and are thought to have formed by subduction zones that

were around long before the dispersion—some 750 million years ago—of the supercontinent Rodinia. Aided by the phase transformation, the temperature would partially melt the slabs, to form a dense heavy melt that pools and forms the ULVZ structures at the bottom of the CMB closer to the LLSVP than the slab graveyards (Figure 11). The rest of the material is then carried upwards due to chemical buoyancy and contributes to the high levels of basalt found at the mid-ocean ridge. The resulting motion forms clusters of small plumes right above the CMB that combine to form larger plumes and then contribute to "superplumes". The Pacific and African LLSVP, in this scenario, are originally created by a discharge of heat from the core (4000 K) to the much colder mantle (2000 K), the recycled LS is only fuel that helps to drive the superplume convection. Since it would be difficult for the Earth's core to maintain this high heat by itself, it gives support for the existence of radiogenic nuclides in the core, as well as the indication that if fertile subducted LS stops subducting in locations preferable for superplume consumption, it will mark the demise of that superplume.

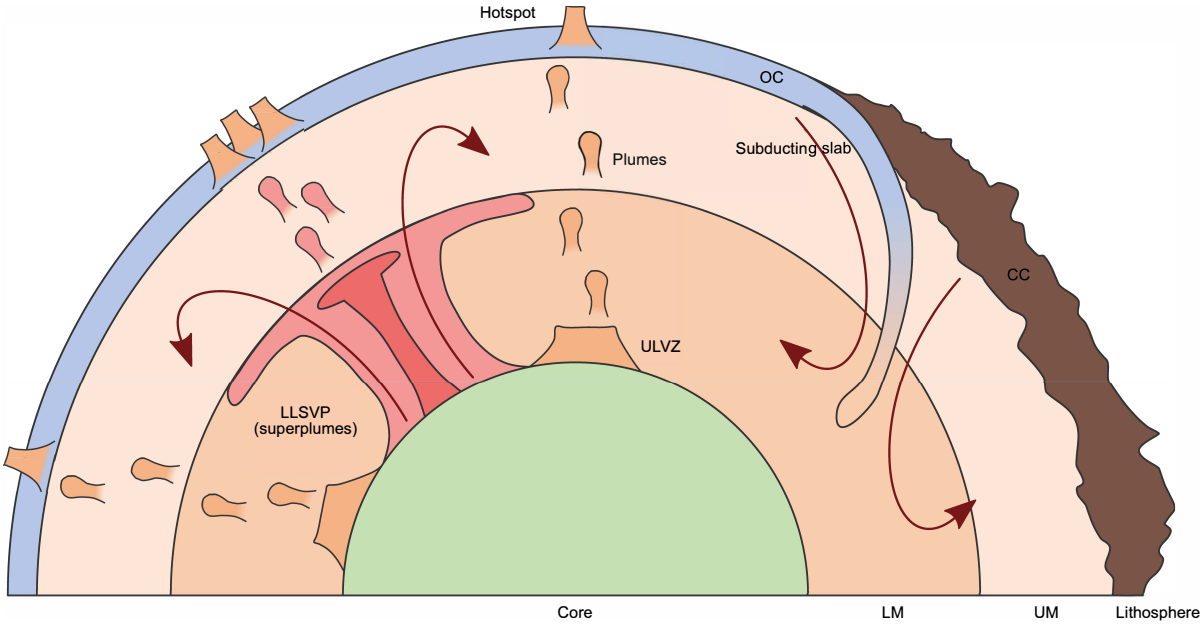

Figure 11. Schematic picture of main mantle features and the dynamic processes causing mantle inhomogeneities.

The continuous evolution of our knowledge on the mantle was reflected in the last decades in a multitude of different geochemical models proposed, predicting (i) an homogeneous model, with an upper and lower mantle of similar compositions [17, 24, 51, 52] and (ii) a layered model, with an upper and lower mantle of distinctly different compositions [53-56]. Rather than using the usual seismic separation at 410 km, variants on these models envisage a compositional layering involving only parts of the lower mantle, hence distinguishing the mantle in a so-called enriched mantle (EM) and a depleted mantle (DM).

These concepts include basal mantle cumulate layers resultant from early Earth magma ocean conditions [57, 58], or gravitationally sequestered layers of early-enriched crust [59].

2.2 Energetics of the Earth

2.2.1 The measured heat power (Q)

Heat flow measurements at Earth's surface tell us that our planet is cooling down: in other words, it is losing energy. After many decades of research, the cooling of the Earth is still a central issue of the today's debate in solid Earth Sciences. In contrast with the leading theory of the last century, conduction is not the only way in which Earth is releasing heat. As a matter of fact, convective motions driving the oceanic plates and radioactive decays of HPEs are responsible for a large fraction of surface heat loss [60-62].

The Earth's heat flow brings to surface crucial information regarding the thermal conductivity and heat production of the Earth's interior. Heat flux measurements are characterized by strong variability on different spatial scale and are function of multiple variables, such as geologic age and geological settings. The spatial integration of individual measurements of heat flux over the surface represents the most direct method for calculating the heat loss rate of the Earth and for obtaining global maps of surface heat flux [63]. The weak points of this approach are mainly two: heat flow observations are (i) sparse and non-uniformly distributed across the globe and (ii) not reliable in the oceans. Oceanic heat flux measurements suffer by systematic errors due to the specific environment: the conventional measurement techniques only account for conductive heat transport (i.e. conduction through soil matrix in permeable rock and sediments). The quantitative assessment of heat transport by hydrothermal circulation (i.e. the water flow through pores and fracture into the sea) remains difficult and feasible only in small-scales studies. For this reason, the energy loss through the sea floor is generally estimated by means of models validated in selected environments whose results are compared with the mantle temperature beneath mid-ocean ridge and the evolution of seafloor bathymetry [61]. The half-space models or plate cooling models imply diverse boundary conditions, but all assume that the oceanic lithosphere is hot at its formation at the mid-oceanic ridge, and it cools moving away from the spreading centers. The heat flux from the oceans can be calculated on the basis of temperature variation with depth, distance to the spreading center and different parameters such as thermal properties of the cooling litosphere, the age of the sea floor and temperature of the magma ascending [64]. For the continents, the

situation appears less complicated since to date more than 50000 heat flux measurements [65] from the continents and their margins are available. Nevertheless, as previously mentioned, the irregular and biased spatial distribution motivates a careful statistical treatment of the raw heat-flow dataset including removal of obvious outliers, opportune weighted averaging and combining of statistical errors [66].

From the 1970s, comprehensive estimates of the global surface heat flux were undertaken by different authors adopting measurements of thermal conductivity of rocks and temperature gradients within bore holes for continents and energy loss-models for oceans. The measurements continue to increase and to be refined over time until they achieve Earth's surface heat flux estimates agreeing at around 44-47 TW [63]. The only exception is the lower limit estimation (31 TW) provided by [67] whose approach is based on direct heat flow measurements on sea floor. The remaining references report a global heat loss ranging from 41 to 47 TW of which the 62–77% is attributed to the energy loss occurring in oceans. The analysis reported in [67] were controversially commented by [68] who consider biased and misleading their understanding of heat flow of the Earth. The difference of ~10 TW respect to the previous estimates is attributable, according to [68], to the misconception of hydrothermal circulation which lead to a failed estimate of oceanic heat flow. This key issue was further discussed in [69] which on the opposite defines the half space cooling model as "failing paradigm" against the direct heat flux measurements adopted in the estimates previously published. Although [65] provide a new estimate (Q = 44 TW, see Table 2) based on about 70000 measurements and high resolution studies for hydrothermal calculation, I adopted the value Q = 47 ± 2 TW [66], which comes from a dataset with less measurements (~40000) but presenting a comprehensive treatment of the uncertainties.

Table 2. Integrated terrestrial surface heat fluxes (Q) estimated by different authors. If available, the contribution to the heat power from the continents (Q_{CT}) and from the oceans (Q_{OCS}) are reported together with the mean heat flux (q_{CT} and q_{OCS}) and the surface areas (A_{CT} and A_{OC}).

	Continents			Oceans			Total
REFERENCE	**q_{CT} [mWm^{-2}]**	**A_{CT} [10^6 km^2]**	**Q_{CT} [TW]**	**q_{OCS}[mWm^{-2}]**	**A_{OC} [10^{6}km^2]**	**Q_{OCS} [TW]**	**Q [TW]**
Williams et al., 1974 [70]	61	148	9 ± 1	92	362	33	43 ± 6
Davies, 1980 [71]	55	204	11	95 ± 10	306	30	41 ± 4
Sclater et al., 1980 [72]	57	202	12	99	309	30	42
Pollack et al., 1993 [73]	65 ± 2	201	13[a]	101 ± 2	309	31[a]	44 ± 1
Hofmeister and Criss, 2005 [67]	61[b]	-	-	65[b]	-	-	31 ± 1
Jaupart et al., 2015 [61]	65	210	14 ± 1	107	300	32 ± 2	46 ± 2
Davies and Davies, 2010 [66]	71	207	15	105	303	32	47 ± 2
Davies, 2013 [63]	65	-	-	96	-	-	45
Lucazeau, 2019 [65]	66.7	211.3	14.1	89.0	299.9	26.7	44[c]
Adopted	**71**	**207**	**15**	**105**	**303**	**32**	**47 ± 2**

[a] Values inferred based on the percentage contribution of continents (30%) and of oceans (70%) reported in the reference.
[b] Median value of "All data" reported in Table 1 of the reference.
[c] Obtained forcing oceanic heat flow with a conductive model fitting subsidence and heat flow.

2.2.2 Earth's heat budget

The understanding of the Earth's present heat budget provides constraints on the internal processes characterizing the convective engine, on the ancient state and on the evolution through geological time of our planet. In this contest, the crux of the matter is represented by the study of the mantle convection which accounts for specific phenomena of present-day dynamics, and it aims to the evaluation of past and active geological processes. The mantle convection models must be defined in a time-dependent framework and must satisfy both the present-day energy budget and the spatial distribution of heat flux at the surface. While the latter is well constrained by measurements on continents and plate cooling model for oceans, the balance of the main sources of the total energy remain uncertain [64]. On a global scale, the flux measured on surface can be seen as the results of the internal processes which occurs inside the Earth: radioactive heat production in the lithosphere (H_{LS}) and in the sublithospheric mantle (H_M), mantle cooling (C_M) and heat loss from the core (C_C) (Figure 12). Negligible contributions come from tidal dissipation (~ 0.1 TW) and gravitational potential energy released by the differentiation of crust from the mantle (~ 0.2 TW).

Subtracting the radiogenic energy production (H) from the total heat loss (Q), we can obtain the present Earth' secular cooling (C) which means having insights on the thermal

conditions of Earth's formation and on the dynamical processes in the mantle and core convection. If H_{LS} can be envisioned and constrained through direct observations, the determination of H_M remains a tangled task. Geoneutrino detection comes into plays right here: taken for granted the accurate calculation of lithospheric flux, valuable insights can be derived about the mantle radioactivity and in turn on its relative contribution to the Earth's energy budget.

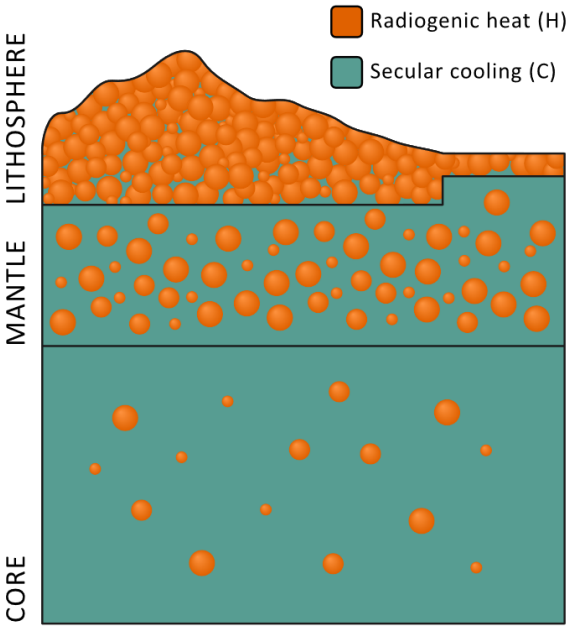

$$C = Q - H$$

$$C_M = Q - H - C_C$$

$$H_M = H - H_{LS} - H_C$$

$$H_{LS} = H_{CC} + H_{OC} + H_{CLM}$$

$$U_R = \frac{H - H_{CC}}{Q - H_{CC}}$$

	Range [TW]	Adopted [TW]
H	[10 ; 37]	19.3 ± 2.9
H_{LS}	[6 ; 11]	$8.1^{+1.9}_{-1.4}$
H_M	[0 ; 31]	$11.0^{+3.3}_{-3.4}$
H_C	[0 ; 5]	0

	Range [TW]	Adopted [TW]
C	[8 ; 39]	28 ± 4
C_{LS}	~ 0	0
C_M	[1 ; 29]	17 ± 4
C_C	[5 ; 17]	11 ± 2

Figure 12. Schematic drawing of the Earth's profile illustrating the main contributions to the Earth's heat budget (not in scale). The surface heat flux (Q) is the sum of secular cooling of the core (C_C) and mantle (C_M) and of the radiogenic heat from the core (H_C), mantle (H_M) and lithosphere (H_{LS}). Other negligible heat's sources (e.g. tidal dissipation) are ignored. The convective Urey ratio (U_R) is defined as the ratio between heat production and heat loss, leaving out H_{CC} from both H and Q. The ranges of H_{LS} and of H_C, C_M and C_C are provided considering available information reported in Chapter 2.2.3 and 2.2.4. The lower and upper range of H are given by the lowest and the higher value for the Low-H and Rich-H models respectively. The upper (lower) bounds of the range of H_M is obtained subtracting the lower (upper) bound of H_{LS} from the upper (lower) bound of H. The adopted value for the each component are chosen according the following criteria: (i) for H the central value is the average value of all models while the uncertainty is the average uncertainty with which every model value is estimated (i.e. 15%); (ii) for H_{LS}, I adopted the value reported in [14] (see Chapter 2.6.1); (ii) the values of H_M, C and C_M are obtained according to the equations reported in the figure considering the terms as linearly independent and Q = 47 ± 2 TW; (iii) C_{LS} and H_C are set to zero; (iv) the central value of C_C is the average value of all models while the uncertainty is 1/6 of the range amplitude.

In the comprehensive understanding of the Earth thermal budget, a key parameter is represented by the Urey ratio that can be easily seen as the ratio of heat production over heat loss. In other words, it measures the efficiency of the Earth's convective engine in evacuating heat generated by radioactive decay [61].

It is worth mentioning that geophysicists and geochemists defined this nondimensional number in two different ways [60]: the Bulk Earth Urey ratio and the convective Urey ratio.

Commonly, in the geochemical community, the Urey ratio denotes the Bulk Urey ratio calculated as follows:

$$U_R = \frac{H}{Q}\ (Bulk\ Earth) \tag{1}$$

where H is the radiogenic power of the entire Earth and Q is the total surface heat flux (see Chapter 2.2.1). The convective Urey ratio, extensively used in geophysical literature is given by:

$$U_R = \frac{H - H_{CC}}{Q - H_{CC}}\ (Convective) \tag{2}$$

where the radiogenic power of the continental crust (H_{CC}, see Chapter 2.6.2) is leaved out from both heat loss and the heat production since the continental heat sources are not taken into account because they are not involved in mantle convection. The convective Urey ratio, hereafter Urey ratio (U_R), corresponds to the "original" Urey ratio appeared in [74]. According to its definition, U_R assumes that the entire mantle convects as single layer (whole mantle convection) [60]. Given a total Earth heat flux (Table 2), U_R is a BSE model-dependent parameter: [75] sets a range of present U_R between 0.02 (low HPEs content) and of 0.75 (high HPEs content) while 0.29 and 0.23 are the best estimates proposed by [61] and [60] respectively. According to thermal evolution models, the U_R was close to 1 until ~ 3 Ga ago, when it started to decrease with the emergence of plate tectonics [60].

2.2.3 Radiogenic heat production (H)

The radiogenic heat production inside the Earth is due to the energy released by the decays of radioactive nuclides which indeed play a starring role in the comprehension of geodynamical processes. Neglecting a fractional contribution coming from rare radionuclides (^{87}Rb, ^{138}La, ^{147}Sm, ^{176}Lu, ^{187}Re and ^{190}Pt), the 99.5% of the present Earth's radiogenic heat production is due to the decay (or the decay chains) of ^{40}K, ^{232}Th, ^{235}U and ^{238}U, long-lived radionuclides ($T_{1/2} > 10^8$ years) created at the time of the Solar System formation and still extant now [76]. Due to their different half-lives, the relative amounts of heat-producing nuclides, and in turn their contribution to radiogenic budget, changed with time. At the early stages of Solar System, the concentration of ^{40}K, ^{232}Th, ^{235}U and ^{238}U were approximately 12, 1.25, 84 and 2 times higher respectively. In the first ~10 Myr of the

Solar System, the short-lived radionuclides ^{26}Al ($T_{1/2}$ = 0.7 Myr) and ^{30}Fe ($T_{1/2}$ = 1.2 Myr), now extinct in planetary bodies, were the dominant radiogenic sources [77]. Given the masses of K, U, Th in the present Earth and their decay properties, it is possible to trace the evolution of the Earth radiogenic power through the time together with the contribution of the different HPEs. In Figure 13a, the Earth radiogenic power is plotted respect to the time for the last 3.7 Gyr adopting a BSE composition of the medium-H model reported in [17] following the updated a(K)/a(U) from [10] (Chapter 2.3). The percentage contribution of the four long-lived radioisotopes changed with the time (Figure 13b) due to their different ratios. A decreasing trend is clearly observable of the ^{40}K contribution which is now less than the half of that of the early stages of the Solar System; conversely the contribution of ^{238}U and ^{232}Th increased with the time up to reach respectively the 37% and 42% of the present radiogenic power. ^{235}U contribution reached a negligible present value of 2%.

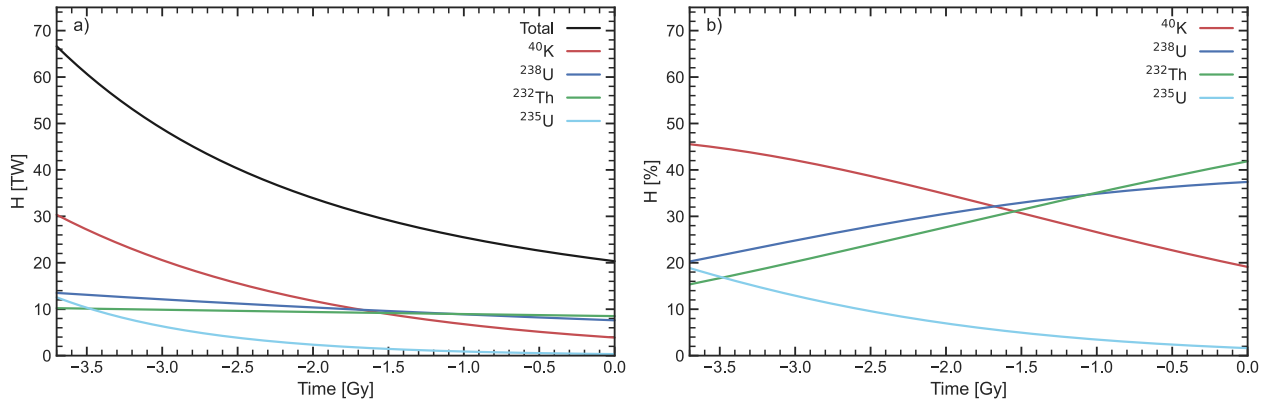

Figure 13. Earth's Radiogenic heat (H) in TW (a) and relative contributions in percentage (b) from ^{238}U, ^{235}U, ^{232}Th and ^{40}K over the last 3.7 Gyr. The compositional model is from [17] with the updated a(K)/a(U) reported in [10].

For each radioactive decay, the heat production rate is strictly related to the energy released in the process (Q-value), i.e. the difference between the mass of the parent (m_p) and the daughter nuclide(s) (m_d). In α decays, since all the decay products readily interact with matter losing all their energy, all of the decay energy is transformed into heat: the Q-value is thus an optimal approximation for heat production. For β^-, β^+ and electron capture, the heat production E_H must be calculated by subtracting from the Q-value the energy carried away by the (anti)neutrino $\langle E_{\bar{\nu}} \rangle$, which does not contribute to heat production [77]:

$$E_H = (m_p - m_d) - \langle E_{\bar{\nu}} \rangle \quad (3)$$

The specific heat production (h) is given by:

$$h = E_H \lambda \tag{4}$$

where $\lambda = \frac{\ln 2}{T_{\frac{1}{2}}}$. The simplified assumption that the neutrino always carries away 2/3 of the decay energy made by different authors [78-80] may generate overestimation or underestimation of the real value; these could be canceled in long decay chains (e.g. U and Th decay chain) but not in short decay chains. In a recent work, [77] reevaluated and updated the radioactive heat production data of ^{26}Al, ^{40}K, ^{60}Fe, ^{232}Th, ^{235}U and ^{238}U, using newest available information (nuclear and atomic properties) and accounting for details of the decay processes. The results obtained for the four long-lived nuclides relevant for geosciences are listed in Table 3. For ^{40}K, [77] observed a difference of 1-2% between the calculated values and the values reported by [81] and [80] that is mostly due to the difference in the mean β energy used for the calculation. An excellent agreement for all the radionuclides is instead highlighted with [82] who adopted a similar approach based on decay spectra.

Table 3. Total (Q-value) and Heat-Effective Decay Energy per Atom (E_H), specific heat production (h) of ^{40}K, ^{232}Th, ^{235}U, and ^{238}U, elemental specific heat production (h') for K, U and Th. The decay energies of ^{40}K are the weighted means of the two principal decay modes. For ^{238}U are included the fraction/contribution of ^{234}U. Adapted from [77].

	Q-value [MeV]	E_H [MeV]	h [W/kg]	h' [W/kg]
^{40}K	1.332	0.677	2.8761×10^{-5}	3.4302×10^{-9}
^{232}Th	42.646	40.418	2.6368×10^{-5}	2.6368×10^{-5}
^{235}U	46.397	44.380	5.6840×10^{-4}	9.8314×10^{-5}
^{238}U	51.694	47.650	9.4946×10^{-5}	

For an Earth reservoir (X), the radiogenic power (H_X) is given by:

$$H_X = M(K)_X \cdot h'_K + M(Th)_X \cdot h'_{Th} + M(U)_X \cdot h'_U \tag{5}$$

where M(K), M(Th) and M(U) are respectively the potassium, thorium and uranium masses in the reservoir. The radiogenic production of the Earth is attributable to the HPEs amount in the BSE (Figure 12). The presence of these elements, and in particular of K, in the Earth's core is envisaged by some authors but is still controversial and under debate. According to [25] a certain amount of K could alloy with Fe at pressure > 26 GPa and incorporated into the core during the early core formation stage of the Earth. The K abundances proposed by different authors [25-30] ranges between 0.2 – 250 μg/g to which corresponds a heat

generation of 0.01 – 1.7 TW. Although U and Th are considered essentially lithophile and resident only in the silicate phase, [83] suggested the a small fraction of U (10 ng/g) and Th (21 ng/g) may also partition into the metallic phase of the core and produce an additional heat source (~ 3 TW). In this study, I do not take in consideration the presence of K in the core, setting H_C=0 (Figure 12).

The concentration of K, U and Th determines the present contribution of the radiogenic heat to the Earth's heat budget. Most compositional models of the BSE use the chondritic meteorites to describe the starting material of the Earth and in turn to determine the present concentration of HPEs. The Chapter 2.3 serves the purpose to illustrate and compare the classes of models which imply different estimates of heat generation in the bulk Earth. The lower and upper range of H can be defined on the basis of the lowest and the highest value for the Low-H and Rich-H models, respectively. The mean value of all available models is H = 19.3 ± 2.9, where the uncertainty is given by the average relative uncertainty (15%) with which every model is estimated (Figure 12).

The estimates provided by available models [14, 61, 84] (see Chapter 2.6.1) prove that H_{LS} varies between 7.8 and 8.2 TW (Table 17) with an average relative uncertainty of ~25%. Considering the errors associated to each value, we can define for H_{LS} a the 1σ range of 6 – 10 TW. For the purpose of the extraction of the mantle radiogenic power from the geoneutrino signal, I adopted $H_{LS} = 8.1^{+1.9}_{-1.6}$ TW [75] obtained with the same lithospheric model [14] adopted for the geoneutrino signal estimation (Figure 12). Thanks to the increasing availability of oceanic and subcrustal rock samples, the most recent models provide detailed information about the radiogenic heat from the LS components. While the earlier estimates took into account only the heat from the CC, nowadays we can quantify as ~5% the contribution given by the HPEs in the OCC (H_{OCC}) and in the CLM (H_{CLM}) (Table 4).

Table 4. Radiogenic heat power of the continental crust (H_{CC}), oceanic crust (H_{OCC}) and continental lithospheric mantle (H_{CLM}) reported by different authors.

REFERENCE	H_{CC} [TW]	H_{OCC} [TW]	H_{CLM} [TW]
Taylor and McLennan, 1995 [85][a]	5.6	-	-
Rudnick and Fountain, 1995 [86][a]	7.7	-	-
Wedepohl, 1995 [87][a]	8.5	-	-
Mantovani et al., 2004 [88][b]	8.4	0.2	-
McLennan, 2001 [89][a]	6.3	-	-
Rudnick and Gao, 2003 [90][a]	7.4	-	-
Stacey and Davis, 2008 [91]	8	-	-
Hacker et al., 2011 [92] [a]	7.9	-	-
Dye, 2010 [93]	7.71 ± 1.5	0.24 ± 0.04	-
Šrámek et al., 2013 [94]	7.8 ± 0.9	0.22 ± 0.03	-
Huang et al., 2013 [14][c]	$6.8^{+1.4}_{-1.1}$	0.3 ± 0.1	$0.8^{+1.1}_{-0.6}$
Wipperfurth, 2020 [84] (Litho 1.0)[d]	$7.1^{+2.1}_{-0.6}$	0.2	$0.5^{+0.8}_{-0.3}$
Wipperfurth, 2020 [84] (Crust 1.0)[d]	$6.7^{+2.1}_{-0.6}$	0.3	$0.6^{+1.5}_{-.04}$
Wipperfurth, 2020 [84] (Crust 2.0)[d]	$7.0^{+2.0}_{-1.6}$	0.2	$0.6^{+1.6}_{-.04}$

[a] As appeared in [14].

[b] Obtained on the basis of radiogenic heat of the bulk crust and relative masses in continental and oceanic crust reported in the reference.

[c] The H_{CLM} is taken as appeared from [75].

[d] The H_{OCC} is obtained summing the heat of Sed and C of OC reported in Table S2, S3 and S4 of the reference.

Starting from these findings, one can infer a first model-based estimate of the radiogenic heat of the mantle (H_M = 11.3 ± 3.3 TW) by subtracting the relatively well constrained and independent contribution of H_{LS} from H (Figure 12).

2.2.4 Secular Cooling (C)

Beyond the radiogenic heat production, the loss of internal energy of the Earth is balanced by the secular cooling (C), i.e. the gradual decrease of the primordial heat content. Nowadays, the cooling rate is estimated to exceed 100 K Gyr^{-1} but it has not remained constant. As suggested by geological data and physical constraint on the thermal structure or the early Earth [61], the cooling rate increased with the time. Assuming a U_R ranging from 0.08 to 0.38, [60] proposes a range 50 - 100 K Gyr^{-1} for an average over the last 3 Gyr with a present value of 124 ± 22 K Gyr^{-1} compatible with the value 106 K Gyr^{-1} reported by [61].

The heat flow from the core (C_c) remains a controversial parameter of the thermal evolution models and, despite its not negligible value, was often ignored or embedded with the mantle heat flow. As a matter of fact, the core must have cooled by hundreds of degrees since its

formation and sustained the operation of the geodynamo. The requirement of dynamo action in the core represents a constraint for the estimation of the heat across the CMB. In this puzzle, the thermal conductivity of high-pressure iron is the most important parameter [60]; recent laboratory measurements and theoretical ab-initio calculation set its value at 90 $Wm^{-1}K^{-1}$, which is a factor 2-3 higher than the previous estimates [62]. [95] uses the entropy balance of the core and assumes a thermal conductivity increasing with depth to estimate C_c = 13.25 TW. [61] and [60] propose C_c = 11 TW (with a range 5 – 17 TW) and C_c = 4.5 TW respectively and report diverse values estimated by different authors on the basis of different arguments: 3.5 TW [91] and 5 TW [96] if the C_c assumed identical to the heat carried by hot spots, 6 – 12 TW [97] from the expected thermal structure around CMB, 9 – 12 TW from postperovskite phase diagram [37], 13 TW from numerical simulation [98] and 10 – 30 TW from seismic tomography [99].

The composition of MORB can be used to calculate the temperature of the mantle and its cooling rate. A long-term average cooling rate of 50 K Gyr^{-1} corresponding to $C_M \sim 7$ TW is suggested by petrological studies on Archean MORB rocks [64]. Higher estimates can be found calculating C_M from the difference between the output (Q) and the input range (H_{CC} + H_M + C_C). Adopting this approach, the values of Q, H_{CC}, H_M and C_C proposed by [60] lead to an estimate of C_M = 23 TW. [61] found in the same way a preferred value of 16 TW and, taking into account all the uncertainties, a wide range 1 – 29 TW.

2.3 Bulk Silicate Earth models

2.3.1 Is the Earth compositionally similar to a primitive meteorite?

Although the Earth is the planet most familiar to us, direct probes provide a more uncertain geochemical bulk composition than the Sun's one [100]. The deepest hole that has ever been dug is about 12 km deep [101], while the deepest rock that has ever been recovered comes from ~700 km beneath the surface of our planet [102]. Hence, a coherent chemical description of our planet requires to embrace several indirect inputs.

It can be tempting to naively build an Earth in the image and likeness of a primitive meteorite. Indeed, $\sim 10^7$ kg of interplanetary solid material hit the Earth every year, with $\sim 10^4$ kg of meteorites falling to the ground [103]. Although chondritic meteorites are very common in the Solar System, they are the rarest to find on Earth's surface because of their resemblance to stones. On the other hand, they are also one of the most precious materials,

since their thermal history partially preserved the initial chemical cocktail of our Solar System's formation. The most chemically primitive meteorites are carbonaceous chondrites that, together with enstatite chondrites, represent 5% and 2% of the stony meteorites fallen on Earth [104]. These two classes of meteorites are grouped according to their distinctive compositions (Table 5). Although their U and Th abundances can vary of a factor ~2 among the different groups, their Th/U ratio remains basically constant. The terrestrial radiogenic heat power (H) calculated adopting HPE abundances from the different chondritic groups is constrained in the range 21-26 TW.

Table 5. Uranium, thorium (in ng/g) and potassium (in µg/g) abundances (a_{ch}) [105] and their ratios for different chondrite groups belonging to carbonaceous and enstatite classes. The radiogenic heat (H) is calculated employing Eq. (5) by assuming a bulk earth mass (Table 1) with chondritic abundances (a_{ch}).

Class	Group	a_{ch}(U) [ng/g]	a_{ch}(Th) [ng/g]	a_{ch}(K) [µg/g]	a_{ch}(Th)/ a_{ch}(U)	a_{ch}(K)/a_{ch}(U) [10^4]	H [TW]
Carbonaceous	CI	8.2	29	560	3.5	6.8	20.8
	CM	11	40	400	3.6	3.6	20.9
	CO	13	45	345	3.5	2.7	21.8
	CV	17	60	310	3.5	1.8	25.8
Enstatite	EH	9	30	800	3.3	8.9	26.4
	EL	10	35	735	3.5	7.4	26.4

The chondrites with the chemical composition closest to the solar photosphere are the ones belonging to the CI carbonaceous group[3] [24], while those having the isotopic composition most similar to terrestrial samples are the enstatite chondrites [55, 106]. The enstatite (carbonaceous) chondrites are characterized by the lowest (highest) oxidized and highest (lowest) metallic iron content. These peculiarities are relevant for two reasons: (i) a low (high) degree of oxidation proves a formation in an oxygen-poor (rich) environment, corresponding to inner (outer) portions of the solar nebula, (ii) a high (low) metallic iron content is a predisposing factor to the metallic core formation in planets. Indeed, a BSE compositional model employing carbonaceous or enstatite chondrites as its fundamental building blocks must comply with the essential constraint of having enough metallic iron to form Earth's core.

The gravitational segregation of metallic Fe and FeS melts in Earth's core started in the first 2-3 Myr and presumably lasted till 60-100 Myr since planetary formation [107]. The

[3] Even in these meteorites volatile elements have been depleted to various degrees, including the six most abundant elements (H, He, C, N, O and Ne) and lithium.

differentiation of a metallic core of mass M_C from the BSE (M_{BSE}) brought incompatible elements, such as U and Th, to accumulate in the remaining silicate portion of the Earth, hence enriching their abundances of a factor:

$$f_C = \frac{M_{Earth}}{M_{Earth} - M_C} = \frac{M_{Earth}}{M_{BSE}} = 1.48 \quad (6)$$

Therefore, the abundances of U and Th in the BSE appear ~50% higher than what observed in bulk carbonaceous and enstatite chondrites.

The differentiation of a metallic core was not the only process leading to an enrichment of U and Th in the silicate Earth. The loss of volatile elements in the planetary accretion stage is thought to have further increased the RLE abundances of the BSE [108], as suggested by several evidences: (i) the BSE is found to have ~2-3 times higher RLEs concentration than chondrites [108], (ii) the BSE abundances of the volatile lithophile elements show a coherent depletion pattern (when compared to chondrites) as a function of their T_C [19, 20], (iii) high temperatures in the early stages of Earth's formation (as testified by isotopic $\Delta^{17}O$ considerations) [109] and/or collisional erosions [19] were all predisposing factors for the loss of lighter elements. Without going into the details of the debate about the different volatilization mechanisms, we can parametrize the removal of part of the BSE with a depletion enrichment factor:

$$f_D = \frac{M_{BSE}}{M_{BSE} - M_V} \quad (7)$$

where M_V is the mass of the material which left the Earth because of volatilization and/or collisional erosion. Therefore, following the two different mechanisms (core-mantle differentiation and mass depletion) leading to U and Th enrichment in the BSE, the abundances $a_{BSE}(U;Th)$ of these elements in the silicate Earth can be calculated from their chondritic abundances $a_{Ch}(U;Th)$ as:

$$a_{BSE}(U;Th) = f_C \cdot f_D \cdot a_{Ch}(U;Th) \quad (8)$$

Whilst there's wide agreement on f_C, which is known at the level of a few percent, the enrichment factor due to volatilization f_D spans a wider range, between 0.8 and 3.3, according to different authors (Table 6). Among the proposed models, the one and only predicting f_D<1 is the collisional erosion model from [21], coherently with their hypothesis

of preferential collisional erosion of the RLE-enriched crust (which hence removed part of the U and Th masses). All the BSE models starting from enstatite compositions predict f_D~1, reflecting the implicit conditions of enstatite material being virtually volatile-free [55] and thus not requiring any depletion correction. Models starting from carbonaceous chondrites predict f_D values in the range 1.4-2.0 (1.7 on average), implicitly suggesting the removal of volatiles for as much as ~40% the mass of the silicate Earth. This is a consequence of the observation that the BSE is highly enriched in RLEs respect to carbonaceous chondrites. Models based on Earth's mantle dynamics predict f_D>2, independently by the chosen compositional building block, being it enstatitic or carbonaceous. For every model, the f_D values obtained from Th abundances are higher than those obtained from U. This comes directly from the observation that the a(Th)/a(U) ratio of the BSE is expected to be bigger than what observed in chondrites (Table 5 and Table 9).

Table 6. Estimated volatilization enrichment factor (f_D) according to different models. f_D(U) and f_D(Th) are calculated by reversing Eq. (7), assuming a core-mantle differentiation enrichment factor of f_c=1.48 and chondritic abundances for a_{Ch}(U) and a_{Ch}(Th) following Table 5.

Reference	Chondrite	a_{BSE}(U) [ng/g]	f_D(U)	a_{BSE}(Th) [ng/g]	f_D(Th)
Jackson and Jellinek, 2013	CI-EH	14 ± 3	1.2	55 ± 11	1.3
O'Neill and Palme, 2008	CI-EH	10	0.8	40	0.9
Javoy and Kaminski, 2014	EH	15 ± 2	1.2	51 ± 4	1.2
Javoy et al., 2010	EH	12 ± 2	0.9	43 ± 4	1.0
McDonough and Sun, 1995	C	20 ± 4	1.7	80 ± 12	1.9
Lyubetskaya and Korenaga, 2007	C	17 ± 3	1.4	63 ± 11	1.5
Palme and O'Neill, 2007	C	22 ± 3	1.8	83 ± 13	1.9
Arevalo, 2010	C	20 ± 4	1.6	80 ± 13	1.9
Wang et al., 2018	C	20 ± 2	1.6	75 ± 7	1.7
Palme and O'Neill, 2014	C	23 ± 3	1.9	85 ± 13	2.0
Turcotte, 2002*	CI-EH	35 ± 4	2.8	140 ± 14	3.3
Turcotte, 2014	CI-EH	31	2.5	124	2.9

[+]as reported in [94]

The correlation among abundances of refractory lithophile elements observed in chondrites and solar photosphere has always been the driver in the development of Earth chemical composition paradigms. In 2005 detailed ^{142}Nd/^{144}Nd ratio measurements on terrestrial MORBs, carbonatites and kimberlites cast doubt upon the long-standing idea of a common origin between Earth and chondrites [59]. Although subsequent corrections for nucleosynthetic effects [110, 111] tidied up this ratio in a chondritic framework, these studies highlight the need to go beyond a model based on a particular type of chondrite (e.g.

carbonaceous, enstatitic), embracing cosmochemical, geochemical, seismological and heat flow evidences.

A compositional model attempting to accurately describe the Earth must consider several constraints, which are not verified simultaneously by any known class of meteorite. The cosmochemical inputs, which employ assumptions on chondrites and Solar System's compositions to describe the Earth, are not enough. Our understanding of the mantle must rely on compositional models based on:

(i) geochemical information, which makes use of samples and observations of chemical processes occurring on Earth and on the uppermost part of the mantle;
(ii) geodynamical observations, which show whole-mantle convection and require a substantial energy input to justify the observed convective processes.

Indeed, regardless of Earth's composition's similarities with a class of chondrites rather than another, our planet is not a chondrite and hence has its peculiar and singular composition. For this reason, scientists proposed a wide variety of BSE compositional models (Table 8), which can be grouped on the basis of their expected radiogenic heat production (H) [84] in (i) poor-H models, (ii) medium-H models and (iii) rich-H models (Table 7).

Table 7. Masses of U, Th and K in the BSE, Th/U and K/U mass ratios and the radiogenic heat (H) expected from poor-H, medium-H and rich-H BSE models together with the corresponding Urey ratio (U_R). For each class, the masses of the HPEs are obtained multiplying the adopted abundances reported in Table 8, Table 9 and Table 10 by the BSE mass (Table 1). The standard deviations on the masses are obtained by propagating the errors on the abundances, here considered as the only source of uncertainty. For each model class, H is calculated multiplying the masses of U, Th and K by the specific heat production coefficients h' reported in Table 3. The obtained values are then summed to obtain H(U+Th) and H(U+Th+K). Their uncertainties are propagated from the masses' standard deviations, considering U, Th and K as fully correlated. The uncertainty on the coefficients h' is here neglected.

Classes	$M_{BSE}(U)$ [10^{16} kg]	$M_{BSE}(Th)$ [10^{16} kg]	$M_{BSE}(K)$ [10^{19} kg]	$M_{BSE}(Th)/M_{BSE}(U)$	$M_{BSE}(K)/M_{BSE}(U)$ [10^4]	$H_{BSE}(U+Th)$ [TW]	$H_{BSE}(U+Th+K)$ [TW]	U_R
Poor-H	5.2 ± 0.9	19.1 ± 2.4	67.3 ± 11.5	3.7	1.3	10.1 ± 1.5	12.4 ± 1.9	$0.14^{+0.06}_{-0.05}$
Medium-H	8.2 ± 1.3	31.3 ± 4.6	98.7 ± 16.9	3.8	1.2	16.3 ± 2.5	19.7 ± 3.1	0.32 ± 0.08
Rich-H	13.3 ± 1.5	53.3 ± 5.3	133.2 ± 13.3	4.0	1.0	27.1 ± 2.9	31.7 ± 3.4	0.62 ± 0.09

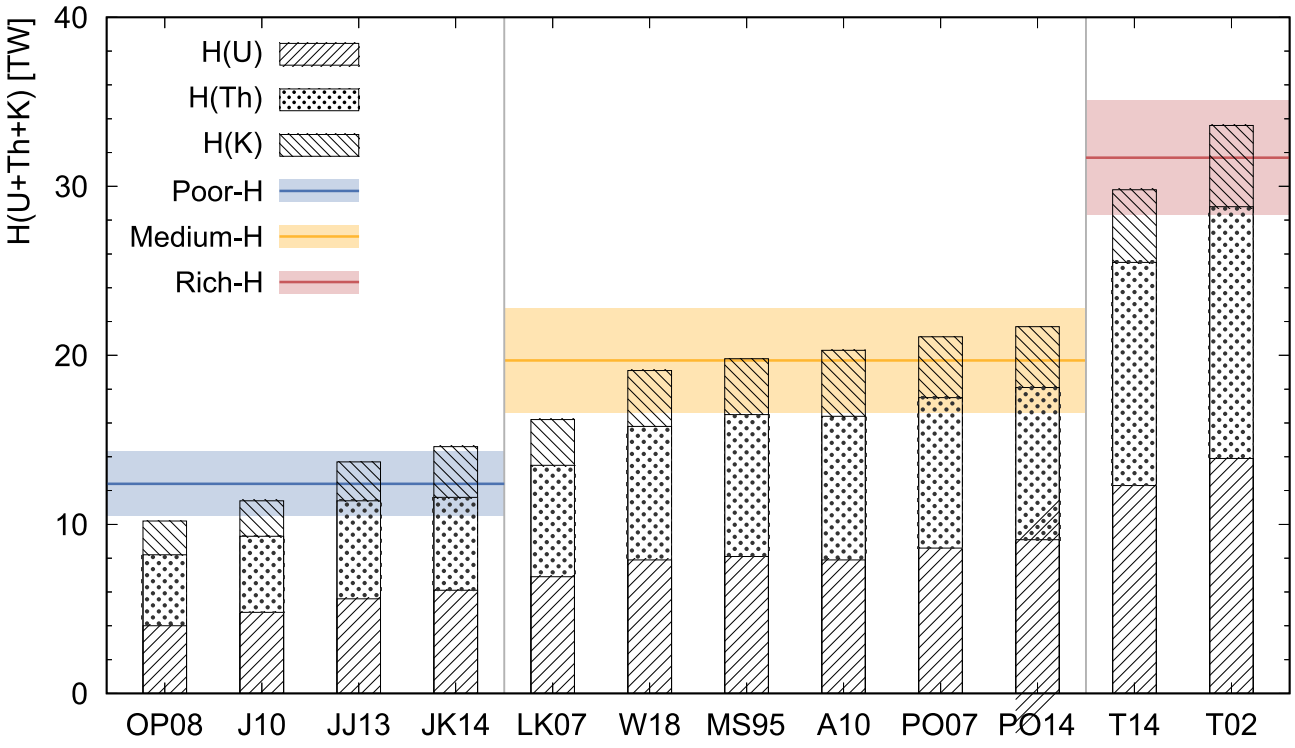

Figure 14. Histogram of the predicted radiogenic heat production H(U+Th+K) (in TW) according to the different BSE compositional models reported in Table 8, Table 9 and Table 10. Each bar is subdivided according to the relative contribution of U, Th and K to the overall radiogenic power. The horizontal bands represent the H(U+Th+K) (together with its standard deviation) expected from the adopted poor-H (in blue), medium-H (in yellow) and rich-H (in red) BSE classes reported in Table 7.

2.3.2 Poor-H BSE models

The BSE enstatite models [55, 112, 113] are based on a mixture of enstatite chondrites composition (~2/3 of EH chondrites and ~1/3 of EL chondrites) since this class of meteorites (i) are the chondrite group isotopically most similar to the Earth [55], (ii) share a common oxygen reservoir with our planet [114], (iii) are largely degassed, so that the total mass reduction to match the depleted Earth is estimated to 4.7 ± 1.6% [113], (iv) have sufficiently high iron content to explain the metallic core and the observed oxidized iron in the mantle. All these observations seem to suggest a common origin between Earth and enstatite chondrites, thus making this meteorite type a good candidate as the building block of our planet. However, since the enstatite Mg/Si ratio is 35% lower than that of the measured in the UM [115], these models implicitly require compositional layering of the mantle [55]. Because of the small mass correction due to volatilization (f_D~1), the predicted BSE composition ends up being low in U and Th, constraining H in the range [10, 16] TW assuming a a(K)/a(U) ratio of 14000 [10].

Non-chondritic and collisional erosion models consider the Earth to be either an unsampled material or a combination of chondritic materials altered by collisional erosion processes [21]. In particular, these models observe that (i) terrestrial mantle rocks' isotopic ratios of $^{142}Nd/^{144}Nd$, $^{187}Os/^{188}Os$, the atmospheric $^{84}Kr/^{130}Xe$ and the isotopic anomalies in $\Delta^{17}O$, $\varepsilon^{48}Ca$, $\varepsilon^{50}Ti$, $\varepsilon^{54}Cr$, $\varepsilon^{64}Ni$, $\varepsilon^{92}Mo$, $\varepsilon^{100}Ru$, and $\mu^{142}Nd$ [106] are not matched by any known meteorite and cannot be explained by the nucleosynthetic variability among chondrites [19, 114, 116], (ii) Moon isotopic composition seems to match Earth's one, hinting to a collisional origin caused by large impact after Earth differentiation, (iii) the Earth's volatility pattern shows a depletion dependence on incompatibility, suggesting volatilization from early-formed crust during the latter stages of accretion. This assumption would explain the apparent paradox of the missing ^{40}Ar planetary budget, otherwise requiring degassed hidden reservoirs [19, 116]. As a consequence of preferential collisional erosion, these models suppose that the BSE (which initially could have accreted in chondritic proportions) was largely deprived of its HPEs by the removing of 10% of the RLE-enriched crust during intense collisions with large impacts. Therefore, these models predict low HPEs abundances and constrain H at ~10 TW.

Table 8. Uranium, thorium (in ng/g) and potassium (in µg/g) abundances, masses, and predicted radiogenic heat (H) for different poor-H BSE compositional models. The masses of U, Th and K are obtained multiplying the HPEs abundances by the BSE mass (Table 1). The standard deviations on the masses are obtained by propagating the errors on the abundances, here considered as the only source of uncertainty. H is calculated multiplying the masses of U, Th and K by the specific heat production coefficients h' reported in Table 3. The obtained values are then summed to obtain H(U+Th) and H(U+Th+K). Their uncertainties are propagated from the masses' standard deviations, considering U, Th and K as fully correlated. The uncertainty on the coefficients h' is here neglected. The last row reports the HPEs abundances, masses and H (together with their standard deviations) adopted in this study to represent poor-H models. The abundances central values are calculated by averaging all the values proposed by the different models considered. The errors on the abundances are calculated by considering the average relative uncertainty of the different models and multiplying it by the central value. The adopted abundances are then employed to obtain the HPEs masses and predicted radiogenic heat as explained above.

			a_{BSE}(U) [ng/g]	a_{BSE}(Th) [ng/g]	a_{BSE}(K) [µg/g]	M_{BSE}(U) [10^{16} kg]	M_{BSE}(Th) [10^{16} kg]	M_{BSE}(K) [10^{19} kg]	M_{BSE}(Th)/ M_{BSE}(U)	M_{BSE}(K)/M_{BSE}(U) [10^4]	H(U+Th) [TW]	H(U+Th+K) [TW]
Poor-H	Jackson and Jellinek, 2013	JJ13	14 ± 3	55 ± 11	166 ± 33	5.6 ± 1.2	22.2 ± 4.4	67.0 ± 13.3	3.9	1.2	11.4 ± 2.4	13.7 ± 2.8
	O'Neill and Palme, 2008	OP08	10	40	140	4.0	16.1	56.5	4.0	1.4	8.2	10.2
	Javoy and Kaminski, 2014	JK14	15 ± 2	51 ± 4	216 ± 25	6.2 ± 0.7	20.7 ± 1.8	87.0 ± 10.2	3.3	1.4	11.6 ± 1.2	14.6 ± 1.5
	Javoy et al., 2010[+]	J10	12 ± 2	43 ± 4	146 ± 29	4.8 ± 0.8	17.4 ± 1.6	58.9 ± 11.7	3.6	1.2	9.3 ± 1.2	11.4 ± 1.6
	Adopted values		**13 ± 2**	**47 ± 6**	**167 ± 29**	**5.2 ± 0.9**	**19.1 ± 2.4**	**67.3 ± 11.5**	**3.7**	**1.3**	**10.1 ± 1.5**	**12.4 ± 1.9**

[+]as reported in [94]

2.3.3 Medium-H BSE models

Geochemical models recognize that there is no group of meteorites that has a bulk composition matching that of the Earth, but combine observations from chondrites and the residuum-melt relationship between peridotites and basalts to estimate the composition of the BSE [17, 117, 118]. Earth is assumed to have a bulk major-element composition matching that of CI chondrites since this class of meteorites (i) are chemically the most primitive and not differentiated known meteorites, (ii) they perfectly match the photosphere composition, (iii) they correctly set the Mg/Si ratio and the absolute abundances of the refractory element abundances [24]. However, these models do not explain the isotopic anomalies of our planet and require large volatilization corrections to match Earth's depletion pattern [20]. As a consequence of the ~40% degassing correction, these models appear 2-3 times enriched in HPEs when compared to CI chondrites and predict H to be in the range [13.3, 25.0] TW.

Table 9. Uranium, thorium (in ng/g) and potassium (in µg/g) abundances, masses, and predicted radiogenic heat (H) for different medium-H BSE compositional models. The masses of U, Th and K are obtained multiplying the HPEs abundances by the BSE mass (Table 1). The standard deviations on the masses are obtained by propagating the errors on the abundances, here considered as the only source of uncertainty. The radiogenic heat H is calculated multiplying the masses of U, Th and K by the specific heat production coefficients h' reported in Table 3. The obtained values are then summed to obtain H(U+Th) and H(U+Th+K). Their uncertainties are propagated from the masses' standard deviations, considering U, Th and K as fully correlated. The uncertainty on the coefficients h' is here neglected. The last row reports the HPEs abundances, masses and radiogenic heat (together with their standard deviations) adopted in this study to represent medium-H models. The abundances central values are calculated by averaging all the values proposed by the different models considered. The errors on the abundances are calculated by considering the average relative uncertainty of the different models and multiplying it by the central value. The adopted abundances are then employed to obtain the HPEs masses and predicted radiogenic heat as explained above.

			a_{BSE}(U) [ng/g]	a_{BSE}(Th) [ng/g]	a_{BSE}(K) [µg/g]	M_{BSE}(U) [10^{16} kg]	M_{BSE}(Th) [10^{16} kg]	M_{BSE}(K) [10^{19} kg]	M_{BSE}(Th)/ M_{BSE}(U)	M_{BSE}(K)/ M_{BSE}(U) [10^4]	H(U+Th) [TW]	H(U+Th+ K) [TW]
Medium - H	McDonough and Sun, 1995ˆ	MS95	20 ± 4	80 ± 12	240 ± 48	8.2 ± 1.6	32.1 ± 4.8	96.8 ± 19.4	3.9	1.2	16.5 ± 2.9	19.8 ± 3.5
	Lyubetskaya and Korenaga, 2007	LK07	17 ± 3	63 ± 11	190 ± 40	7.0 ± 1.2	25.3 ± 4.3	76.7 ± 16.1	3.6	1.1	13.5 ± 2.3	16.2 ± 2.9
	Palme and O'Neill, 2007	PO07	22 ± 3	83 ± 13	260 ± 39	8.8 ± 1.3	33.7 ± 5.0	104.9 ± 15.7	3.8	1.2	17.5 ± 2.6	21.1 ± 3.2
	Arevalo, 2009°	A10	20 ± 4	80 ± 13	280 ± 60	8.1 ± 1.6	32.3 ± 5.2	113.0 ± 24.2	4.0	1.4	16.4 ± 3.0	20.3 ± 3.8
	Wang et al., 2018	W18	20 ± 2	75 ± 7	237 ± 25	8.0 ± 0.8	30.1 ± 2.7	95.6 ± 10.1	3.8	1.2	15.8 ± 1.5	19.1 ± 1.9
	Palme and O'Neill, 2014	PO14	23 ± 3	85 ± 13	260 ± 39	9.2 ± 1.4	34.3 ± 5.1	104.9 ± 15.7	3.7	1.1	18.1 ± 2.7	21.7 ± 3.3
	Adopted values		**20 ± 3**	**78 ± 11**	**245 ± 42**	**8.2 ± 1.3**	**31.3 ± 4.6**	**98.7 ± 16.9**	**3.8**	**1.2**	**16.3 ± 2.5**	**19.7 ± 3.1**

°derived from [17] following the updated a(K)/a(U) from [10]

ˆuncertainties on a(U) and a(Th) (20% and 15% respectively) should be updated to 10% following the suggestion of [119]

2.3.4 Rich-H BSE models

Geodynamical models try to estimate the abundances of the HPEs on the basis of the energetic constraints dictated by past and active geological processes, mantle dynamics and

surface heat flow [120]. They seek to solve the balance of mantle forces between thermal/momentum diffusivity versus viscosity and buoyancy examining the time evolution of the secular cooling and radiogenic contributions. These parameterized thermal evolution models require a significant fraction of the present-day mantle energy source to be contributed by radiogenic heating to prevent extremely high temperatures in Earth's early history [121]. Most of these models predict U_R of 0.6-0.8, thus requiring high HPEs abundances to justify the high energy demand. These models do not treat or explain Earth's isotopic anomalies and Earth's elemental ratios and thus implicitly or explicitly require layered mantle convection to explain Earth's Mg/Si ratio and UM composition [120, 122]. These models predict H to be in the range [29.8, 37.2] TW, but trade-offs in assigned values of thermal conductivity, core-mantle heat exchange or viscosity can result in alternative solutions ranging from poor-H to rich-H compositional models.

Fully radiogenic models assume that the terrestrial heat flow is fully accounted by radiogenic production [75, 88]. This can be obtained by keeping the BSE abundance ratios fixed at chondritic values and scaling the HPEs bulk abundances to match the expected radiogenic production of 47 TW (Chapter 2.2.1). These models represent maximal scenarios and do not account for any chemical or physical evidence of our planet.

Table 10. Uranium, thorium (in ng/g) and potassium (in µg/g) abundances, masses, and predicted radiogenic heat (H) for different rich-H BSE compositional models. The masses of U, Th and K are obtained multiplying the HPEs abundances by the BSE mass (Table 1). The standard deviations on the masses are obtained by propagating the errors on the abundances, here considered as the only source of uncertainty. The radiogenic heat H is calculated multiplying the masses of U, Th and K by the specific heat production coefficients h' reported in Table 3. The obtained values are then summed to obtain H(U+Th) and H(U+Th+K). Their uncertainties are propagated from the masses' standard deviations, considering U, Th and K as fully correlated. The uncertainty on the coefficients h' is here neglected. The last row reports the HPEs abundances, masses and radiogenic heat (together with their standard deviations) adopted in this study to represent rich-H models. The abundances central values are calculated by averaging all the values proposed by the different models considered. The errors on the abundances are calculated by considering the average relative uncertainty of the different models and multiplying it by the central value. The adopted abundances are then employed to obtain the HPEs masses and predicted radiogenic heat as explained above.

			a_{BSE}(U) [ng/g]	a_{BSE}(Th) [ng/g]	a_{BSE}(K) [µg/g]	M_{BSE}(U) [10^{16} kg]	M_{BSE}(Th) [10^{16} kg]	M_{BSE}(K) [10^{19} kg]	M_{BSE}(Th)/M_{BSE}(U)	M_{BSE}(K)/M_{BSE}(U) [10^4]	H(U+Th) [TW]	H(U+Th+K) [TW]
Rich - H	Turcotte, 2002[+]	T02	35 ± 4	140 ± 14	350 ± 35	14.1 ± 1.6	56.5 ± 5.6	141.2 ± 14.1	4.0	1.0	28.8 ± 3.1	33.6 ± 3.6
	Turcotte, 2014	T14	31	124	310	12.5	50.0	125.1	4.0	1.0	25.5	29.8
	Adopted values		**33 ± 4**	**132 ± 13**	**330 ± 33**	**13.3 ± 1.5**	**53.3 ± 5.3**	**133.2 ± 13.3**	**4.0**	**1.0**	**27.1 ± 2.9**	**31.7 ± 3.4**

[+]as reported in [94]

2.4 What are geoneutrinos?

2.4.1 Geoneutrino properties

Geoneutrinos are antineutrinos produced by the decay of radioactive isotopes present inside the Earth [123]. They belong to the families with a half-life comparable to or longer than the Earth's age (4.543 Gyr) with ^{238}U, ^{232}Th, ^{40}K, which are naturally present in the Earth as progenitors[4] (Table 11). While decaying, these isotopes produce not only antineutrinos, but also energy[5], the so-called *radiogenic heat* of the present Earth. For this reason, these elements are usually referred to as *Heat-Producing Elements* (HPEs). The production of antineutrinos and radiogenic heat occurs in a well-fixed ratio (Chapter 2.2) and for this reason a measurement of the geoneutrino flux can be used as a probe for estimating the radiogenic heat production of the inaccessible Earth.

Table 11. Main properties of ^{238}U, ^{232}Th decay chains and ^{40}K β^- decay. For each parent nucleus the table presents the natural isotopic abundance X_{iso} and the half-life $T_{1/2}$ from the most recent Nuclear Data Sheets [1, 124, 125], where the numbers in brackets represent the uncertainty on the last digits of the value. The number N of antineutrinos emitted per decay of the parent nucleus represents the number of β^- decays needed to reach a stable nucleus: for ^{40}K this is represented by its β^- branching ratio [1]. The maximal energy of the emitted antineutrino E_{max} are taken from [78], while the antineutrino production rates for unit mass of the isotope ($\epsilon_{\bar{\nu}}$) and for unit mass at natural isotopic abundance ($\epsilon'_{\bar{\nu}}$) are derived from X_{iso}, $T_{1/2}$ and N. Production rates $\epsilon_{\bar{\nu}}$ and $\epsilon'_{\bar{\nu}}$ for ^{40}K are higher than previous reports because of the recently updated ^{40}K's half-life $T_{1/2}$ estimation [1], which is respectively 2.6%, 2.3% and 1.1% lower than what reported in [78], [82] and [126].

Decay family	X_{iso} [mole fraction]	$T_{1/2}$ [Gyr]	N [decay^{-1}]	E_{max} [MeV]	$\epsilon_{\bar{\nu}}$ [kg^{-1} s^{-1}]	$\epsilon'_{\bar{\nu}}$ [kg^{-1} s^{-1}]
$^{238}U \rightarrow {}^{206}Pb + 8\alpha + 6e^- + 6\bar{\nu}_e$	0.992742 (10)	4.468 (6)	6	3.26*	7.46 x 10^7	7.41 x 10^7
$^{232}Th \rightarrow {}^{208}Pb + 6\alpha + 4e^- + 4\bar{\nu}_e$	1	14.0 (1)	4	2.25	1.63 x 10^7	1.63 x 10^7
$^{40}K \rightarrow {}^{40}Ca + e^- + \bar{\nu}_e$ (89.28%)	1.17 × 10^{-4} (1)	1.248 (3)	0.8928 (11)	1.311	2.37 x 10^8	2.83 x 10^4

*The ^{238}U decay chain contains β^- decays (e.g. ^{210}Tl) producing geoneutrinos with energies >3.26 MeV. Historically, these are not considered for geoneutrino analyses because of their low intensities, impossible to observe through current experiments.

[4] Geoneutrinos emitters include ^{40}K, ^{87}Rb, ^{113}Cd, ^{115}In, ^{138}La, ^{176}Lu, ^{187}Re and the elements belonging to the decay chains of ^{232}Th, ^{235}U and ^{238}U. Because of their longer half-lives or higher abundances, the most important emitters in terms of luminosity are ^{40}K and the ones belonging to ^{232}Th and ^{238}U decay chains, with only the latter two observable with present detection techniques. Differently from the other mentioned isotopes (which only undergo β^- decays), ^{40}K can produce both neutrinos and antineutrinos (Chapter 2.9). However, the detection of neutrinos is prevented by their low energy and the overwhelming solar neutrino flux which is nearly three orders of magnitude higher.

[5] More precisely, all decay products but neutrinos and antineutrinos readily interact with matter, losing all their energy in the form of heat. Because of their low cross section, neutrinos and antineutrinos can instead escape without interacting, carrying with them their kinetic energy, which is thus not transformed into heat.

2.4.2 Modelling the geoneutrino flux

The unoscillated geoneutrino flux at position $\bar{r}$ on Earth's surface ($\Phi(i,\bar{r})$) depends only on the abundance and distribution of the HPEs inside the planet and can be modelled as:

$$\Phi(i,\bar{r}) = \epsilon'_{i,\bar{\nu}} \cdot \int_0^{E_{max}} dE_{\bar{\nu}} \cdot Sp(i,E_{\bar{\nu}}) \int d^3r' \cdot \frac{a(i,\bar{r}') \cdot \rho(\bar{r}')}{4\pi|\bar{r}-\bar{r}'|^2} \tag{9}$$

where $a(i,\bar{r}')$ is the abundance of the i-th HPE as a function of its position $\bar{r}'$ inside the Earth, $\rho(\bar{r}')$ is Earth's mass density function, $|\bar{r}-\bar{r}'|$ is the distance between the antineutrino production point and the detector, $\epsilon'_{i,\bar{\nu}}$ is the antineutrino production rate for unit mass of the element i at natural isotopic composition and $Sp(i,E_{\bar{\nu}})$ is the energy spectrum of the produced geoneutrino (Figure 15) which results in N (Table 11) once integrated over the entire antineutrino energy.

The detection technique permitting to current and future experiments to measure this flux is based on Inverse Beta Decay (IBD) on free protons, a charged current interaction which makes detectable only electron-flavoured antineutrinos ($\bar{\nu}_e$). Since geoneutrinos, as all neutrinos and antineutrinos, undergo a phenomenon called neutrino oscillation, the effective geoneutrino flux $\Phi'(i,\bar{r})$ observed at detector site appears reduced by this flavor oscillation. The transformation matrix ruling these oscillations is called Pontecorvo–Maki–Nakagawa–Sakata matrix (PMNS matrix) [127], a presumably unitary matrix [128] depending on the mixing angles between neutrinos eigenstates θ_{12}, θ_{13} and θ_{23}, the square mass differences δm^2 and Δm^2 between these states and the δ phase accounting for the possible CP violation (Table 12).

Table 12. Updated oscillation parameters for neutrino oscillation together with their 1σ range. Values are taken from [127], considering normal ordering in the mass hierarchy.

	Best fit	**1σ range**
δm^2	7.34×10^{-5} eV^2	$[7.20 - 7.51] \times 10^{-5}$ eV^2
$sin^2\theta_{12}$	3.04×10^{-1}	$[2.91 - 3.18] \times 10^{-1}$
$sin^2\theta_{13}$	2.14×10^{-2}	$[2.07 - 2.23] \times 10^{-2}$
$\lvert\Delta m^2\rvert$	2.455×10^{-3} eV^2	$[2.423 - 2.490] \times 10^{-3}$ eV^2
$sin^2\theta_{23}$	5.51×10^{-1}	$[4.81 - 5.70] \times 10^{-1}$
δ	1.32 π	[1.14 π – 1.55 π]

By taking into account this flavor oscillation[6], the *survival probability*, namely the probability of observing an antineutrino of energy $E_{\bar{\nu}}$ which travelled a distance L from its emission point as still electron-flavored, can be approximated to [131]:

$$P_{ee}(L, E_{\bar{\nu}}) \sim cos^{\,4}\theta_{13}\left(1 - sin^{\,2}2\theta_{12} sin^{\,2}\left(\frac{\delta m^2 L}{4E_{\bar{\nu}}}\right)\right) + sin^{\,4}\theta_{13} \tag{10}$$

Hence, by making use of this equation, the effective *oscillated flux* ($\Phi'(i,\bar{r})$) detectable by IBD-based experiments can be modelled as:

$$\Phi'(i,\bar{r}) = \epsilon'_{i,\bar{\nu}} \cdot \int dE_{\bar{\nu}} \cdot Sp(i, E_{\bar{\nu}}) \int d^3r' \cdot P_{ee}(|\bar{r} - \bar{r}'|, E_{\bar{\nu}}) \cdot \frac{a(i,\bar{r}') \cdot \rho(\bar{r}')}{4\pi|\bar{r} - \bar{r}'|^2} \tag{11}$$

By inputting in this equation model-dependent assumptions based on geochemistry and geophysics evidences ($a(i,\bar{r}') \cdot \rho(\bar{r}')$) and integrating on Earth's volume, it is possible, starting from the geoneutrino energy spectra $Sp(i, E_{\bar{\nu}})$, to estimate the flux energy spectra $\Phi'(\bar{r}, E_{\bar{\nu}})$ at a given position (Figure 15, Chapter 2.4.4). Typically, the expected geoneutrino flux at surface is ~10^6 cm^{-2} s^{-1}, which is dominated by the crustal contributions (Chapter 2.6.1). In order to recover any kind of information on Earth's radiogenic heat production from a flux measurement, the final goal is the extraction of $a(i,\bar{r}')$. However, recovering this information is not straightforward, since the experimentally measured geoneutrino flux represents a volume integral weighted by the inverse square distance, and modulated by the P_{ee} oscillation probability. While the latter two ingredients are known with good accuracy, the volume distribution of Th and U is subjected to relatively large uncertainties, especially in the mantle (Chapter 2.3). Hence, to disentangle interesting pieces of information from geoneutrino measurements, scientists need an interdisciplinary approach capable of including supplementary constraints and assumptions from Earth science.

[6] An exact calculation of the oscillation probability of geoneutrinos crossing our planet would require the inclusion of the Mikheyev-Smirnov-Wolfenstein matter effect. However, since (i) this would require the calculation of Earth's density profile for each point and (ii) the overall effect on the flux has been estimated to account for less than 0.3%, it is usually safely neglected [129. Wan, L., et al., *Geoneutrinos at Jinping: Flux prediction and oscillation analysis*. Physical Review D, 2017. **95**(5): p. 053001, 130. Mao, X., R. Han, and Y.-F. Li, *Non-negligible oscillation effects in the crustal geoneutrino calculations*. Ibid.2019. **100**(11).]

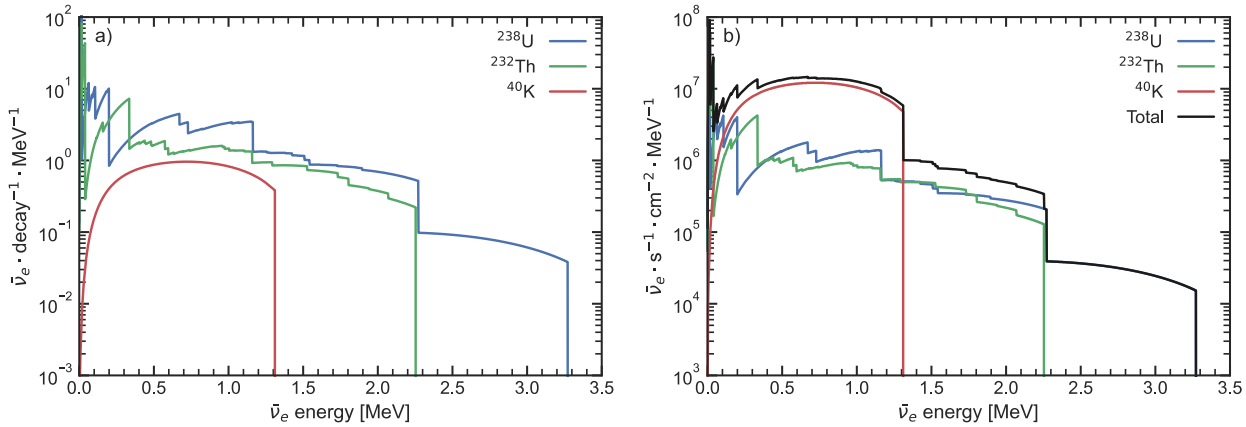

Figure 15. (a) Geoneutrino energy spectra of ^{238}U (in blue), ^{232}Th (in green) and ^{40}K (in red) from [132]. All spectra are normalized to one decay of the head element of the chain, leading to a total of 6, 4 and 0.89 geoneutrinos for the energy spectra of ^{238}U, ^{232}Th and ^{40}K, respectively. **(b)** Estimated oscillated fluxes of ^{238}U (in blue), ^{232}Th (in green), ^{40}K (in red) geoneutrinos and their sum (in black) at Laboratori Nazionali del Gran Sasso (LNGS) as a function of the geoneutrino energy.

Because of the homogeneity of geoneutrino production inside the Earth and the wide energy range of their spectra, most authors make the reasonable approximation of oscillation-averaged P_{ee}. Under this approximation, the oscillation term $\sin^2\left(\frac{\delta m^2 L}{4E}\right)$ is averaged over energy and distance at its approximated value of 0.5. Hence, the survival probability for electron flavored antineutrinos can be simplified to [131]:

$$\langle P_{ee} \rangle \cong \cos^4 \theta_{13} \left(1 - \frac{1}{2}\sin^2 2\theta_{12}\right) + \sin^4 \theta_{13} \tag{12}$$

The survival probability rapidly converges to its approximated value $\langle P_{ee} \rangle$ for distances >100 km. Instead, for distances <100 km, the survival probability has a stronger impact in the flux estimation and for this reason the Earth's region in the vicinity of the detector needs a refined modeling (Chapter 2.6.4). A functional approach to flux estimations consists in utilizing the precise survival probability for local regions, and the average survival probability for the rest of the Earth. The *a posteriori* assessment of the effect of this approximation [131] justifies its use, as the impact on the estimated signal is <0.2%, well below the experimental sensitivity reached so far (Figure 16).

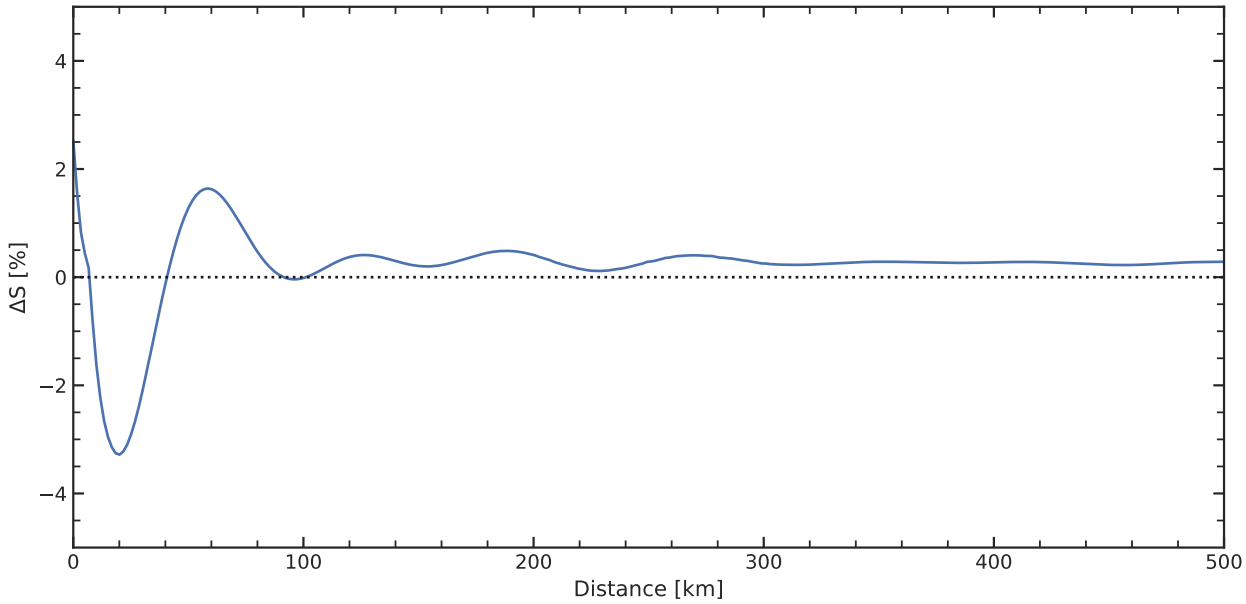

Figure 16. Percentage difference between the signal calculated by employing non-averaged (Eq. (10)) and averaged (Eq. (12)) survival probability normalized to the former signal as a function of the distance at which the survival probability is approximated at its average value of 0.55. Oscillation probability is calculated using best fit coefficients from Table 12.

The increasingly important achievements in the field of neutrino physics led to a continued refinement of the oscillation parameters. Because of the different values associated to θ_{12} and θ_{13}, the average survival probability $\langle P_{ee} \rangle$ used by the different authors changed along the years (Table 13), leading to slightly different flux estimates.

Table 13. Oscillation parameters ($\sin^2\theta_{12}$, $\sin^2\theta_{13}$) and derived average survival probability ($\langle P_{ee} \rangle$) used by different authors in the calculation of geoneutrino signals.

Reference	$\sin^2\theta_{12}$	$\sin^2\theta_{13}$	$\langle P_{ee} \rangle$
Mantovani et al., 2004 [88]	0.315 ± 0.035	-	0.57
Fogli et al., 2006 [133]	$0.31^{+0.06}_{-0.05}$	$0.009^{+0.023}_{-0.009}$	0.57
Enomoto et al., 2007 [134]	$0.29^{+0.05}_{-0.04}$	-	0.595
Dye, 2010 [93]	$0.32^{+0.03}_{-0.02}$		0.56 ± 0.02
Fiorentini et al., 2012 [131]	0.306 ± 0.017	0.021 ± 0.007	0.551 ± 0.015
Huang et al., 2013 [14]	-	-	0.55
Šrámek et al., 2016 [135]	-	-	0.553

After 2012, the adopted value for $\langle P_{ee} \rangle$ has converged to 0.55. When comparing recent estimates with signals obtained before 2012, careful attention must be given to rescaling the results to the up-to-date average survival probability.

2.4.3 Modelling the geoneutrino signal

The only two running experiments in the world capable of measuring geoneutrinos are Borexino and KamLAND (Chapter 2.5). Both experiments make use of the IBD reaction on free protons to detect antineutrinos:

$$\bar{\nu} + p \rightarrow e^{+} + n - 1.806\ MeV \tag{13}$$

In this reaction, the incoming antineutrino collides with a proton, producing a positron and a neutron (Figure 17). The outgoing positron promptly annihilates, producing two 511 keV gammas, usually referred as *prompt signal*. The outgoing neutron takes a mean time of ~⩾200 μs (254.5 ± 1.8 μs in Borexino and 207.5 ± 2.8 μs in KamLAND) to thermalize and then to be captured by a proton, producing a deuteron with the emission of a 2.2 MeV gamma (*delayed signal*), with an 1.1% of neutrons captured by a ^{12}C nucleus, with the emission of a 4.95 MeV gamma. Whereas these prompt and delayed signals are both time and space correlated, background-induced signals are not. Hence, this delayed coincidence method provides an extremely powerful background suppression, working as a very effective tagging technique for antineutrino interactions. KamLAND and Borexino employ the hydrogen atoms (protons) attached to hydrocarbon molecules as targets for IBD. Both use pseudocumene (1,2,4-trimethylbenzene) as scintillator solvent and PPO (2,5-diphenyloxazole) as fluor, but with slightly different percentages: in Borexino the PPO has a concentration of 1.5 g/l, while in KamLAND the concentration is 1.36 g/l. In addition, in KamLAND an 80% of an oil, dodecane, is added.

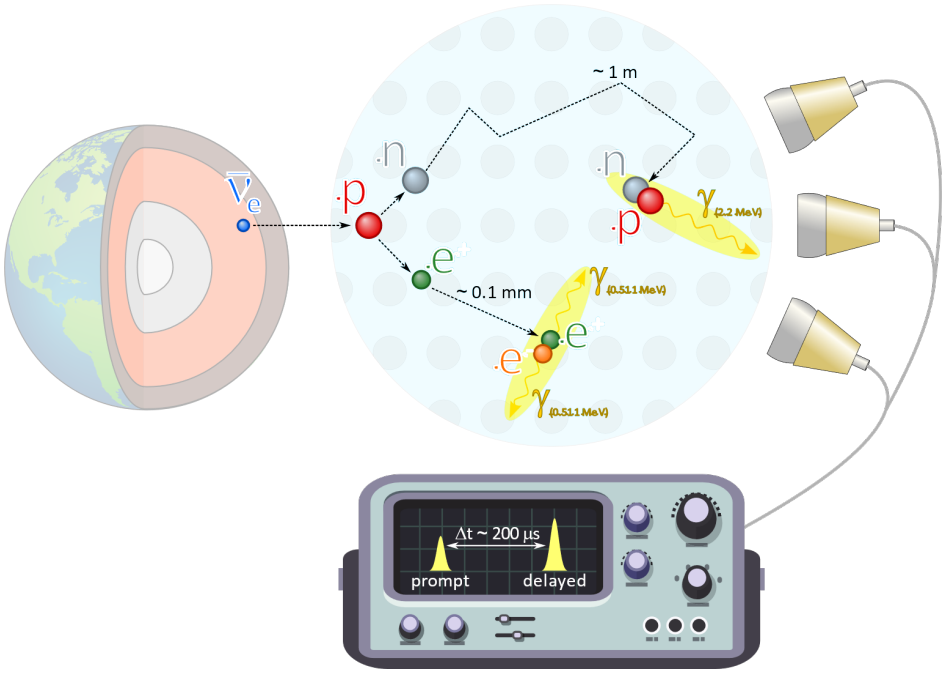

Figure 17. A scheme of the IBD reaction. An incoming antineutrino collides with a proton (p) inside the liquid scintillator, producing a neutron (n) and a positron (e^+). The positron readily annihilates producing two 0.511 MeV photons (γ) which excites the scintillator molecules, producing scintillating light seen by the photomultiplier tubes (PMTs) as a prompt signal. After thermalizing (typically in ~⩾200 μs), the neutron is later captured by a proton producing a 2.2 MeV photon, seen by the PMTs as a delayed signal.

The IBD (Chapter 2.9.4), whose cross section σ is known with 0.4% uncertainty, allowed KamLAND and Borexino to collect data even in periods when it is impossible to study neutrino interactions, as during operations in the detector or with the detector equipped for other scientific purposes. However, this reaction has a kinematic threshold of 1.806 MeV due the mass difference between the produced neutron and the target proton. Consequently, only 38% of the geoneutrinos emitted by the ^{238}U decay chain and 15% from ^{232}Th one remain above this threshold, while those from ^{40}K remain undetectable (Chapter 2.9).

The U and Th geoneutrino signals rates $S(U,\bar{r})$ and $S(Th,\bar{r})$ observed by a detector at position $\bar{r}$ can be calculated convolving the differential oscillated geoneutrino fluxes with the IBD cross section σ:

$$S(U,\bar{r}) = N_p \cdot T \cdot \epsilon'_{U,\bar{\nu}} \cdot \eta \cdot \int dE_{\bar{\nu}} \cdot \sigma(E_{\bar{\nu}}) \cdot Sp(U,E_{\bar{\nu}}) \cdot \int d^3r' \cdot P_{ee}(|\bar{r}-\bar{r}'|,E_{\bar{\nu}}) \cdot \frac{a(U,\bar{r}') \cdot \rho(\bar{r}')}{4\pi|\bar{r}-\bar{r}'|^2}$$
$$S(Th,\bar{r}) = N_p \cdot T \cdot \epsilon'_{Th,\bar{\nu}} \cdot \eta \cdot \int dE_{\bar{\nu}} \cdot \sigma(E_{\bar{\nu}}) \cdot Sp(Th,E_{\bar{\nu}}) \cdot \int d^3r' \cdot P_{ee}(|\bar{r}-\bar{r}'|,E_{\bar{\nu}}) \cdot \frac{a(Th,\bar{r}') \cdot \rho(\bar{r}')}{4\pi|\bar{r}-\bar{r}'|^2} \quad (14)$$

where $E_{\bar{\nu}}$ is the antineutrino energy integrated from 0 up to the endpoint of the antineutrino spectra, N_p is the number of proton targets available in the detector, T is the exposure time and η is the detector efficiency. Historically, geoneutrinos signals have been measured in *Terrestrial Neutrino Units* (TNU), where 1 TNU corresponds to 1 antineutrino event measured over 1 year by a detector containing 10^{32} free protons target, assuming 100% detection efficiency. By convolving the oscillated fluxes shown in Figure 15 with the IBD cross section σ, it is possible to estimate the signal energy spectra expected at detector position (Figure 18).

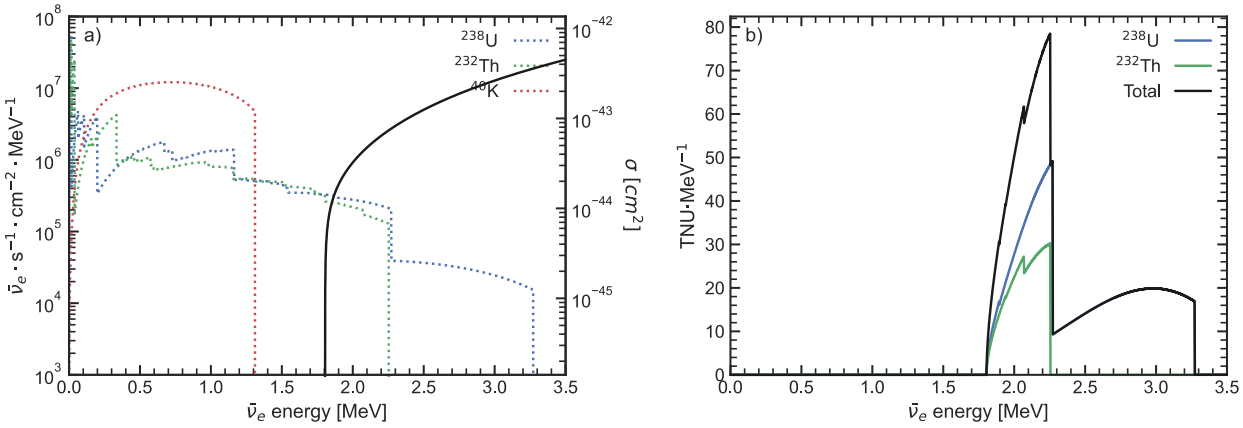

Figure 18. (a) IBD cross section σ (in black, expressed in cm^2) as a function of geoneutrino energy (in MeV). The dotted lines in the background show the oscillated fluxes of ^{238}U (in blue), ^{232}Th (in green) and ^{40}K (in red) geoneutrinos at LNGS (Figure 15). Because of the IBD kinematic threshold at 1.806 MeV, only 38% and 15% of the ^{238}U and ^{232}Th fluxes are detectable. The entire ^{40}K flux is instead below threshold. (b) ^{238}U (in blue), ^{232}Th (in green) and total (in black) geoneutrino signals (in TNU) expected at LNGS. These spectra are the results of the convolution between geoneutrino fluxes and IBD cross section depicted in (a).

As done for the fluxes, the formulas obtained for the geoneutrino signals can be simplified with some assumptions. Indeed, by substituting in Eq. (14) the average survival probability $\langle P_{ee} \rangle$ it is possible to separately integrate on volume (hence recovering the cumulative unoscillated antineutrino flux Φ) and on energy. The energy integral $\int \sigma(E_{\bar{\nu}}) \cdot Sp_i(E_{\bar{\nu}}) \cdot dE_{\bar{\nu}}$ is usually referred to as the integrated IBD cross section $\langle \sigma \rangle$, which can be easily calculated from the IBD cross section. For U and Th spectra, $\langle \sigma \rangle$ assumes the values $\langle \sigma(U) \rangle = 2.8\, TNU \cdot 10^{-6} s \cdot cm^2$ and $\langle \sigma(Th) \rangle = 4.04\, TNU \cdot 10^{-6} s \cdot cm^2$ [75], hence permitting to express the geoneutrino signals as:

$$S(U, \bar{r}) \cong \langle \sigma(U) \rangle \cdot \langle P_{ee} \rangle \cdot \Phi(U, \bar{r}) = 12.8 \cdot \langle P_{ee} \rangle \cdot \Phi(U, \bar{r})$$
$$S(Th, \bar{r}) \cong \langle \sigma(Th) \rangle \cdot \langle P_{ee} \rangle \cdot \Phi(Th, \bar{r}) = 4.04 \cdot \langle P_{ee} \rangle \cdot \Phi(Th, \bar{r}) \quad (15)$$

where signals S and the unoscillated fluxes Φ are expressed in TNU and $10^6 s^{-1} \cdot cm^{-2}$.

2.4.4 Numerically estimating the geoneutrino signal

The prediction of the IBD geoneutrino signal at a given experimental site requires the modelling of the three geoneutrino life-stages, i.e. (i) production inside the Earth, (ii) propagation to the detector site and (iii) detection via the IBD reaction on a given target as expressed by Eq. (14).

In order to perform this geoneutrino signal calculation it is necessary to adopt a 3-dimensional voxel-wise Earth model according to which each elemental volume is assigned with an HPE abundance and a volumetric density. At this scope, the Earth is typically divided into its two main HPEs bearing reservoirs, i.e. the lithosphere (shallow and relatively rich in HPEs) and the mantle (thick and relatively poor in HPEs) [14], while the core is typically considered as devoid of HPEs. The lithosphere (Chapter 2.6.1) is the outermost Earth's shell with an average thickness of 170 km, comprising (from top to bottom) sediments (compositionally subdivided in continental and oceanic sediments), continental and oceanic crust and continental lithospheric mantle. The continental crust is further subdivided in upper, middle, and lower crust, typically presenting different HPEs abundances (Chapter 2.6.2). The mantle has instead a typical thickness of 2800 km and extends from the bottom of the lithosphere to the core-mantle boundary.

The geophysical structure of the Earth is quite well established from seismic and gravimetric measurements both in terms of reservoir thicknesses and density [14]; on the other hand, a wide range of compositional models of the Bulk Silicate Earth (BSE) has been proposed in the past decades (Chapter 2.3). By adopting a chosen geophysical and geochemical model, the physical properties and the HPEs abundance of each 3D voxel can be assigned, and the resulting geoneutrino signal at surface can be numerically computed for each Earth's reservoir (Figure 19, Figure 20).

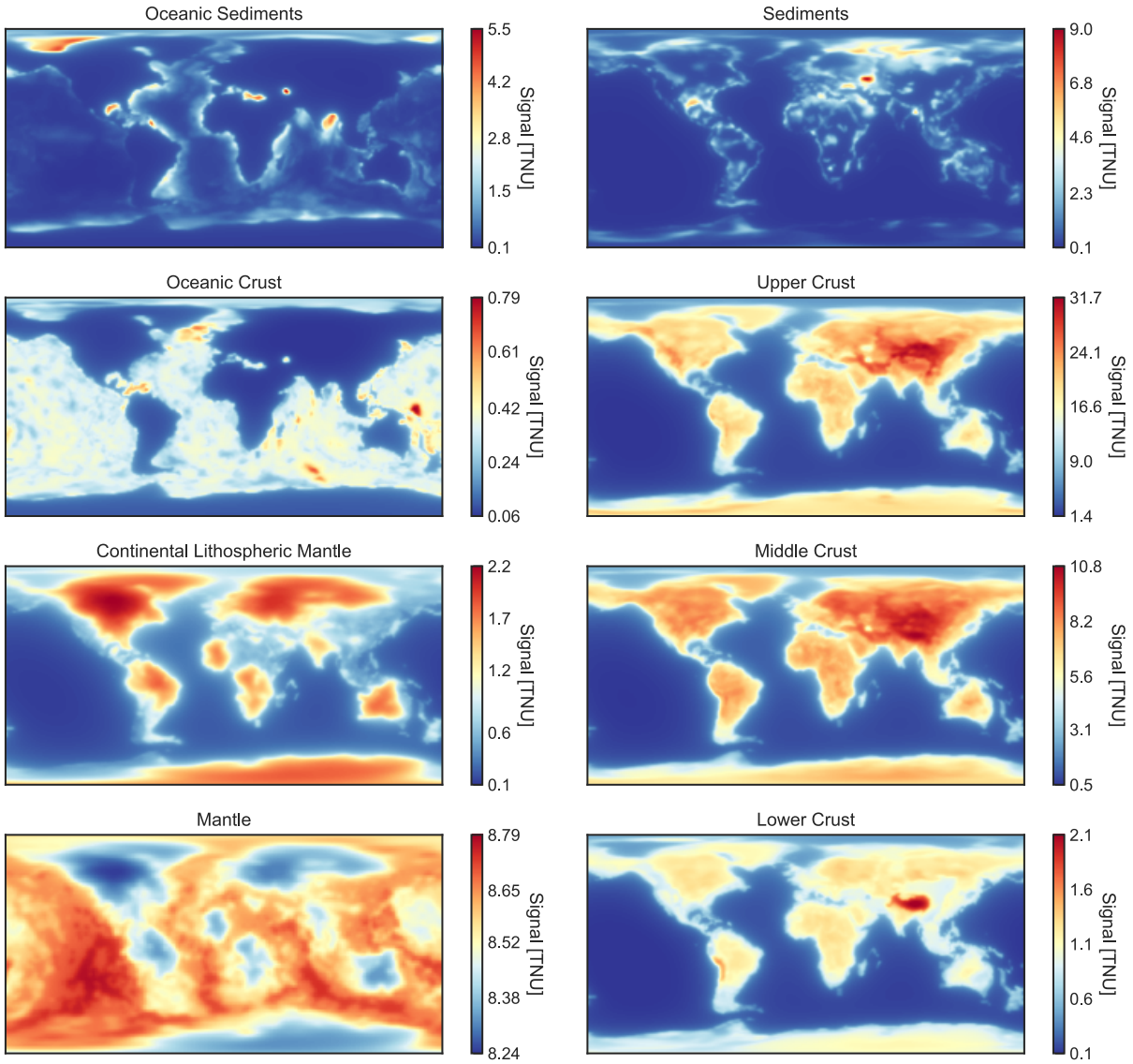

Figure 19. Geoneutrino signal at surface estimated for different Earth's reservoirs. In order to perform the estimation, Earth has been subdivided in 1° x 1° voxels, adopting a geophysical model from [136] and HPEs abundances from [14].

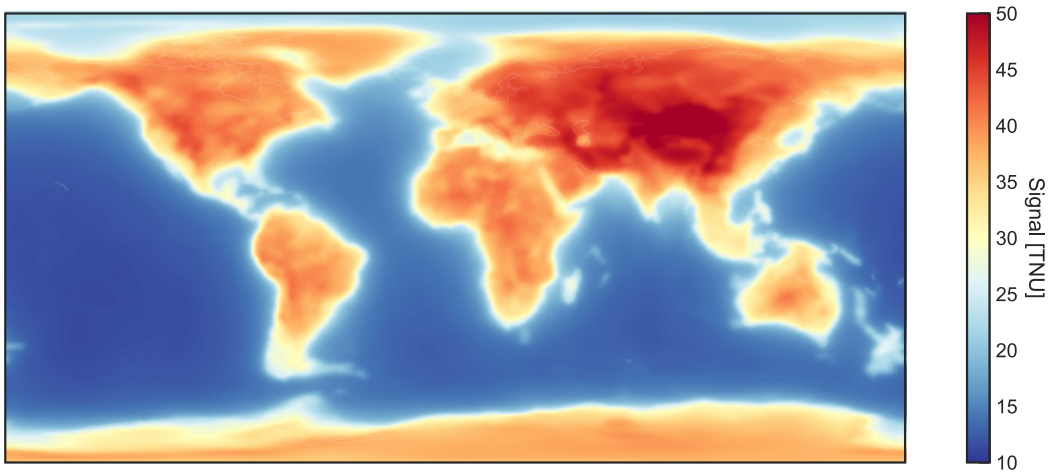

Figure 20. Total estimated geoneutrino signal at surface. In order to perform the estimation, Earth has been subdivided in 1° x 1° voxels, adopting the geophysical model from [136] and HPEs abundances from [14]. The total signal has been calculated by summing all contributions coming from the different reservoirs of Figure 19.

2.4.5 Numerically estimating antineutrino signals from other sources

The only other significant source of antineutrinos on Earth is nuclear fission inside reactors. The modelling of the reactor antineutrino signal is, in a way, easier than the estimation of geoneutrinos' one. Indeed, while the Earth can be seen as a continuous and extended source of geoneutrinos, reactor cores can be equated to point-like emitters.

Computationally, the stages of antineutrino propagation to the detector site and detection via the IBD reaction follow the exact same procedure adopted for geoneutrinos. The production stage requires instead a different modelling.

In commercial power plants, antineutrinos are primarily emitted by the fissions of four isotopes: ^{235}U, ^{238}U, ^{239}Pu, and ^{241}Pu. Fissions of other isotopes contribute less than 0.3%. A precise calculation of the antineutrino energy spectra resulting from these four isotopes' fissions is in general not a trivial task, but at first order the i-th isotope's spectrum Sp_i can be parametrized as [137, 138]:

$$Sp_i(E_{\bar{\nu}}) = \exp\left(\sum_{p=1}^{6} a_{i,p}\, E_{\bar{\nu}}^{p-1}\right) \tag{16}$$

where a are isotope-specific polynomial coefficients [138].

Once in possession of the antineutrino spectra, the total luminosity L can be estimated starting from the nominal thermal power P_{th} of the reactor as:

$$L(E_{\bar{\nu}}) = P_{th}\, LF \sum_{i=1}^{4} \frac{p_i}{Q_i} Sp_i(E_{\bar{\nu}}) \tag{17}$$

where p_i is the power fraction (i.e., P_i/P_{th}) of the i-th isotope, Q_i is the average energy released per fission and LF is the Load Factor (i.e., the percentage quantity expressing the effective working condition of a core in a specific period of the operating cycle).

Whilst Q_i and Sp_i are fixed and set by physics, P_{th}, p_i and LF are reactor and time dependent. These quantities can be obtained from the published PRIS database[7], monthly reporting for each operating reactor core the quantities of interest.

Once in possession of all the ingredients for the estimation of the antineutrino luminosity for each reactor's core, the resulting fluxes and antineutrino signals can be evaluated by summing the contributions coming from all reactors (Figure 21).

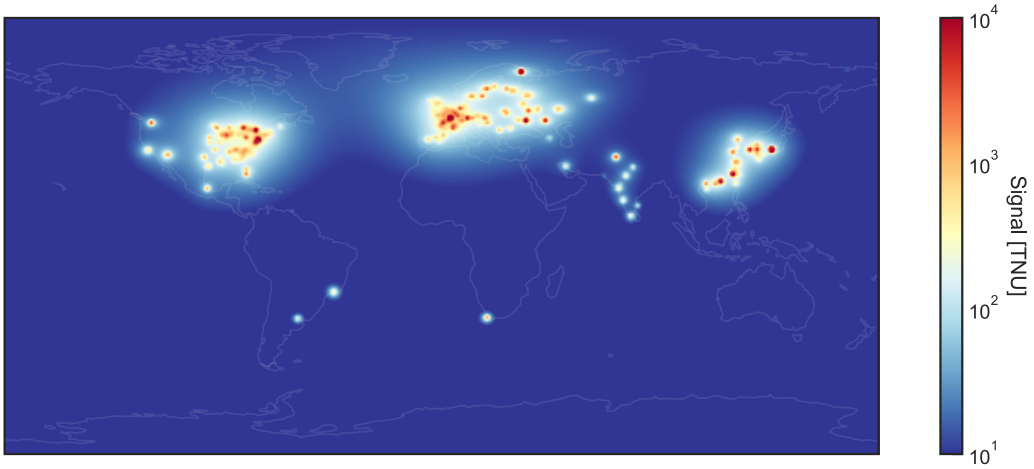

Figure 21. Total estimated reactor antineutrino signal at surface. In order to perform the estimation, the polynomial parametrization from [138] has been used for modeling the antineutrino spectra, while the reactor operating quantities have been derived from the yearly averaged 2019 IAEA database.

Once evaluated both the geoneutrino and reactor antineutrino components it is finally possible to estimate the total antineutrino signal expected at surface by summing these two contributions (Figure 22).

[7] A preprocessed updated database is available at https://www.fe.infn.it/radioactivity/antineutrino

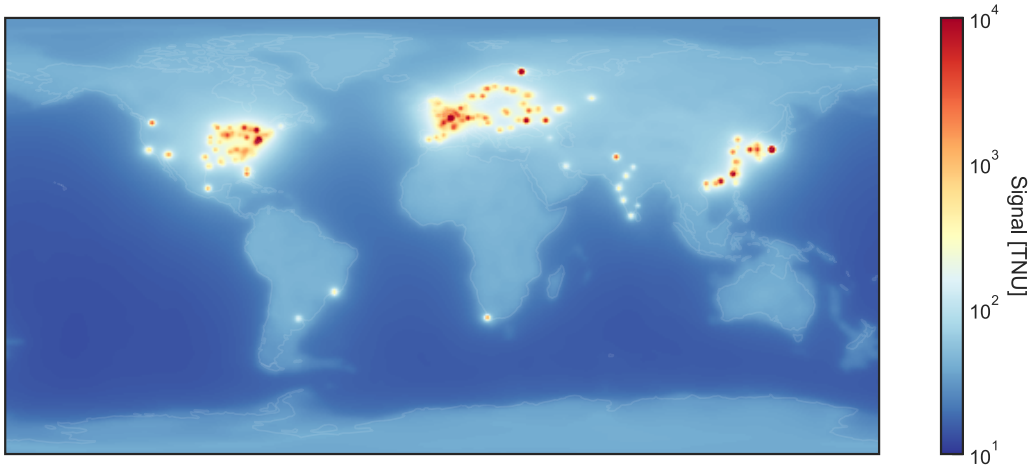

Figure 22. Total estimated reactor antineutrino signal at surface. The total signal has been calculated by summing the geoneutrino and reactor antineutrino components reported in Figure 20 and Figure 21, respectively.

2.5 Current experimental results

KamLAND and Borexino (Figure 23) are the only two running experiments which measured geoneutrinos, and they have been continuously collecting data till now. In July 2005, the KamLAND Collaboration claimed the first evidence of an antineutrino signal truly originating from geoneutrinos [7], later confirmed in 2010 by an independent measurement by the Borexino experiment [8]. In 2019, both collaborations published their latest results coming from the analysis of geoneutrinos, where both experiments observed at >5σ level signals of U and Th antineutrinos coming from the Earth. These experimental results offer an incredible opportunity to investigate the radiogenic production of Earth's mantle in view of currently proposed Earth's geochemical models (Chapters 2.6, 2.7, 2.8).

In the next decade other experiments will permit to study geoneutrinos (Chapter 2.5.3), opening the era of "multi-site detection". The SNO+ experiment in Canada is starting its "pure scintillator phase", which will allow the experiment to detect geoneutrinos, the JUNO experiment in China is currently under construction and expected to start its operations in 2023.

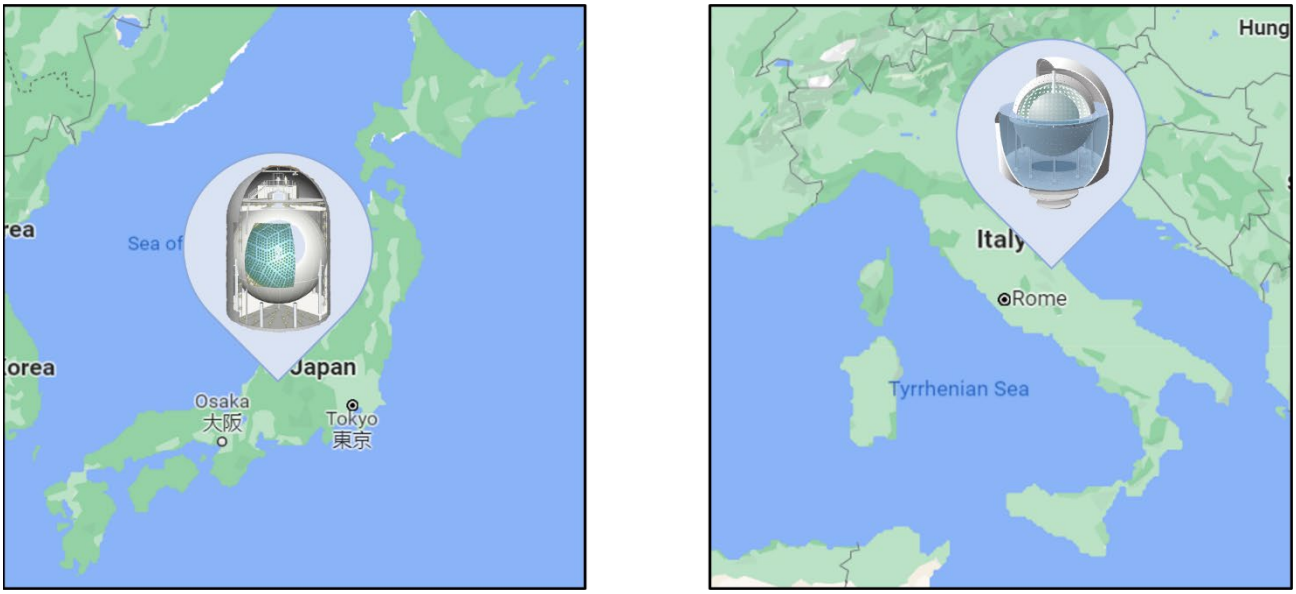

Figure 23. Locations of the KamLAND (left) and Borexino (right) experiments, respectively situated in Japan (36.423° N, 137.315° E) and Italy (42.454° N, 13.576° E).

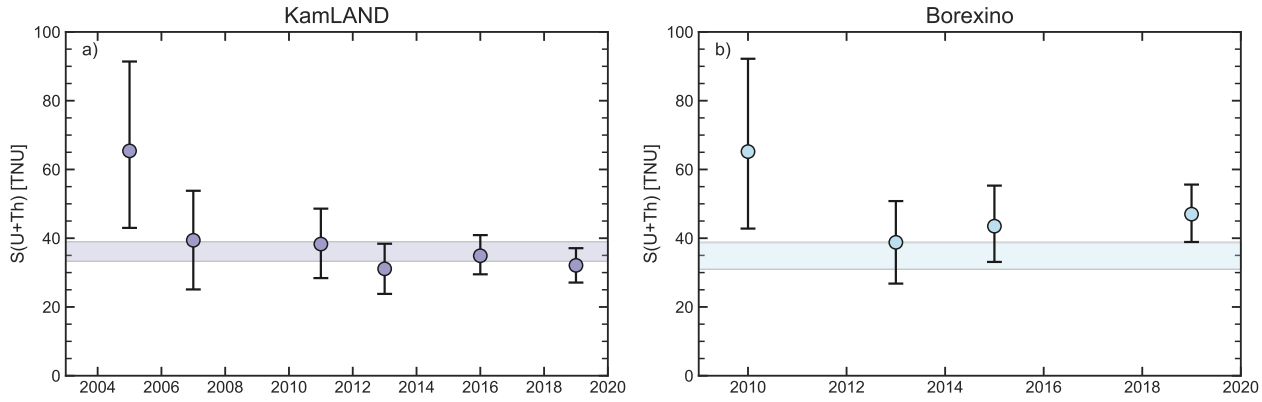

Figure 24. Comparison of the geoneutrino signal S(U+Th) (in TNU) measured by (a) KamLAND and (b) Borexino during the last decades. KamLAND and Borexino results are taken from [7, 9, 134, 139-141] and from [8, 75, 142, 143] respectively. Horizontal bars represent the 1σ C.L. of the signal expected following the arguments presented in Chapter 2.6.

2.5.1 KamLAND

KamLAND (Kamioka liquid scintillator antineutrino detector) is a 1000-ton liquid scintillator detector situated in a horizontal shaft mine in the Japanese Alps. The detector sits at a depth of 1000 m, corresponding to a shielding capacity of ~2700 m water equivalent. The overlying Ikenoyama mountain acts as an effective shield for cosmic radiation, reducing the muon flux in the detector by a factor of 10^5 with respect to the surface. Thanks to its pioneering sensitivity and its low background, KamLAND was the first experiment to detect an antineutrino signal originating from geoneutrinos.

In 2019, the KamLAND collaboration preliminarily published their latest results [141] (Table 14) of the geoneutrino analysis which resulted in a total signal coming from U and Th of $32.1^{+5.0}_{-5.0}$ TNU.

Table 14. Preliminary results from KamLAND analysis adapted from [141]. Reported results correspond to the median values together with the corresponding 68% confidence level deriving from both systematic and statistical uncertainties.

Th and U independent	**U**	**Th**	**U+Th**
Events	$123.3^{+41.2}_{-39.1}$	$41.6^{+24.6}_{-24.7}$	$164.5^{+28.7}_{-27.6}$
Signal [TNU]	$23.3^{+7.8}_{-7.4}$	$8.1^{+4.8}_{-4.8}$	$31.3^{+5.5}_{-5.2.}$

Th/U fixed at 3.9	**U**	**Th**	**U+Th**
Events	$138.0^{+22.3}_{-20.5}$	$34.1^{+5.4}_{-5.1}$	$168.8^{+26.3}_{-26.5}$
Signal [TNU]	$26.1^{+4.2}_{-3.9}$	$6.6^{+1.1}_{-1.0}$	$32.1^{+5.0}_{-5.0}$

2.5.2 Borexino

Borexino is a 280-ton liquid scintillator detector located in the Hall C of Laboratori Nazionali del Gran Sasso (LNGS), one of the largest underground laboratories in the world, situated under about 1400 m of rock with shielding capacity of 3800 m water equivalent. At this depth, the muon flux is suppressed by a factor of 10^6 with respect to the surface, which greatly reduces muon and muon induced backgrounds.

Thanks to the unprecedented radio-purity of the employed scintillator, the highly purified water used as an outer shield, the depth of the detector, and the use of custom-designed ultra-pure materials, Borexino resulted in very low background experiment representing an excellent apparatus for geoneutrino detection.

Since the start of its data taking period in May 2007, Borexino continued collecting data until October 2021. In 2019, the Borexino collaboration published their latest results [75] (Table 15) of the geoneutrino analysis which resulted in a total signal coming from U and Th of $47.0^{+8.4}_{-7.7}(\text{stat.})^{+2.4}_{-1.9}(\text{sys.})$ TNU.

Table 15. Summary of the geoneutrino events and the corresponding signal in TNU measured by Borexino [75]. Reported results correspond to the median values together with the corresponding 68% confidence level deriving from both systematic and statistical uncertainties.

Th and U independent	U	Th	U+Th
Events	$29.0^{+14.2}_{-13.0}$	$21.4^{+9.4}_{-9.2}$	$50.4^{+23.6}_{-22.2}$
Signal [TNU]	$25.7^{+12.5}_{-11.5}$	$19.5^{+8.5}_{-5.3}$	$45.0^{+21.1}_{-19.8}$

Th/U fixed at 3.9	U	Th	U+Th
Events	$41.1^{+7.5}_{-7.1}$	$11.5^{+2.2}_{-1.9}$	$52.6^{+9.6}_{-9.0}$
Signal [TNU]	$36.3^{+6.7}_{-6.2}$	$10.5^{+2.1}_{-1.7}$	$47.0^{+8.6}_{-8.1}$

2.5.3 Future experiments

The recent observations of geoneutrinos from the progenies of U and Th promise to add a new piece in the puzzle of Earth global properties. Although KamLAND and Borexino results can already provide constraints on the radiogenic contribution to the heat power (Chapter 2.8), we shall learn more by including data from the next generation of detectors.

The SNO+ experiment in Canada will soon start its "pure scintillator phase" which will include geoneutrinos detection; in China, the Jiangmen Underground Neutrino Observatory (JUNO) is currently under construction in the Guangdong province and in the Sichuan province is proposed the realization of a new detector in the China Jinping Underground Laboratory. These detectors are characterized by peculiar features in terms of depth and entity of background sources (reactor antineutrino and cosmic muon flux) (Table 16) from which arise different responses to the geoneutrinos signal. The plots reported in Figure 25 highlight that SNO+ and the proposed Jinping have the lowest cosmic-ray muon fluxes while at JUNO is expected the highest muon flux together with the highest reactor antineutrino signal.

As depicted in Figure 26, while the above-mentioned experiments are located on continental crust, the pioneering proposal of the Ocean Bottom Detector (OBD) aims to realize the first detector sited in oceanic crust providing a strong sensitivity to geoneutrinos originating from Earth's mantle.

Table 16. Location, depth and water equivalent depth (in km) expected muon flux (in cm^{-2} s^{-1}), active mass (in ktons) and expected antineutrino signals (in TNU) for SNO+, JUNO and Jinping detectors. Detectors depths are taken from [144], [145] and [146], while reported muon fluxes come from [144], [147] and [146]. For each detector, the total expected geoneutrino signal S(U+Th), the lithospheric signal S_{LS}(U+Th) and the mantle contribution S_M(U+Th) are calculated according to H13. For SNO+, the obtained lithospheric signal is updated adopting the refined crustal model of [148] for the NFC. The expected reactor antineutrino (S_{Rea}) signals in the Geoneutrino Energy Region (GER, from 1.8 MeV to 3.3 MeV) and in the Full Energy Region (FER, 1.8 MeV to 10 MeV)) at detector site were calculated from 2019 PRIS data following [137]. The ratios between S(U+Th)/S_{Rea}(GER) and S_M(U+Th)/S(U+Th) are also reported.

	SNO+ (46.4667°N, 81.1703°W)	**JUNO (22.1181°N, 112.5181°E)**	**Jinping (28.1532°N, 101.7114°E)**
Depth [km] (Water equivalent [km.w.e.])	2.1 (5.9)	0.7 (1.8)	2.4 (6.7)
Mass [kton]	0.78	20.0	4.0
Muon flux [cm^{-2} s^{-1}]	$3.3 \cdot 10^{-10}$	$4 \cdot 10^{-7}$	$3.53 \cdot 10^{-10}$
S(U+Th) [TNU]	$42.9^{+9.2}_{-5.3}$	$39.7^{+6.5}_{-5.2}$	$54.6^{+10.7}_{-8.9}$
S_{LS}(U+Th) [TNU]	$34.2^{+9.2}_{-5.3}$	$30.9^{+6.5}_{-5.2}$	$46.0^{+10.7}_{-8.9}$
S_M(U+Th) [TNU]	8.7	8.8	8.6
S_{Rea}(GER) [TNU]	$47.1^{+1.7}_{-1.4}$	$282.3^{+35.4}_{-32.3}$	$4.7^{+0.1}_{-0.1}$
S_{Rea}(FER) [TNU]	$189.7^{+4.6}_{-4.2}$	$631.9^{+44.8}_{-40.4}$	$17.9^{+0.4}_{-0.4}$
S(U+Th)/S_{Rea}(GER)	0.91	0.14	11.6
S_M(U+Th)/S(U+Th)	0.20	0.22	0.16

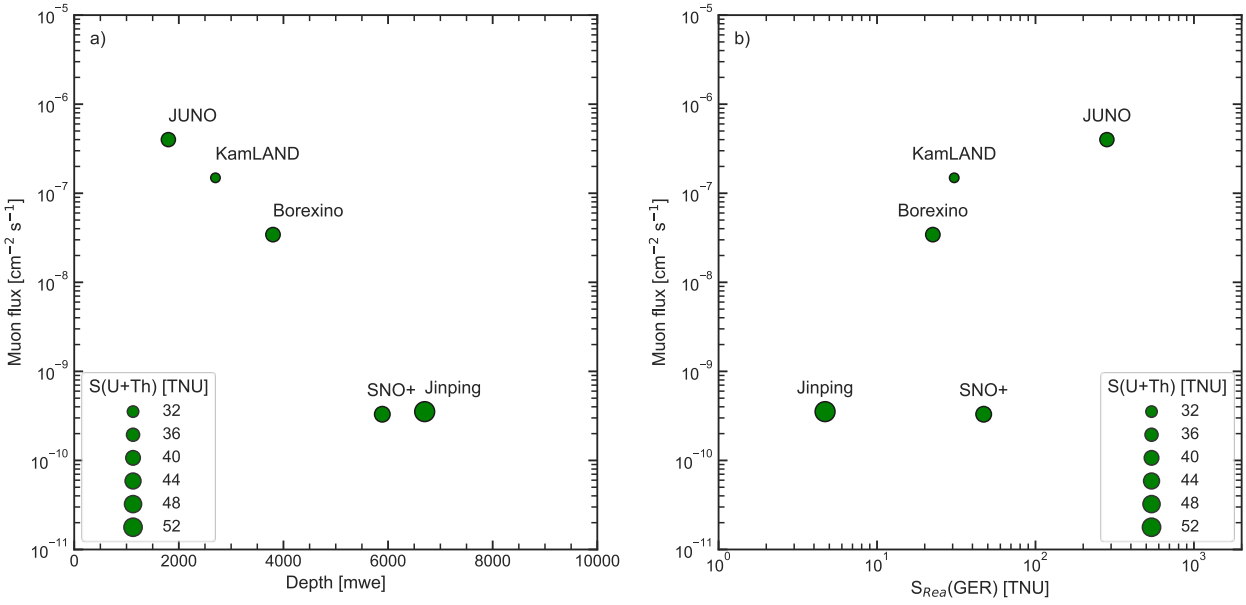

Figure 25. Muon flux expected at detector site vs water equivalent depth of the detectors **(a)** and vs **(b)** reactor antineutrino signal in the geoneutrino energy region (S_{Rea}(GER)) expected at detector site.

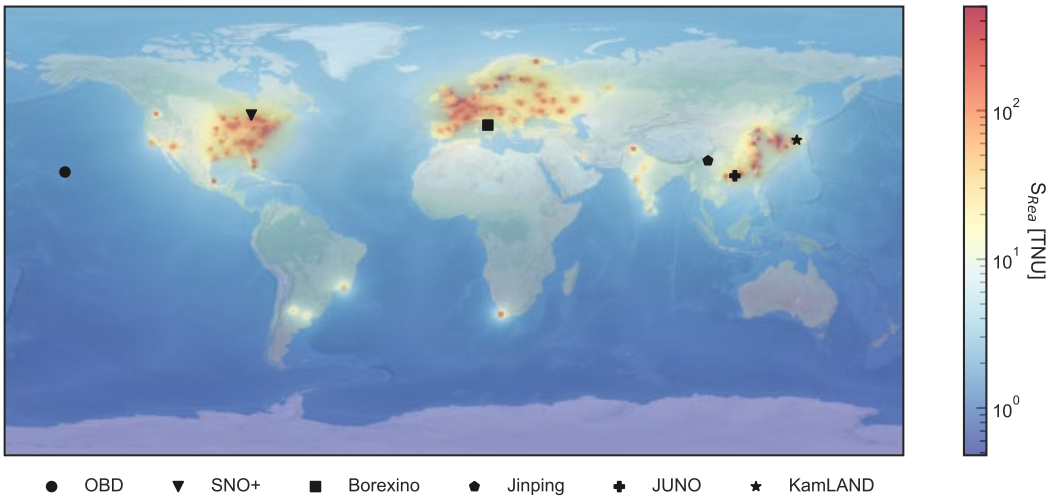

Figure 26. Map of the worldwide predicted antineutrino signals from nuclear power plants in the geoneutrino energy region (S_{Rea}) expressed in TNU. For each 1°x 1° cell, the signal is yearly calculated from 2019 PRIS data following [137]. The adopted numerical data are available at www.fe.infn.it/radioactivity/antineutrino/index.html**.** The locations of current and future liquid scintillator experiments are superimposed with different marker symbols.

2.6 Interpreting experimental results

2.6.1 Review of lithospheric models and their uncertainties

From 25% to 85% of the geoneutrino signal detected at surface comes from the closest Earth reservoir, the lithosphere [14, 149].

The use of geoneutrinos as probes for Earth's interior (i.e. the mantle) requires a deep knowledge of the lithospheric signal, so as to remove its contribution and to isolate the signal coming from the most interior reservoirs. Since the differentiation of the different signal contributions has proven difficult from the experimental point of view, the current evaluation of the lithospheric signal has to rely on geophysical and geochemical 3D models of the outer parts of our planet.

The main geophysical reservoirs composing the LS (Figure 27) are the crust, subdivided in CC and OCC and covered by a sedimentary layer (SED), and the CLM (Chapter 2.6.3). In Table 17 are reported masses, mass ratios and radiogenic heat of U, Th e K in the LS estimated according to the model reported in [14] (H13) and in [84]; the latter includes three different geophysical models, i.e. CRUST 2.0 (W20 – C2), CRUST 1.0 (W20 – C1) and LITHO 1.0 (W20 – L1).

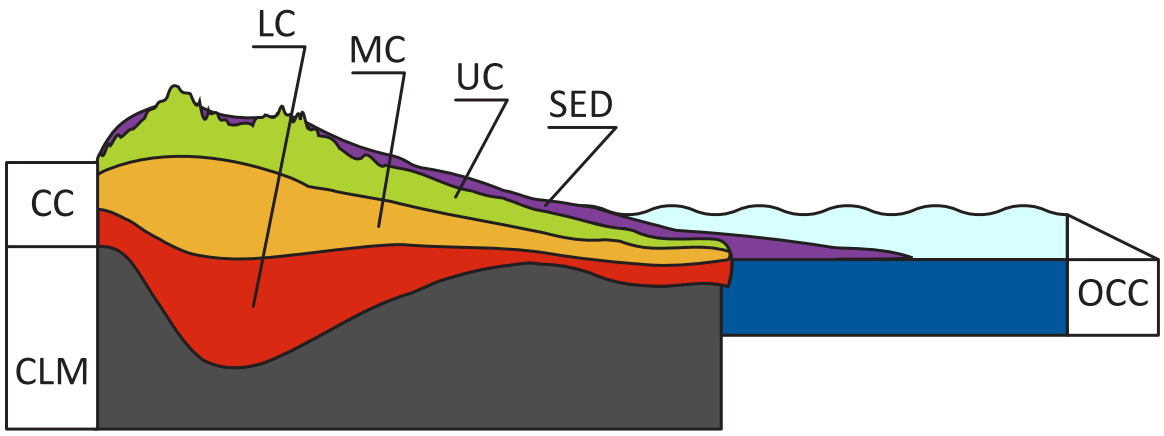

Figure 27. Schematic drawing of the structure of the lithosphere (not to scale). The continental crust (CC) is covered by the sedimentary layer (SED) and subdivided in the seismically defined upper crust (UC), middle crust (MC) and lower crust (LC). Under the CC we can distinguish the continental lithospheric mantle (CLM), not present in correspondence of the oceanic crust (OCC).

Table 17. HPEs' masses (M), mass ratios, radiogenic heat of the lithosphere (H_{LS}) considering the global lithospheric models: H13 based on [14], W20-C2, W20-C1 and W20-L1 based on [84].

	M_{LS}(U) [10^{16} kg]	M_{LS}(Th) [10^{16} kg]	M_{LS}(K) [10^{19} kg]	M_{LS}(Th)/ M_{LS}(U)	M_{LS}(K)/ M_{LS}(U) [10^4]	H_{LS}(U+Th) [TW]	H_{LS}(U+Th+K) [TW]
H13[a] [14]	$3.3^{+0.8}_{-0.7}$	$14.3^{+4.8}_{-2.8}$	$36.9^{+8.4}_{-6.0}$	4.3	1.2	$6.9^{+1.6}_{-1.2}$	$8.1^{+1.9}_{-1.4}$
W20 – C2[b] [84]	$3.3^{+1.0}_{-0.7}$	$14.5^{+5.3}_{-3.6}$	$36.3^{+11.0}_{-8.0}$	4.4	1.1	$6.9^{+2.6}_{-1.9}$	$8.1^{+2.3}_{-1.8}$
W20 – C1[b] [84]	$3.1^{+1.0}_{-0.7}$	$14.1^{+5.5}_{-3.6}$	$35.8^{+11.4}_{-7.1}$	4.5	1.2	$6.5^{+2.5}_{-1.8}$	$7.8^{+2.5}_{-1.8}$
W20 – L1[b] [84]	$3.2^{+0.9}_{-0.7}$	$14.2^{+4.6}_{-3.4}$	$36.6^{+10.2}_{-7.9}$	4.4	1.1	$6.9^{+2.3}_{-1.8}$	$8.2^{+2.6}_{-1.9}$
Adopted	$\mathbf{3.3^{+0.8}_{-0.7}}$	$\mathbf{14.3^{+4.8}_{-2.8}}$	$\mathbf{36.9^{+8.4}_{-6.0}}$	**4.3**	**1.2**	$\mathbf{6.9^{+1.6}_{-1.2}}$	$\mathbf{8.1^{+1.9}_{-1.4}}$

[a] As appeared in [75].

[b] Calculated based on data of Bulk CC, LM, OC (Sed and C) reported in Supplementary materials of the reference.

2.6.2 The Bulk Crust (BC)

The crust can be categorized in a dense and thinner (5–20 km thick) oceanic crust (OCC) and a lighter and thicker (20–70 km thick) continental crust (CC) (Figure 27). While the latter is generally acid and in turn characterized by higher HPE abundances (a(U)~1 ppm, a(Th)~10 ppm and a(K)~1%), the OCC is basic and depleted in HPEs (a(U)~0.1 ppm, a(Th)~0.1 ppm and a(K)~0.1%) [14]. Present antineutrino experiments such as KamLAND and Borexino (and future planned experiments, Chapter 2.5.3) sit on top of the CC, where the crustal contribution to the geoneutrino signal reaches ~65% and ~70%, respectively [14]. Along the years, the proposal of an "oceanic detector" placed on top of the OCC has been repeatedly formulated, but not realized until now due to the technical difficulties foreseen for its construction. Such a detector would permit to minimize the impact of the

crustal contribution, which would represent only ~20% of the detected signal, with the remaining ~80% being representative of the mantle [14].

The CC is not homogeneous, it exhibits a fine structure marked by the seismic Conrad discontinuity at 15-20 km deep [150]. The structure of the CC is seismically defined to consist of upper, middle, and lower crustal layers (UC, MC and LC, respectively) (Figure 27), which show increasing densities and seismic velocities ($\rho_{UC} = 2.72 \pm 0.05 \frac{g}{cm^3}$, $\rho_{MC} = 2.81 \pm 0.05 \frac{g}{cm^3}$, $\rho_{LC} = 2.95 \pm 0.06 \frac{g}{cm^3}$ and $V_{UC} = 6.0 \pm 0.2 \frac{km}{s}$, $V_{MC} = 6.4 \pm 0.2 \frac{km}{s}$, $V_{LC} = 6.9 \pm 0.2 \frac{km}{s}$) [151]. This gradual shift in the geophysical properties is accompanied by a smooth change in composition. Given the observed anticorrelation between seismic velocities and the SiO_2 content of rocks [14], deeper crust layers exhibit mafic/basic characteristics, while shallower layers show greater felsic/acidic components. As a result, the observed abundance of HPEs in the crust decreases with depth, with UC, MC and LC typically showing ~3 ppm, ~1 ppm and ~0.2 ppm of U and ~10 ppm, ~5 ppm and ~1 ppm of Th, respectively [14].

Along the past few decades, several geophysical models of increasing complexity and spatial resolution were proposed [152]. The first global geophysical model, 3SMAC [153], appeared in 1996. It included a tomographic model reporting the thickness and physical properties of all ice layers, sediment accumulations and oceanic and continental crust from Earth's surface to the upper mantle. In 1998, the 3SMAC model has been replaced by CRUST 5.1 [154], a model having a 5° x 5° resolution grid reporting the thickness and physical properties of lithospheric layers and the depth profile of seismic velocities. This model was further refined along the years, integrating an increasing amount of geophysical and geochemical data including new reflection and refraction seismic data, until the release of more resolute updates called CRUST 2.0 [155], having a 2° x 2° spatial resolution, and the 1° x 1° resolution Crust 1.0 [151]. Finally, the geophysical information included in CRUST 1.0 was used as starting model and perturbed to fit high-resolution surface wave dispersion to obtain LITHO 1.0 [136], a tessellated model of the crust and uppermost mantle of the Earth which interpolates the data over a ~1° triangular tin providing a continuous database of lithospheric properties on the Earth's surface.

Combining the geophysical information provided by the abovementioned global models and the chemical inputs obtained from geochemistry, authors produced in turn a variety of different crustal compositional models for predicting the expected geoneutrino signal at surface (Table 18).

Table 18. Abundances of uranium and thorium (in μg/g) for the different reservoirs of the continental (CC) and oceanic crust (OCC) according to different authors.

	a(U) [μg/g]						*a(Th)* [μg/g]					
	CC				OCC		CC				OCC	
Reservoir	**Sed**	**UC**	**MC**	**LC**	**Sed**	**OCC**	**Sed**	**UC**	**MC**	**LC**	**Sed**	**OCC**
Mantovani et al., 2004 [88]	1.68	2.5	1.6	0.62	1.68	0.1	6.9	9.8	6.1	3.7	6.9	0.22
Enomoto et al., 2007 [134]	2.8	2.8	1.6	0.2	1.7	0.10	10.7	10.7	6.1	1.2	6.9	0.22
Dye, 2010 [93]	2.70 ± 0.57	2.70 ± 0.57	1.30 ± 0.40	0.20 ± 0.16	1.70 ± 0.34	0.10 ± 0.02	10.5 ± 1.1	10.5 ± 1.1	6.50 ± 0.52	1.20 ± 0.96	6.90 ± 0.69	0.22 ± 0.02
H13* [14]	1.73 ± 0.09	2.7 ± 0.6	$0.97^{+0.58}_{-0.36}$	$0.16^{+0.14}_{-0.07}$	1.73 ± 0.09	0.07 ± 0.02	8.10 ± 0.59	10.5 ± 1.0	$4.86^{+4.50}_{-2.25}$	$0.96^{+0.18}_{-0.51}$	8.10 ± 0.59	0.21 ± 0.06
W20 – L1 [84]	2.7 ± 0.4	2.7 ± 0.6	$0.78^{+0.76}_{-0.38}$	$0.16^{+0.23}_{-0.09}$	1.73 ± 0.07	0.07 ± 0.02	10.49 ± 0.64	10.5 ± 1.0	$3.55^{+5.22}_{-2.11}$	$0.16^{+0.23}_{-0.09}$	8.10 ± 0.43	0.21 ± 0.05
W20 – C1 [84]	2.7 ± 0.4	2.7 ± 0.6	$0.87^{+0.84}_{-0.43}$	$0.18^{+0.26}_{-0.11}$	1.73 ± 0.07	0.07 ± 0.02	10.49 ± 0.65	10.5 ± 1.0	$4.22^{+6.21}_{-2.51}$	$1.10^{+2.75}_{-0.78}$	8.09 ± 0.44	0.21 ± 0.05
W20 – C2 [84]	2.7 ± 0.4	2.7 ± 0.6	$0.76^{+0.78}_{-0.38}$	$0.15^{+0.21}_{-0.09}$	1.73 ± 0.07	0.07 ± 0.01	10.49 ± 0.71	10.41 ± 0.99	$3.31^{+5.50}_{-2.07}$	$0.80^{+1.87}_{-0.56}$	8.10 ± 0.44	0.21 ± 0.04

By employing the abundances reported in Table 18 with different geophysical models, authors produced a variety of different crustal models predicting different HPEs masses and in turn different radiogenic heat production for the bulk crust (H_{BC}) (Table 19). Studies focused on the impact of geophysics variability showed that geoneutrino signal estimates obtained through the use of different geophysical models (Litho1.0, Crust 1.0 and Crust 2.0) yield similar results [84]. Hence, the main factor affecting the variability in the predicted signal at surface proves to be the HPEs abundances employed for the different crustal layers. The crustal signal rates at KamLAND and Borexino experimental sites calculated according to the different crustal models of Table 19 are reported in Table 20. Other authors produced crustal models reporting the expected geoneutrino flux for different experimental sites [135], while others produced interactive websites and maps predicting the geoneutrino flux at surface [156, 157].

Table 19. Masses of uranium, thorium (in 10^{16} kg) and potassium (in 10^{19} kg) together with the associated $M_{BC}(Th)/M_{BC}(U)$, $M_{BC}(K)/M_{BC}(U)$ ratios and the predicted radiogenic heat production coming from U+Th and U+Th+K (in TW) for the Bulk Crust (BC) reported by different authors. The recalculation of the radiogenic heats based on the updated h' coefficients (Table 3) is estimated to be less than 5%.

Model	**$M_{BC}(U)$ [10^{16} kg]**	**$M_{BC}(Th)$ [10^{16} kg]**	**$M_{BC}(K)$ [10^{19} kg]**	**$M_{BC}(Th)/M_{BC}(U)$**	**$M_{BC}(K)/M_{BC}(U)$ [10^4]**	**$H_{BC}(U+Th)$ [TW]**	**$H_{BC}(U+Th+K)$ [TW]**
Mantovani et al., 2004 [88]	3.53 ± 0.35	14.5 ± 1.5	36.7 ± 3.9	4.1	1.0	7.3 ± 0.7	8.6 ± 0.9
Enomoto et al., 2007 [134]	3.4	12.9	/	3.8	/	7.0	/
Dye, 2010 [93]	3.1 ± 0.8	13.9 ± 1.8	36.1 ± 6.1$^+$	4.3	1.1	/	7.8 ± 1.5^o
H13 [14]	$2.8^{+0.6}_{-0.5}$	$12.3^{+3.2}_{-2.1}$	$33.0^{+6.5}_{-4.9}$	4.4	1.2	$5.9^{+1.4}_{-1.2}$	$7.0^{+1.4}_{-1.1}$
W20 – C2 [84]	$2.9^{+0.8}_{-0.6}$	$12.5^{+0.8}_{-0.6}$	$33.9^{+9.6}_{-7.5}$	4.3	1.1	$5.9^{+2.0}_{-1.6}$	$7.2^{+2.0}_{-1.6}$
W20 – C1 [84]	$2.7^{+0.7}_{-0.6}$	$12.3^{+4.1}_{-3.0}$	$32.2^{+9.2}_{-7.1}$	4.5	1.2	$5.9^{+2.2}_{-1.7}$	$7.0^{+2.1}_{-1.6}$
W20 – L1 [84]	$2.9^{+0.8}_{-0.6}$	$12.8^{+3.1}_{-1.4}$	$32.4^{+8.9}_{-7.0}$	4.4	1.2	$6.2^{+2.1}_{-1.6}$	$7.4^{+2.1}_{-1.6}$
Adopted	$\mathbf{2.8^{+0.6}_{-0.5}}$	$\mathbf{12.3^{+3.2}_{-2.1}}$	$\mathbf{33.0^{+6.5}_{-4.9}}$	**4.4**	**1.2**	$\mathbf{5.9^{+1.4}_{-1.2}}$	$\mathbf{7.0^{+1.4}_{-1.1}}$

*As appeared in [75].

+Calculated considering a ^{40}K isotopic abundance from Table 11.

Table 20. Geoneutrino signals (in TNU) of the bulk crust expected at Borexino and KamLAND experimental sites according to different authors. In order to obtain comparable signal estimates, models based on out-of-date oscillation parameters [88, 93, 134] were scaled according to the updated $\langle P_{ee} \rangle = 0.55$.

Model	Borexino	KamLAND
	S_{BC}(U+Th) [TNU]	S_{BC}(U+Th) [TNU]
Mantovani et al., 2004 [88]*	29.6 ± 2.9	24.7 ± 2.4
Enomoto et al., 2007 [134]°	/	24.2 ± 2.2
Dye, 2010 [93]°	29.5 ± 7.1	23.5 ± 5.6
H13 [14]	$29.0^{+6.0}_{-5.0}$	$20.6^{+4.0}_{-3.5}$
W20 – C2 [84]	$31.6^{+8.1}_{-6.4}$	$23.5^{+5.9}_{-4.7}$
W20 – C1 [84]	$31.1^{+8.0}_{-6.4}$	$24.6^{+6.6}_{-5.2}$
W20 – L1 [84]	$33.0^{+7.9}_{-6.4}$	$27.0^{+7.1}_{-5.6}$

*Obtained applying Eq. (15) to the reported fluxes of U and Th with $\langle P_{ee} \rangle = 0.55$, summed as fully correlated.
°Scaled according to the approach illustrated in Appendix A.3.

2.6.3 Continental Lithospheric Mantle (CLM)

The CLM is a portion of the mantle underlying the CC included between the MOHO and the LAB (Chapter 2.1.1). Previous models of geoneutrino flux [88, 93, 133, 134] relied on the density profile of the mantle as given by the Preliminary Reference Earth Model (PREM) [12]. In these models, the crust and the mantle were treated as two separate geophysical and geochemical reservoirs. In particular, the mantle was conventionally described as a shell between the crust and the core and considered compositionally homogeneous [93, 134]. These models did not consider the heterogeneous topography of the base of the crust, or the likely differences in composition of the lithospheric mantle underlying the oceanic and continental crusts. In more recent models [14, 84, 135], the CLM beneath the continents is instead treated as a distinct geophysical and geochemical reservoir that is coupled to the crust in the reference Earth model, forming the LS. The assumption is that the lithospheric mantle beneath the oceans is compositionally identical to the DM, and therefore, constraining its thickness, it is not crucial in modelling the geoneutrino signal. On the other hand, the lithospheric mantle under the CC (i.e. CLM) is compositionally different from both the CC and the DM, with its top starting from the MOHO surface and the bottom being difficult to constrain.

It is only recently that authors started to include the CLM in the geochemical and geophysical modelling of the LS. Despite the adoption of different geophysical models, both the models proposed by H13 and W20 employed the same geochemical abundances $a_{CLM}(U) = 0.03^{+0.05}_{-0.02}$ µg/g , $a_{CLM}(Th) = 0.15^{+0.28}_{-0.10}$ µg/g and $a_{CLM}(K) = 0.03^{+0.04}_{-0.02}$ %, which in turn produced consistent predicted masses and radiogenic heat for the LS (Table 21).

By employing the reported HPE masses, authors estimated the expected geoneutrino signals $S_{CLM}(U+Th)$ at KamLAND and Borexino experimental sites, listed in Table 22 together with the values adopted for the mantle signal extraction from experimental results. Coherently with the strategy followed for the estimation of the signal produced by the BC (Chapter 2.6.4), the adopted CLM signal is taken from [14] both for KamLAND and Borexino experiments.

Table 21. Masses of uranium, thorium (in 10^{16} kg) and potassium (in 10^{19} kg) together with the associated $M_{CLM}(Th)/M_{CLM}(U)$, $M_{CLM}(K)/M_{CLM}(U)$ ratios and the predicted radiogenic heat production coming from U+Th and U+Th+K (in TW) for the CLM.

Model	$M_{CLM}(U)$ [10^{16} kg]	$M_{CLM}(Th)$ [10^{16} kg]	$M_{CLM}(K)$ [10^{19} kg]	$M_{CLM}(Th)/M_{CLM}(U)$	$M_{CLM}(K)/M_{CLM}(U)$ [10^4]	$H_{CLM}(U+Th)$ [TW]	$H_{CLM}(U+Th+K)$ [TW]
H13 [14]	$0.29^{+0.54}_{-0.20}$	$1.45^{+2.94}_{-0.94}$	$3.1^{+4.7}_{-1.8}$	5.0	1.1	$0.7^{+1.1}_{-0.5}$	$0.8^{+1.1}_{-0.6}$
W20 – C2 [84]	$0.24^{+0.61}_{-0.17}$	$1.06^{+3.06}_{-0.79}$	$2.3^{+5.6}_{-1.6}$	4.4	1.0	$0.4^{+1.1}_{-0.3}$	$0.5^{+0.8}_{-0.3}$
W20 – C1 [84]	$0.20^{+0.60}_{-0.15}$	$0.91^{+2.97}_{-0.70}$	$1.9^{+5.5}_{-1.4}$	4.6	1.0	$0.4^{+1.1}_{-0.3}$	$0.5^{+1.6}_{-0.4}$
W20 – L1 [84]	$0.19^{+0.28}_{-0.12}$	$0.88^{+1.54}_{-0.56}$	$1.9^{+2.5}_{-1.1}$	4.6	1.0	$0.5^{+1.4}_{-0.4}$	$0.6^{+1.6}_{-0.4}$
Adopted	$\mathbf{0.29^{+0.54}_{-0.20}}$	$\mathbf{1.45^{+2.94}_{-0.94}}$	$\mathbf{3.1^{+4.7}_{-1.8}}$	**5.0**	**1.1**	$\mathbf{0.7^{+1.1}_{-0.5}}$	$\mathbf{0.8^{+1.1}_{-0.6}}$

Table 22. Continental lithospheric mantle geoneutrino signals (in TNU) expected at Borexino and KamLAND experimental sites according to different authors together with the values adopted in this study (taken from H13).

Model	Borexino	KamLAND
	$S_{CLM}(U+Th)$ [TNU]	$S_{CLM}(U+Th)$ [TNU]
H13 [14]	$2.2^{+3.1}_{-1.3}$	$1.6^{+2.2}_{-1.0}$
W20 – C2 [84]	$1.8^{+3.0}_{-1.1}$	$1.3^{+2.2}_{-0.8}$
W20 – C1 [84]	$1.7^{+2.9}_{-1.1}$	$1.4^{+2.4}_{-0.9}$
W20 – L1 [84]	$0.8^{+1.2}_{-0.5}$	$0.8^{+1.2}_{-0.5}$
Adopted	$\mathbf{2.2^{+3.1}_{-1.3}}$	$\mathbf{1.6^{+2.2}_{-1.0}}$

2.6.4 Geoneutrinos from the region near the detectors

In geoneutrino science, multiple sites geoneutrino studies appear as the most reliable tool for disentangling the unresolved riddles about the Earth's heat budget, BSE compositional paradigms and mantle convection. Given the predicted signal of the accessible lithosphere, the mantle component is assumed to be the same for diverse geoneutrino detectors and it can be indirectly inferred from a combined treatment of experimental signals [94, 131] (Chapter 2.7). A correct discrimination of the mantle geoneutrino signal must be grounded on a solid prediction of the crustal component and its uncertainty. In this puzzle, the geophysical and geochemical modelling of the crust, especially of the portion near to the detector, is certainly the most compelling task and, at the same time, the thorniest charge for scientists of the geoneutrino community.

Borexino and KamLAND - but also the forthcoming SNO+ and JUNO - measure a geoneutrino signal whose mantle contribution is about one quarter of the total [14, 135].

The site-dependent crustal component represents the dominant contribution due to the concomitance of diverse factors affecting the geoneutrino production, propagation, and detection.

The ~30 km thick CC hosting and standing above the underground detectors is characterized by U and Th abundances which are globally at least one order of magnitude higher respect to OCC or CLM (Table 18).

The distance dependency of the antineutrino survival probability makes the geoneutrino signal from the Near-Field Crust (NFC) even more influential for the indirect study of the mantle radioactivity. While the average survival probability ($\langle P_{ee} \rangle = 0.55$) could be a reasonable approximation for describing the oscillation during the propagation at long distances (~10000 km), a particular attention must be paid if dealing with small distances (~100 km) (Figure 16). The result is an amplification/reduction effect of the geological peculiarities of the NFC which can be translated in a not negligible (1 - 2 TNU) difference between the signals calculated with an average or a precise oscillation probability [130].

Additionally, the isotropic $1/4\pi r^2$ spherical scaling factor ensures that the geoneutrino flux reaching a detector is dominated by the natural radioactivity surrounding the detector. This contribution can be, in a first attempt, estimated exploiting the global models of the LS illustrated in Chapter 2.6.1 (Table 23). H13, W20 – C2, W20 – C1 and W20 – L1. The geophysical structure of the 9° × 9° area centered in the Borexino and KamLAND detectors depicted in the four global models is represented in Figure 30.

For the KamLAND region (Figure 28), all the global models predict a SED layer with a rather homogenous thickness with an average value of 0.8 km and the higher values (> 1.2 km) recorded in the eastern area of the Japan sea. For the continental area, the average SED thickness is ~ 0.4 km (Figure 28a) but a clear disagreement among the four models is observed, particularly in the region at southwest of the detector (Figure 28d, f, h), and in turn for the BC (Figure 28j), an opposite trend is observed: the global models substantially agree on the values for the continental area while this does not happen for the Japan sea where the percent relative range is always higher than 100%. In the continental area the average thickness of UC and LC is 12 km (Figure 28c, g), while the MC appears thinner (~10 km) (Figure 28e), resulting in a total BC thickness ranging from 28 km to 38 km (Figure 28i). In the oceanic region thickness values ranging from 3 – 6 km are observed for the three

crustal layers (c, e, g), while the average value for the BC varies between 8 and 18 km (Figure 28i).

According to the global crustal models the thickness of the SED layers in the area hosting Borexino is characterized by a high variability (Figure 29a), with an average value ranging from 0.7 km in the proximity of the detector to 7 km in the Adriatic Sea (eastern area). Moreover, the four global crustal model present values that differ greatly from each other with a percentage relative range that is ~ 200% in the 3° × 3° tiles surrounding Borexino (Figure 29b). For the UC, a percentage relative range higher (~100%) is observed only in the Tyrrhenian sea area (Figure 29d) while the global models substantially agree on a homogeneous average value of 4 km in the rest of the region (Figure 29c). The same trend is observed for the MC and the LC (Figure 29f - h) which have an average thickness respectively of 5 km and 8 km in the Tyrrhenian sea area and of 12 km in the rest of region (Figure 29e - g). The BC thickness is characterized by an increasing trend from southwest to northeast with average values ranging from 15 to 48 km (Figure 29i). The high discrepancy among the global models in the predicted thickness of the BC is observed in the sea region and in the area at south of the detector where the percentage relative range is ~50% (Figure 29j).

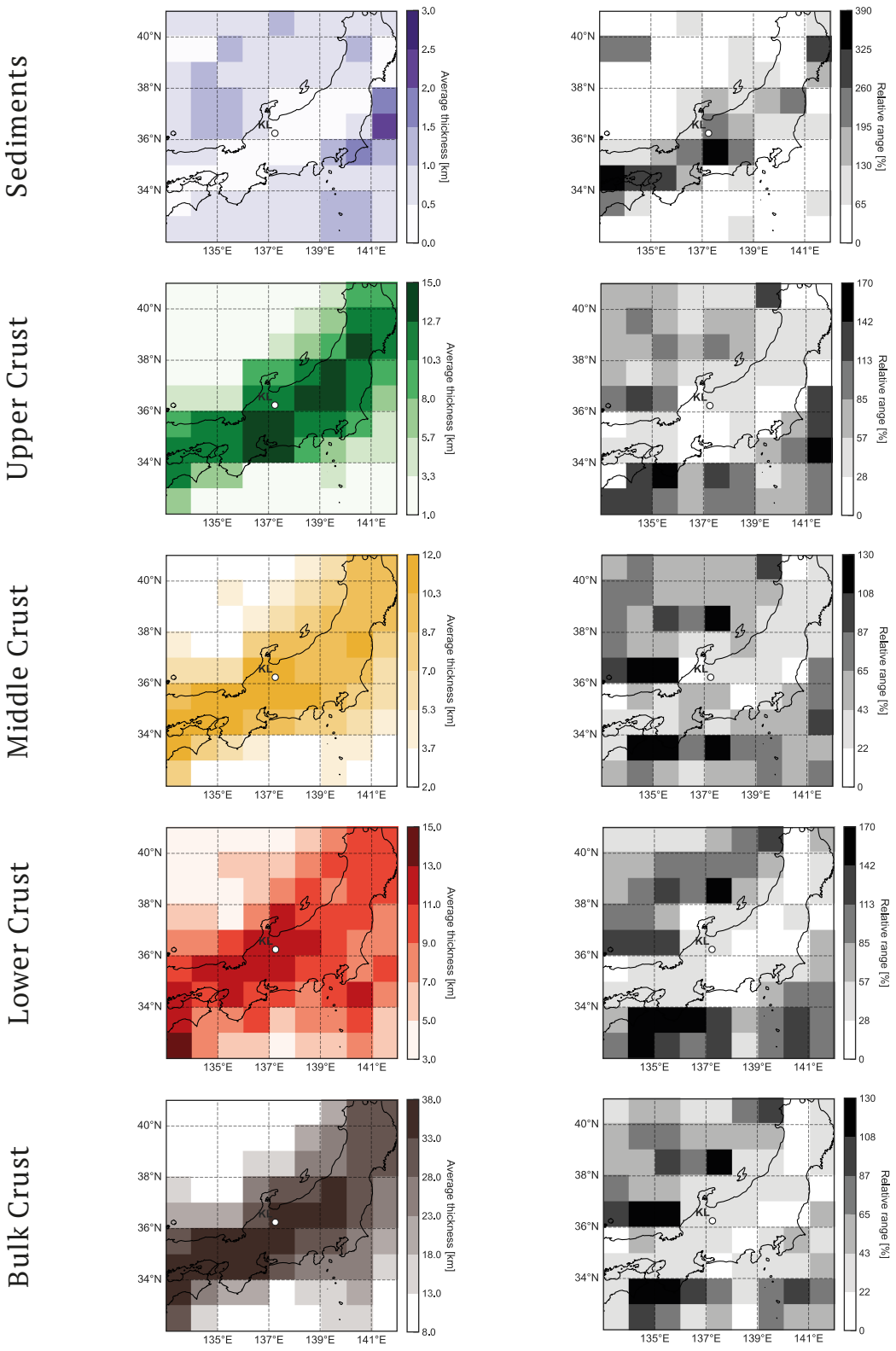

Figure 28. Left panels: thickness of the Sediments (SED), Upper Crust (UC), Middle Crust (MC), Lower Crust (LC) and Bulk Crust (BC) of the 9° × 9° area centered in the KamLAND detector. The value of each 1° × 1° tile is the average obtained considering the model, CRUST 2.0, CRUST 1.0, Litho 1.0 and H13 models. Right panels: percent relative range [(maximum value – minimum value)/average value *100) of the models obtained for each tile for SED, UC, MC, LC and BC.

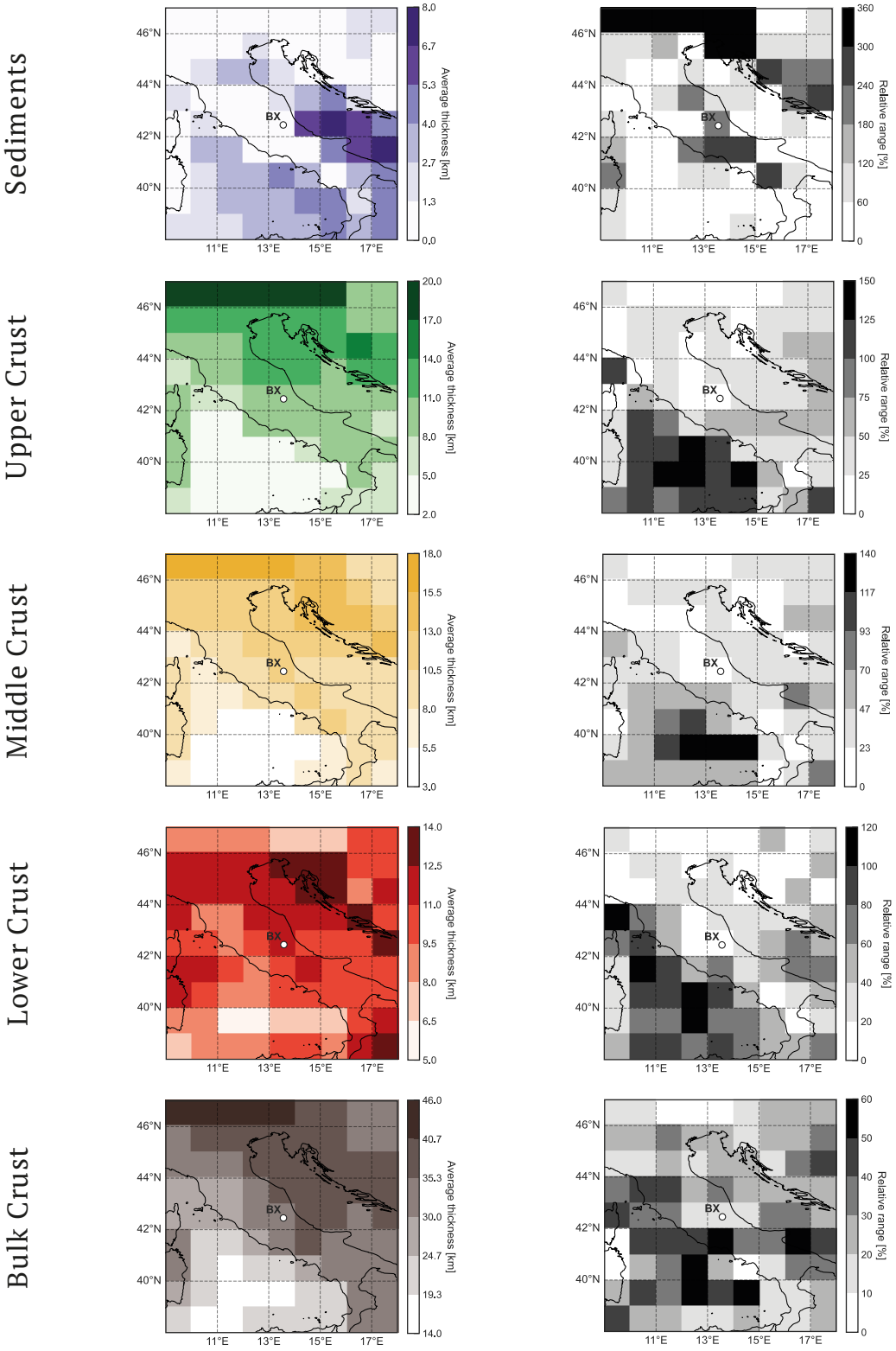

Figure 29. Left panels: thickness of the Sediments (SED), Upper Crust (UC), Middle Crust (MC), Lower Crust (LC) and Bulk Crust (BC) of the 9° × 9° area centered in the Borexino detector. The value of each 1° × 1° tile is the average obtained considering the model, CRUST 2.0, CRUST 1.0, Litho 1.0 and H13 models. Right panels: percent relative range [(maximum value – minimum value)/average value *100) of the models obtained for each tile for SED, UC, MC, LC and BC.

The geochemical modeling performed by [14] and [84] have some common ground: the SED and the UC are considered compositionally homogenous while the uranium and thorium abundances in MC and LC in each voxel depend on seismic arguments (Chapter 2.6.2). Looking into details, the abundances assigned to UC, SED and crust of OCC are identical, but the continental sediments are treated with two different approaches (Table 18). [84] assume that, due to the weathering effect, the sediments have the same U and Th abundances of UC, higher than those assigned by [14] on the basis of the Global Subducting Sediments II model [158]. Due to the proximity of this layer to the detectors, this divergence is the main origin of the increasing trend of the geoneutrino signals reported in [84] (Table 23).

Despite these differences, the mentioned global models obtained a similar ratio between the geoneutrino signal from the NFC, i.e. the 24 voxels close to the detectors (Figure 30), and the BC geoneutrino signal that is S_{NFC}/S_{BC} ~ 0.67 for KamLAND[8] and S_{NFC}/S_{BC} ~ 0.55 for Borexino. These results prove that such small regions account for the most relevant contribution to the geoneutrino signal. For this reason, local refined models based on specific geophysical and geochemical data were developed to provide a more accurate and reliable predictions. For KamLAND experiment, [159] and [134] proposed a site-specific geophysical and geochemical modeling of the crust near the detector while a 3D geophysical and geochemical model of the crust surrounding the Borexino detector was proposed by [160].

The Japan island arc, hosting the KamLAND detector, is part of a continental shelf located close to the eastern margin of the Eurasian plate. The Philippine plate and the Pacific plate are moving towards the Eurasian plate and are subducting respectively beneath the southern and the northern part of Japan. The submarine trenches are thus formed with parallel uplifted areas and intense igneous activity. The KamLAND site is sited in a typical continental crust of Island Arc and Forearc environment. The Sea of Japan, situated between the Japan island arc and the Asian continent, is classified as marginal sea and it is bordered by islands and expanded basins on the back-arc side (back arc basin). [131] and [134] adopted the same geophysical and geochemical inputs and additionally studied the effects on geoneutrino signal of the peculiarities characterizing the subducting slab and the Japan Sea crust.

[8] Note that the NFC defined by Wipperfurth et al. 2020 is not coincident with the NFC defined by Huang et al. 2013 (Figure 30).

The Gran Sasso range, where the Borexino experiment is located, is a massif of the Central sector of the Apennines, a peri-Mediterranean chain part of the Adria plate. The actual geological structure of the Apennine chain is the result of the geodynamical processes occurred during its orogenesis began in the early Neogene (20 million years ago). A refined reference model for the Gran Sasso area was developed by [160] in which local and specific geophysical and geochemical information were used to provide an estimate of the geoneutrino signal originated from the NFC (Figure 30). The model subdivides the study area in two zones, the central tile (CT) and the rest of the region (RR), which are described with different degrees of resolution.

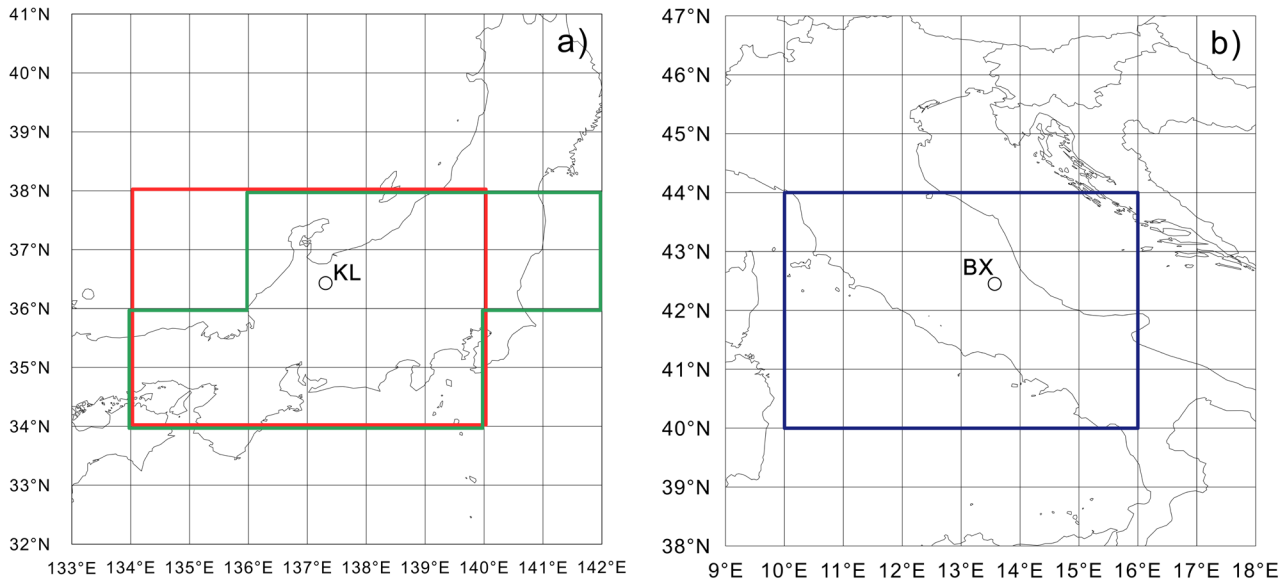

Figure 30. (a) Near Field Crust (NFC) identified by [84] (red box) and by [14] and [131] (green box) for KamLAND. (b) NFC identified for Borexino: all authors chose the same region (blue box).

The geoneutrino signals expected at KamLAND and Borexino calculated adopting the above mentioned global and refined models are reported in Table 23 for the NFC, the Far Field Crust (FFC) and the BC (BC = NFC + FFC) together with the adopted values for the purpose of mantle signal extraction from experimental results (Chapter 2.7). Since for Borexino the crustal portion of NFC, and as a consequence for the FFC, is the same for all the references reported (Figure 30b), the BC signal can be calculated integrating the refined estimate of NFC [160] with the FFC contribution given by any global model. Conversely, for KamLAND, due to the spatial differences of the NFC (Figure 30a) attention may be paid in the calculation of the BC signal: starting from the refined estimate [131] for the NFC, only the FFC signal reported in [14] can be adopted. With the aim to have a coherent mantle signal

extraction, the same model is used for the FFC contribution at Borexino together with the most updated estimates for the NFC given by [75].

As already highlighted for global models, for KamLAND the NFC contribution estimated by the refined model is higher respect to the Borexino case. Note that for the BC estimates reported in [134], the NFC and FFC signals with their corresponding uncertainties could not be inferred since only percentage contribution are reported.

For Borexino all the refined models provide NFC and FFC signals estimates with central values that are approximately the same; for the NFC the uncertainties are different because in [160] the maximal and minimal excursions of various input values and uncertainties are taken as the ± 3σ error range. The discrepancy recorded in FFC signals uncertainties, for [160] and [131] has to be ascribed to the different geochemical and geophysical datasets considered.

Table 23. The geoneutrino signals expected at Borexino and KamLAND according to global and refined models for the Near Field Crust (NFC), the Far Field Crust (FFC) and the corresponding adopted value for the mantle signal calculation (see Chapter 2.7).

Experiment	Type of model	Reference	S_{NFC} (U+Th) [TNU]	S_{FFC} (U+Th) [TNU]
KamLAND	Global	Huang et al., 2013 [14]	$13.4^{+2.3}_{-2.1}$	$7.3^{+1.5}_{-1.2}$
		Wipperfurth et al., 2020 [84] – CRUST 2.0	$15.8^{+3.9}_{-3.1}$	$7.8^{+2.1}_{-1.7}$
		Wipperfurth et al., 2020 [84] – CRUST 1.0	$16.7^{+4.5}_{-3.5}$	$7.8^{+2.2}_{-1.7}$
		Wipperfurth et al., 2020 [84] – LITHO 1.0	$18.2^{+4.7}_{-3.7}$	$8.8^{+2.5}_{-1.9}$
	Refined	Enomoto et al., 2007 [134]	26.0 ± 2.4	
		Fiorentini et al., 2012 [131]	17.7 ± 1.4	8.8 ± 1.4
		Adopted	17.7 ± 1.4	$7.3^{+1.5}_{-1.2}$
Borexino	Global	Huang et al., 2013 [14]	$15.3^{+2.8}_{-2.3}$	$13.7^{+2.8}_{-2.3}$
		Wipperfurth et al., 2020 [84] – CRUST 2.0	$17.4^{+4.3}_{-3.5}$	$14.1^{+3.8}_{-3.0}$
		Wipperfurth et al., 2020 [84] – CRUST 1.0	$17.5^{+4.3}_{-3.5}$	$13.6^{+3.8}_{-2.9}$
		Wipperfurth et al., 2020 [84] – LITHO 1.0	$18.2^{+3.9}_{-3.2}$	$14.8^{+4.0}_{-3.2}$
	Refined	Coltorti et al., 2011 [160]	9.67 ± 3.82	15.65 ± 1.50
		Fiorentini et al., 2012 [131]	9.67 ± 1.26	15.67 ± 2.43
		Agostini et al., 2020 [75]	9.2 ± 1.2	$13.7^{+2.8}_{-2.3}$
		Adopted	9.2 ± 1.2	$13.7^{+2.8}_{-2.3}$

2.7 Extracting the mantle signal

The KamLAND (KL) and Borexino (BX) experiments observed at >5σ level signals of U and Th geoneutrinos coming from the whole Earth (Chapter 2.5). In absence of an experimental way (e.g. directionality) to disentangle the contribution from the lithosphere and the

mantle, the employment of geological models is required to estimate the mantle geoneutrino component.

The mantle signals $S_M^{BX}(U+Th)$ and $S_M^{KL}(U+Th)$ can be inferred by subtracting the estimated lithospheric components from the experimental total signals, $S_{Exp}^{BX}(U+Th)$ for BX and $S_{Exp}^{KL}(U+Th)$ for KL (Chapter 2.4):

$$\begin{aligned} S_M^{BX}(U+Th) &= S_{Exp}^{BX}(U+Th) - S_{NFC}^{BX}(U+Th) - S_{FFC}^{BX}(U+Th) - S_{CLM}^{BX}(U+Th) \\ S_M^{KL}(U+Th) &= S_{Exp}^{KL}(U+Th) - S_{NFC}^{KL}(U+Th) - S_{FFC}^{KL}(U+Th) - S_{CLM}^{KL}(U+Th) \end{aligned} \quad (18)$$

where the lithospheric signals are modelled in three independent components: (i) the NFC ($S_{NFC}^{BX}(U+Th)$ and $S_{NFC}^{KL}(U+Th)$), (ii) the FFC ($S_{FFC}^{BX}(U+Th)$ and $S_{FFC}^{KL}(U+Th)$) (Chapter 2.6.4) and (iii) the CLM ($S_{CLM}^{BX}(U+Th)$ and $S_{CLM}^{KL}(U+Th)$) (Chapter 2.6.3).

It has to be noted that even if the different components are considered uncorrelated for KL and BX separately, the FFC and the CLM signals of KL and BX are fully correlated ($S_{FFC}^{KL}(U+Th) \propto S_{FFC}^{BX}(U+Th)$ and $S_{CLM}^{KL}(U+Th) \propto S_{CLM}^{BX}(U+Th)$) since they are derived from the same geophysical and geochemical model.

Using only the experimental signals published by BX and KL collaborations without any spectral information, the PDFs of $S_{Exp}^{BX}(U+Th) = 47.0^{+8.6}_{-8.1}$ TNU and $S_{Exp}^{KL}(U+Th) = 32.1 \pm 5.0$ TNU are reconstructed for inferring the following mantle signals at KL and BX: $S_M^{KL}(U+Th) = 4.8^{+5.6}_{-5.9}$ TNU and $S_M^{BX}(U+Th) = 20.8^{+9.4}_{-9.2}$ TNU (Table 24).

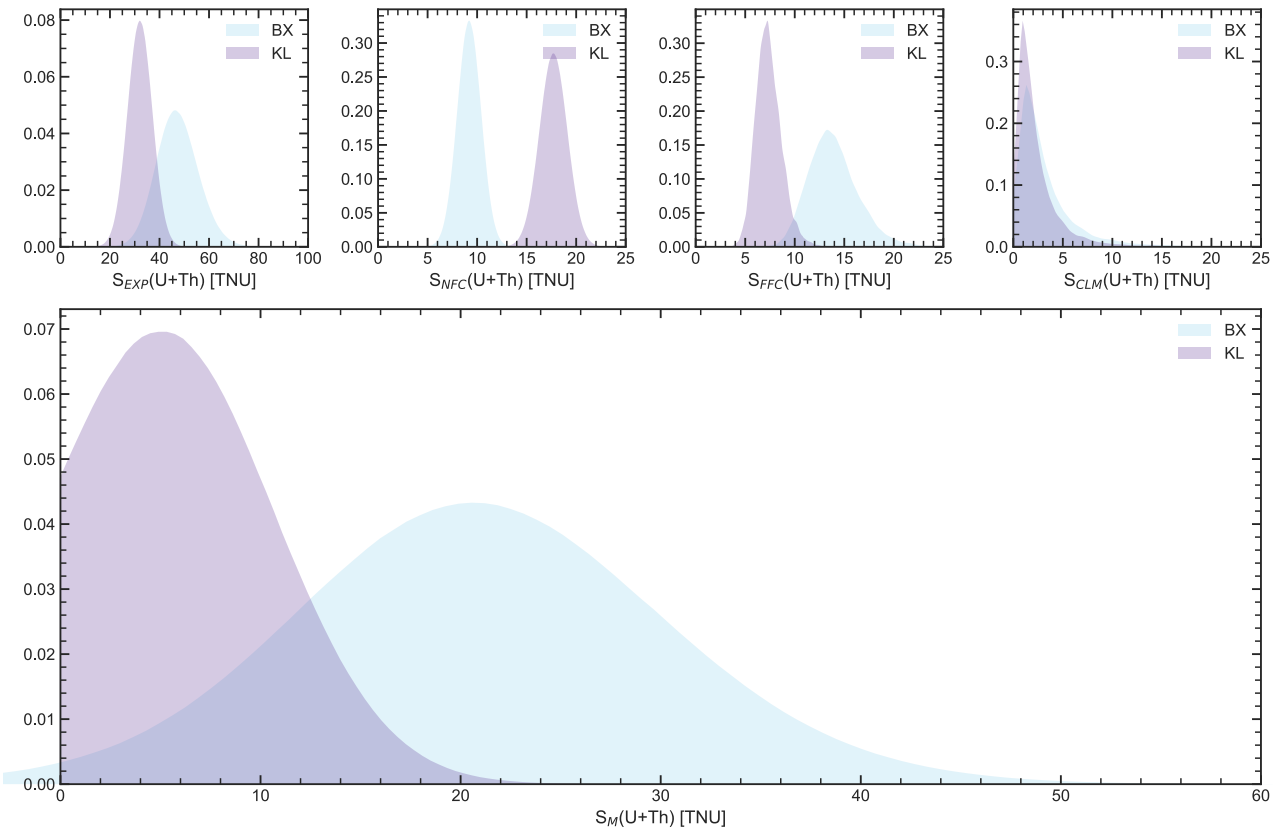

Figure 31. Probability density functions adopted for the estimation of KamLAND and Borexino geoneutrino mantle signals S_M(U+Th). The adopted signals for experimental (S_{EXP}), Near Field Crust (S_{NFC}), Far Field Crust (S_{FFC}) and Continental Lithospheric Mantle (S_{CLM}) components are reported in Table 24.

Note that the KL mantle signal $6.0^{+5.6}_{-5.7}$ TNU preliminarily published in [141] includes also the CLM contribution, since it is obtained by subtracting the BC contribution according to [134]. Moreover, it is worth to highlight that the BX mantle signal of $21.2^{+9.6}_{-9.0}$ TNU provided in [75] derives from a comprehensive fitting procedure accounting for the spectral information, but proves compatible with the estimate of present work.

Since both KL and BX adopt the same assumption of chondritic ratio $M_{BSE}(Th)/M_{BSE}(U) = 3.9$ [119, 161] in the extraction of the geoneutrino signal (Chapter 2.4), the above results can be properly combined in the estimation of a joint bivariate PDF ($S_M^{KL+BX}(U+Th)$) under the assumption of site-independent mantle signal. In principle, because of the different depth of the Lithosphere-Asthenosphere boundary under the two experimental sites, a slight difference exists in the mantle signal detected by KL and BX. However, this difference is expected to account for less than 2% [14] and it can be here neglected in view of present experimental uncertainties.

The joint distribution $S_M^{KL+BX}(U+Th)$ can be inferred from the PDFs $S_M^{BX}(U+Th)$ and $S_M^{KL}(U+Th)$ by requiring that the estimated signals $S_M^{BX}(U+Th) = S_M^{KL}(U+Th)$ are two observations of the same underlying quantity (Figure 32). Under these hypotheses, the combination of KL and BX constrains the mantle geoneutrino signal to $S_M^{KL+BX}(U+Th) = 8.9^{+5.1}_{-5.5}$ TNU. This result can be inserted in a trend of combined mantle geoneutrino signals published in the last 10 years (Figure 33) providing a valuable indication for testing the mantle signals expected from BSE compositional models (Chapter 2.3).

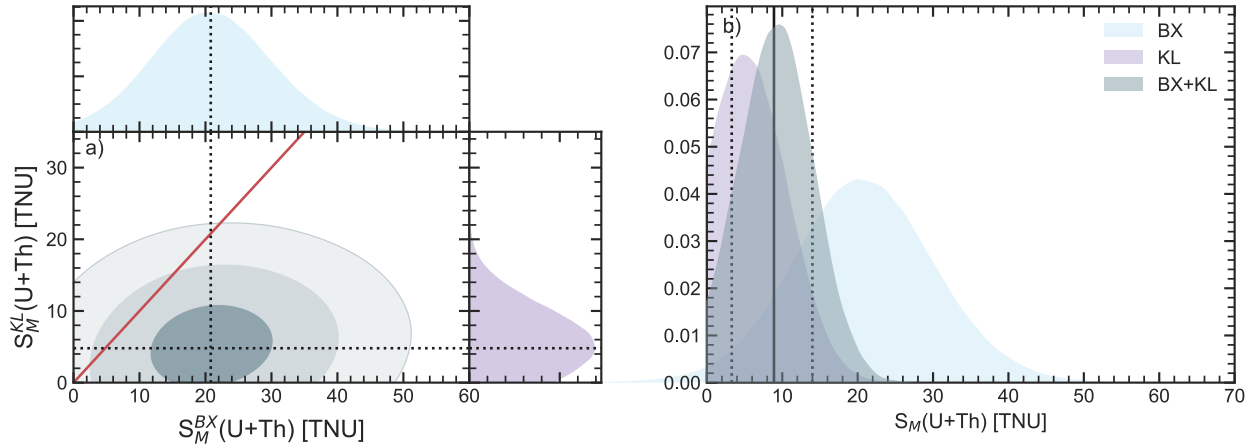

Figure 32. (a) Probability density functions of the extracted mantle signals (in TNU) for KL ($S_M^{KL}(U+Th)$, in violet) and BX ($S_M^{BX}(U+Th)$, in blue) together with the joint bivariate distribution ($S_M^{KL+BX}(U+Th)$, in grey). The dashed vertical and horizontal black lines represent the median values obtained for BX and KL respectively. The grey contours mark the areas corresponding to the 2D coverage of 39.3%, 86.5% and 98.9%. The red line represents the constraint $S_M^{BX}(U+Th) = S_M^{KL}(U+Th)$. (b) Probability density functions of the extracted mantle signals (in TNU) for KL (in violet) and BX (in blue) together with the joint distribution $S_M^{KL+BX}(U+Th)$ (in grey) resulting from their combination. The black vertical line represents the median value of the distribution, while the vertical dashed lines report the 1σ interval.

Table 24. Experimental signals (S_{Exp}) and adopted values for the modelled signals of the NFC (S_{NFC}), FFC (S_{FFC}) and CLM (S_{CLM}) for Borexino (BX) and KamLAND (KL), together with their derived mantle signals (S_M). The last row reports the mantle signal resulting from the combination of KL and BX observations.

	S_{Exp}(U+Th) [TNU]	S_{NFC}(U+Th) [TNU]	S_{FFC}(U+Th) [TNU]	S_{CLM}(U+Th) [TNU]	S_M(U+Th) [TNU]
KL	32.1 ± 5.0	17.7 ± 1.4	$7.3^{+1.5}_{-1.2}$	$1.6^{+2.2}_{-1.0}$	$4.8^{+5.6}_{-5.9}$
BX	$47.0^{+8.6}_{-8.1}$	9.2 ± 1.2	$13.7^{+2.8}_{-2.3}$	$2.2^{+3.1}_{-1.3}$	$20.8^{+9.4}_{-9.2}$
KL+BX	-	-	-	-	$8.9^{+5.1}_{-5.5}$

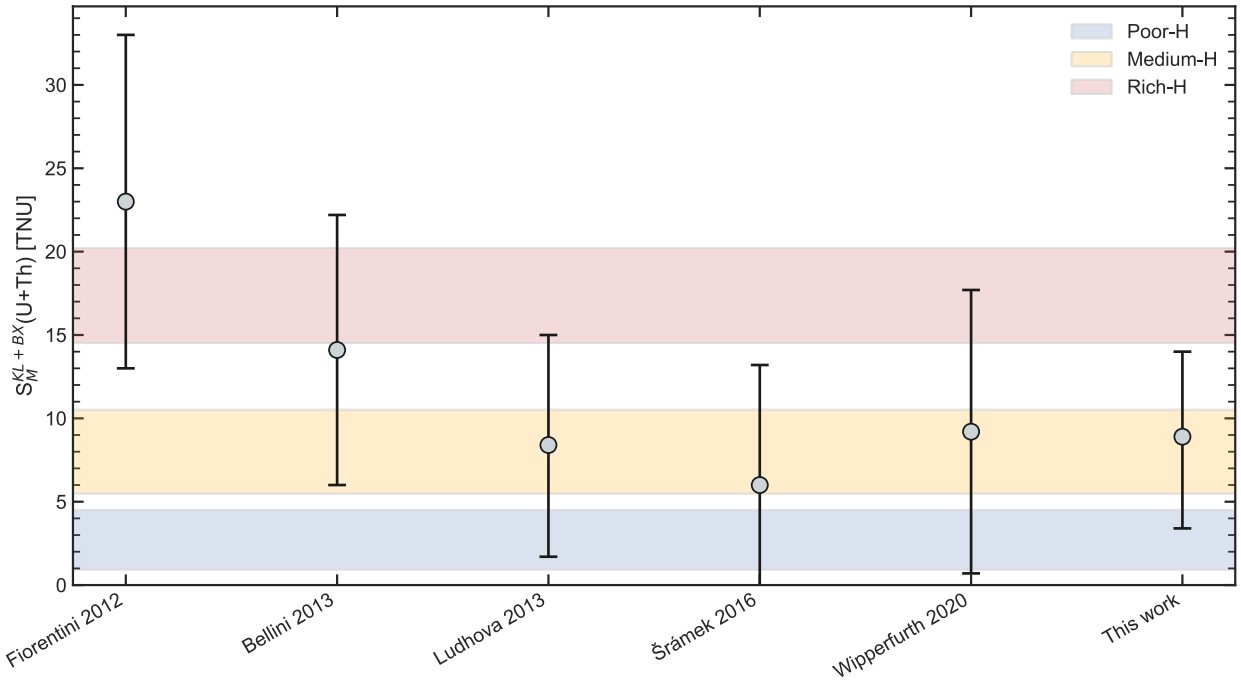

Figure 33. Collection of the published mantle signals ($S_M^{KL+BX}(U+Th)$) obtained from the combination of Borexino and KamLAND experimental results, together with the predictions (horizontal bands) of Poor-H, Medium-H and Rich-H models presented in Table 7. The reported model-dependent signals for the mantle are taken from [126, 131, 135, 142, 162] and this study. The horizontal blue, red and yellow bands correspond to the 68% coverage interval for the mantle signal predicted by Poor-H, Medium-H and Rich-H models (Table 25), calculated by substituting predicted mantle heat ($H_M(U+Th)$) in Eq. (22).

In the perspective of multi-site mantle investigation, a joint effort among the experimental collaborations in building a common analysis framework could improve the impact in geoscience. The formalization of a global χ^2 (or likelihood) function incorporating correlations, embedding U and Th experimental event rates, neutrino oscillation parameters and experimental statistical/systematic uncertainties would greatly boost the robustness of the extracted geoneutrino mantle signal, as detailed in [131, 163].

2.8 What can we learn from geoneutrinos?

2.8.1 Mantle radiogenic power and composition

The mantle geoneutrino signal potentially brings to the surface valuable information about the unexplored Earth and particularly on the mantle radioactivity and the Earth's energetics. Since the adopted radiogenic heat power of the LS (H_{LS} (U+Th)= $6.9^{+1.6}_{-1.2}$ TW, Table 17) is independent from the BSE model, the discrimination capability of the combined geoneutrino measurement among the different BSE models can be studied in the space

$S_M(U+Th)$ vs $H_M(U+Th)$. The mantle signal ($S_M(U+Th)$) can be expressed as a linear function of the mantle radiogenic heat ($H_M(U+Th)$):

$$S_M(U+Th) = \beta \cdot H_M(U+Th) \tag{19}$$

where the β coefficient depends only on U and Th distribution in the mantle and ranges between β_{low} = 0.75 TNU/TW and β_{high} = 0.98 TNU/TW. The lower and upper values are obtained assuming that the HPEs' masses are placed in a layer just above the CMB (low scenario) (Figure 34a) and assuming that they are homogeneously distributed in the mantle (high scenario) (Figure 34b) [75].

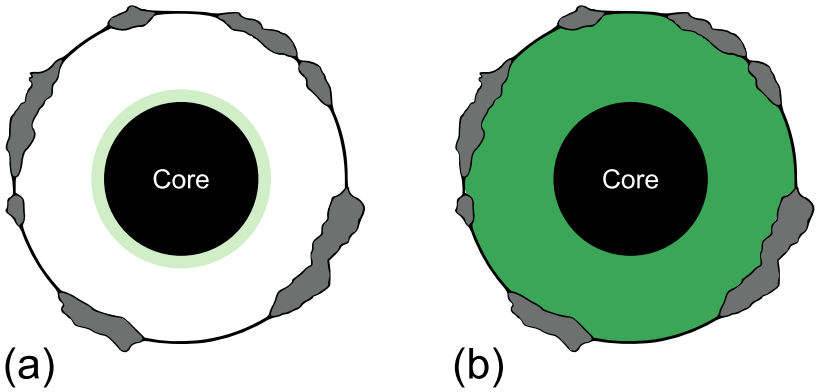

Figure 34. Cartoons of the distribution of HPEs' masses in the mantle predicted according to two different scenarios. (a) Low scenario: the HPEs are placed in a thin layer (in light green) above the CMB (b) High scenario: the HPEs are distributed homogenously (in dark green) in the mantle (modified after [75]).

The radiogenic power of the mantle $H_M(U+Th)$ can be further expressed as function of the U mass in the mantle $M_M(U)$:

$$H_M(U+Th) = h'(U) \cdot M_M(U) + h'(Th) \cdot M_M(Th) = [h'(U) + 3.7\, h'(Th)] \cdot M_M(U) \tag{20}$$

where the Th/U mass ratio $\frac{M_M(Th)}{M_M(U)} = 3.7$ is constrained by the $\frac{M_{LS}(Th)}{M_{LS}(U)} = 4.3$ in the LS according to the H13 model (Table 17) and the $\frac{M_{BSE}(Th)}{M_{BSE}(U)} = 3.9$ adopted in the extraction of the geoneutrino signal at KL and BX (Chapter 2.4). Considering the equations above, it follows:

$$S_M(U+Th) = \beta \cdot [h'(U) + 3.7\, h'(Th)] \cdot M_M(U) \tag{21}$$

The linear relation between $S_M(U+Th)$ and $H_M(U+Th)$ is plotted in Figure 35. Assuming that the U and Th abundances in the mantle are radial, non-decreasing function of the depth and in a fixed ratio, the area between the two extreme lines (green lines) depicts the region allowed by all possible distributions of the U and Th in this reservoir. The maximal and minimal excursions of mantle geoneutrino signal is taken as a proxy for the 3σ error range. The solid black horizontal line in Figure 35 traces the combined signal $S_M^{KL+BX}(U+Th) = 8.9^{+5.1}_{-5.5}$ TNU, which falls within the prediction of the Medium-H models. The 68% coverage interval falls outside the prediction of the Rich-H models and results compatible with Poor-H models.

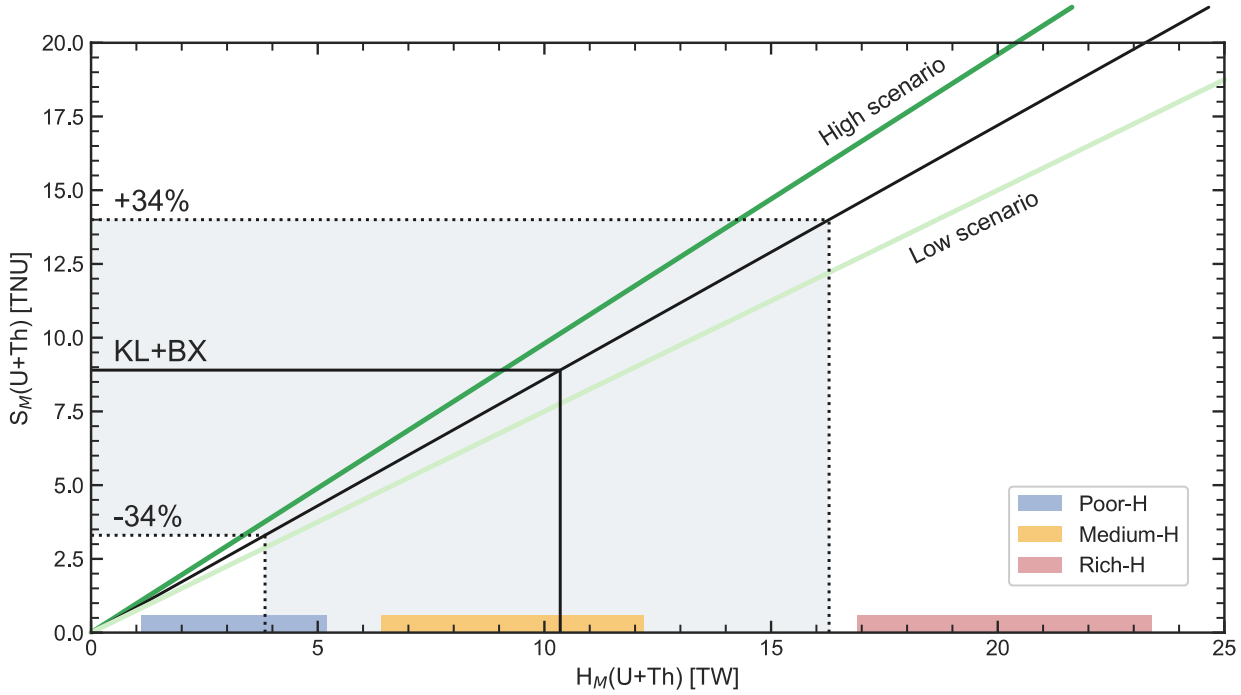

Figure 35. Mantle geoneutrino signal ($S_M(U+Th)$) as a function of U and Th mantle radiogenic heat $H_M(U+Th)$: the area between the green lines denotes the full range allowed between a homogenous mantle (high scenario, Figure 34b) and unique rich layer just above the CMB (low scenario, Figure 34a). The slope of the central inclined black line (β_{centr} = 0.86 TNU/TW) is the average of β_{low} and β_{high}. The blue, red and yellow bands on the X-axis correspond to the 68% coverage interval of the mantle radiogenic heat ($H_M(U+Th)$) of Poor-H, Medium-H and Rich-H models (Table 25), respectively. The black solid horizontal line represents the median mantle signal obtained by the combination of experimental signals from KL and BX $S_M^{KL+BX}(U+Th)$ (Table 24). The dashed horizontal black lines represent the 68% coverage interval.

The combined mantle signal ($S_M^{KL+BX}(U+Th)$) can be converted to the corresponding radiogenic heat by inverting the Eq. (19). Since the experimental error on the mantle signal is much larger than the systematic variability associated to the U and Th distribution in the mantle, the radiogenic power from U and Th in the mantle $H_M^{KL+BX}(U+Th)$ inferred from the combined mantle signal $S_M^{KL+BX}(U+Th)$ can be obtained with:

$$H_M^{KL+BX}(U+Th) = (1/\beta_{centr}) \cdot S_M^{KL+BX}(U+Th) = 1.16 \cdot S_M^{KL+BX}(U+Th) \quad (22)$$

Starting from $S_M^{KL+BX}(U+Th) = 8.9^{+5.1}_{-5.5}\ TNU$ it can be derived $H_M^{KL+BX}(U+Th) = 10.3^{+5.9}_{-6.4}\ TW$. The implications of this estimate in terms of total radiogenic heat (H), HPEs abundances (a_M(U), a_M(Th) and a_M(K)) and masses (M_M(U), M_M(Th) and M_M(K)) in the mantle can be studied with the comparison with the estimates provided by the Poor-H, Medium-H and Rich-H models (Table 25). The combined mantle geoneutrino measurement constrains at 68% C.L. the mantle composition to a_M(U) > 5 ng/g, a_M(Th) > 19 ng/g and a_M(K) > 60 μg/g and the mantle radiogenic heat power to $H_M(U+Th) > 4.0\ TW$ and $H_M(U+Th+K) > 4.8\ TW$.

Table 25. HPEs' abundances and masses, radiogenic heat in the mantle according to the classes of BSE models and obtained based on the combined geoneutrino measurement. The HPEs abundances are derived from the HPEs masses adopting the mass of the sublithospheric mantle $M_M = 3.911 \times 10^{24}\ kg$ from the H13 model (Table 1). The masses and the radiogenic heat for the Poor-H, Medium-H and Rich-H models are obtained subtracting from the corresponding value of the BSE (Table 7) the adopted estimates of the LS according to the H13 model (Table 17) and considering them linearly independent. For the combined measurement the HPEs masses constrained by the combined measurement are obtained adopting M_M(Th)/ M_M(U) = 3.7 and M_M(K)/ M_M(U) = 1.2 × 10^4; the H_M(U+Th) and H_M(U+Th+K) are obtained using the Eq. (5) and assuming that the K contribution to the total radiogenic heat is 17%.

Model	a_M(U) [ng/g]	a_M (Th) [ng/g]	a_M (K) [μg/g]	M_M(U) [10^{16} kg]	M_M (Th) [10^{16} kg]	M_M (K) [10^{19} kg]	H_M (U+Th) [TW]	H_M (U+Th+K) [TW]
Poor-H	5 ± 3	12^{+10}_{-12}	76^{+34}_{-36}	$1.9^{+1.1}_{-1.2}$	$4.6^{+3.8}_{-4.6}$	$29.6^{+13.4}_{-14.2}$	$3.2^{+2.0}_{-2.1}$	$4.2^{+2.4}_{-2.6}$
Medium-H	13 ± 4	42^{+14}_{-17}	155^{+47}_{-48}	$4.9^{+1.5}_{-1.6}$	$16.5^{+5.6}_{-6.5}$	$60.7^{+18.4}_{-18.8}$	9.3 ± 2.9	$11.4^{+3.5}_{-3.6}$
Rich -H	26^{+4}_{-5}	98^{+16}_{-18}	244^{+38}_{-40}	$10.0^{+1.7}_{-1.8}$	$38.4^{+6.4}_{-7.0}$	$95.4^{+15.0}_{-15.7}$	$20.2^{+3.2}_{-3.3}$	$23.4^{+3.8}_{-3.9}$
Combined KL+BX	13 ± 8	50^{+29}_{-31}	157^{+90}_{-97}	$5.3^{+3.0}_{-3.3}$	$19.5^{+11.2}_{-12.1}$	$61.5^{+35.3}_{-38.0}$	$10.3^{+5.9}_{-6.4}$	$12.5^{+7.1}_{-7.7}$

2.8.2 Studying Earth's energetics with geoneutrinos

The mantle radiogenic heat constrained by the combined geoneutrino measurement of KL and BX allows for making the first step towards the understanding of the Earth's present heat budget, the evolution through geological time of our planet and the ratio of heat production over heat loss (Chapter 2.2).

In Table 26 are reported the results in terms of contributions to the Earth's heat budget obtained on the basis of the combined mantle geoneutrino signal and compared to the adopted value presented in Figure 12. Summing to $H_M^{KL+BX}(U+Th+K)$ the radiogenic power of the lithosphere H_{LS}(U + Th + K) = $8.1^{+1.9}_{-1.4}$ TW, the inferred Earth's radiogenic

power is $H^{KL+BX}(U+Th+K) = 20.8^{+7.3}_{-7.9}\ TW$ which falls in the 68% coverage range of the Medium-H models and it is compatible at 1σ level with the Poor-H models (Figure 36a).

Table 26. Comparison between the contributions to the Earth's heat budget based on the constraints set by the combined geoneutrino measurement of KL and BX and the adopted values described in Chapter 2.4 (see Figure 12). The value of the total heat power (Q), radiogenic heat of LS (H_{LS}(U+Th+K)) and secular cooling of the core (C_C) are the same for both the cases. The Earth's radiogenic heat (H(U+Th+K)) is obtained summing the independent components of H_{LS}(U+Th+K) and H_M(U+Th+K). The secular cooling of the Earth (C) and of the mantle (C_M) are obtained according to the equations reported in Figure 12 considering the terms as linearly independent.

	Adopted	**Combined KL + BX**
Q [TW]	47 ± 2	-
H_{LS} (U+Th+K) [TW]	$8.1^{+1.9}_{-1.4}$	-
H_M (U+Th+K) [[TW]	$11.3^{+3.3}_{-3.4}$	$12.5^{+7.1}_{-7.7}$
H (U+Th+K) [TW]	19.3 ± 2.9	$20.8^{+7.3}_{-7.9}$
C_M [TW]	16 ± 4	15 ± 8
C_C [TW]	11 ± 2	-
C [TW]	27 ± 4	26 ± 8

The total radiogenic heat $H^{KL+BX}(U+Th+K)$ can be used also to extract the convective Urey ratio U_R (Chapter 2.2) according to Eq. (2), taking into account the adopted Q and radiogenic heat of the continental crust (H_{CC} (U + Th + K) $= 6.8^{+1.4}_{-1.1}$ TW, Table 4). The 68% C.L. of the resulting value $U_R^{KL+BX} = 0.35^{+0.19}_{-0.20}$, if compared to the U_R predicted by the three classes of BSE models (Figure 36b), shows an agreement with the corresponding range of the Medium-H models and a slight compatibility with both Poor-H and High-H models.

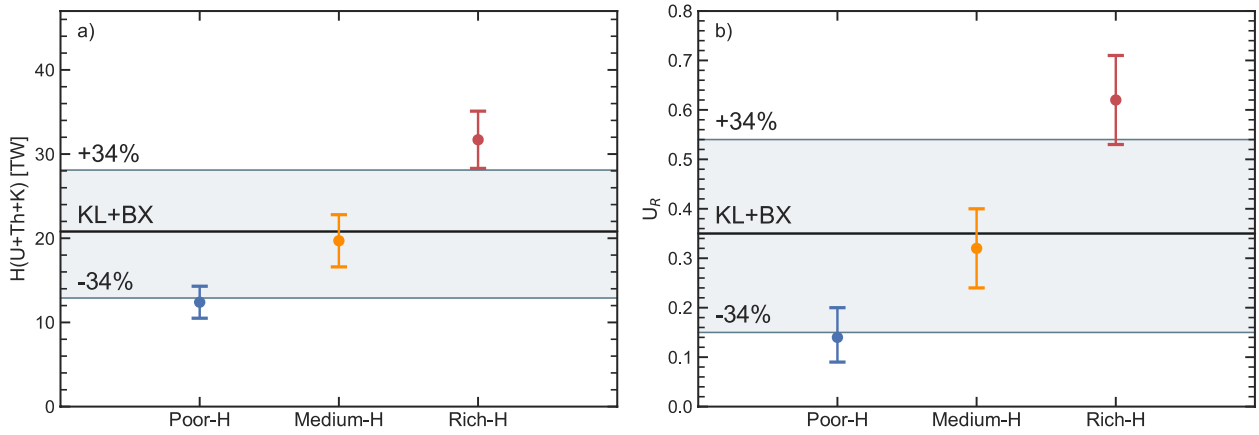

Figure 36. (a) Comparison of the Earth's radiogenic heat (H(U+Th+K) constrained by the combined geoneutrino measurement of KL and BX with the estimates of the Poor-H, Medium-H and Rich-H models (Table 7). The lithospheric component is the same for all BSE models and for the combined measurement and it corresponds to the adopted value of the H13 model $H_{LS}(\mathrm{U+Th+K}) = 8.1^{+1.9}_{-1.4}$ TW (Table 17). **(b)** Comparison of the convective Urey ratio (U_R) constrained by the combined geoneutrino measurement of KL and BX with the estimates (68% coverage interval) of the Poor-H, Medium-H and Rich-H models. The U_R is calculated according to Eq. (2), assuming that the total heat power Q = 47 ± 2 TW (Table 2) and the radiogenic heat of the continental crust H_{CC} (U+Th+K) = $6.8^{+1.4}_{-1.1}$ TW (Table 4). The grey band represents the 68% coverage interval of $U_R^{KL+BX} = 0.35^{+0.19}_{-0.20}$.

Subtracting the total radiogenic heat $H^{KL+BX}(U+Th+K)$ from the adopted total heat power $Q = 47 \pm 2\ TW$ (Table 2), it follows that Earth's secular cooling is $C = 26 \pm 8\ TW$. Moreover, taking into account the adopted value of secular cooling of the core $C_C = 11 \pm 2\ TW$, the secular cooling of the mantle is $C_M = 15 \pm 8\ TW$. These results led to estimate the percentage contributions of the radiogenic heat and of the secular cooling to the Earth's heat budget (Figure 37). More than half (C~56%) of the total heat power is given by the heat loss of the mantle (C_M~32%) and from the core (C_C~24%). The remaining heat is attributable to the total radiogenic heat (H) which is due mainly to the contribution of the mantle (H_M~27%).

The results of the combined geoneutrino measurement of KL and BX in terms of Earth's energetics agree with the estimates of the Medium-H models.

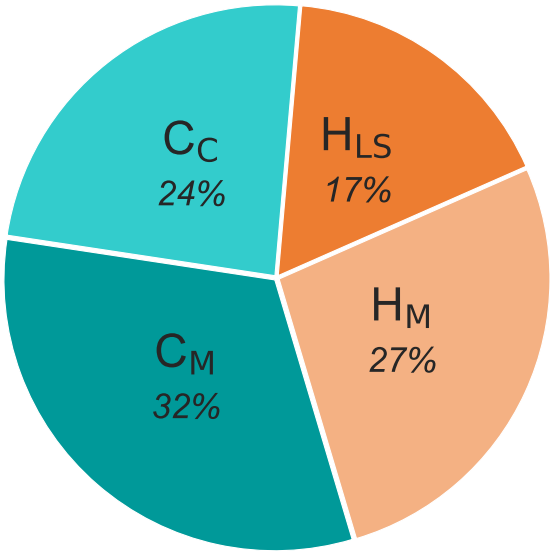

Figure 37. Percentage contributions, constrained by the combined measurement of KL and BX, to the total heat power Q = 47 ± 2 TW of the secular cooling from the mantle (C_M) and from the core (C_C) and of the radiogenic heat from the lithosphere (H_{LS}) and from the mantle (H_M).

2.9 ^{40}K: the missing piece

In the process of interpreting geoneutrino results for the comprehension of the mantle, a model-dependent ratio between the volatile K and the refractory U was assumed to estimate the portion of radiogenic heat not accessible to U and Th geoneutrinos. A further step in the comprehension of our planet will require the direct observation of ^{40}K geoneutrinos.

While abundances of refractory elements are well constrained by chondritic observations, the silicate Earth seems strongly depleted in those elements which condensed from the early gas disc at temperatures less than ~1300° K. Normalized abundances of terrestrial lithophile elements uniformly decrease with their condensation temperatures, and the slope of this behavior is what determines the so-called volatility pattern. Potassium, the only volatile element across the HPEs, is no exception: our planet seems to show from ~1/3 [164] to ~1/8 [55] potassium when compared to chondrites, making its expected bulk mass span of a factor ~2 across different Earth models. Two theories on the fate of the mysterious "missing K" include loss to space during accretion [164] or segregation into the accreting core [165], but no experimental evidence has been able to confirm or rule out any of the hypotheses, yet.

While a direct measurement of ^{40}K-$\bar{\nu}_e$ flux at surface would constrain potassium bulk mass per se, more stringent considerations can be drawn from its decay to ^{40}Ar, a more accurate benchmark for volatiles. Whilst argon in the Sun and presumably in the primordial

atmosphere and Earth's Mantle [53] is mostly ^{36}Ar and ^{38}Ar, the argon found today in atmosphere is 99.6% ^{40}Ar [166]. It follows that most of the terrestrial argon derives from ^{40}K decays, which suggests a strong correlation between terrestrially-produced argon and Earth's potassium's content ($M(^{40}Ar) = 1.14 \cdot M_{BSE}(^{40}K)$). Since near all ^{40}Ar must be degassed from the original rock (like all other volatile elements) and volatiles' ratios (e.g. H/^{40}Ar) are constant for a wide variety of rocks, from the amount of ^{40}Ar in different layers of the silicate Earth, it is possible to derive the behavior of other volatiles (i.e. H, N, C and noble gases) during planetary formation and evolution, water included. In fact, if the amount of water in exosphere is well constrained by experimental and observational studies, the actual storage capacity of the mantle (including all aqueous fluids, as well as water that is bound within minerals or dissolved in magma) is estimated to range from about a quarter the mass of H_2O in the world's oceans ($1.37 \times 10^{21} kg$) to ~4 ocean masses [167, 168]. Reducing the uncertainties in the knowledge of the global deep H_2O cycle is a necessary step to answer questions about the presence of the actual amount of water that makes Earth a unique planet for life evolution [169].

While accepting that a large fraction of potassium could have been lost to space during Earth's formation, the hypothesis of potassium segregation in Earth's core cannot be ignored. The presence of a radioactive source in Earth's core is required to satisfy at the same time the constraints on Earth's energetics and its geophysical structure [170]. An Inner Core with a well-defined radius of 1220 km [12] and a magnetic field that ranges from 25 to 65 μT at surface [171] and which has been running continuously for at least 3 Gyr [172] require the assumption of an additional source of energy in the core [170] which, if entirely satisfied by potassium decays, necessitates an abundance of $a_{Core}(K) = 400\ ppm$. Recent experimental measurements at high pressure (1.5 GPa) and temperatures (>1400 °C) proved that up to 10 ppb of uranium and thorium could have been solved in a sulfur rich core, producing 2.4 TW of heat, sufficient to power the geo-dynamo, even without a contribution from potassium. On the other hand, other experiments seem to suggest that, under extreme conditions of temperature and pressure, also potassium can exhibit a siderophile behavior [25, 27, 173, 174], thus permitting the inclusion of K into a metallic core up to $a_{Core}(K) = 250\ ppm$ [173]. This would translate into an increase of the ^{40}K-$\bar{\nu}_e$ flux of ~10% at a "continental site" like Laboratori Nazionali del Gran Sasso and ~30% at an "oceanic detector" located at Hawaii.

Solving the intriguing riddle of the "missing K" with a direct measurement is crucial since potassium decays may have been the dominant heat source for the primordial Earth, due to the shorter half-life of ^{40}K relative to ^{238}U and ^{232}Th.

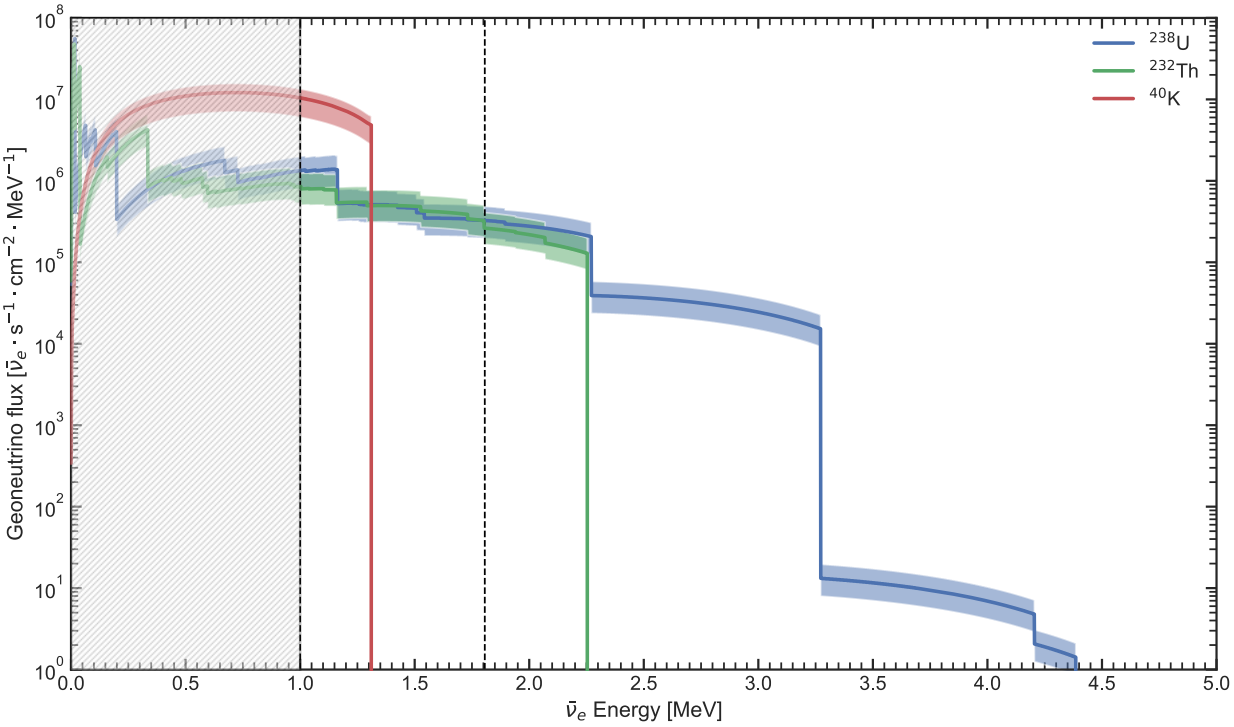

Figure 38. Geoneutrino energy spectra. A plot of the ^{238}U (blue), ^{232}Th (green) and ^{40}K (red) geoneutrino fluxes estimated at Laboratori Nazionali del Gran Sasso as a function of the antineutrino energy. The shaded bands show the variability range due to the isotopes' masses and distributions in the Earth according to the models and the scenarios reported in Figure 14 and Figure 34. The black vertical dashed line at 1.806 MeV represents the energy threshold of the Inverse Beta Decay reaction on free protons, i.e., the reaction used by current liquid scintillator geoneutrino experiments. All contributions below the threshold are not practically measurable with today's technology. The ^{238}U spectrum above 3.272 MeV has traditionally not been shown because of its very low intensity. The black vertical dashed region below 1.022 MeV represents the lowest threshold reachable with charged-current antineutrino capture on stable nuclear targets.

The ^{40}K geoneutrino spectrum cannot be detected via the IBD on protons (Figure 38). In order to explore this low energy region of the geoneutrino spectrum, considered today as being practically impossible, a set of new reactions with an energy threshold lower than 1.311 MeV needs to be discussed, together with a possible experimental detection technique. The scientific and technological development foreseen for detecting these low energy antineutrinos, together with their relevance in Earth sciences, makes the ^{40}K geoneutrino measurement the "holy grail" for neutrino geoscientists.

2.9.1 Possible detection channels

Detecting geoneutrinos, ^{40}K antineutrinos in particular, can be really challenging. These leptons do not ionize matter and they cannot be directly detected. They interact only by weak interaction (and gravity), which has a tiny cross section. The way in which a geoneutrino can interact with matter and hence be detected are of two types:

- Neutral Current (NC) interactions: they are mediated by the exchange of a Z^0 boson and provide a mechanism for neutrino elastic scattering in matter. These interactions are so weak because of the high mass of the Z^0 boson, which is M_{Z^0}~91.2 GeV. Indeed, these interactions are disfavored compared to electromagnetic interactions due to the larger temporary energy non conservation involved in the emission of the virtual boson, which implies a much smaller interaction probability [175].
- Charged Current (CC) interactions: they are mediated by the exchange of a W^+ or a W^- boson. They describe inelastic interactions for neutrinos thanks to which e^-, μ and τ can be converted into the corresponding neutrinos and vice versa (provided the interaction energy is at least equal to the particle rest mass energy). The same happens for their antiparticles. These interactions are nearly as weak as the NC ones because of the masses of the W bosons which are M_W~80.4 GeV [175].

2.9.2 Neutral Current interactions

The three main NC interaction processes for incoming electron antineutrinos on ordinary matter are: (i) elastic scattering on electrons, (ii) coherent elastic scattering on nucleus and (iii) nuclear excitation.

The reaction of elastic scattering (ES) on electrons is characterized by the presence of an antineutrino and of an electron both in the initial and in the final state:

$$\bar{\nu}_X + e^- \rightarrow \bar{\nu}_X + e^-$$

In this interaction part of the initial antineutrino momentum is transferred to the electron. The differential cross section can be expressed as a function of the final recoil kinetic energy of the electron T as [176, 177]:

$$\frac{d\sigma}{dT} = \frac{G_F^2 m_e}{2\pi}\left[(g_V + x + g_A)^2 + (g_V + x - g_A)^2\left(1 - \frac{T}{E_\nu}\right)^2 + (g_A^2 - (g_V + x)^2)\frac{m_e T}{E_\nu^2}\right] + \frac{\pi\alpha^2\mu_\nu^2}{m_e^2}\left(\frac{1}{T} - \frac{1}{E_\nu}\right)$$

with $g_V = 2\sin^2\theta_W + \frac{1}{2}$ for $\bar{\nu}_e$ and $g_V = 2\sin^2\theta_W - \frac{1}{2}$ for $\bar{\nu}_\mu/\bar{\nu}_\tau$, $g_A = -\frac{1}{2}$ for $\bar{\nu}_e$ and $g_A = +\frac{1}{2}$ for $\bar{\nu}_\mu/\bar{\nu}_\tau$ and $x = \frac{\sqrt{2}\pi\alpha\langle r^2\rangle}{3G_F}$, where α is the strong coupling constant, $G_F$is the Fermi coupling constant, θ_W is the weak mixing angle, $\langle r^2\rangle$ is the neutrino charge radius and μ_ν is the neutrino magnetic moment. For ν_X the cross section has the same formulation, but $g_A(\nu) = -g_A(\bar{\nu})$, enhancing the probability of interaction.

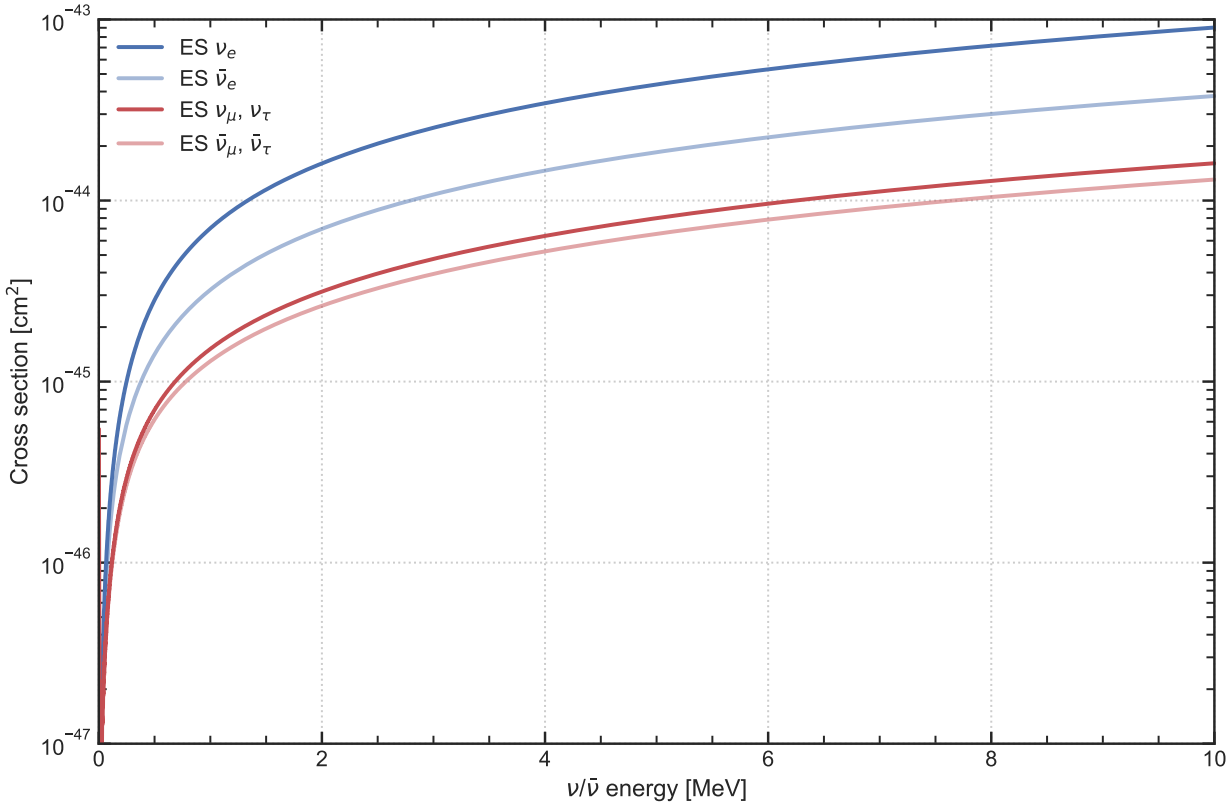

Figure 39. Integrated cross section for Elastic Scattering (ES) on electrons as a function of the incoming neutrino/antineutrino energy. Blue lines display the cross section for electron neutrinos (dark blue) and antineutrinos (light blue), while red lines report the cross section for muonic and tauonic neutrinos (dark red) and antineutrinos (light red).

The integrated cross section (Figure 39) thus depends on the minimum kinetic energy T_{min} detectable for the recoil electron, which can vary between 0 and a $T_{max} = \frac{E_\nu}{1+m_e/2E_\nu}$. This interaction has the potential to detect ^{40}K geoneutrinos, since the actual energy threshold

is set by the detector calorimetric capabilities rather than by the interaction kinematics (Figure 40). The expected signal obtainable for ^{40}K- $\bar{\nu}_e$ is at least 2 orders of magnitude higher than what obtainable with any CC interaction (1.9 TNU for ES when integrating electron recoils energies above 800 keV [177], compared to 0.1 TNU obtained with CC interactions Table 29).

The problem in detecting geoneutrinos using ES is that also ν_X can undergo the same process and the flux from solar neutrinos ($\Phi_\nu \sim 7 \cdot 10^{10} cm^{-2} s^{-1}$ at surface [178]) would overcome the geoneutrinos' one ($\Phi_{\bar{\nu}} \sim 2 \cdot 10^{7} cm^{-2} s^{-1}$ at surface [14]) by more than 3 orders of magnitude. Recent proposals for ^{40}K geoneutrino detection [177, 179] suggest to rely on directionality to disentangle solar neutrinos from geoneutrinos. The idea is to use the recoil electron track direction using gaseous detectors (under R&D) or to reconstruct the electron's direction from the Cherenkov light produced amongst more copious scintillation light in a liquid scintillator detector. However, even if the solar neutrino background could be reduced by directionality, other recoil electron backgrounds (e.g. natural β^- decays) would be isotropic and abundant. Techniques relying on electron detection therefore imply an extraordinary level of radiopurity of the detector, far better than today's state-of-the-art levels achieved by Borexino [180].

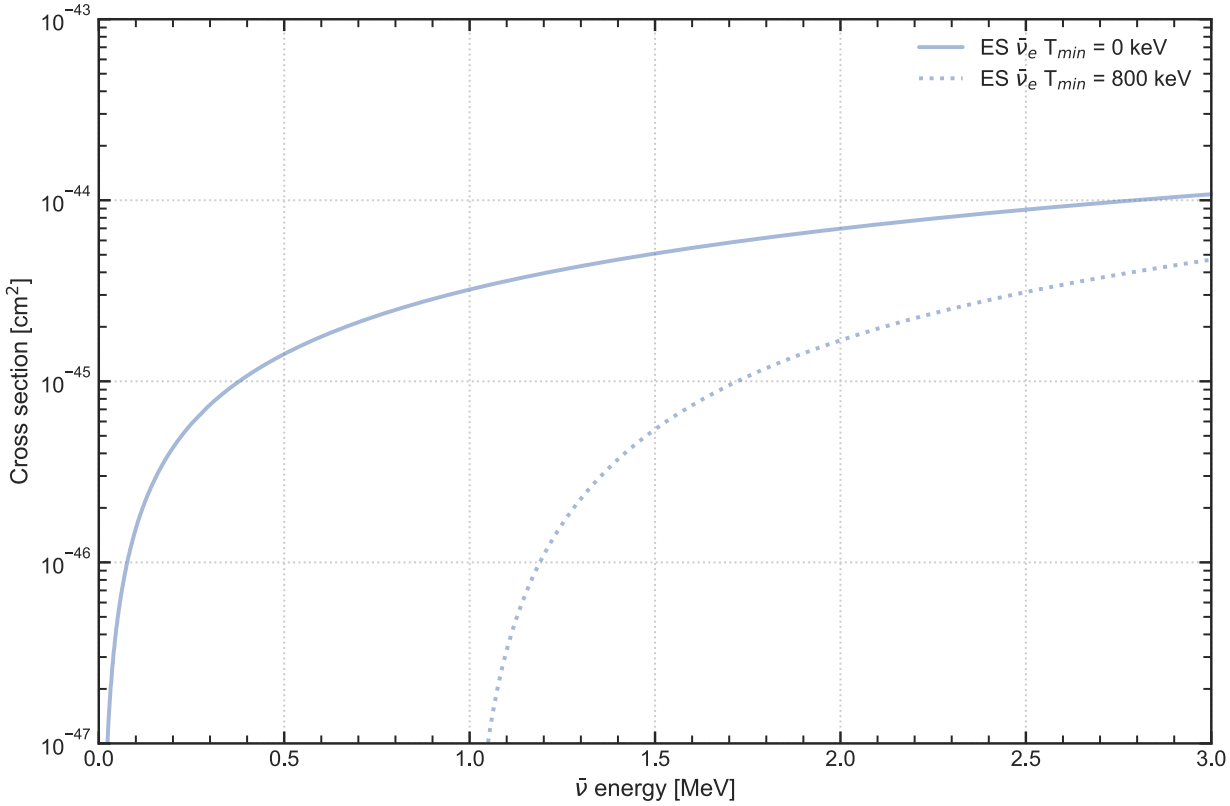

Figure 40. Integrated cross section for Elastic Scattering (ES) on electrons as a function of the incoming antineutrino energy. While the solid line reports the theoretical cross section obtained by integrating on all possible electron recoil energies, the dashed line displays the cross section obtained by integrating the recoil energy T over a minimum threshold of 800 keV.

A second process for antineutrino detection is represented by the coherent elastic scattering on nuclei (CEνNS):

$$\bar{\nu}_X + {}^{A}_{Z}N \rightarrow \bar{\nu}_X + {}^{A}_{Z}N$$

which would be the most probable process for low-energy neutrinos and antineutrinos [181]. Similarly to ES, the differential cross section can be expressed as a function of the final recoil kinetic energy of the nucleus T as [182]:

$$\frac{d\sigma}{dT} = \frac{G_F^2}{4\pi} Q_W^2 \, M \, F(Q^2)^2 \cdot \left(1 - \frac{M \cdot T}{2E_\nu^2}\right)$$

where M is the nucleus mass, $Q_W = N - Z(1 - 4\sin^2\theta_W)$ is the weak current term for a nucleus having N neutrons and Z protons and $F(Q^2)$ is the nuclear form factor as a function of the transferred momentum. As for ES, the integrated cross section (Figure 41) depends on the minimum kinetic energy detectable for the recoil nucleus, which can vary between 0

and a $T_{max} = \frac{E_\nu}{1+M/2E_\nu}$. Because of the large mass of nuclei compared to typical geoneutrino energies, the detection of ^{40}K geoneutrinos would pose a huge technological challenge to overcome: mature detection technique for detecting nuclear recoils at <1 keV is still missing. Moreover, as for the ES, this interaction process would be also affected by the high solar neutrino background and directionality information would be nearly impossible to recover for heavy nuclei.

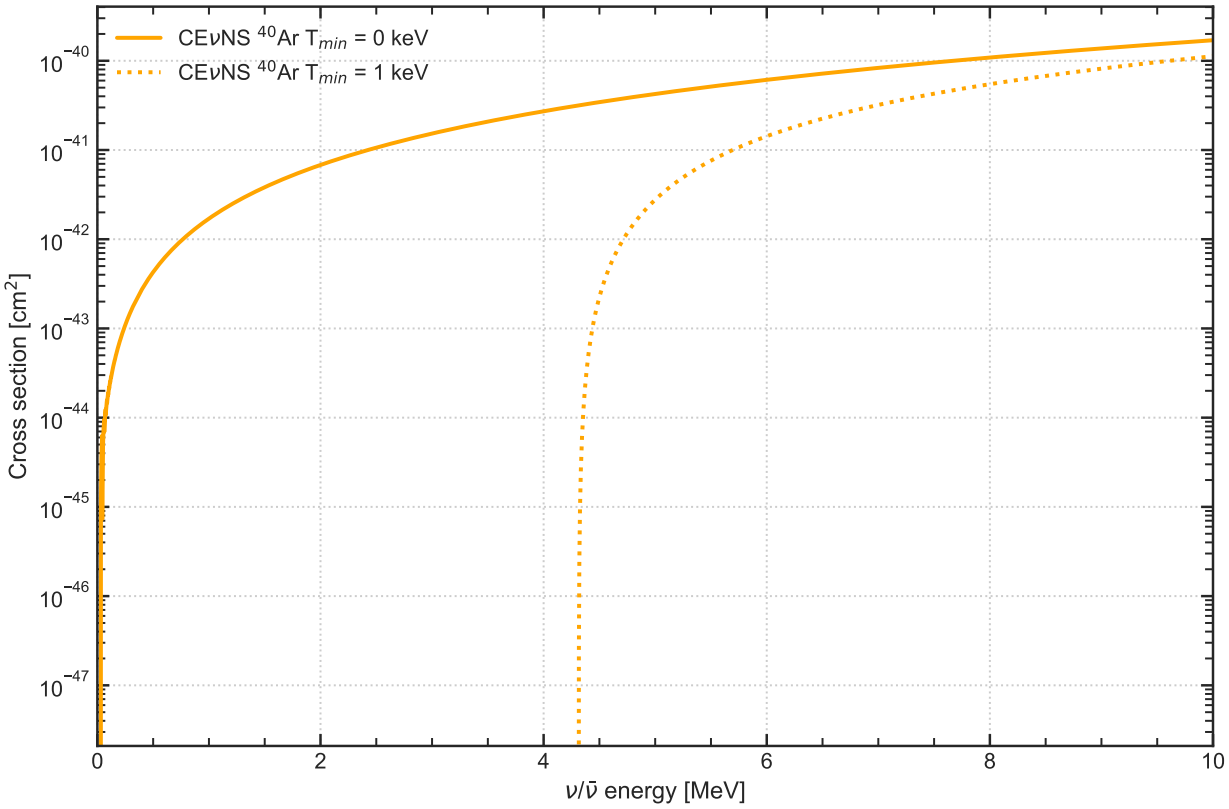

Figure 41. Integrated cross section for coherent elastic scattering (CEνNS) on a ^{40}Ar nucleus as a function of the incoming neutrino/antineutrino energy. While the solid line reports the theoretical cross section obtained by integrating on all possible nuclear recoil energies, the dashed line displays the cross section obtained by integrating the recoil energy T over a minimum threshold of 1 keV.

The last option for NC interactions would be the nuclear excitation (NUEX). In this process, initially proposed by [183] to solve the solar-ν deficit problem, the energy transferred by the antineutrino leaves the nucleus in an excited state, which will subsequently emit a photon to reach its ground state:

$$\bar{\nu}_X + {}^{A}_{Z}X \rightarrow \bar{\nu}_X + {}^{A}_{Z}X^* \rightarrow \bar{\nu}_X + {}^{A}_{Z}X + \gamma$$

As for all other NC interactions, the major drawback is the insurmountable background represented by solar neutrinos and natural radioactivity in the detector, since directional information would be hardly recovered.

2.9.3 Charged Current interactions

A more suitable option for geoneutrino detection seems to be represented by CC interactions. These interactions have the big advantage to distinguish neutrinos from antineutrinos, avoiding the problem of the solar neutrino background.

There are two main processes for CC interaction. The first one is represented by the resonant orbital electron capture on nuclei:

$$\bar{\nu}_e + (e^- + {}^{A}_{Z+1}Y) \rightarrow {}^{A}_{Z}X^* \rightarrow {}^{A}_{Z}X + \gamma$$

In this process, at the arrival of an electron antineutrino, one of the *s*-orbital electrons can be captured by the nucleus. The result is an atom in an excited state. The hole in the *s*-shell gets covered by an outer electron by emission of a photon. Since antineutrino induced electron capture is a two-body process with an unstable intermediate state, its cross section has a resonant character, and it occurs with high probability only for antineutrinos in a small range around the resonant energy, which is $E_{res} = m(X) - m(Y) + B.E.(e^-)$. The antineutrino energy must be slightly higher than the E_{res} to be absorbed, since a small fraction of the neutrino energy is used for the kinetic energy of the final state. This interaction process has relatively large cross section only for an almost monochromatic source of antineutrinos of the right energy (depending on the target nucleus) and therefore will not give access to the entire geoneutrino spectrum.

The only way left to detect antineutrinos with a CC interaction is the Inverse Beta Decay (IBD). In this process an antineutrino gets absorbed by a nucleus, which transforms one of its protons into a neutron with the simultaneous emission of a positron:

$$\bar{\nu}_e + {}^{A}_{Z+1}Y \rightarrow {}^{A}_{Z}X + e^+$$

This is the detection method currently adopted by liquid scintillator experiments, by using protons in hydrogen atoms as targets. However, protons are not the only targets capable of undergoing IBD as we will see in the next chapter. Historically, IBD has been the detection channel via which, in 1956, the existence of antineutrinos was first confirmed by the famous and glorious Cowan–Reines experiment.

The IBD reaction has an energy threshold, which means that a minimum antineutrino energy is required for the process to occur (Figure 42). The threshold can be calculated by imposing the conservation of the four-momentum and is given by:

$$E_{th} = \frac{\left(m(^{A}_{Z}X) + 2m(e^{-})\right)^{2} - m(^{A}_{Z+1}Y)^{2}}{2\, m(^{A}_{Z+1}Y)} \cong Q_{\beta^-} + 2m(e^{-})$$

where $Q_{\beta^-} = m(^{A}_{Z}X) - m(^{A}_{Z+1}Y)$ represents the energy difference between the two nuclear states, that is the total energy released in a spontaneous β^- decay from $^{A}_{Z}X$ to $^{A}_{Z+1}Y$.

The existence of this energy threshold excludes a large number of target nuclei for which the detection of geoneutrinos will be possible. This is a major issue for the experimental observation of ^{40}K geoneutrinos as the ^{40}K geoneutrino spectrum is the one having the lowest geoneutrino end point energy (1.311 MeV), to be compared with the relatively much higher end points of the ^{232}Th (2.25 MeV) and ^{238}U (3.36 MeV) geoneutrino spectral components. The minimum energy threshold reachable through IBD ($Q_{\beta^-} = 0$) on stable nuclei is 1.022 MeV, leaving an energy window narrower than 300 keV to detect these geoneutrinos.

Note that in the CC interaction scenario as for IBD reactions, nuclear reactors represent an extremely intense electron antineutrino source overshadowing the geoneutrino signal. As the energy spectrum of reactor antineutrinos overlaps with that of geoneutrinos and since nuclear cores are the strongest man-made antineutrino sources ($L_{\bar{\nu}_e} \sim 10^{20}\ \bar{\nu}/s$), a deep knowledge of the reactor background is required for the estimation of the geoneutrino signal.

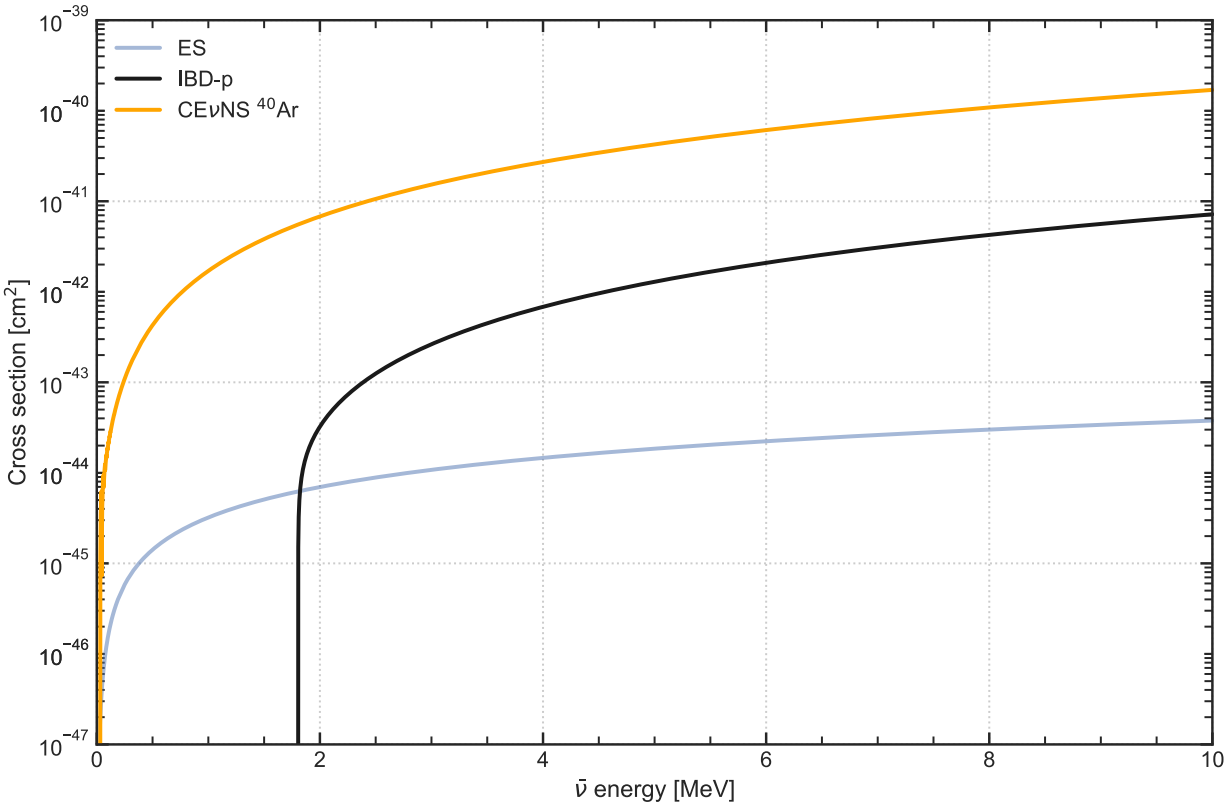

Figure 42. Comparison between the cross section per target obtained for Elastic Scattering (ES) on electrons, Inverse Beta Decay (IBD) on free protons and coherent elastic scattering (CEνNS) on a ^{40}Ar nucleus.

2.9.4 Inverse Beta Decay cross section

Despite all the technical difficulties, in July 2005 IBD on protons (IBD-p) allowed for the first evidence of a signal truly originating from geoneutrinos, claimed by the KamLAND Collaboration [7], then confirmed in 2010 by an independent measurement by the Borexino experiment [8]. In the following years, the detection of IBD-p events in liquid scintillation detectors was demonstrated to be really effective in short baseline reactor antineutrino experiments (Double Chooz in France, RENO in South Korea, Daya Bay in China).

The problem with IBD-p is that, unfortunately, the energy threshold for the reaction is $E_{th} = 1.806\ MeV$, that is not low enough to detect ^{40}K geoneutrinos, which have a maximum energy of $E_{max} = 1.311 MeV$. A possible solution to overcome this problem and lowering the energy threshold would be the utilization of a target nucleus different from free protons. The problem posed by the use of nuclei instead of protons is that the former prevents the creation of a free neutron in the final state. In the absence of a delayed signal from neutron capture, it would be nearly impossible to distinguish a positron created by an IBD reaction

from a signal caused by any of the other predominant sources of background (e.g. cosmic rays, high energy gammas). Anyway, in the presence of a way to effectively tag and detect single positrons inside the detector (encouraging progresses provided in [184]), the detection of IBD events induced by ^{40}K geoneutrinos could be seriously taken under consideration. For this reason, a study on possible isotopes has become necessary.

In order to evaluate which isotope would better fit for a ^{40}K geoneutrino detector, the parameters that rule the IBD interaction have to be fully understood. Following [185], we can start from the simplest process we can describe, which is IBD on a free proton $\bar{\nu}_e + p \rightarrow n + e^+$. The cross section for this process can be easily estimated by considering Fermi's Golden Rule.

Consider a state $|i>$, eigenstate of a free Hamiltonian H_0, which describes the initial state of the proton-antineutrino system. Then consider a small perturbation V so that the Hamiltonian becomes $H = H_0 + V$ and a state $|f>$ describing the final state of the positron-neutron system. The interaction probability per unit of time from $|i>$ to $|f>$ λ in natural units ($\hbar = 1$ and $c = 1$) is given to first order in the perturbation by Fermi's Golden Rule:

$$\lambda = 2\pi \left|V_{fi}\right|^2 \rho(E_f)$$

where $\rho(E_f) = \frac{dn}{dE_f}$ is the density of final states (number of continuum states per unit of energy) and $\left|V_{fi}\right|^2$ is the squared matrix element of the interaction potential.

The evaluation of $V_{fi} = \int \psi *_f V \psi_i \, d^3x$, with ψ_i and ψ_f corresponding respectively to the wave functions of the initial and final states, requires some special attention. The potential V can in principle be replaced by one (or more) of the five operators O_X (where X means it can be a scalar S, a pseudoscalar P, a vector V, an axial vector A or a tensor T). Only experimental symmetries and spatial distributions can reveal which one to choose. The current experimental evidence suggests O_X to be a V-A operator. For now, we treat the general case $V = k\, O_X$, where the value of the constant k determines the strength of the weak interaction.

By explicitly inserting the expression for the potential V, V_{fi} then becomes:

$$V_{fi} = k \int \psi *_n \; \phi *_e \; O_X \, \psi_p \, \phi_\nu \, \mathrm{d}^3\mathrm{x}$$

where ψ_p and ψ_n are the initial and the final nuclear states' functions (proton and neutron respectively, in our case). ϕ_ν and ϕ_e are the antineutrino and the positron wave functions and can be represented as plain waves:

$$\phi_\nu = N \cdot e^{i\bar{q}\cdot\bar{r}} \quad and \quad \phi_e = N \cdot e^{i\bar{p}\cdot\bar{r}}$$

where $N = \frac{1}{\sqrt{Vol}}$ is a normalization factor and $\vec{p}$ and $\vec{q}$ represent the antineutrino and the positron momentum, respectively. It is worth noting that p and q are strongly linked with $p = \sqrt{E^2 - m_e^2}$ and $E = q - (Q_{\beta^-} + m_e)$. In the geoneutrino framework, p and q can never reach a value higher than $p_{max} = 3.273\, MeV$, that is the endpoint of the geoneutrino spectrum. On the other hand, nuclear radii can assume (in extreme cases) maximum values of $r{\sim}15fm \sim 7.5 \times 10^{-2} MeV^{-1}$ (for uranium). In this scenario ϕ_ν and ϕ_e can be safely assumed to be constant over the nuclear volume. Indeed, considering that $\bar{p} \cdot \bar{r}$ can reach at maximum a value of $0.04 \ll 1$ under our previous assumptions, the relation $e^{i\bar{p}\cdot\bar{r}} = 1 + i\,\bar{p} \cdot \bar{r} + \ldots \approx 1$, holds. Therefore, we can simplify V_{fi} to:

$$V_{fi} = k\, N^2 \int \psi *_n \; O_X \, \psi_p \, \mathrm{d}^3\mathrm{x} = \; k\, N^2 M_{fi}$$

where $M_{fi} = \int \psi *_n \; O_X \, \psi_p \, \mathrm{d}^3\mathrm{x}$ is the nuclear matrix element evaluated between the proton (initial) and neutron (final) states.

The next step will be evaluating $\rho(E_f)$, which is the number of accessible states for the decay products per unit of energy. Under the assumption of negligible neutron recoil, the number of final states comes only from the positron and is:

$$dn_e = C \cdot 4\pi p^2 dp$$

where p is the positron momentum, and $C = \frac{Vol}{(2\pi)^3}$ a normalization factor.

Finally, we can write the transition probability per unit time as:

$$\lambda = 2\pi\, k^2 \left|M_{fi}\right|^2 \frac{4\pi p^2}{(2\pi)^3} \frac{dp}{dE_f}$$

and define the cross section for the interaction as:

$$\sigma = \frac{\text{transition probability per unit time and target nucleus}}{\text{incident flux of } \bar{\nu}_e}$$

Considering that in the massless approximation for $\bar{\nu}_e$ the incident flux is $j = \frac{1}{Vol}$ and $\frac{dp}{dE_f} = \frac{E}{p}$, we can then write the cross section as:

$$\sigma = \frac{k^2}{\pi} |M_{fi}|^2 p\, E$$

This result is a good approximation, but it is not accurate enough to describe the behavior of different isotopes as targets. As suggested by [186], several corrections have to be taken into account.

The first one is the Coulomb distortion of the wave functions. While the plain wave approximation is perfectly fine for the antineutrino wave function, it is not accurate for the outgoing positron, which can interact with the nuclear state also through electromagnetic interaction. For this reason, a corrective factor has to be introduced, given by the Fermi Function F:

$$F(Z,E,R) = \frac{|\phi_e(R)_{Coulomb}|^2}{|\phi_e(R)_{Free}|^2} = 2(1+\gamma)(2pR)^{2\gamma-2} e^{\pi\eta} \left| \frac{\Gamma(\gamma + i\eta)}{\Gamma(2\gamma+1)} \right|^2$$

with $\Gamma(z) = \int_0^\infty x^{z-1} e^{-x} dx = (z-1)!$, $\eta = -\frac{\alpha(Z-1)E}{p}$ and $\gamma = \sqrt{1-\alpha^2(Z-1)^2}$

where α is the fine structure constant, Z the target atomic number, R the final state nuclear radius and E the electron energy. The Fermi Function is identically 1 for Hydrogen (Z=1), then strongly lowers the cross section as Z increases.

The elements that are still left out from the calculation are the coupling constant k and the squared matrix element $|M_{fi}|^2$. Once experiments determined the potential O_X is V-A, the weak coupling constant k could be fixed to $G_F \cdot \cos\theta_C$ for semi-leptonic processes (see [186] for a detailed derivation), where θ_C is the Cabibbo angle ($\theta_C = 13.02°$ [175]) and G_F is the Fermi coupling constant ($G_F = 1.1663787 \times 10^{-5}\ GeV^{-2}$[175]).

The evaluation of $|M_{fi}|^2$ turns out to be the most difficult part of the calculation. However, at MeV scales, the matrix element $|M_{fi}|^2$ for an IBD reaction $\bar{\nu}_e + {}^A_Z X \rightarrow e^+ + {}^A_{Z-1} Y$ can be derived from the associated β decay ${}^A_{Z-1} Y \rightarrow {}^A_Z X + e^- + \bar{\nu}_e$ amplitude by correcting for the spin state of the system. Hence, $|M_{fi}|^2$ can be derived in the simplest case for nucleons (see [186] for a detailed derivation) as:

$$|M_{fi}|^2 = \frac{2\pi^3 \ ln\ 2}{ft\ \ {m_e}^5\ {G_F}^2\ \cos^2\theta_C} \frac{(2\,J_f\ +\ 1)}{(2\,J_i\ +\ 1)}$$

where *ft* is the comparative half-life of the associated β transition. Experiments on β decays can help to fix its value for different elements. This parameter usually ranges between $10^3 s$ to $10^{20} s$ [185] and for this reason it is more often presented as Log(ft). Considering the range of *ft* values and the inverse proportionality of *ft* with respect to the cross section, it is at first order the main parameter regulating the magnitude of the IBD reaction cross section, and therefore the expected event rate.

Finally by substituting the expression obtained for $|M_{fi}|^2$, the IBD cross section (in natural units) [182] can thus be calculated as:

$$\sigma(E) = \frac{2\pi^2 \ln 2}{ft\ m_e^5}\ p_e E_e F(Z,E,R) \frac{(2\,J_f\ +\ 1)}{(2\,J_i\ +\ 1)} \tag{23}$$

2.9.5 Inverse Beta Decay targets for ^{40}K

The Nuclear Data Section of the IAEA provides a user-friendly API[9] that can be used to query nuclear data and investigate isotope's properties. According to the Evaluated Nuclear Structure Data File (ENSDF) contained in the IAEA database [187], a total of 515 different β^- emitters exist for a total of 523 possible transitions to ground state. We are interested in these β^- decaying isotopes since their products are suitable targets for the inverse process, namely the IBD.

Among these 515 emitters, we are interested in those having a threshold at E_{th}<1.311 MeV, the energy endpoint of the ^{40}K geoneutrino spectrum. There are a total of 26 possible targets satisfying this condition, not all, however, stable (Table 27).

[9] Instructions available at https://www-nds.iaea.org/relnsd/vcharthtml/api_v0_guide.html

Table 27. List of the β^- emitters presenting an energy threshold (Q-value + $2m_e$) lower than the energy endpoint of ^{40}K geoneutrino spectrum. For each parent nucleus (P) it is reported the spin state J^π, its half-life, and the Log(*ft*) value ruling the transition amplitude of the decay to the daughter nucleus (D). For each daughter nucleus, the spin state is reported, together with the half-life when the atom is not stable. All data are taken from the ENSDF database of IAEA at present time (19 October 2021).

Parent (P)	PJ^π	$Pt_{1/2}$ [s]	Log(*ft*)	E_{th} [MeV]	Daughter (D)	DJ^π	$Dt_{1/2}$ [s]
^{3}H	1/2+	$3.89 \cdot 10^{8}$	3.0524	1.041	^{3}He	1/2+	Stable
^{14}C	0+	$1.80 \cdot 10^{11}$	9.04	1.178	^{14}N	1+	Stable
^{32}Si	0+	$4.95 \cdot 10^{9}$	8.21	1.249	^{32}P	1+	$1.23 \cdot 10^{6}$
^{33}P	1/2+	$2.19 \cdot 10^{6}$	5.022	1.270	^{33}S	3/2+	Stable
^{35}S	3/2+	$7.55 \cdot 10^{6}$	5.0088	1.189	^{35}Cl	3/2+	Stable
^{45}Ca	7/2-	$1.40 \cdot 10^{7}$	6	1.282	^{45}Sc	7/2-	Stable
^{63}Ni	1/2-	$3.19 \cdot 10^{9}$	6.7	1.089	^{63}Cu	3/2-	Stable
^{66}Ni	0+	$1.97 \cdot 10^{5}$	4.3	1.274	^{66}Cu	1+	$3.07 \cdot 10^{2}$
^{79}Se	7/2+	$1.03 \cdot 10^{13}$	10.77	1.173	^{79}Br	3/2-	Stable
^{87}Rb	3/2-	$1.57 \cdot 10^{18}$	17.514	1.304	^{87}Sr	9/2+	Stable
^{93}Zr	5/2+	$5.08 \cdot 10^{13}$	12.1	1.113	^{93}Nb	9/2+	Stable
^{106}Ru	0+	$3.21 \cdot 10^{7}$	4.31	1.061	^{106}Rh	1+	$3.01 \cdot 10^{1}$
^{107}Pd	5/2+	$2.05 \cdot 10^{14}$	9.9	1.056	^{107}Ag	1/2-	Stable
^{106}Ag	1+	$1.44 \cdot 10^{3}$	4.1	1.212	^{106}Cd	0+	Stable
^{135}Cs	7/2+	$7.26 \cdot 10^{13}$	13.48	1.291	^{135}Ba	3/2+	Stable
^{147}Pm	7/2+	$8.28 \cdot 10^{7}$	7.4	1.246	^{147}Sm	7/2-	$3.35 \cdot 10^{18}$
^{151}Sm	5/2-	$2.84 \cdot 10^{9}$	7.51	1.099	^{151}Eu	5/2+	$5.36 \cdot 10^{25}$
^{155}Eu	5/2+	$1.50 \cdot 10^{8}$	8.62	1.274	^{155}Gd	3/2-	Stable
^{171}Tm	1/2+	$6.06 \cdot 10^{7}$	6.318	1.118	^{171}Yb	1/2-	Stable
^{187}Re	5/2+	$1.37 \cdot 10^{18}$	11.195	1.024	^{187}Os	1/2-	Stable
^{194}Os	0+	$1.89 \cdot 10^{8}$	7.6	1.119	^{194}Ir	1-	$6.94 \cdot 10^{4}$
^{210}Pb	0+	$7.01 \cdot 10^{8}$	7.9	1.085	^{210}Bi	1-	$4.33 \cdot 10^{5}$
^{227}Ac	3/2-	$6.87 \cdot 10^{8}$	7.1	1.067	^{227}Th	1/2+	$1.62 \cdot 10^{6}$
^{241}Pu	5/2+	$4.52 \cdot 10^{8}$	5.788	1.043	^{241}Am	5/2-	$1.37 \cdot 10^{10}$
^{249}Bk	7/2+	$2.85 \cdot 10^{7}$	7.03	1.146	^{249}Cf	9/2-	$1.11 \cdot 10^{10}$
^{255}Es	7/2+	$3.44 \cdot 10^{6}$	7.3	1.311	^{255}Fm	7/2+	$7.23 \cdot 10^{4}$

A realistic geoneutrino experiment will require a large number of target nuclei and a high level of radiopurity. This consideration is sufficient of itself alone to discard all the unstable candidates. I thus discuss only targets which are stable or can considered stable on the time scale of a geoneutrino experiment (as the ones having half-lives comparable or higher than Earth's age, ^{151}Eu and ^{147}Sm), ending up with a total of 17 targets leading to 20 possible IBD transitions.

Table 28. List of the target isotopes considered for the IBD detection of ^{40}K geoneutrinos. For each target isotopes, the nuclear inputs necessary for the evaluation of the cross section are here reported together with the isotope produced (product) by the antineutrino capture. The considered nuclear inputs are the atomic number Z, the spin states J of the atoms, the nuclear radius R, the natural isotopic abundance (I.A.), the energy threshold of the IBD reaction together with the Log(*ft*) value ruling the amplitude of the cross section.^{1}H is here reported for comparison.

Target	Z_i	J_i	R_i [10^{-15}m]	I.A.	Product	J_f	E_{th} [MeV]	Log(ft)
^{1}H	1	1/2+	0.878	99.9885%	^{1}n	1/2+	1.806	3.017
^{3}He	2	1/2+	1.97	0.000134%	^{3}H	1/2+	1.041	3.0524
^{14}N	7	1+	2.56	99.636%	^{14}C	0+	1.178	9.04
^{33}S	16	3/2+	3.27	0.75%	^{33}P	1/2+	1.271	5.022
^{35}Cl	17	3/2+	3.37	75.76%	^{35}S	3/2+	1.189	5.0088
^{45}Sc	21	7/2-	3.55	100%	^{45}Ca	7/2-	1.282	6
^{63}Cu	29	3/2-	3.88	69.15%	^{63}Ni	1/2-	1.089	6.7
					^{63}Ni*	5/2-	1.176	5
^{79}Br	35	3/2-	4.16	50.69%	^{79}Se	7/2+	1.173	10.77
					^{79}Se*	1/2+-	1.268	5
^{87}Sr	38	9/2+	4.22	7.00%	^{87}Rb	3/2-	1.304	17.514
^{93}Nb	41	9/2+	4.32	100%	^{93}Zr	5/2+	1.113	12.1
^{107}Ag	47	1/2-	4.55	51.839%	^{107}Pd	5/2+	1.056	9.9
^{106}Cd	48	0+	4.54	1.25%	^{106}Ag	1+	1.212	4.1
^{135}Ba	56	3/2+	4.83	6.592%	^{135}Cs	7/2+	1.291	13.48
^{147}Sm	62	7/2-	4.99	14.99%	^{147}Pm	7/2+	1.246	7.4
^{151}Eu	63	5/2+	5.05	47.81%	^{151}Sm	5/2-	1.099	7.51
					^{151}Sm	5/2+	1.266	5
^{155}Gd	64	3/2-	5.13	14.80%	^{155}Eu	5/2+	1.274	8.62
^{171}Yb	70	1/2-	5.29	14.09%	^{171}Tm	1/2+	1.119	6.318
^{187}Os	76	1/2-	5.39	1.96%	^{187}Re	5/2+	1.024	11.195

Among the identified isotopes, there are three candidates exhibiting low E_{th} values and also possible allowed transitions to an excited state: ^{63}Cu, ^{79}Br and ^{151}Eu. As we will see in the next chapter, such targets are of particular interest because of their potential background rejection capabilities. For these transitions, the $\bar{\nu}_e$ reaction energy threshold must include the energy of the excited state and still be below the ^{40}K geoneutrino spectrum endpoint. This is the case for all three of these isotopes and their possible (allowed) excited states. However, only an approximate value of Log(*ft*) = 5 [188] is assumed for the excited states, with an admissible range of 4-6 (with some even larger values occurring) [186]. Indeed, while for ^{79}Br → ^{79}Se* the Log(*ft*) value can be analytically estimated (using the ^{79}Se* → ^{79}Br branching ratio, its half-life, and the Fermi function of the state), for ^{63}Cu → ^{63}Ni* and ^{151}Eu → ^{151}Sm* the lack of knowledge of the branching ratio and/or the half-life of the final state prohibits a Log(*ft*) calculation. As the cross section is inversely proportional to *ft*, a 2-unit change in Log(*ft*) will result in a 2 orders of magnitude variation in the cross section. Even a small (10%) increase (decrease) in Log(*ft*) will provide a cross section that is reduced (enhanced) by a factor 3 with respect to the central value estimate. This large uncertainty calls for refined nuclear physics input coming from theory and/or experiments.

When considering the suitability of a given isotope as a ^{40}K-$\bar{\nu}_e$ target in a large liquid scintillator detector, there are three main factors (aside from their cost) to take into account: (i) the *ft* value ruling the amplitude of the cross section, (ii) the energy threshold which must be as low as possible to observe larger portions of the spectrum, (iii) the natural isotopic abundance of the target. Considering that a realistic geoneutrino detector requires a large target mass and that the cost of isotopic enrichment is prohibitive at this scale, natural isotopic abundance needs to enter the candidate selection. Consequently, it is reasonable to consider an abundance-weighted cross sections when evaluating promising targets for IBD (Figure 43).

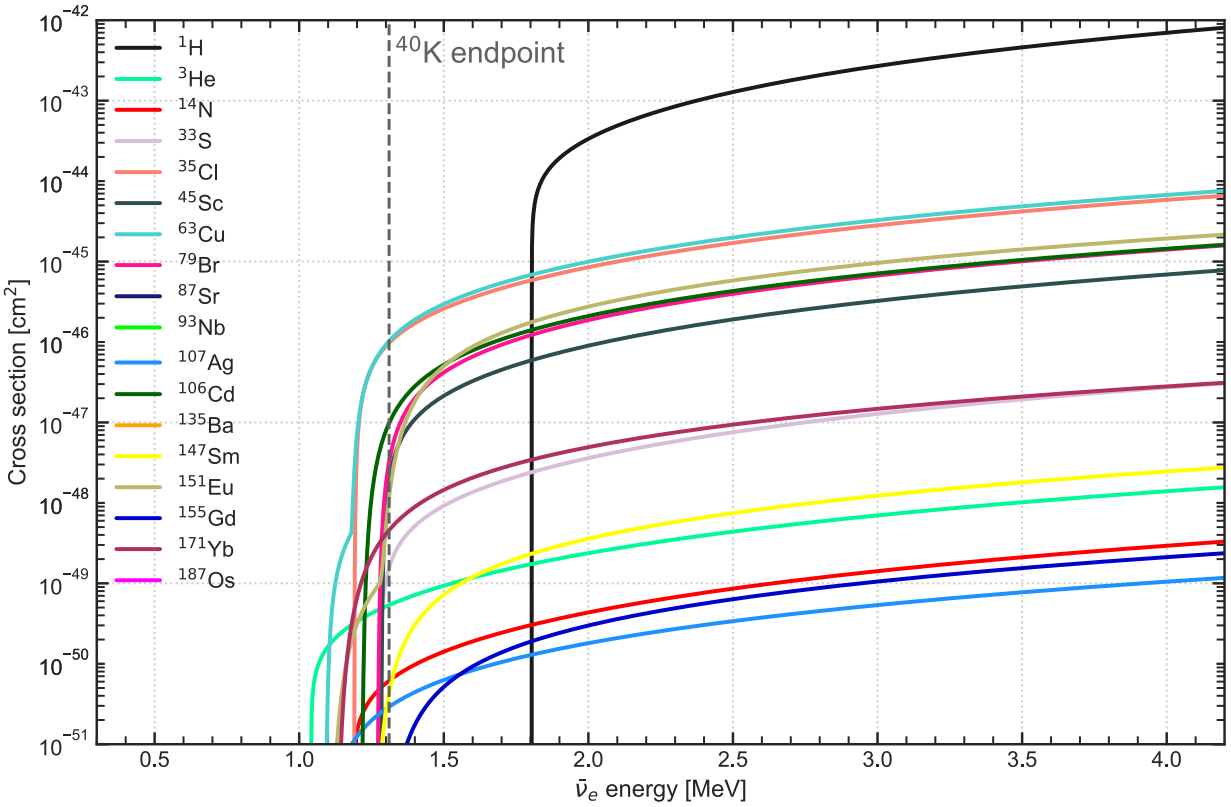

Figure 43. Inverse Beta Decay (IBD) cross sections evaluated for the target isotopes listed in Table 28. The cross section for the IBD reaction is calculated according to Eq. (23) by employing nuclear inputs reported in Table 28 and then weighted by the natural isotopic abundance of the targets. The grey dashed vertical line indicates the endpoint of the ^{40}K geoneutrino spectrum at 1.311 MeV.

^{3}He would be an excellent target with a high cross section (low *ft*) and one of the lowest energy thresholds. However, its scarcity ($1.3 \cdot 10^{-4}$ % isotopic abundance) and extremely high cost would make its choice prohibitive. Similar arguments apply to ^{106}Cd, ^{33}S, which would require isotopic enrichment to increase isotopic abundance from the natural 1.25% and 0.75%. Moreover, only an upper limit for the ^{106}Ag → ^{106}Cd beta decay branching ratio is available (BR<1% [187]), limiting the knowledge of ^{106}Cd cross section to an estimated maximum value (Log(*ft*) > 4.1). For ^{45}Sc, ^{79}Br, ^{87}Sr, ^{135}Ba, ^{147}Sm, ^{151}Eu and ^{155}Gd the energy threshold is too close to the ^{40}K endpoint to enable the detection of a relevant portion of the spectrum (estimations not showed here lead to ^{40}K signals $<10^{-3}$ TNU). Although ^{14}N is characterized by low Z (i.e., small Fermi Coulomb correction) and by a ~100% isotopic abundance, the ${}^{14}_{6}C \rightarrow {}^{14}_{7}N + e^- + \bar{\nu}_e$ allowed β decay is disfavoured (high *ft* value). This makes ^{14}N a poor target choice due to its small antineutrino cross section. A similar argument applies to ^{93}Nb, ^{171}Yb, ^{107}Ag and ^{187}Os, whose low *ft* value strongly limits the amplitude of the IBD cross section, excluding them from the possible targets.

In conclusion, by considering the *ft* value, the natural isotopic abundance and the proximity of the E_{th} value to the ^{40}K spectrum endpoint, ^{63}Cu and ^{35}Cl were identified as the most promising targets for the detection of ^{40}K geoneutrinos. However, the signals estimated for these two targets are more than an order of magnitude lower than their counterpart in IBD on protons (Table 29, Figure 44) and will require a substantial technological advancement in the detection techniques to be employed in real world scenarios.

Table 29. Most promising Inverse Beta Decay (IBD) target isotopes and their expected geoneutrino signals. The 1st column lists the target and product atoms involved in the IBD reaction, the 2nd column the IBD target Isotopic Abundance (IA) in percentage, the 3rd column the IBD reaction energy threshold (E_{th}) in MeV, the 4th column the Log ft value for the corresponding β decay of the final state. The IA, E_{th} and Log ft values are taken by the ENSDF database [187] which points to the literature references disclosed in the 5th column. Columns 6th, 7th and 8th report, as central values, the expected geoneutrino signal in the [E_{th} ; 3.272] MeV energy range at the Laboratori Nazionali del Gran Sasso originating respectively from uranium, thorium and potassium distributed in the Earth's Lithosphere and Mantle. The range in square brackets provides a variability on the expected signal in terms of minimum and maximum values obtained by respectively adopting a "minimal" and "maximal" scenario for the masses and distributions of heat producing elements in the Earth according to the models and the scenarios reported in Figure 14 and Figure 34. The expected geoneutrino signals are given in Terrestrial Neutrino Units (TNUs), corresponding to a 1-year acquisition time and 10^{32} atoms for each chemical species (i.e. a number of IBD target atoms corresponding to 10^{32} scaled by the isotopic abundance). Chlorine ^{35}Cl and copper ^{63}Cu represent the most promising targets for ^{40}K geoneutrinos detection, while hydrogen ^{1}H is here reported for comparison.

Target process	IA [%]	E_{th} [MeV]	Log(*ft*)	Ref	S(U) [TNU]	S(Th) [TNU]	S(K) [TNU]
$^{1}H \rightarrow {}^{1}n$	99.99	1.806	3.0170	[189]	31.5 [24.0; 47.0]	9.0 [6.4; 14.1]	/
$^{63}Cu \rightarrow {}^{63}Ni$	69.15	1.089	6.7	[187]	0.85 [0.64; 1.26]	0.49 [0.35; 0.77]	0.10 [0.07; 0.13]
$^{63}Cu \rightarrow {}^{63}Ni^{*}$		1.176	5	[188]			
$^{35}Cl \rightarrow {}^{35}S$	75.76	1.189	5.0088	[190]	0.73 [0.56; 1.09]	0.43 [0.30; 0.67]	0.10 [0.07; 0.13]

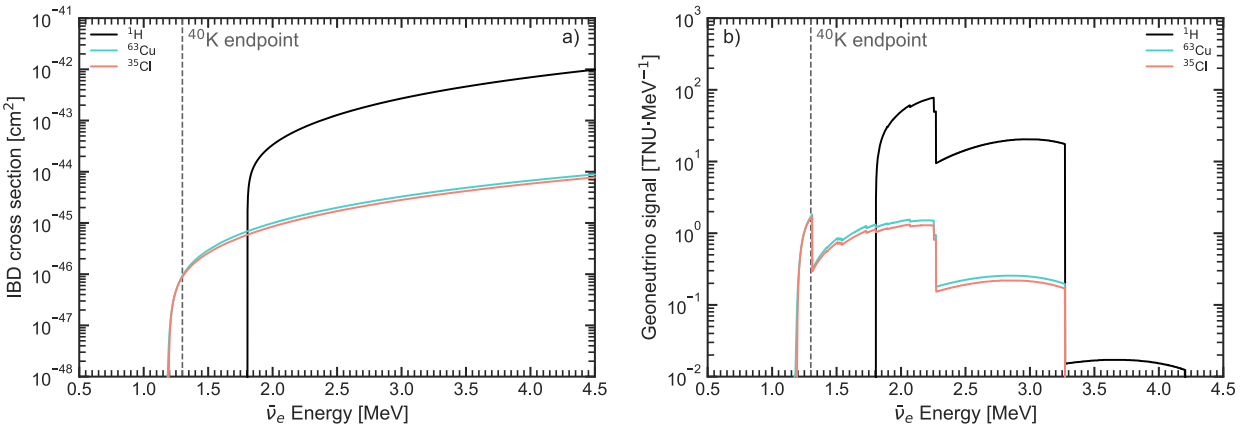

Figure 44. Cross sections and expected geoneutrino measured spectra for the ^{1}H, ^{35}Cl, ^{63}Cu Inverse Beta Decay (IBD) targets. **a)** shows the cross section for the IBD reaction for the 2 different targets as a function of the incoming antineutrino energy, weighted by the corresponding isotopic abundance of each target (see Table 29). **b)** shows the expected geoneutrino measured spectra at the Laboratori Nazionali del Gran Sasso (Italy) originating from uranium, thorium and potassium distributed in the Earth's Lithosphere and Mantle as described in [14]. The expected geoneutrino spectra are given in Terrestrial Neutrino Units (TNUs), corresponding to a 1-year acquisition time and 10^{32} atoms for each chemical species. In both panels the grey dashed vertical line indicates the endpoint of the potassium geoneutrino spectrum at 1.311 MeV.

2.9.6 Detection strategy

There are two main technical difficulties impeding the employment of heavy nuclei in current liquid scintillation detectors: (i) the challenges in loading large fractions of these atoms and the resulting reduction in the transparency of the scintillator, (ii) an effective way to accurately tag single positron (e^+) events in the absence of the neutron capture delayed signal employed in standard IBD on protons.

In general, even if e^+ events are characterized by a unique antimatter signature with resilient background rejection power, the explicit antimatter nature of the e^+ is rarely exploited in today's detectors and in the past has required segmented detectors that attempted to detect the annihilation gamma rays from the e^+ (e.g. the first antineutrino detection by [191]) for their identification.

Present state-of-the-art technology showed that loading fractions (i.e. the mass fraction of the scintillator represented by the dopant) of ~10% are somehow achievable (e.g. Indium loading in the proposed LENS experiment [192]), but ^{40}K-$\bar{\nu}_e$ detection will require R&D for approaching loading fractions up to 50% in order to reach the statistical significance needed for the detection of these geoneutrinos. Recently developed techniques exploiting opaque scintillators and optic fibres for light collection promise to enable the loading of large fractions of dopant in the scintillator [193], opening the possibility of high loading of heavy nuclei in detectors. Such techniques based on light confinement also promise to allow the detection of single e^+ in the detector without the requirement of a delayed coincidence signal. While promising, the exploitation of the antimatter signature of e^+ alone is not enough to reach the level of background suppression needed for ^{40}K-$\bar{\nu}_e$ detection, as we will discuss later.

From now on, I will discuss the employment of the proposed target isotopes for IBD (^{35}Cl and ^{63}Cu) requiring a loading fraction of 50%, assuming that a technology enabling high-loading and tolerance to transparency reduction will become available in the future. For instance, chlorine can be easily loaded in an organic liquid scintillator and there are several possible ways to achieve high loading. Chlorine can be loaded in a typical liquid scintillator by mixing in a non-fluorescing chlorinated solvent such as tetrachloroethylene (C_2Cl_4). Moreover, several chlorinated-benzene compounds, such as (but not limited to) dichlorobenzene ($C_6H_4Cl_2$), fluoresce and can work as (or with) a liquid scintillator. Copper could instead be loaded in aqueous solution in scintillator cocktails miscible with water. Organocopper compounds also exist, and the chemistry of copper is arguable more varied

than that of chlorine. These and other different loading options would require dedicated R&D to fully develop feasible deployment scenarios.

A scintillator loaded with copper or chlorine will offer two distinct detection channels: IBD on protons (IBD-p) and IBD on the chosen target isotope (IBD-^{35}Cl or IBD-^{63}Cu). For what concerns IBD-^{35}Cl and IBD-^{63}Cu, the ^{40}K geoneutrino signal is nearly an order of magnitude larger than each of the U and Th geoneutrino backgrounds and the expected reactor antineutrino signal in the ^{40}K energy window (Table 30). Additionally, the contribution of U, Th and reactors can be further independently estimated and subtracted via the alternate detection channel offered by IBD-p, which is statistically favoured by more than three orders of magnitude.

Table 30. Expected geoneutrino and reactor antineutrino signals for a liquid scintillator experiment located at the Laboratori Nazionali del Gran Sasso (Italy). Full details regarding the calculation of geoneutrinos' and reactor antineutrinos' events are described in Chapter 2.4. Reported signals in TNU refers to the number of IBD interactions occurring on 10^{32} nuclei of that element in 1 year, assuming natural isotopic abundance and 100% efficiency.

Detection reaction	Energy range	Antineutrino signal [TNU]			
		Reactors	^{238}U	^{232}Th	^{40}K
IBD-p	[1.806 – 3.27] MeV	22.2	31.5	9.0	/
IBD-^{35}Cl	[1.189 – 1.311] MeV	$1.8 \cdot 10^{-3}$	$9.0 \cdot 10^{-3}$	$8.9 \cdot 10^{-3}$	$1.0 \cdot 10^{-1}$
IBD-^{63}Cu	[1.176 – 1.311] MeV	$1.9 \cdot 10^{-3}$	$9.3 \cdot 10^{-3}$	$9.2 \cdot 10^{-3}$	$1.0 \cdot 10^{-1}$

2.9.7 Possible experimental backgrounds

There are potential backgrounds that can produce true e^+ in the detector. These backgrounds are represented by other antineutrinos (from U and Th geoneutrinos and from nuclear power reactor) and by β^+ emitting background sources. While the formers can be reduced via IBD-p driven subtraction, the latter represents an irreducible background.

This consideration immediately brings us to assess whether any β^+ emitter appears among the isotopes of the elements chosen as targets. Natural chlorine contains trace amounts (~10^{-13}) of the radioisotope ^{36}Cl. This isotope is produced in the atmosphere by spallation of ^{36}Ar and in the top meter of the lithosphere by thermal neutron activation of ^{35}Cl. ^{36}Cl has a half-life of about $3 \cdot 10^5$ years and a positron decay branch with 0.02% probability. Therefore, this isotope is expected to produce ~10^{10} positrons per year per 10^{32} chlorine atoms, completely overwhelming the ^{40}K-$\bar{\nu}_e$ expected event rate in the same energy region, thus excluding ^{35}Cl as a potential target for ^{40}K-$\bar{\nu}_e$ detection. Copper does not have natural

long-lived positron emitting isotopes. However, ^{64}Cu, which is a positron emitter with a half-life of ~12 h, can be produced by neutron activation and may be difficult to tag over such a long time. An estimation of cosmogenic neutron production in the detector is therefore needed to quantify the e^+ event rate from ^{64}Cu.

In natural radioactivity, there is perhaps only one important β^+ emitter, that being ^{40}K itself. Low background physics experiments have learned how to eliminate this background to achieve very low levels ($<10^{-14}$ g-K/g-scintillator) [194], with the primary concern typically being the 1.46 MeV gamma ray that is emitted following the electron capture decay branch 10.67% of the time. However, even by carefully estimating the actual amount of ^{40}K via the detection of its gamma emission, the sole statistical impact that this e^+ background would have on the detection significance greatly limits the capability to discern the signal of interest over the background (Figure 45). An alternative strategy to suppress backgrounds needs to be identified.

2.9.8 Detection significance calculation

In this context, where the expected number of background events is uncertain but can be constrained by a separate measurement, the background nuisance parameter in the likelihood function for a Poisson counting experiment can also be well constrained, thus essentially reducing the significance calculation to counting statistics of anticipated signal versus known background.

To estimate the ^{40}K geoneutrino detection significance one can thus consider the Poisson probability distribution of the hypothetical observation of N or greater events compared to the null hypothesis that the experimental observation came from only backgrounds. This can be calculated as:

$$\sum_{n=N}^{\infty} P(n;\ \mu + \Delta\mu) \tag{24}$$

where N is the number of observed events, μ is the mean expected number of background events (in the null hypothesis), and the uncertainty of the total background Δμ (statistical and systematic) can be accounted for by adding it to the mean [195]. A more formal calculation using a likelihood approach yields similar results because of the small rates and uncertainties involved. In this case, the separate measurement of the U and Th geoneutrino background in the ^{40}K geoneutrino energy range comes from the IBD-p events. Due to the

relatively high rate of the IBD-p events, the fractional uncertainty of this background contribution will be small in comparison. One of the keys to yield maximal discovery sensitivity is the data-driven subtraction of the U+Th signal, which cannot be removed using only geological arguments. The statistical and systematic uncertainties in the reactor background contribution in the ^{40}K geoneutrino energy range must also be included. Even if those uncertainties are fractionally larger, they will have minimal impact since the absolute event rate from reactor events is so much smaller (Table 30). All systematic uncertainties (U+Th+reactor) can be included in the $\Delta\mu$ term, in the calculation of the background expectation and Poissonian probabilities. The fact that U+Th geoneutrino and reactor antineutrino backgrounds events are directly measured by IBD-p events in the same detector helps when constraining many systematics related to the relative cross section ratio. There are some systematics to be included that affect the low-energy (< 1.8 MeV) IBD-^{35}Cl or IBD-^{63}Cu signal differently than the higher-energy IBD-p signal, such as reaction cross section uncertainties, U, Th and reactor spectrum shape uncertainties, and detector-related systematics that are energy dependent. Some of these systematics effects could be explored by taking ancillary data close to a reactor, which would provide a large and known antineutrino flux for an experimental measurement of the ^{35}Cl and ^{63}Cu antineutrino capture cross sections. Ultimately, systematic uncertainties in all of the background estimations wind up not having much impact on the ^{40}K geoneutrino flux measurement (or significance) since the ^{40}K geoneutrino signal is nearly an order of magnitude larger than each of the U and Th geoneutrino backgrounds (Table 30). The main factor reducing the significance of the detection proves to be the irreducible true e^+ background caused by β^+ decays inside the scintillator (Figure 45).

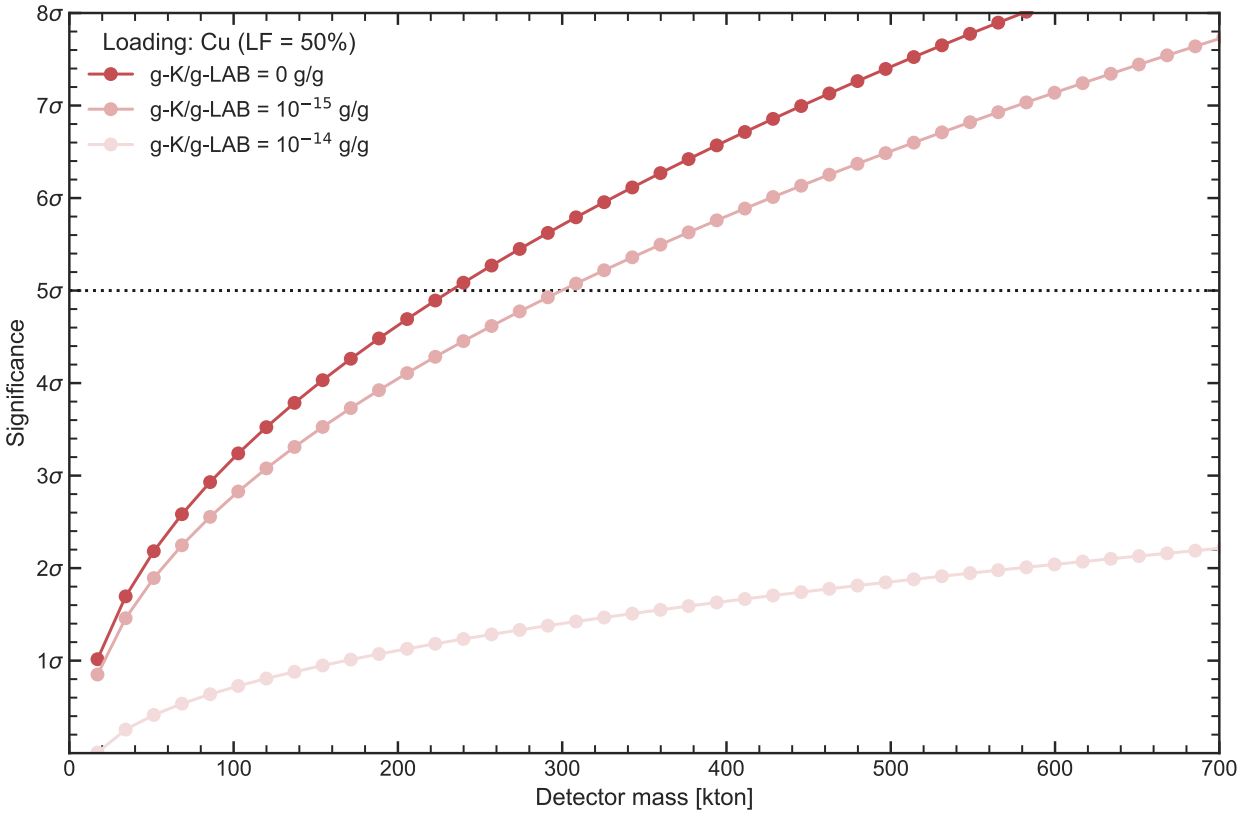

Figure 45. ^{40}K geoneutrino detection significance for a 50% Cu-loaded detector running for 10 years and located at the Laboratori Nazionali del Gran Sasso. The expected geoneutrino signal and the irreducible background reactor signal in the IBD-^{63}Cu potassium energy region [1.176; 1.311] MeV are $S_{IBD\text{-}Cl}(K)$ = 0.10 TNU, $S_{IBD\text{-}Cu}(U+Th)$= $1.9\cdot10^{-2}$ TNU, $S_{IBD\text{-}Cu}$ (reactors)= $1.9\cdot10^{-3}$ TNU. The expected geoneutrino signal and the irreducible background reactor signal in the IBD(p) energy region [1.806 ; 3.272] MeV are $S_{IBD\text{-}p}(U+Th)$= 40.6 TNU[10], $S_{IBD\text{-}p}$(reactors)= 22.2 TNU [137]. The ^{40}K geoneutrino detection significance in number of σ is calculated by conservatively considering a +1σ statistical uncertainty on the number of IBD-p events, which is propagated in the estimation of the background events in the ^{63}Cu potassium energy region (μ+Δμ) (see Eq. (24)). Each data point corresponds to an integer number of events N observed in the ^{63}Cu potassium energy region. The red line shows the significance for ^{40}K geoneutrino detection obtainable by considering only true antineutrino backgrounds. Orange and pink lines show the reduced statistical significance when also considering true positrons background caused by different concentrations of K in the scintillator.

The detection of the sole e^+ as a tracer for IBD-^{35}Cl and IBD-^{63}Cu is not enough to achieve the detection of ^{40}K geoneutrinos. Even radiopurity levels exceeding the already state-of-the-art standards (as Borexino) would produce a significant true positron background (Figure 45).

[10] This estimate is ~6 TNU higher with respect to [14], which adopts U and Th abundances inferred from local samplings [29]. Since this refined model does not report any information about K in the sedimentary deposits of Apennines chain, here we calculate the expected geoneutrino signal using the global model of [30].

An alternative strategy to suppress backgrounds needs to be identified. In the past, ^{106}Cd had been proposed [196] as a promising candidate isotope for ^{40}K geoneutrino detection because of its double coincidence, conceptually similar to the strategy used for IBD-p detection. IBD-^{106}Cd produces ^{106}Ag and an e^+. ^{106}Ag has in turn an electron capture/β^+ decay branch, with the e^+ emitted 59% of the time. Thus, ^{40}K geoneutrino capture on ^{106}Cd can generate two e^+ in a detector, delayed on average by the 24-minute ^{106}Ag half-life. This double-e^+ signal, correlated in space and time, might provide a distinctive signature for ^{40}K geoneutrino detection that would suppress backgrounds. However, as we saw in the previous chapter, the low isotopic abundance of ^{106}Cd limits its employment for ^{40}K detection.

^{63}Cu, the only suitable candidate left, displays a similar interesting feature. The favoured transition channel for ^{63}Cu leads to an excited state of ^{63}Ni*. ^{63}Ni* in turn decays with a half-life of 1.67 μs to its ground state by emitting an 87.13 keV 100% of the times. This precious double coincidence signal could be exploited to suppress all non-antineutrino backgrounds (aside from accidental coincidences) and to clearly decouple the two antineutrino detection channels (Figure 46).

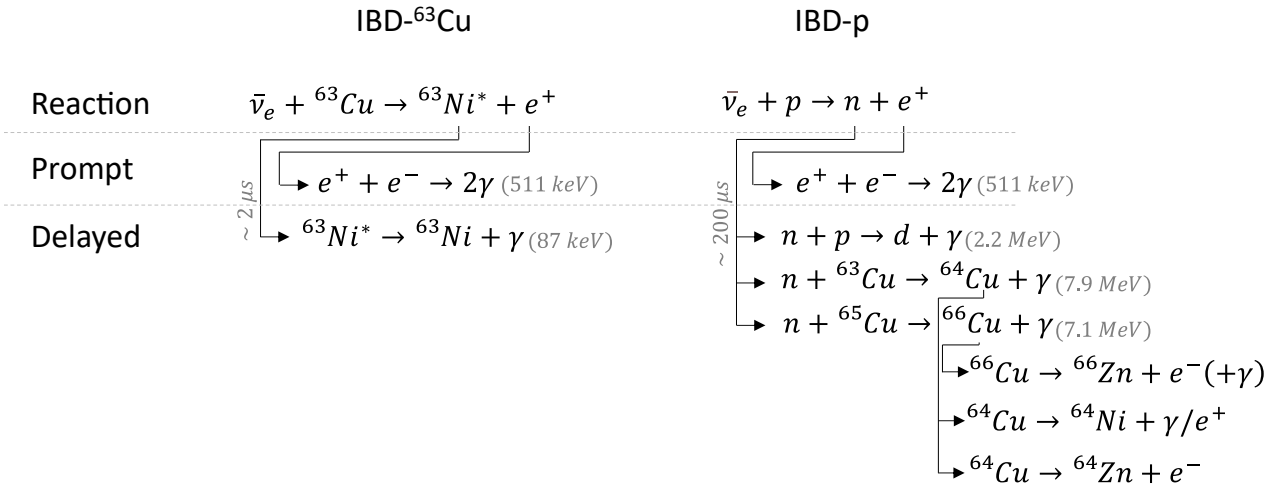

Figure 46. Scheme of the two distinct detection channels for IBD-^{63}Cu and IBD-p. After the capture of the antineutrino, both IBD channels produce a positron (e^+) which readily annihilates producing two back-to-back 511 keV photons (γ). For IBD-^{63}Cu, the produced ^{63}Ni* further decays with a half-life of 1.67 μs to its ground state by emitting an 87.13 keV γ. This double coincidence signature can be employed to distinguish IBD-^{63}Cu from both antineutrino backgrounds coming from the IBD-p channel and from true e^+ backgrounds caused by ^{40}K and ^{64}Cu β^+ decays in the scintillator. For IBD-p, the produced neutron can be captured by protons (i.e., H atoms) or more probably by the two loaded Cu isotopes, which have higher neutron capture cross sections. In any of these neutron capture processes the delayed reaction can be easily tagged via the detection of the one or more high energy gammas (>2.2 MeV) produced in the reaction once that the neutron has thermalized (<200 μs) and then captured.

Whereas these prompt and delayed signals are both time and space correlated, background-induced signals are not. Hence, this delayed coincidence method provides an extremely powerful background suppression, working as a very effective tagging technique for the antineutrino interactions of the two distinct detection channels.

2.10 Concluding remarks

A liquid scintillator detector with a mass slightly under 240 kilotons and 50% loading of copper could enable the ^{40}K geoneutrino signal detection (rejection of the null hypothesis) at 5σ level in 10 years of data taking. The discovery potential of ^{40}K geoneutrinos remains an experimental challenge due to the small event rate, requiring a detector of the size of Hyper-Kamiokande [197]. The small event rate demands a huge background suppression that could be provided by the IBD-^{63}Cu delayed coincidence via the detection of the ^{63}Ni* deexcitation gamma ray. Significant R&D will be required to enable the high loading-fraction (50%) and the tolerance to decreased transparency required for IBD-^{63}Cu employment.

All the considerations on this promising CC detection channel (potentially the only one possible) is however based on the assumption of an estimated Log(*ft*) value for the IBD transition to Ni* excited state. At present time there are no previous measurements of the β decay partial half-life for the ^{63}Ni* nuclear state. The Log(*ft*) value of 5 has been assumed (as done in [188]) noting that the Log(*ft*) value to the ^{63}Ni ground state transition is worse (Log(*ft*) = 6.7*)*. The ^{63}Ni* excited state does have a higher Q value and thus its associated β decay half-life should be shorter, leading to a smaller Log(*ft*) value and to a higher cross section. One would need to confirm this cross section estimate for IBD-^{63}Cu to the excited state using a new measurement (of ^{63}Ni* β decay, maybe exceedingly rare) or perhaps with arguments from nuclear theory (possibly in combination with experimental results from ^{63}Cu(n,p) nuclear reactions).

The impact of the first ^{40}K geoneutrino measurement would be a direct estimation of the bulk mass of potassium in the Earth and would enable an estimate of its content in the deep interior after accounting for the actual knowledge of the amount of potassium in the accessible lithosphere. While current geoneutrino measurements provide radiogenic heat power estimates relying on a model dependent K/U ratio, a direct measurement of the ^{40}K heat power would provide an experimental constraint to the radiogenic fraction of the Earth's internal heat budget. For instance, a fully chondritic Earth would produce a very

large ^{40}K signal and could potentially be excluded [198]. Measuring the K/U ratio also provides critical information about the behaviour of volatile elements during Earth's early stage formation [10]. Finally, a direct measurement of the ^{40}K geoneutrinos would be crucial to shed light on the "missing K" hypothesis and in turn provide insights into Earth's composition, structure, and thermal evolution; thus, this may stand as the most important quest and challenge for geoneutrino research in the near future.

Part of the content of this chapter is based on the following publication:

G. Bellini, K. Inoue, F. Mantovani, **A. Serafini**, V. Strati and H. Watanabe. "Geoneutrinos and Geoscience: an Intriguing Joint-Venture." La Rivista del Nuovo Cimento, (December 2021). https://doi.org/10.1007/s40766-021-00026-7

3.

CHALLENGES IN SMART FARMING

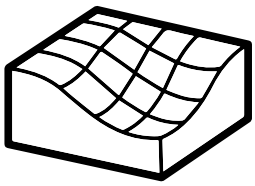

Due to continuing human population growth and the consequent increasing demand for available water, the management of water resources has become a pressing issue for governments and international organizations. Irrigated agriculture accounts for more than 70% of global water withdrawals [199]. Improvement of farming practices is therefore imperative to ensure availability and sustainable management of water in the future, one of the goals of the 2030 Agenda for Sustainable Development [200].

A concrete solution for an adequate irrigation schedule is the use of a decision support system based on novel technologies for a non-invasive and smart monitoring of soil water content (SWC) [201, 202]. The knowledge of the actual SWC represents a strategic element allowing users to manage and use the right amount of water at the right time, leading to an optimal irrigation performance. A crucial step towards the reduction of water wastage and the increase of water security at global scale is the awareness of irrigated lands and of the amount of irrigation water that is really distributed in the soil [203, 204].

In this context, the SWC assumes a great importance since it offers dual information: (i) how much water is necessary for a growing crop and (ii) how much water enters the soil after an irrigation or rainfall event. To exploit these potentialities, it appears evident that knowing which of these two events caused the water precipitation in the soil is mandatory.

A unique equipment that measures the field scale SWC and simultaneously distinguishes irrigation and rain events could be the keystone to face these challenges.

Proximal gamma-ray spectroscopy (PGRS) offers the most effective tool to reach these desiderata, recording the gamma signal coming from ^{40}K and ^{214}Pb decays to study the evolution of SWC in time and discriminating between rain- and irrigation-induced variations, respectively. In this chapter, I present the results of a two-stage PGRS experiment performed on an agricultural test field in Emilia-Romagna (Italy). I demonstrate how the simultaneous observation in a gamma spectrum of a transient increase in the ^{214}Pb signal coupled with a decrease in the ^{40}K signal acts as an effective proxy for rainfall, while a decrease in both ^{214}Pb and ^{40}K signals is a reliable fingerprint for irrigation.

Proximal gamma-ray spectroscopy is a mature and consolidated technology ready to provide a reliable tracing of soil water content during an entire crop season and an unbiased tool for remotely distinguishing rainwater from irrigation without any meteorological support information.

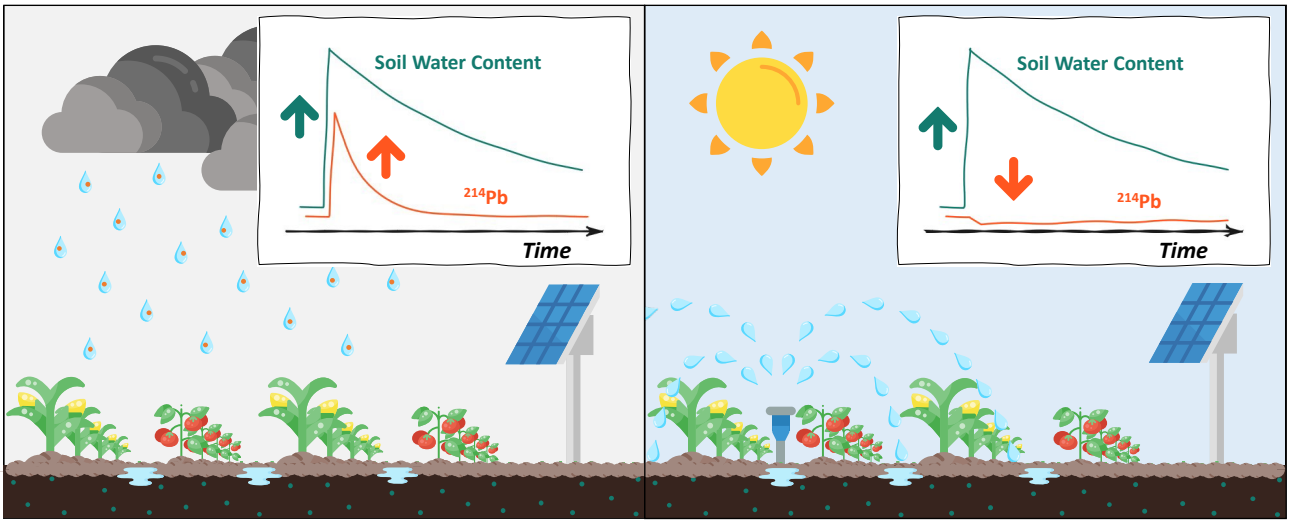

3.1 Proximal Remote Sensing techniques

The only direct method available for measuring the SWC is currently the gravimetric technique [205], a disruptive and time-consuming procedure requiring operator intervention. Conversely, indirect techniques consist of in situ non-disruptive measurements at a punctual scale (~dm^2) or non-invasive remote sensing (RS) methods covering larger areas (up to ~km^2). PGRS [206, 207] is, together with cosmic-ray neutron

sensing (CRNS) [208-210], a field scale non-invasive technique that fills the aforementioned scale gap.

CRNS is based on the measurement of cosmic-ray neutrons that scatter on hydrogen atoms in the ground. These atoms mainly come from the water in the soil, so the CRNS technique can infer the SWC level by studying the scattered neutron flux. Based on the observation of cosmic-ray products, this technique suffers from uncertainties tied to the estimation of the unscattered flux.

PGRS is instead sensitive to the gamma radiation produced by the nuclear decays of ^{40}K and of radionuclides belonging to ^{232}Th and ^{238}U chains, which are naturally present in the soil. The SWC is measured in real time on the basis of the temporal variations of the gamma signal produced by the decays of the ^{40}K that is naturally and homogeneously (in space and time) distributed in cultivated soils. Since water distributed in the terrain shields the terrestrial gamma flux, an inverse relation between SWC and gamma signal measured by a spectrometric station can be clearly observed and used for a quantitative estimation of SWC [207].

The knowledge of irrigated lands cannot rely on the available datasets since most of the existing comprehensive maps of irrigation water are based only on statistical surveys or can identify just the areas equipped for irrigation, rather than the truly irrigated areas [211]. These maps are not global and are not up-to-date, since illegal pumping is not included, there are self-reporting relevant biases, and temporal/spatial coverage is not homogenous [212, 213]. Some vegetation indexes, based on optical and visible RS techniques, are tentatively used as proxies for irrigation monitoring, since irrigated and non-irrigated lands show different spectral responses [214, 215]. Sometimes these methods fail because climate conditions, natural vegetation regimes, and agricultural practices are often unpredictable variables. Recent attempts to integrate these approaches seem to give promising results [216], although temporal and spatial heterogeneity of the information remains a persistent Achilles's heel.

In recent years, an alternative approach for global irrigation monitoring has been developed. Diverse algorithms, one of which is SM2RAIN [217], are based on the inversion of the soil–water balance equation to derive the amount of irrigation water, once the rainfall water fraction is identified and subtracted from the total amount of water. PGRS comes into play here: a single detector can retrieve the SWC from the ^{40}K gamma signal and simultaneously act as an effective proxy for rainfall occurrences. Indeed, PGRS is sensitive

to the ^{214}Pb gamma emitter, a radon progeny concentrated in rain droplets [218, 219]. A transient increase in the ^{214}Pb gamma signal, coupled with a decrease in the ^{40}K signal, can hence be used as an effective proxy for rain events [220]. Irrigation is, instead, characterized by a decrease in both ^{214}Pb and ^{40}K gamma signals.

3.2 The effect of water on the gamma signal

The survival probability for a gamma photon of energy E [MeV] traversing a given material is governed by an exponential attenuation law characterized by the specific material's linear attenuation coefficient $\mu(E)$ [m^{-1}], often expressed as its mass attenuation coefficient $\frac{\mu}{\rho}(E)$ [m^2 kg^{-1}]. In general, soil is a complex system made up of a heterogeneous mixture of solid, liquid and gaseous phases, but the application of gamma ray spectroscopy to precision agriculture essentially treats soil as a two-phase medium constituted by a solid portion (S) and water (W). In the presence of a mixture, the mass attenuation coefficient is obtained as the weighted sum of the mass attenuation coefficients of individual soil material constituents, which in our case comes down to:

$$\mu = \mu_S + \mu_W = \mu_S \cdot \left(1 + \frac{M_W}{M_S}\frac{\mu_W}{\rho_W}\frac{\rho_S}{\mu_S}\right) = \mu_S \cdot \left(1 + \frac{w}{\Omega}\right) \tag{25}$$

where $w = \frac{M_W}{M_S}$ [kg/kg] represents the so-called gravimetric Soil Water Content (SWC) and $\Omega = \left(\frac{\mu_S}{\rho_S}\right)\left(\frac{\rho_W}{\mu_W}\right)$ is a constant depending only on soil composition. From Eq. (25) it appears clear that the attenuation coefficient μ is highly sensitive to variations in the water content of the soil w. When water enters the soil, it fills the pores previously occupied by air (which has a negligible mass attenuation coefficient, nearly three orders of magnitude lower), increasing the total attenuation coefficient of the soil. This intuition is the key for understanding soil water content assessment through gamma ray spectroscopy.

Indeed, the gamma signal measured by a spectrometer is strictly linked to the attenuation coefficient μ. For a generic detector, the gamma signal C [cps] measured for a photopeak of energy E [keV] can be written as:

$$C(E) = \frac{G(E)}{\frac{\mu}{\rho}(E)} a_i \tag{26}$$

where $G(E)$ is a constant comprising the gamma yield [$\gamma/(s \cdot kg)$], an adimensional geometrical factor and a flux-to-signal effective cross section factor [counts/($\gamma \cdot m^2$)], while a_i is the mass abundance of the parent radionuclide [kg/kg] in the soil[11].

By intervening on the geometrical factor, or more specifically by changing the installation height h at which the detector is installed, the footprint area investigated by a gamma detector can be precisely tweaked and adjusted. Once defined a given geometry, any change in the detected signal will then have to be attributed to a change in the soil water content w. This is the key for understanding the lateral and vertical horizons of proximal gamma-ray spectroscopy.

[11] From now on the explicit dependence on the photon energy E will be dropped since we will consider photons belonging to a single gamma line, i.e. having a specific photopeak energy.

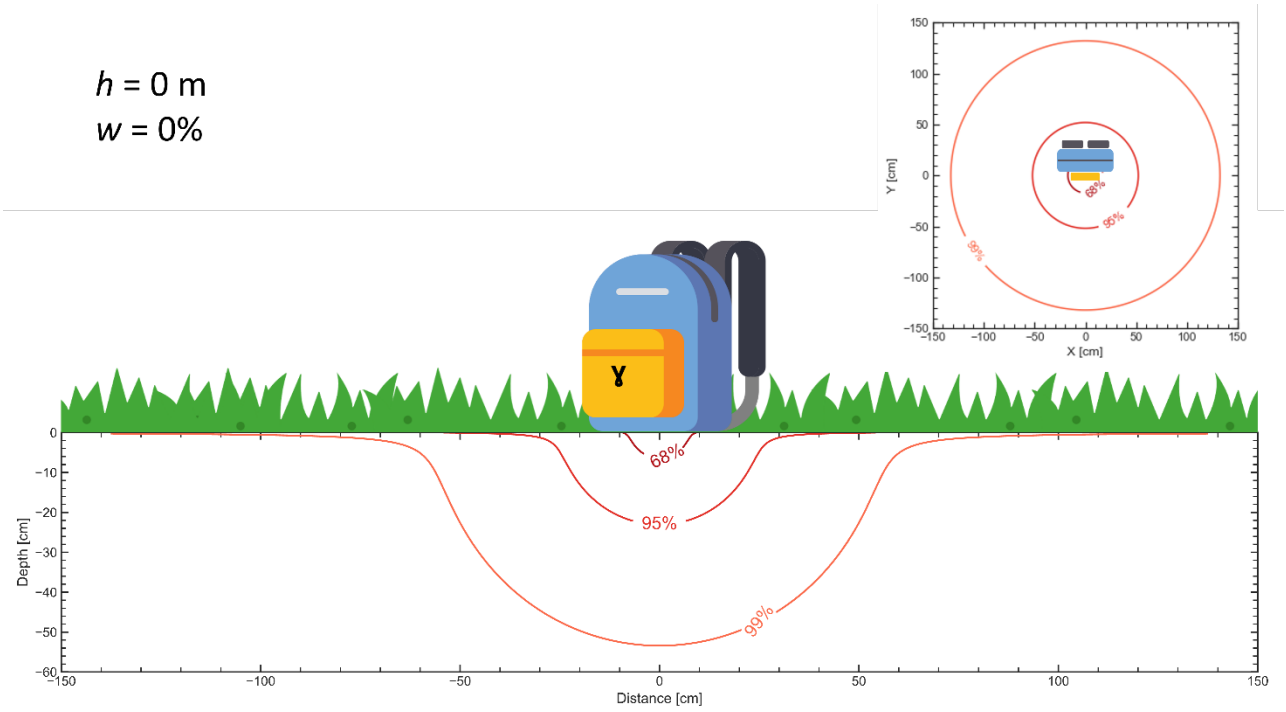

Figure 47. Monte Carlo simulation of vertical and lateral contribution horizons within which 68%, 95% and 99% of the detected gamma signal is produced. The simulation assumes a detector height h = 0 m, gravimetric soil water content w = 0%, a soil bulk density of ρ = 1345 kg/m^3 and a gamma photon energy of E = 1461 keV (i.e., ^{40}K photopeak).

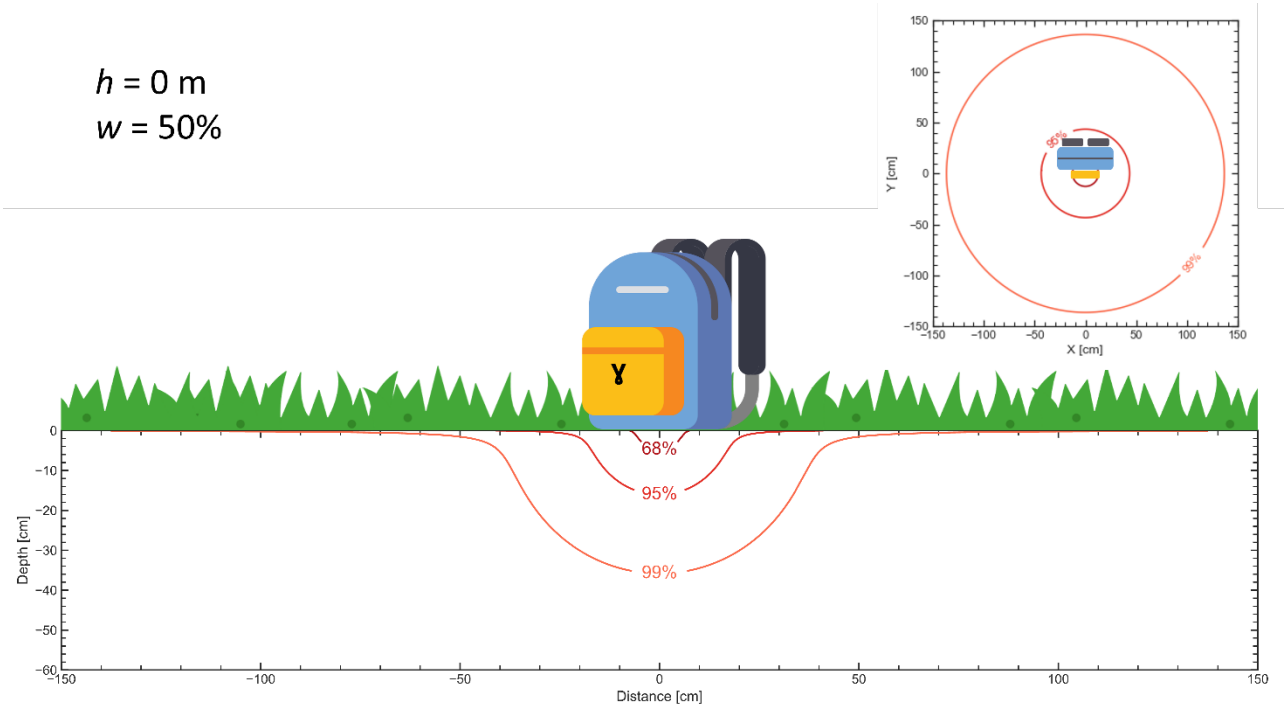

Figure 48. Monte Carlo simulation of vertical and lateral contribution horizons within which 68%, 95% and 99% of the detected gamma signal is produced. The simulation assumes a detector height h = 0 m, gravimetric soil water content w = 50%, a soil bulk density of ρ = 1345 kg/m^3 and a gamma photon energy of E = 1461 keV (i.e., ^{40}K photopeak).

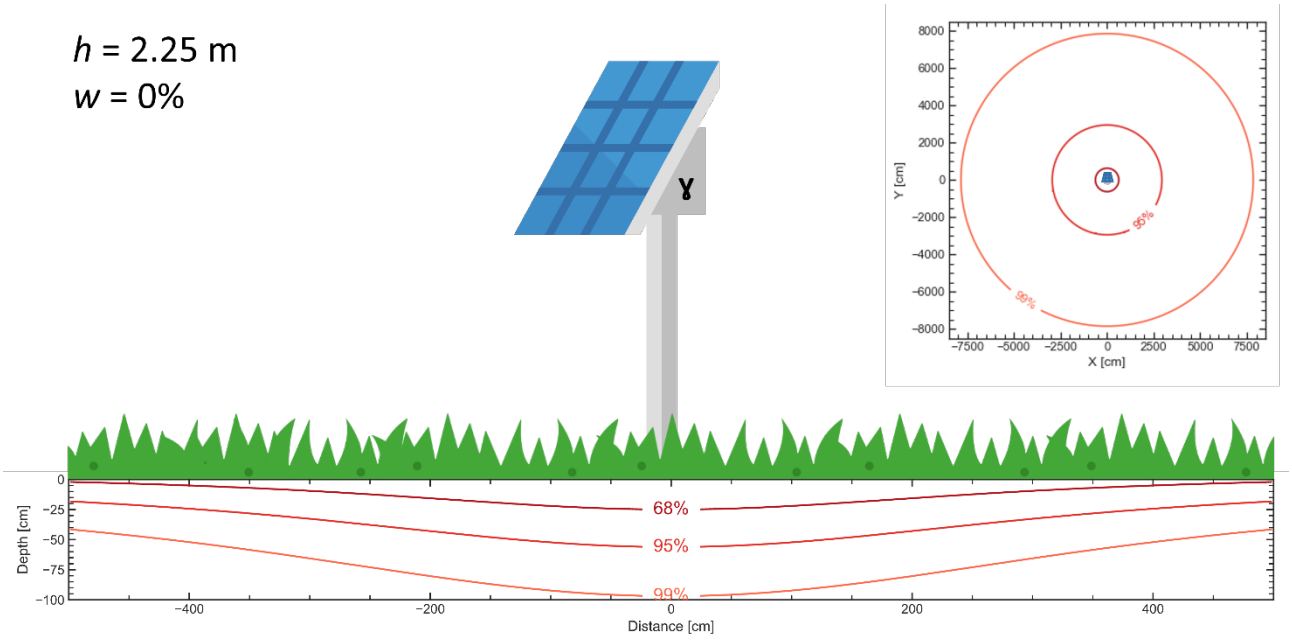

Figure 49. Monte Carlo simulation of vertical and lateral contribution horizons within which 68%, 95% and 99% of the detected gamma signal is produced. The simulation assumes a detector height h = 2.25 m, gravimetric soil water content w = 0%, a soil bulk density of ρ = 1345 kg/m^3 and a gamma photon energy of E = 1461 keV (i.e., ^{40}K photopeak).

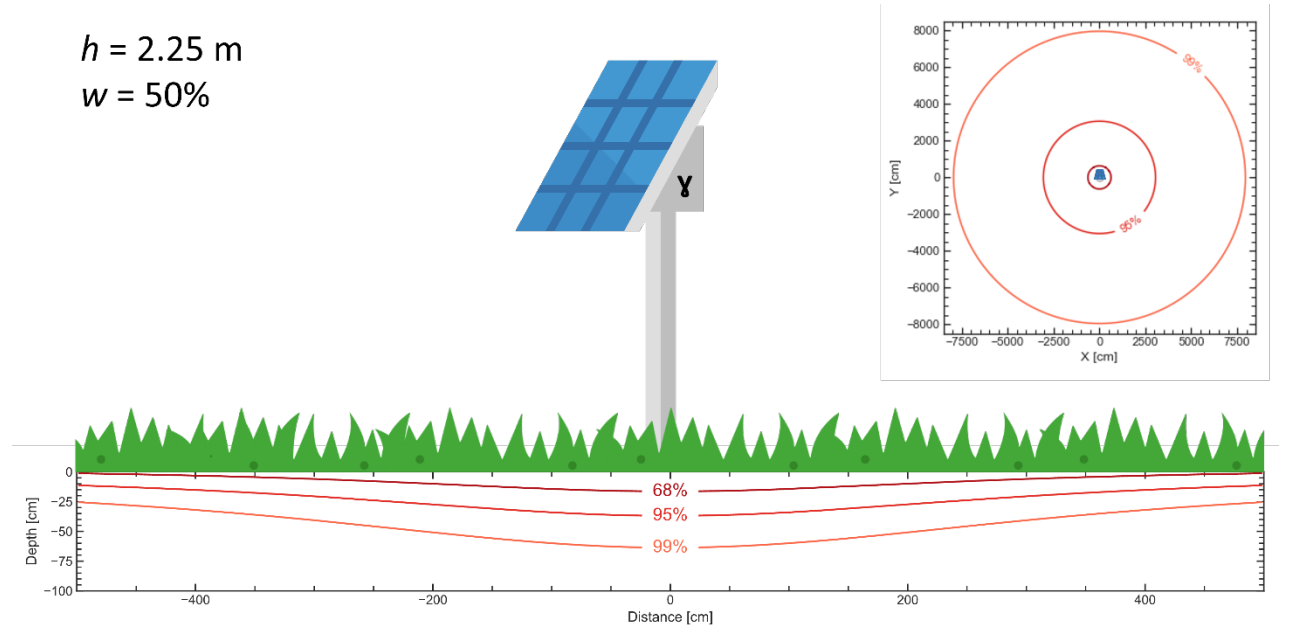

Figure 50. Monte Carlo simulation of vertical and lateral contribution horizons within which 68%, 95% and 99% of the detected gamma signal is produced. The simulation assumes a detector height h = 2.25 m, gravimetric soil water content w = 50%, a soil bulk density of ρ = 1345 kg/m^3 and a gamma photon energy of E = 1461 keV (i.e., ^{40}K photopeak).

The explicit dependence of the gamma detector's Field of View (FOV) is, in principle, non-trivial, but can be modelled via Monte Carlo techniques (Figure 51). The resulting footprint of this techniques (i.e. ∽10 m) makes gamma ray spectroscopy an ideal tool for probing soil moisture content at field scale.

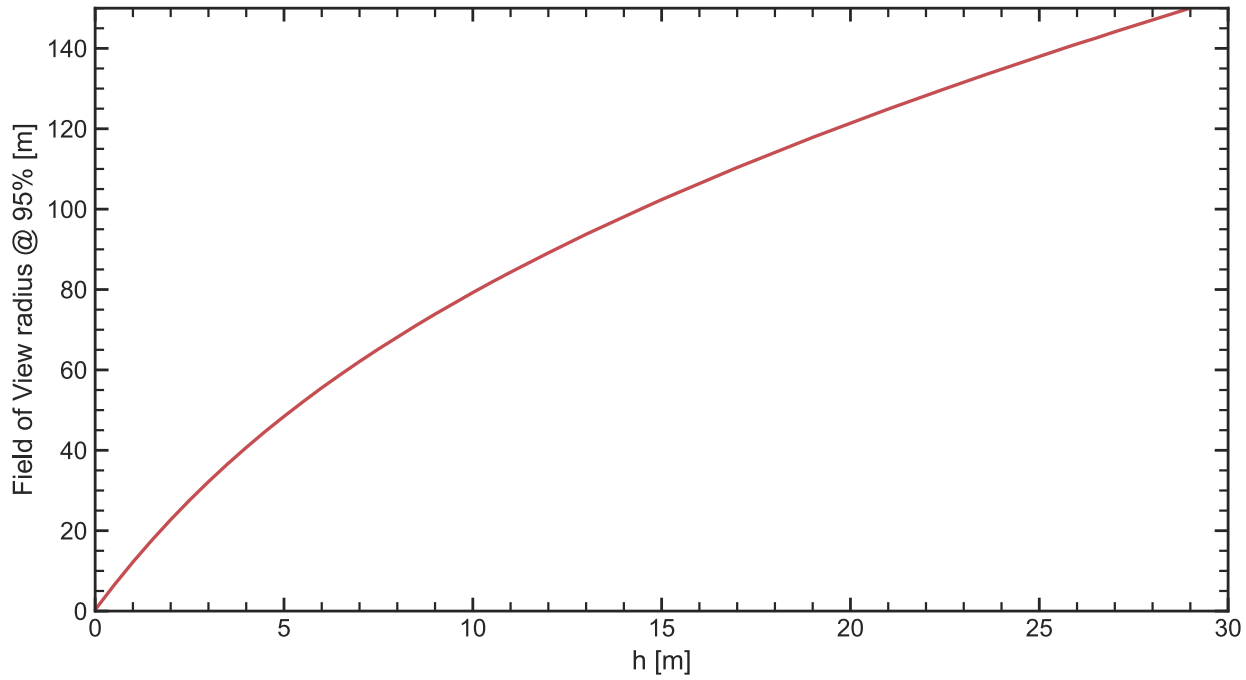

Figure 51. Field of View (FOV) radius as a function of the height of installation *h* of the gamma detector. The FOV radius refers to the radius within which the area producing 95% of the detected signal is contained.

For a given experimental setup, once characterized the signal response of the detector C^{Cal} in the presence of a given soil water content w^{Cal} via an experimental calibration, the inverse relation between the detected signal C and the soil attenuation coefficient μ (Eq. (26)) permits to quantitatively derive the water content of the soil w as:

$$w = \frac{C^{Cal}}{C}[\Omega + w^{Cal}] - \Omega \qquad (27)$$

3.3 Gamma spectroscopy for monitoring water in precision farming

3.3.1 Assessment of Soil Water Content

PGRS is a method particularly sensitive to SWC, since at typical gamma photon energies (~MeV) the mass attenuation coefficient of water is higher than those of typical minerals

commonly present in the soil [221]. As a result, small increments in SWC can be indirectly estimated by measuring the attenuation in the gamma signal coming from the radioisotopes present in the soil.

However, even if the signal attenuation caused by the increased SWC level is qualitatively visible across the entire energy spectrum (Figure 52), a quantitatively assessment of the SWC requires an accurate analysis of specific photopeak's energy regions. Indeed, the fraction of photopeak photons emitted by the ^{238}U, ^{232}Th decay chains and ^{40}K which are shielded by water according to Eq. (26), ends up populating the Compton continuum, thus deforming the detected energy spectrum.

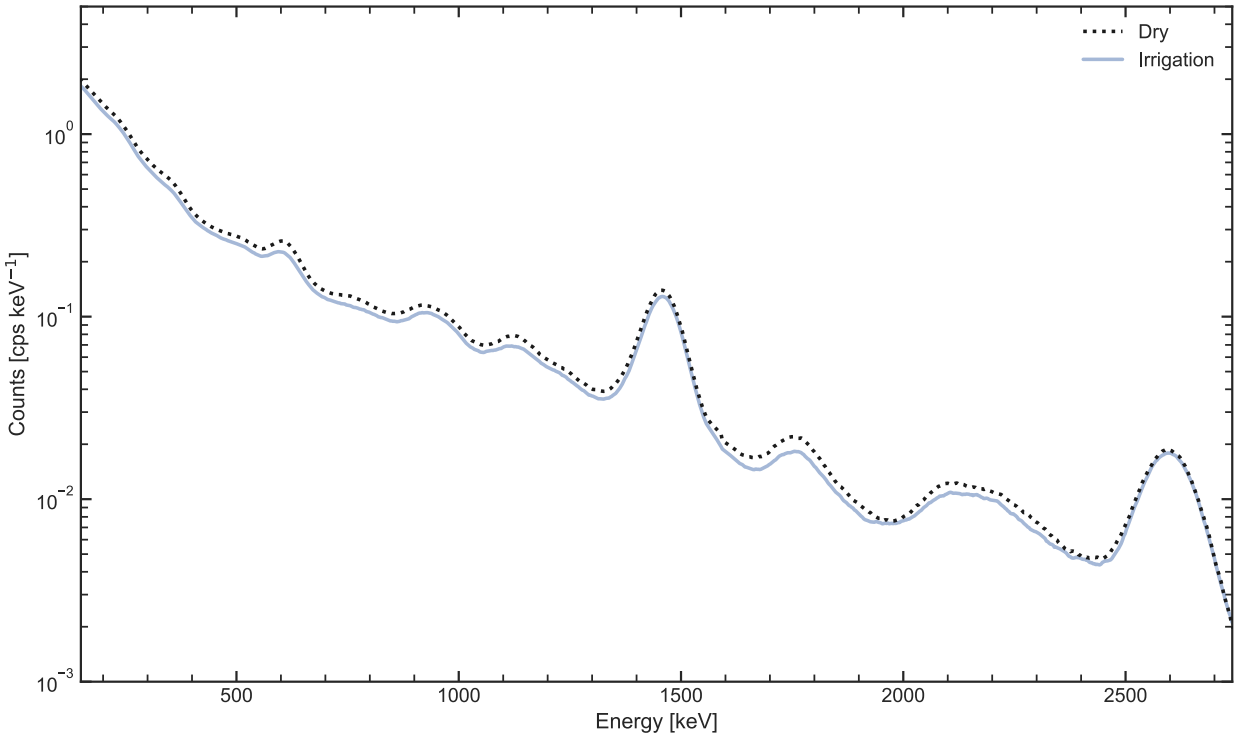

Figure 52. Comparison between the experimental gamma spectra recorded in dry and wet conditions before and after an irrigation, respectively.

In this perspective, the detection of the ^{40}K gamma signal photopeak (1.46 MeV) is convenient in agricultural lands, which are homogenously rich in this element. Potassium is an essential element for the growth of cultivars; it is stored in the soil both inside minerals in the form of crystal lattices (and therefore not available for radical absorption) and dissolved in water solution. About 99% of the soluble potassium, which can be assimilated by plants, is provided by clays which, depending on the type of texture, can

contain from 1% to 10% of the total potassium present in the soil, which on average represents 1%-2% of the soil mass.

In the context of an agricultural field, the relation between ^{40}K photopeak net count rate $C_K(t)$ (in cps) and soil water content $w_\gamma(t)$ in kg/kg, measured at time t, can be expressed by correcting Eq. (27) as:

$$w_\gamma(t) = \frac{C_K^{Cal}}{C_K(t)} \Lambda\left[\Omega + w_g^{Cal}\right] - \Omega \qquad (28)$$

where $C_K^{Cal} = 11.7 \pm 0.2$ (cps) and $w_g^{Cal} = 0.163 \pm 0.008$ (kg/kg) are the ^{40}K net count rate and the gravimetric soil moisture level at calibration time (18 September 2017), respectively [222]. These parameters are site- and detector-dependent and need to be properly measured for an accurate estimation of w_γ. The adimensional coefficient $\Omega = 0.899$ represents the ratio between the mass attenuation coefficient of the solid portion of the soil and the one of water, calculated according to the elemental composition of the soil of the experimental site [222]. In the absence of a detailed mineralogical analysis, a $\Omega = (0.903 \pm 0.011)$ mean value can be employed [222]. The $w_\gamma(t)$ was converted in volumetric soil water content (SWC_γ) in m^3/m^3 by multiplying it by 1.345, namely the ratio between soil bulk density (Table 31) and water density ($\sim 1000\ kg/m^3$).

The added adimensional parameter Λ represents the time-dependent count rate attenuation function that accounts for the biomass water content (BWC), which is an attenuation factor of the gamma signal due to the presence of vegetation. Differently from other vegetation indexes, the BWC refers to the amount of water contained in the entire plant (stems, leaves, and fruits). The effect of the BWC on the C_K is nontrivial and, in principle, it is indistinguishable from that generated by an increase in the SWC_γ. The BWC can be modeled as a layer of some mm of water covering the ground. The presence of a 1.0 mm water layer leads to an overestimation of ~10% for the SWC_γ value (see Figure 7b of [223]): this attenuation needs to be studied and accounted for in order to avoid systematic errors. The quantification of the gamma signal attenuation as a function of the modeled water layer thickness was studied through Monte Carlo simulations [223]. Since the temporal evolution of BWC is tightly related to crop's growth stage, the overall BWC was estimated on the base of gravimetric measurements on stems, leaves, and fruits samples collected at four and six different stages of tomato and maize maturity, respectively. Modeling the evolution of the entire organism by means of a Gompertz sigmoid function

[224], the time-dependent correction to be applied to the measured gamma signal was calculated.

The calibration of the PGRS station was performed only once in 2017 and successfully used for both 2017 and 2020 data-taking campaigns. The value of w_g^{Cal} in Eq. (28) was obtained from the measurements of 16 sampling points distributed within 15 m from the PGRS station (Figure 4 of [223]), which is the area where ~85% of the signal received by the station originates. For each sampling position, three samples were collected in the depth intervals of 0–10 cm, 10–20 cm, and 20–30 cm for a total number of 48 samples. After drying the samples at 105 °C for about 24 h and inferring their gravimetric water content, the vertical weighted mean for each of the 16 sampling points was obtained by assigning to each depth interval a weight based on its contribution to the gamma signal (calculated according to Equation (3) of [222]). Finally, the value w_g^{Cal} was calculated as the mean of the 16 sampling points, with the uncertainty given by their standard deviation, which is of the order of 5%.

As estimated in [223], the uncertainty on w_γ (Eq. (28)) is dominated by that of w_g^{Cal}, rather than by the statistical error of $C_K(t)$ (<1%). Hence, the absolute uncertainty on w_γ is a constant value equal to 0.017 (kg/kg), corresponding to a 0.023 (m^3/m^3) uncertainty on the estimated volumetric SWC_γ values. Since the abundance of ^{40}K in the ground remains constant in time, due to the inverse relation between the C_K signal and w_γ expressed by Eq. (28), a sudden decrease observed by the PGRS station in $C_K(t)$ is related to a SWC increase.

3.3.2 Discrimination of rain and irrigation

From this brief discussion on the shielding effect of water on the detected gamma signal, one may think to observe the same behavior both for the water deposited by the rain and irrigation. On the contrary, gamma spectra recorded during and immediately after a rain event show a pronounced increase in the detected radiation levels instead of being attenuated by the additional water layer (Figure 53).

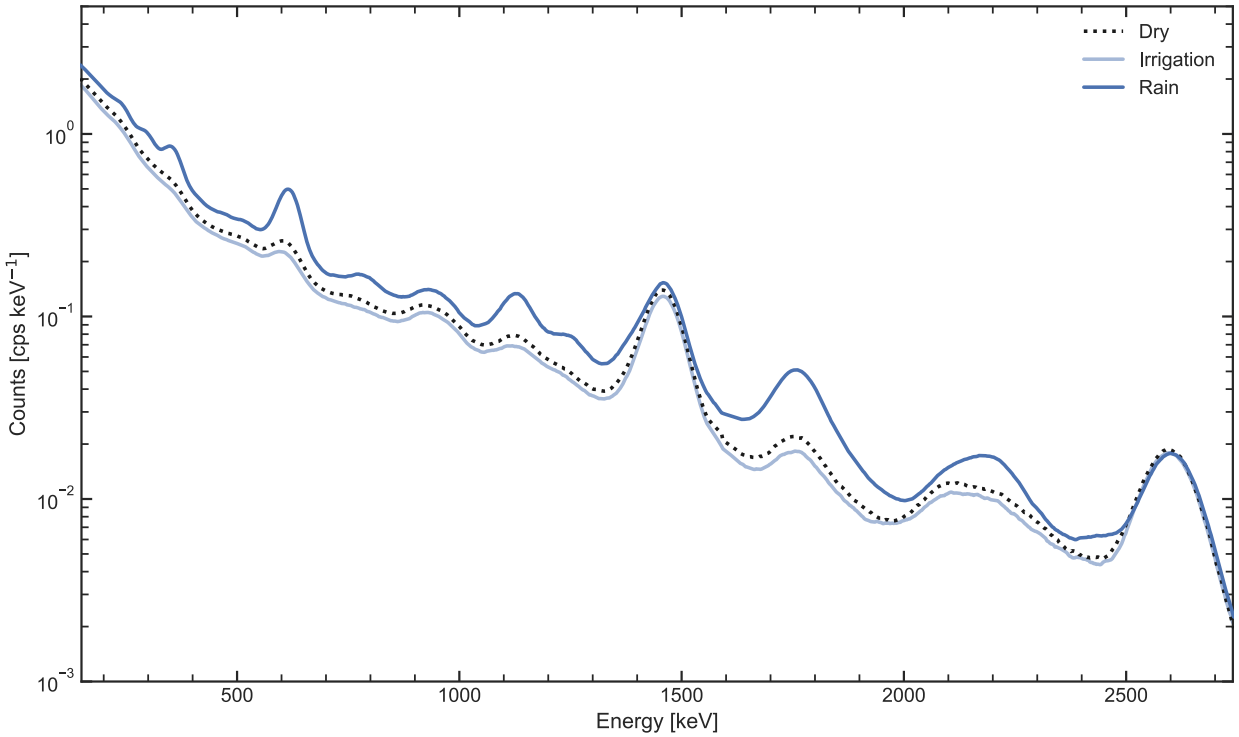

Figure 53. Comparison between the experimental gamma spectra recorded in dry and wet conditions before and after an irrigation (dashed black and light blue lines, respectively) and immediately after a rain event (blue line).

The cause of this phenomenon has to be ascribed to the high volatility of ^{222}Rn, a gaseous radioisotope that easily exhales from the ground and enters the atmosphere. ^{222}Rn is a gaseous parent radionuclide which triggers the decay chain described in Figure 54. Since during an alpha decay few electrons are stripped from the recoil of the parent atom [225], the results of ^{222}Rn decay is a charged ion ^{218}Po^{+} in ~90% of decays [226, 227]. Due to its lower first ionization potential (8.34 eV) with respect to the atmospheric surrounded molecules elements, ^{218}Po^{+} may prevent the process of total neutralization, leaving the atom in a charged state. The fates of ^{214}Pb^{+} and ^{214}Bi^{+}, having ionization potentials 7.42 and 7.29 eV respectively, are expected to be the same [228]. Therefore, radon daughters adhere to the water molecules in the air or react with vapours and trace gases in less than 1 s. The obtained small clusters (0.5 to 5 nm), characterized by a high mobility, attach to aerosol in time scale of 1-100 s forming a "radioactive aerosol" (diameter ~ 100 – 300 μm) [229] which in turn attaches to droplets. ^{222}Rn and its progenies are considered in secular equilibrium in the clouds [230, 231], but when rain droplets begin their descent to ground the equilibrium is broken. These in-cloud scavenging (the so-called rainout) processes are responsible for the radioactive enrichment into rain droplets with an efficiency higher than below-cloud scavenging (washout).

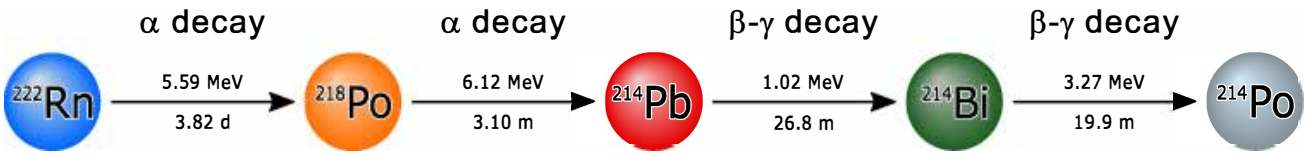

Figure 54. ^{238}U decay sub-chain from ^{222}Rn to ^{214}Po, simplified by excluding the decay channels with branching fractions $< 0.05\%$. The simplified sub-chain comprises two α decays and two β-γ decays. Each α or β-γ decay is represented with a horizontal arrow: the Q-value and the half-life of the father nucleus of a given decay are reported respectively above and below the corresponding arrow. The β- γ decay of interest for the rain-induced gamma activity measurements is the one transforming ^{214}Pb into ^{214}Bi. In this decay the most intense gamma rays are those with characteristic energies of 295 *keV* and 352 *keV*, the latter chosen for the estimation of the experimental ^{214}Pb net photopeak count rate.

Qualitative evidence for the ^{222}Rn progenies' enrichment of rain droplets is clearly observable from the visible photopeaks characterizing an after-rain spectrum, where it is possible to recognize an activity increase in the gamma lines belonging to ^{214}Pb and ^{214}Bi, gamma emitter daughters of ^{222}Rn (Figure 55).

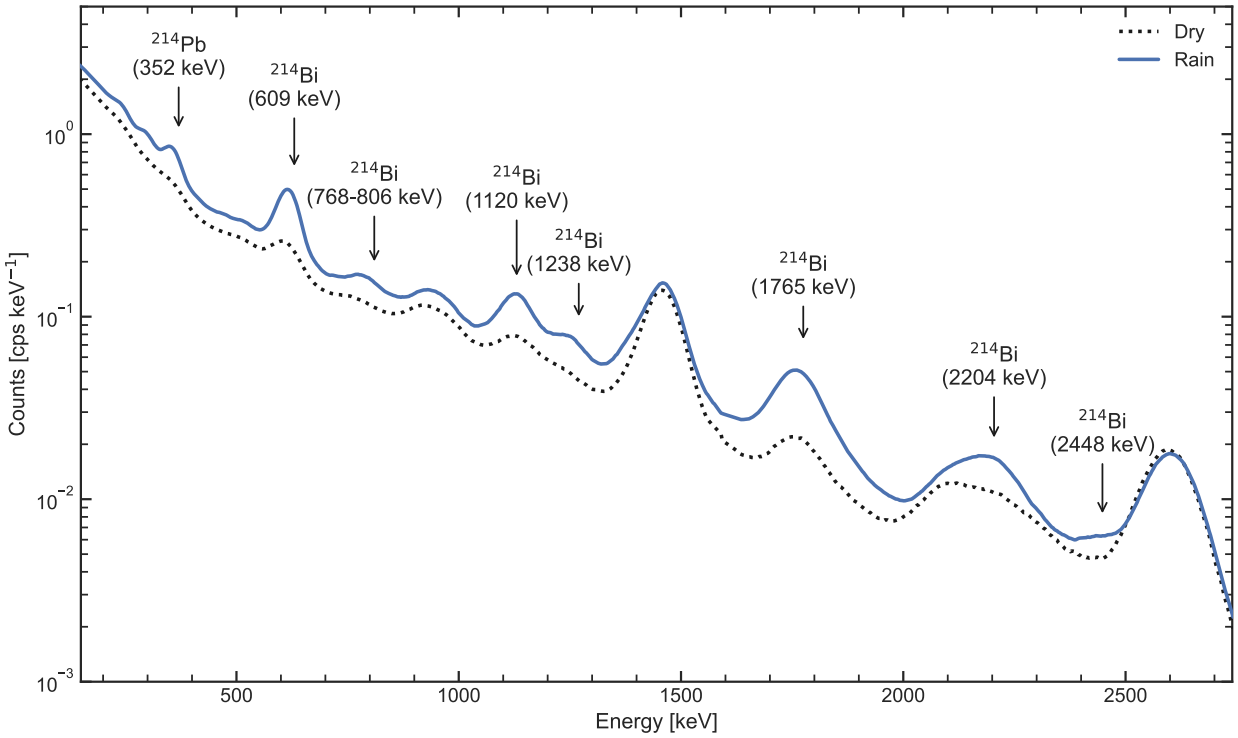

Figure 55. Comparison between the experimental gamma spectra recorded in dry and wet conditions before and immediately after a rain event. The annotations highlight how the increased level of radioactivity is mainly attributable to ^{214}Pb and ^{214}Bi gamma emission lines.

With the purpose of describing the gamma ^{214}Pb and ^{214}Bi net count rate time series during a rain episode, two signal components must be considered: i) the rain induced source term and ii) the radioactive decay term. The source term in the ^{214}Pb Bateman equation due to the ^{218}Po decay is neglected since its half-life (3.1 *min*) is sufficiently short that it will have

decayed to 0.01% of its initial activity by the precipitation age (~ 30 min), i.e. the average time between the removal of the ^{222}Rn progeny from secular equilibrium by rain and their deposition on the ground [230]. The description of the ^{214}Bi net count rate time series during a rain episode would, instead, require an additional time dependent source term due to the ^{214}Pb decays and, consequently, add an additional source of uncertainty. Therefore, even if the gamma signal associated to ^{214}Bi gamma lines is much more intense than its ^{214}Pb counterpart, the latter provides a more solid and direct probe for the description of rain-induced variations.

The variation in time of the number of ^{214}Pb nuclei $N_{Pb}(t)$ per unit of surface dS can thus be written as:

$$\frac{dN_{Pb}(t)}{dS \cdot dt} = + \frac{dN_{Pb}^{Rain}(t)}{dS \cdot dt} - \lambda_{Pb} \cdot \frac{dN_{Pb}(t)}{dS} \tag{29}$$

where dN_{Pb}^{Rain} is the increase in ^{214}Pb nuclei associated to the rain deposition and $\lambda_{Pb} = {}^{1}/_{\tau_{Pb}} = 4.28 \cdot 10^{-4}\ s^{-1} = 1.54\ h^{-1}$ is the ^{214}Pb decay constant which rules the exponential decay. The rain-induced source term $\frac{dN_{Pb}^{Rain}}{dS \cdot dt}$ can be described as a function of the rain rate $R\ \left[\frac{mm}{h}\right]$:

$$\frac{dN_{Pb}^{Rain}(t)}{dS \cdot dt} = n \cdot v_{term} \cdot N_{Pb}^{Drop} = \frac{R}{V_G} \cdot N_{Pb}^{Drop} \tag{30}$$

where $n\left[\frac{drops}{m^3}\right]$ is the density at ground level of number raindrops having identical size, $N_{Pb}^{Drop}\left[\frac{Pb\ nuclei}{drop}\right]$ is the number of ^{214}Pb nuclei in a raindrop having volume $V_G[m^3]$ and $v_{term}\ [\frac{m}{s}]$ is the raindrop terminal velocity. Since in principle N_{Pb}^{Drop} can depend on the rain rate R, the rain induced source term is not expected to linearly scale with R but can be parameterized as a power law of the rain rate R with exponent d:

$$\frac{dN_{Pb}^{Rain}(t)}{dS \cdot dt} \propto R^d \tag{31}$$

As the efficiency, the position, and the field of view of the Proximal Gamma Ray (PGR) spectroscopy station do not change over time, the footprint area of proximal gamma-ray spectroscopy measurement can be considered constant. Consequently, the gamma count

rate increase ΔC $[cps]$ recorded in a time interval ΔT $[h]$ is directly proportional to the number of ^{214}Pb nuclei accumulated to the ground during the same time:

$$\frac{\Delta N_{Pb}^{Rain}}{\Delta T} \propto \frac{\Delta C}{\Delta T} = A \cdot R^d \tag{32}$$

where $A\left[\frac{cps}{mm^d} h^{1-d}\right]$ is a proportionality factor that depends on the response of the 1L NaI(Tl) detector installed in the PGR station and on in-cloud ^{222}Rn concentration.

The experimental observation (Figure 56) of the net counts C_{Pb} in the photopeak of ^{214}Pb (352 keV) put in relation with the measured rain rate R (mm/h) for 82 different rain episodes brought to the empiric relation:

$$\Delta C_{Pb} = A \cdot \Delta T \cdot R^d \tag{33}$$

where $\Delta T = 0.25$ hours is the acquisition time and the parameter $A = 2.15 \pm 0.15$ (cps mm$^{-0.50}$ h$^{-0.50}$) is a detector dependent normalization factor [220] and the obtained parameter $d = 0.50 \pm 0.03$ in excellent agreement with the value $x = (0.5 \pm 0.1)$ published by [232].

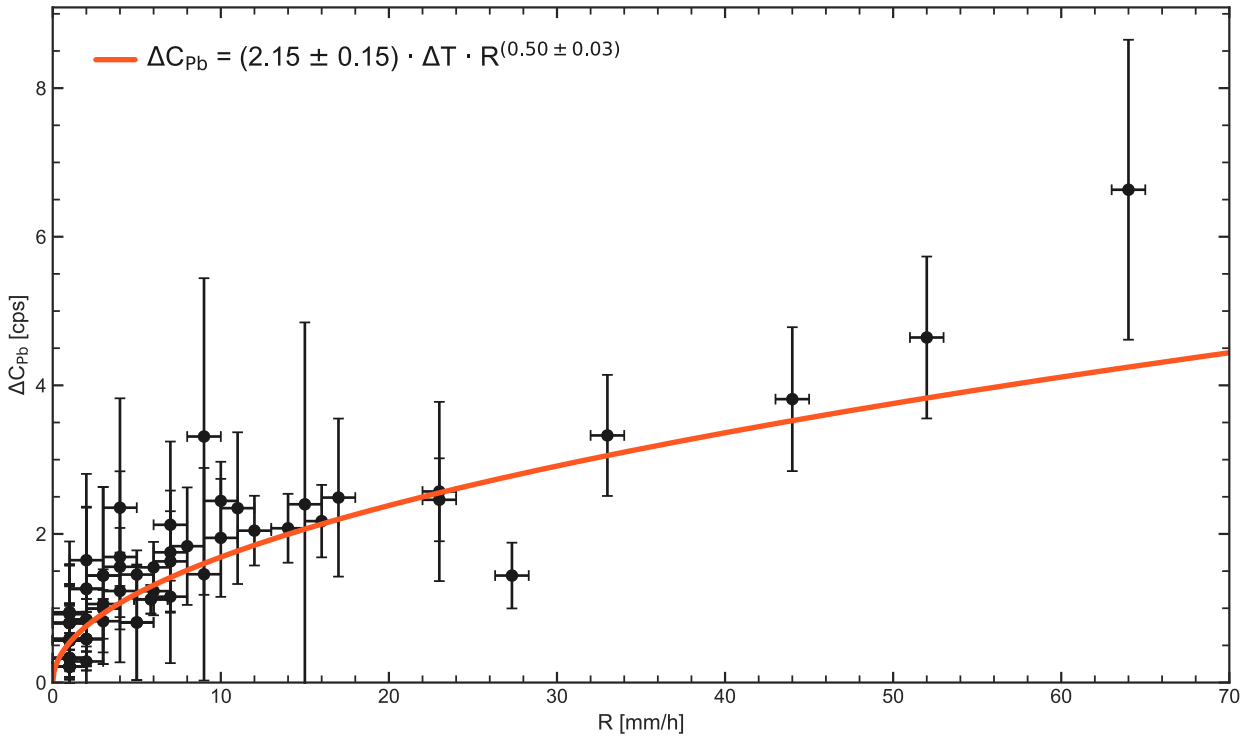

Figure 56. Plot of the ^{214}Pb impulsive count rate increase ΔC as function of the rainfall rate R. The ΔC values were calculated over all the 82 temporal bins ($\Delta T = 0.25$ h) characterized by non-zero rainfall amounts. The best fit curve in red was obtained using Eq. (33) as model function.

The increase in C_{Pb} is thus proportional to the square root ($\sim R^{0.5}$) of the rain rate R (mm/h). A weak rainfall rate of 5 mm/h causes a C_{Pb} jump from a typical environmental background of ~1.0 cps to a value of ~2.2 cps [220].

In summary, the responses of gamma spectra in the 100-2800 keV energy range changes according to different weather conditions (Figure 57). In case of a rain event (Figure 57c), a decrease in the ^{40}K photopeak is coupled with an increase in the ^{214}Pb gamma signal (Figure 57d). During irrigation (Figure 57e) the gamma spectrum (Figure 57f) does not depict this contrasting behavior, showing a common decrease between the ^{40}K and ^{214}Pb photopeaks. Thanks to the different responses of the ^{40}K and ^{214}Pb photopeaks to rainfall and irrigation, it is therefore possible to distinguish between these two events.

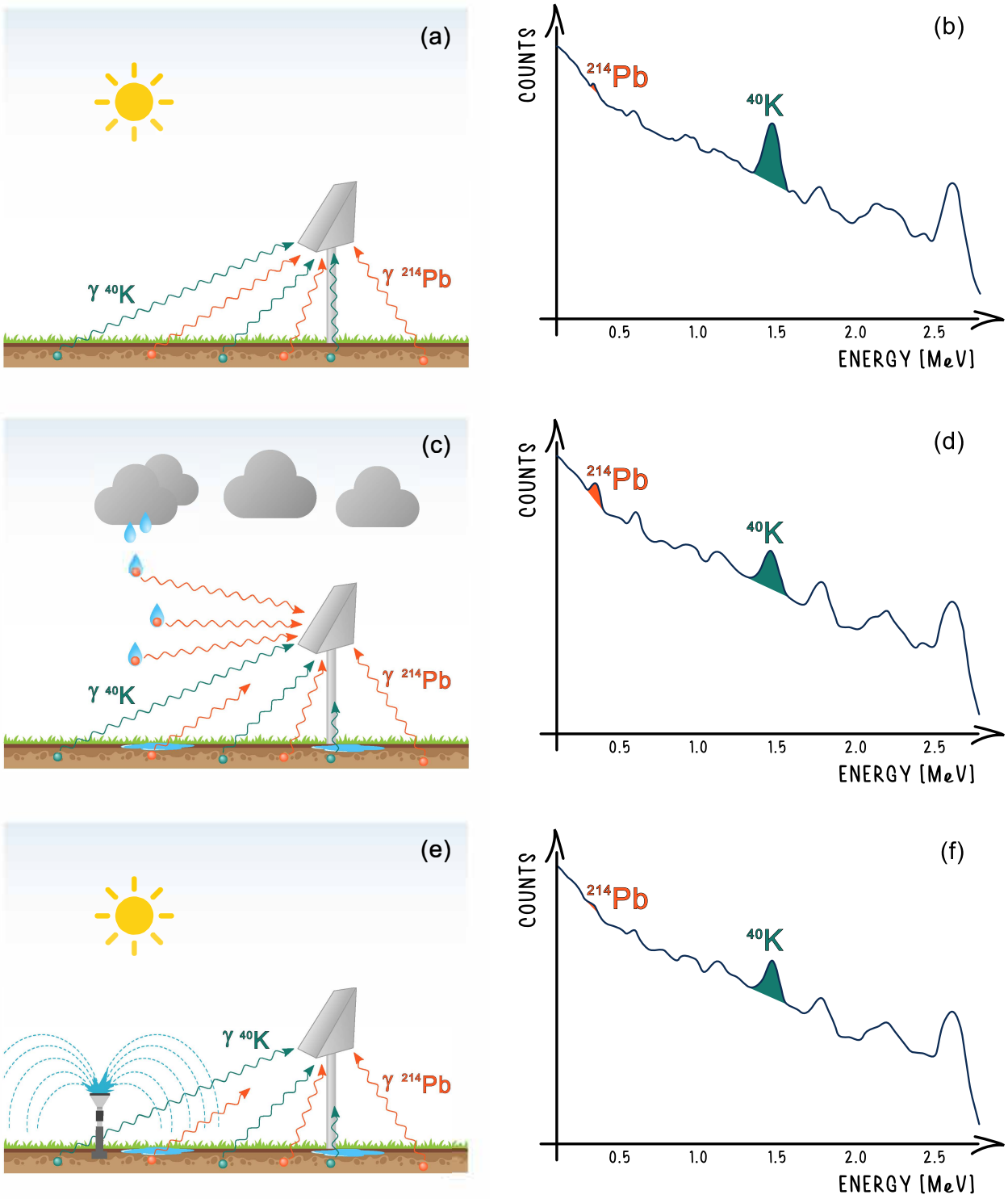

Figure 57. Drawings of the conditions under which the gamma spectra are recorded by the PGRS station ((a), (c) and (e)) and of their respective gamma spectra ((b), (d) and (f)). When no precipitated water is present on the ground (a), we can see the corresponding spectrum with the photopeaks of ^{40}K and ^{214}Pb highlighted (b). During a rain event (c), a decrease in the ^{40}K gamma signal and an increase in the ^{214}Pb photopeak (d) are recorded. In case of an irrigation (e), a decrease in both ^{40}K and ^{214}Pb gamma signals due to the shielding effect of the water layer on the ground (f) can be observed.

3.4 Experimental site

Data were acquired during two different growing seasons: the first data-taking campaign was conducted in the period 4th of April – 2nd of November 2017, while the second was carried out in the period 5th of March – 31st of August 2020. During the first campaign (from now on T2017), the site was dedicated to tomato crop, while in the second (M2020) maize was grown on the field. Both data takings are referred to an agricultural test field of Acqua Campus, a research center of the Emiliano-Romagnolo Canal (CER) irrigation district in the Emilia-Romagna region of Italy (44.57° N, 11.53° E, 16 m above sea level) (Figure 58). The study area is classified, according to the Köppen-Geiger classification [233], in the "Cfa" group which is characterized by a temperate climate without dry seasons and with hot summers, with a mean temperature of 14.0 °C and mean annual precipitation of about 700 mm. Table 31 lists the main physical and hydraulic parameters of the soil, characterized by a loamy texture and a 1.26% organic matter content [234].

Irrigation water was applied with fixed sprinkler system in T2017 and with hose reel irrigator in M2020, following the irrigation scheduling supplied by irrigation advisory service IRRINET [235-237]. The employed surface water was drawn from CER, a derivation of the Po River.

The reliability of the PGRS station is proven by its high duty cycle (i.e., the ratio of effective hours of data taking over the total number of hours), which is above 90% for both T2017 and M2020 (Table 32). The major sources of station downtime were not related to the reliability of the detector but were rather due to extraordinary maintenance required after extreme weather conditions.

Table 31. Physical and hydraulic parameters of the experimental site soil for the depth interval [0–30] cm. Sand, silt, and clay percentage as well as bulk density and organic matter were determined from direct measurements. The soil classification is based on the United States Department of Agriculture method. The soil hydraulic properties, i.e. wilting point (θ_{WP}), field capacity (θ_{FC}) and saturated hydraulic conductivity (K_S) come from [234].

Parameter	Value
Sand [%]	45
Silt [%]	40
Clay [%]	15
Soil textural class	Loamy
Soil bulk density [kg/m^3]	1345
Organic matter [%]	1.26
Wilting Point (θ_{WP}) [m^3/m^3]	0.09
Field Capacity (θ_{FC}) [m^3/m^3]	0.32
Saturation (θ_S) [m^3/m^3]	0.48
K_S [cm/day]	23

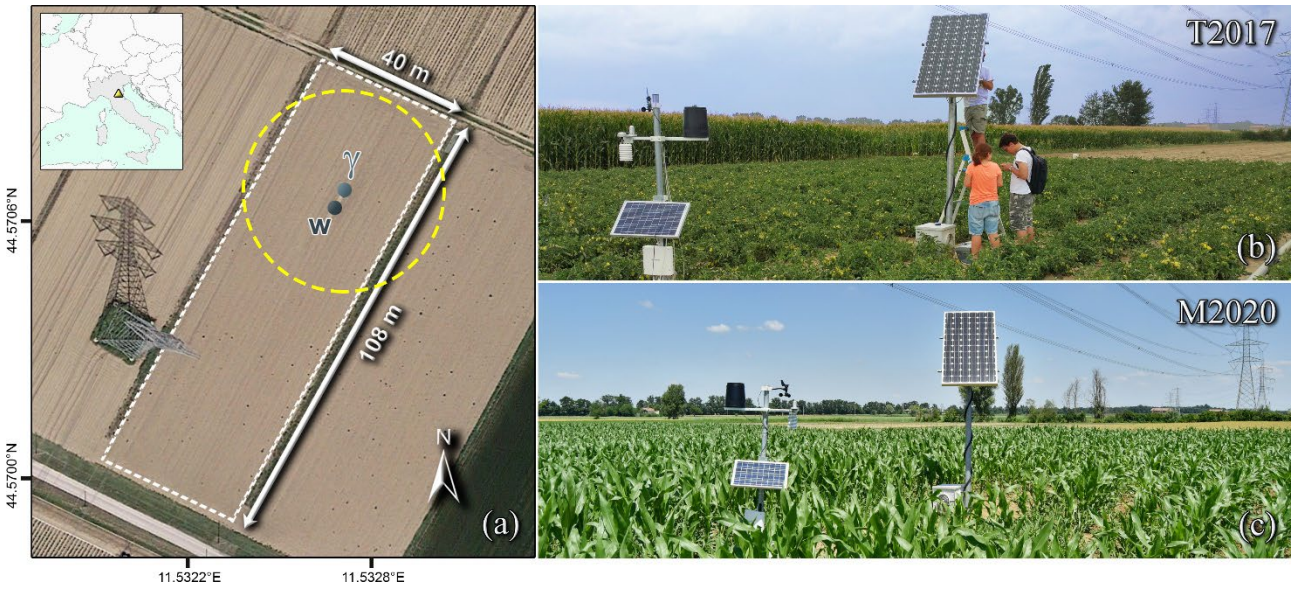

Figure 58. (a) The agricultural test field at Acqua Campus (Emilia Romagna, Italy) together with the positions of the PGRS (γ) and agro-meteorological (w) stations (geographic reference system WGS 84). The yellow circle around the PGRS station represents the corresponding Field of View (FOV) (radius ~ 25 m). (b) Pictures of the two stations in 2017 (tomato crop) (c) Picture of the stations in 2020 (maize crop).

Table 32. Information of the T2017 and M2020 measurement campaigns with the start and the end of the data taking, effective hours of acquisition and effective hours/total hours ratios. The type of the cultivars and planting, sowing, and harvesting dates are reported together with plant density and the total precipitation and irrigation water amounts.

	T2017	**M2020**
Start data taking [DD/MM/YYYY]	04/04/2017	05/03/2020
End data taking [DD/MM/YYYY]	02/11/2017	31/08/2020
Effective hours of acquisition	4871	3981
Effective hours/total hours [%]	95	92
Type of crop	Tomato (*Solanum lycopersicum*)	Maize (*Zea mays*)
Plant density [plants/m^2]	3.5	7.4
Planting-sowing date [DD/MM/YYYY]	23/05/2017	25/03/2020
Harvesting date [DD/MM/YYYY]	14/09/2017	02/09/2020
Total rainwater [mm]	404	228
Total irrigation water [mm]	350	210

3.5 Experimental setup

The experimental setup includes a PGRS station and an agro-meteorological station (MeteoSense 2.0, Netsens) (Figure 58), both equipped with an internet connection and powered by solar panels.

The PGRS station consisted of an external steel box welded on top of a 2.25 m pole and enclosing a 1L sodium iodide (NaI(Tl)) gamma-ray spectrometer: the entire station was designed and built specifically for the experiment [238]. The height of the pole was studied to adapt the Field of View (FOV) of the PGRS station to the field size. As a result, 95% of the detected gamma signal was produced by a disk having radius of approximately 25 m, covering therefore the entire field width.

The NaI(Tl) crystal was coupled to a photo-multiplier tube base and the output was then processed by a digital Multi-Channel Analyzer (MCA, CAEN γstream) having 2048 acquisition channels. The MCA was paired with a small integrated computer which ran the software required for managing the acquisition parameters, such as the start time, the spectral gain, and the operating voltage. Additional software was developed and implemented to make the data-taking continuous and remotely inspect the data acquired in real-time.

The gamma-ray spectrometer was able to detect the photon radiation produced by the decays of natural occurring radionuclides (^{40}K, ^{238}U and ^{232}Th decay chains) in the soil. Data was then sent every hour to a dedicated server through a 3G internet connection, where an energy calibration was performed. As a result, 1-hour acquisition time spectra were obtained. From these spectra, the server obtained the net count rate in the main ^{40}K, ^{214}Pb, ^{214}Bi (^{238}U) and ^{208}Tl (^{232}Th) photopeak energy windows [239] and from their processing was able to obtain the volumetric SWC (expressed in m^3/m^3). All processed data, together with the site coordinates and the sensor validity area, was then made available to be queried through a Web API by any remote client and can be easily integrated with any decision support system.

3.6 Results and discussions

3.6.1 SWC estimation

The PGRS station was able to continuously measure the SWC_γ with hourly resolution during the T2017 and M2020 measurement campaigns. The time evolution of the SWC_γ values recorded during the two data-taking periods (Figure 59) highlighted the ability of the PGRS technique to reliably follow the phases of dampening and subsequent drying following rain and irrigation events both in bare and vegetated soil. The sensor response to water precipitation is immediate: the SWC_γ increases as soon as water falls to the ground and decreases with a week-long timescale immediately after water stops precipitating. The highest value attained by the measured SWC_γ during both periods (0.46 m^3/m^3) never exceeded the 0.48 m^3/m^3 saturation value estimated for the soil, consistently with the soil hydraulic and physical properties (Table 31). The minimum recorded value of 0.09 m^3/m^3 exactly matched the estimated wilting point θ_{WP} (Table 31) and was immediately followed by an irrigation.

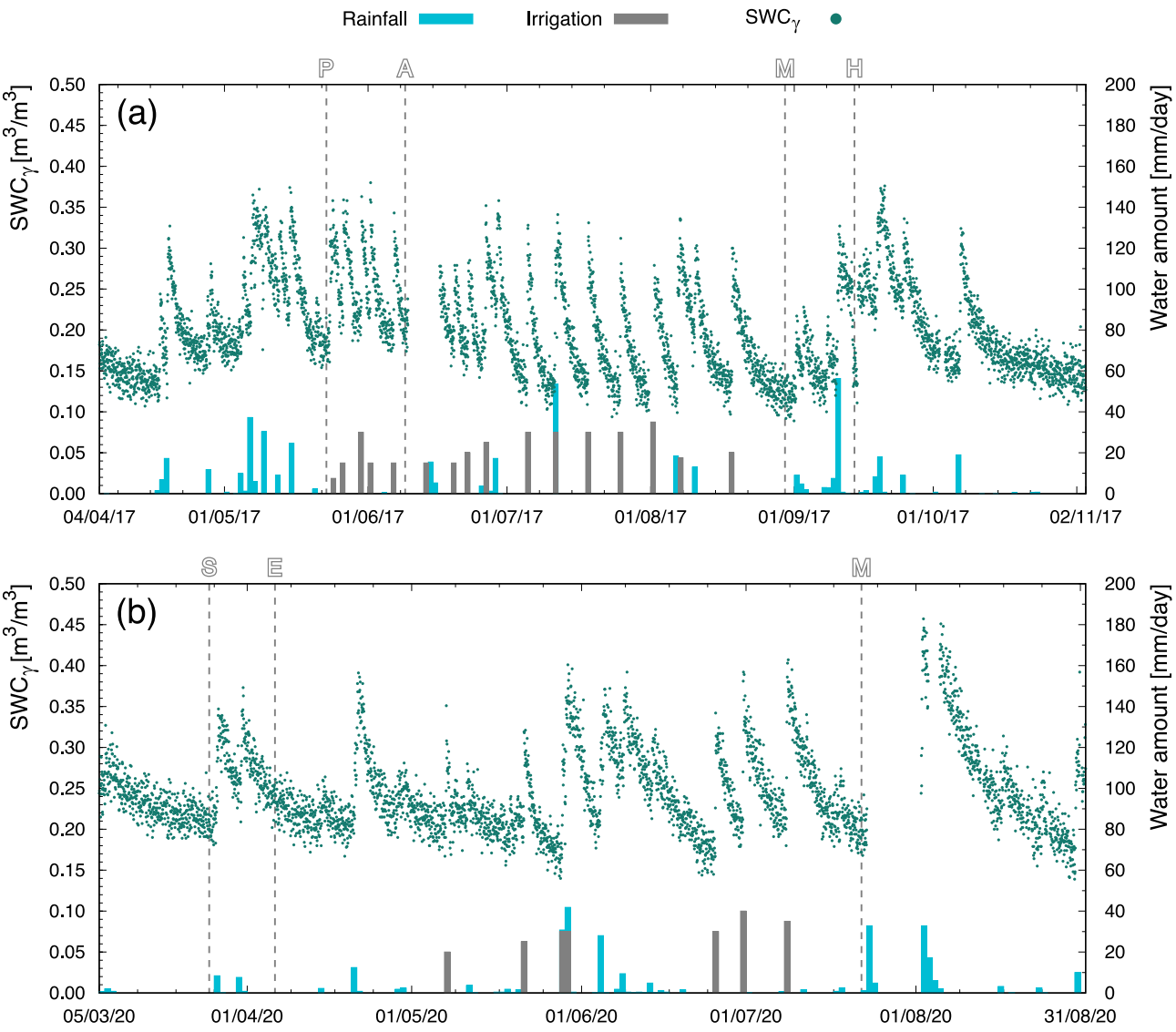

Figure 59. Time series of the volumetric SWC_γ estimated by the PGRS in T2017 (a) and M2020 (b). Letters indicate the crop stages of planting (P), anthesis (A), maturity (M) and harvesting (H) for T2017, and sowing (S), emergence (E) and maturity (M) for M2020. Each green point represents the hourly SWC_γ estimated through the analysis of the ^{40}K signal. The blue and grey bars represent the daily amount of precipitated water (in mm) due to rain and irrigation, respectively. The data gaps from the 9th to the 16th of June 2017 and from the 23rd to the 30th of July 2020 were caused by system shutdowns due to maintenance.

A validation campaign performed via gravimetric sampling under different soil moisture and crop conditions was conducted to test the reliability of the adopted PGRS technique and of the BWC correction (Table 33). In T2017, for each of the 4 sets of gravimetric measurements 48 samples were collected using a soil-auger and the average SWC_g was calculated adopting the same procedure used for the calibration of the PGRS station (Chapter 3.3.1). During M2020, the validation campaign was extended with 7 sets of gravimetric measurements in which the SWC_g was measured on a single bulk sample of the

first 40 cm of soil. The obtained 11 SWC_g validation measurements were hence compared to the SWC_γ estimated by the PGRS station in the same dates for both bare soil and vegetated periods (Table 33, Figure 60).

Table 33. Results of the validation campaigns performed for bare and vegetated soil in T2017 and M2020. The table reports the measured SWC_g values toghether with the corresponding SWC_γ values measured by the PGRS station in the same dates. The reported SWC_γ correspond to the average SWC_γ recorded by the PGRS station during the entire period covering the gravimetric sampling. The uncertainty on SWC_γ was set to the constant value of 0.023 m^3/m^3, as explained in Chapter 3.3.1. The SWC_g uncertainties for T2017 samples were calculated according to the procedure used for the calibration of PGRS station (Chapter 3.3.1). For M2020 measurements, the relative uncertainty assumed for SWC_g data was calculated by averaging the relative standard deviation exhibited by the T2017 validation campaign. The SWC_g measurement of 18/09/2017 (in italics) has been used to calibrate SWC_γ values according to Eq. (28) and has not been considered for the validation of the PGRS technique.

		Date of sampling [DD/MM/YYYY]	SWC_g [m^3/m^3]	SWC_γ [m^3/m^3]
Bare soil	**T2017**	18/09/2017	*0.219 ± 0.011*	*0.219 ± 0.023*
		21/09/2017	0.237 ± 0.015	0.245 ± 0.023
	M2020	06/04/2020	0.235 ± 0.028	0.238 ± 0.023
Vegetated soil	**T2017**	24/07/2017	0.167 ± 0.028	0.161 ± 0.023
		26/07/2017	0.265 ± 0.028	0.231 ± 0.023
		28/07/2017	0.189 ± 0.029	0.166 ± 0.023
	M2020	08/05/2020	0.225 ± 0.027	0.221 ± 0.023
		28/05/2020	0.180 ± 0.022	0.182 ± 0.023
		08/06/2020	0.246 ± 0.030	0.272 ± 0.023
		22/06/2020	0.168 ± 0.020	0.172 ± 0.023
		22/07/2020	0.171 ± 0.020	0.185 ± 0.023
		11/08/2020	0.234 ± 0.028	0.286 ± 0.023

A single calibration carried out on bare soil (Chapter 3.3.1) permitted to the PGRS station to perform unbiased measurements of the SWC_γ during both data-taking campaigns. The estimated SWC_γ and SWC_g exhibited an excellent agreement for both T2017 and M2020: all the measurements proved to be compatible at 1σ level (Table 33). Although the SWC_γ appears weakly underestimated (overestimated) in the vegetated period of 2017 (2020), the experimental uncertainties do not allow to identify it as a systematic trend. The accuracy of the PGRS station appears even more appreciable from the correlation plot between SWC_γ and SWC_g (Figure 60). The best fit line linking SWC_g measurements to SWC_γ exhibits a slope and an intercept compatible at less than 1σ level to 1 and 0, respectively. The accuracy of the method extends to both bare soil and tomato-maize covered soil, confirming that, once

the BWC is properly modeled, the cultivar type does not affect SWC_γ estimations through PGRS.

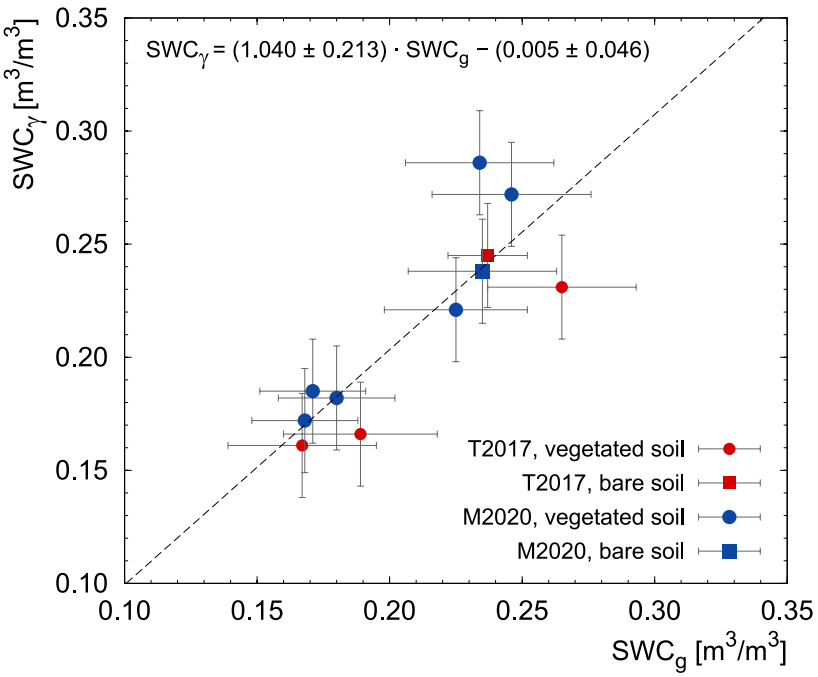

Figure 60. Scatter plot between SWC_g and SWC_γ measurements performed during T2017 (in red) and M2020 (in blue), in bare soil conditions (squares) and with vegetated soils (circles). The black dashed line represents the best fit linear curve having slope and intercept parameters respectively equal to (1.040 ± 0.213) and (-0.005 ± 0.046) m^3/m^3.

3.6.2 Irrigation and rain discrimination

The PGRS station offers the ability to independently understand the origin of the water precipitation. In particular, the observation of the time series of C_{Pb} enables an unambiguous identification of irrigation and rain events. This ability appears evident from two significant time intervals during T2017 (Figure 61) and M2020 (Figure 62), when irrigation and rain happened shortly after each other. Whilst the estimated SWC_γ increases in correspondence of both irrigation and rainfalls, the measured C_{Pb} decreases during the former and drastically increases in the latter case. These increases in C_{Pb}, amounting to more than 6 cps, appear clearly distinguishable from both the typical statistical fluctuations in the ^{214}Pb window (~0.2 cps) and the variability ascribed to well-known day-night oscillations (~0.3 cps) related to atmospheric radon [240-242].

Both the estimations of SWC_γ and of the rain-induced enhancement of C_{Pb} come from two complementary uses of the same technique, although the time variation of these quantities is related to completely distinct processes characterized by different timescales. After each

precipitation, the increase in SWC_γ is followed by a week-long decrease caused by the drying of the soil. These very low variations do not require high temporal resolutions: a 1-hour sampling represents a compromise between low statistical errors and a good temporal sampling. On the other hand, the increased C_{Pb} due to the rainwater precipitation of additional ^{214}Pb atoms to the ground exponentially decreases following a 26.8-min half-life. A 15-min resolution thus allows to properly characterize both the C_{Pb} variation due to the rain event and the exponential decrease due to ^{214}Pb decays.

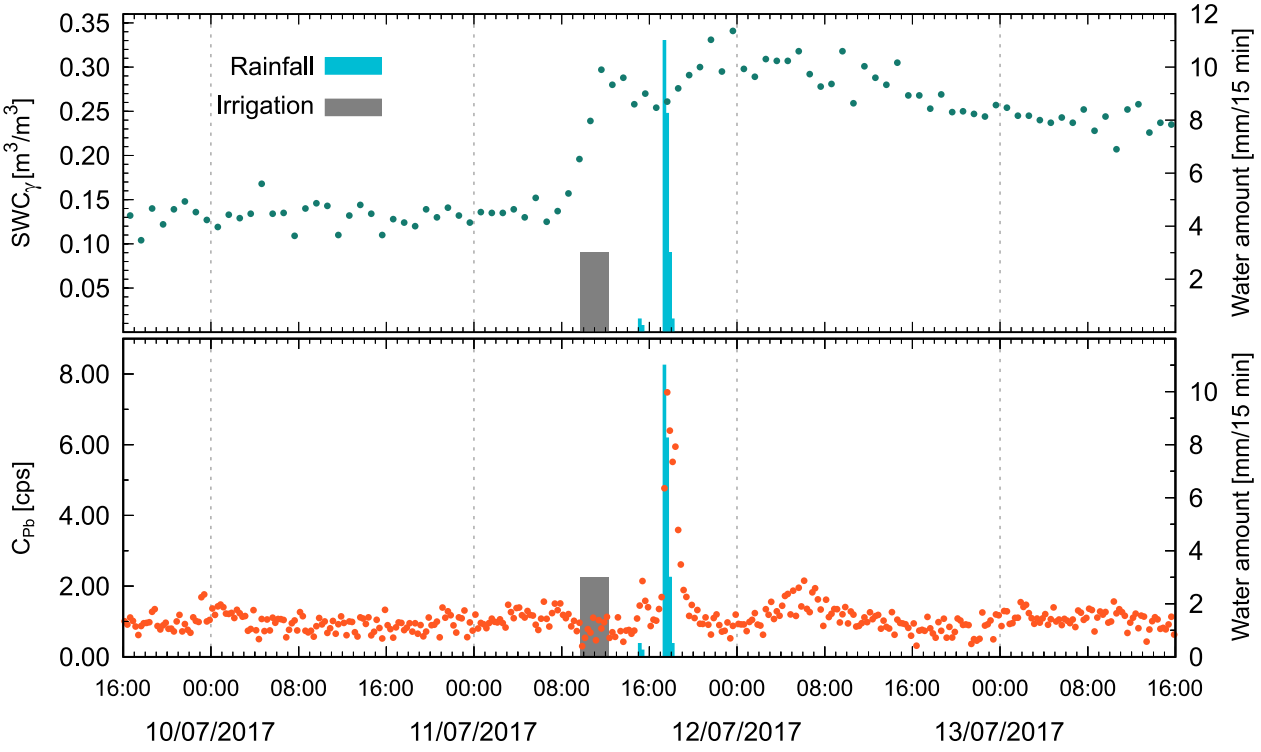

Figure 61. Temporal evolution of SWC_γ and of C_{Pb} from 09/07/2017, 16:00 to 13/07/2017, 16:00 together with the water amount of irrigation (grey bar) and rainfall (blue bars).

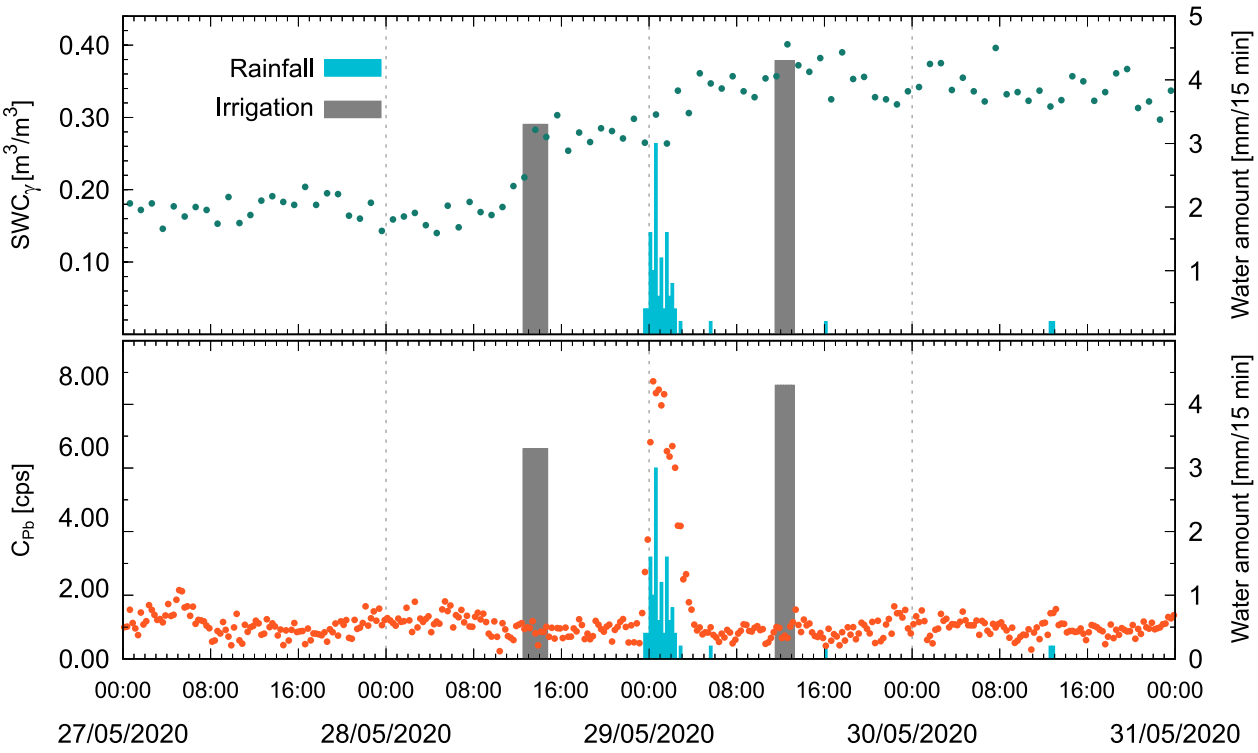

Figure 62. Temporal evolution of SWC$_\gamma$ and of C_{Pb} from 27/05/2020, 00:00 to 31/05/2020, 00:00 together with the water amount of irrigation (grey bar) and rainfall (blue bars).

The above illustrated behavior was regularly found during all precipitations recorded during the two data taking periods (Figure 63, Figure 64, Table 34). Regardless of the origin of the precipitated water, the observed SWC$_\gamma$ spiked in value for both rains and irrigation events, with an increase (typically of ~0.10 m^3/m^3 in response to ~10 mm of precipitated water) clearly distinguishable from the detector systematic uncertainties (0.023 m^3/m^3).

As soon as rainfall started, C_{Pb} immediately increased proportionally to the amount of rainwater precipitated (Figure 63a, b, c and Figure 64a, b, c), reaching peak values even 5 times larger than before-rain values. This increase could not be mistaken for statistical fluctuations, typically of the order of ~ 0.2 cps [220]. This appeared particularly evident from the positive variation of the average C_{Pb} value recorded before and after rains (Table 34), which proved to act as an effective smoking gun for rainfalls. On the other hand, during irrigation events (Figure 63d, e, f and Figure 64d, e, f) water precipitation was not followed by any transient increase in C_{Pb}; instead the additional water layer precipitated to soil surface shielded part of the gamma radiation coming from the ground, leading to a negative variation in the average C_{Pb} values recorded before and after irrigation.

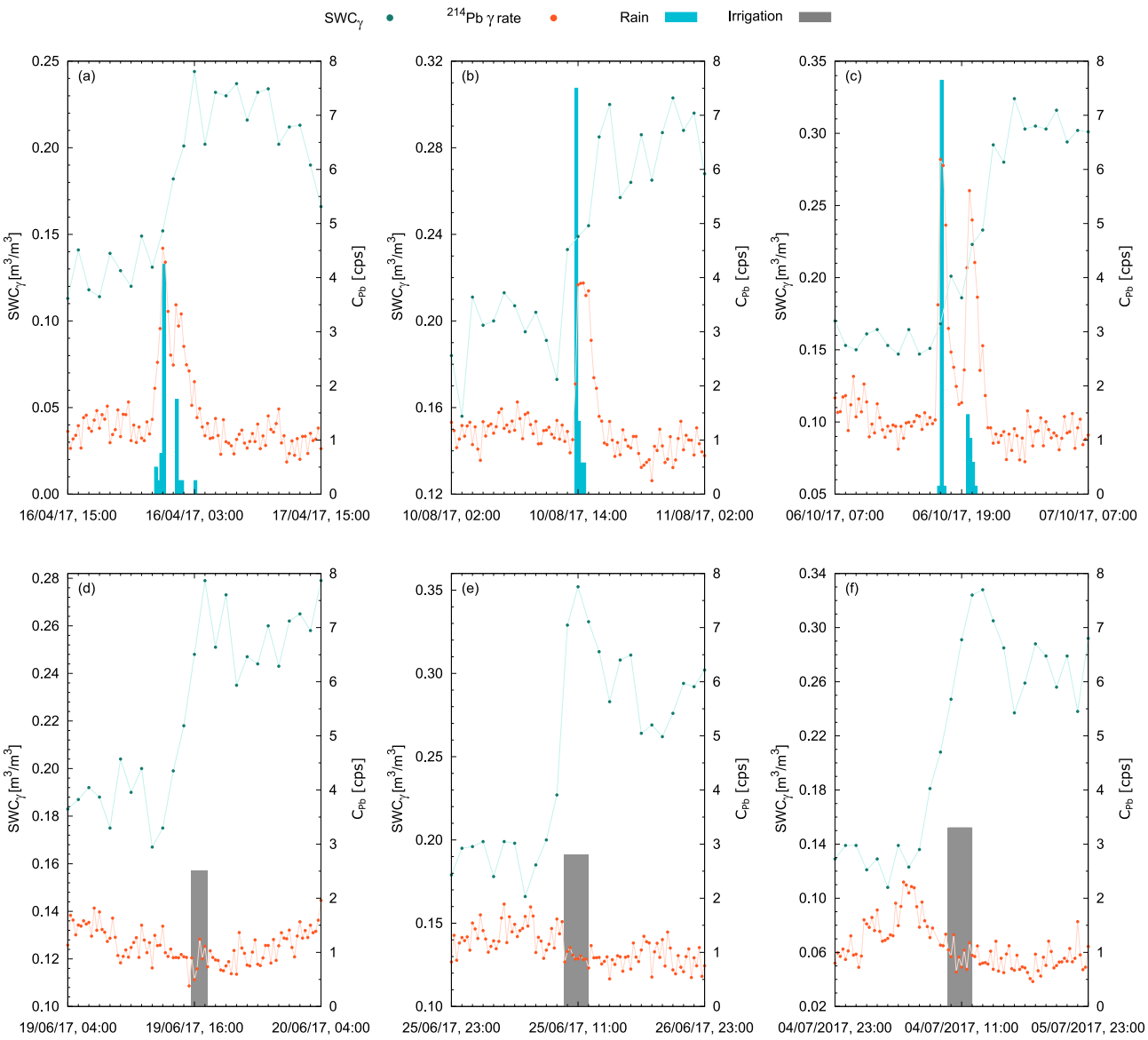

Figure 63. Temporal evolution of SWC_γ (in green) and $\boldsymbol{C_{Pb}}$ (in orange) during three rainfalls (a, b, c) and three irrigation events (d, e, f) occurred in T2017. The SWC_γ (in green) is hourly estimated, while the $\boldsymbol{C_{Pb}}$ (in orange) and the water amount (in blue for rain, in grey for irrigated water) have a 15-min time resolution.

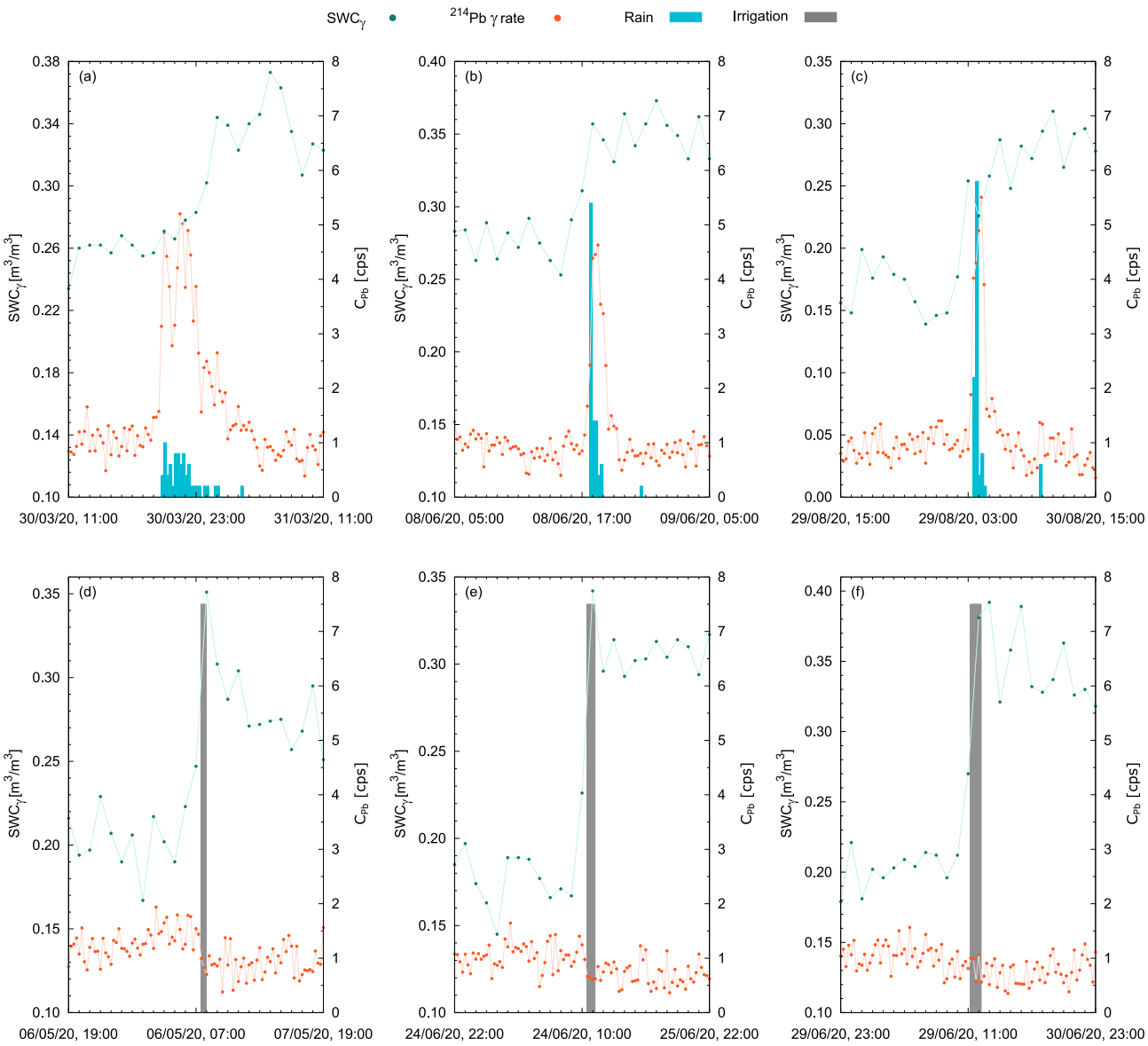

Figure 64. Temporal evolution of SWC$_\gamma$ (in green) and $\boldsymbol{C_{Pb}}$ (in orange) during three rainfalls (a, b, c) and three irrigation events (d, e, f) occurred in M2020. The SWC$_\gamma$ (in green) is hourly estimated, while the $\boldsymbol{C_{Pb}}$ (in orange) and the water amount (in blue for rain, in grey for irrigated water) have a 15-min time resolution.

Table 34. Relative variations (in percentage) of C_{Pb} and SWC_γ before and after rains and irrigation episodes shown in Figure 63 and Figure 64, together with their start date and time, duration and total water precipitated. SWC_γ variations are calculated comparing the average values measured in the 4 hours before rain/irrigation and in the 4 hours after their end. C_{Pb} variations are calculated considering the 4 hours before and the 4 hours after rain/irrigation started.

Event	Start date and time	Duration [h]	Total water [mm]	ΔSWC_γ [%]	ΔC_{Pb} [%]
Rain	16/04/2017, 23:15	4.00	8.3	+70	+130
	10/08/2017, 13:45	1.00	13	+36	+103
	06/10/2017, 16:45	3.75	19	+85	+187
	30/03/2020, 19:45	5.50	8.4	+36	+238
	08/06/2020, 17:45	1.25	9.2	+28	+130
	30/08/2020, 03:30	1.25	9.4	+48	+102
Irrigation	19/06/2017, 15:45	1.50	15	+33	-16
	26/06/2017, 09:45	2.25	25	+59	-33
	05/07/2017, 09:45	2.25	30	+91	-45
	07/05/2020, 07:30	0.50	20	+45	-41
	25/06/2020, 10:30	0.75	30	+65	-34
	30/06/2020, 11:15	1.00	40	+64	-19

3.7 Background due to atmospheric radon

In absence of precipitation or irrigation water, C_{Pb} statistically fluctuated around the typical background of ~1 cps (Figure 63, Figure 64). However, this background is not constant in time: it follows a diurnal and seasonal variation caused by the oscillation of its progenitor ^{222}Rn content in the atmosphere. This phenomenon is tightly bound to factors affecting ^{222}Rn mobility, mainly pressure and temperature (Figure 65), and causes a 1-day-period oscillation cycle in the observed C_{Pb} (Figure 66).

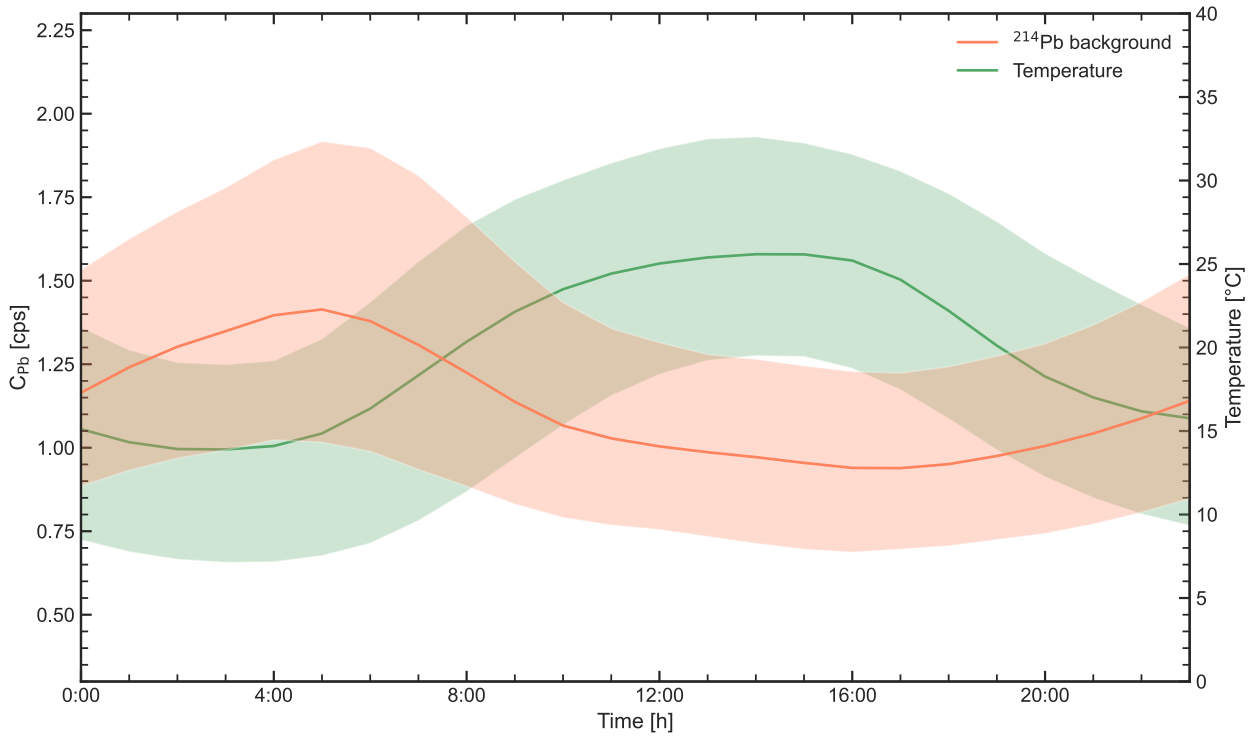

Figure 65. Diurnal oscillation of C_{Pb} (in orange) and temperature (in green) as a function of the hour of the day. For each of the 268 sunny days of the two data-taking, the 15-min resolution data have been grouped in 24 1h-bins according to the time of the day in which they were acquired. The lines show the median values recorded, while the band shows their 1σ intervals.

The non-stop measurement of C_{Pb} during the 268 sunny days occurred in T2017 and M2020 allowed a high-statistics characterization of these oscillations. On average, the C_{Pb} variability exhibited in each hour of the day during the entire data taking (i.e., the half-width of the 1σ band of Figure 66) was 0.33 cps.

However, diurnal C_{Pb} oscillations do not have any effect on our ability to identify rain events. Firstly, the discrimination of rains and irrigations is based on the relative increase of C_{Pb} over the background, so the increase remains visible regardless of the before-rain C_{Pb} value. Secondly, these oscillations occur with a period of 24 hours, which is much longer than the timescales of rain-induced C_{Pb} variations. Finally, the observed variability of 0.33 cps (obtained in the worst-case scenario by aggregating all data) is lower than rain-induced variations: the C_{Pb} increase due to a rain rate of 1 mm/h is roughly 0.5 cps, while for a rain rate of 5 mm/h is 1.2 cps (Eq. (33)). This means that it is still possible to identify a 1 mm/h rain from the background at 1σ, and a 5 mm/h rain at 3σ level.

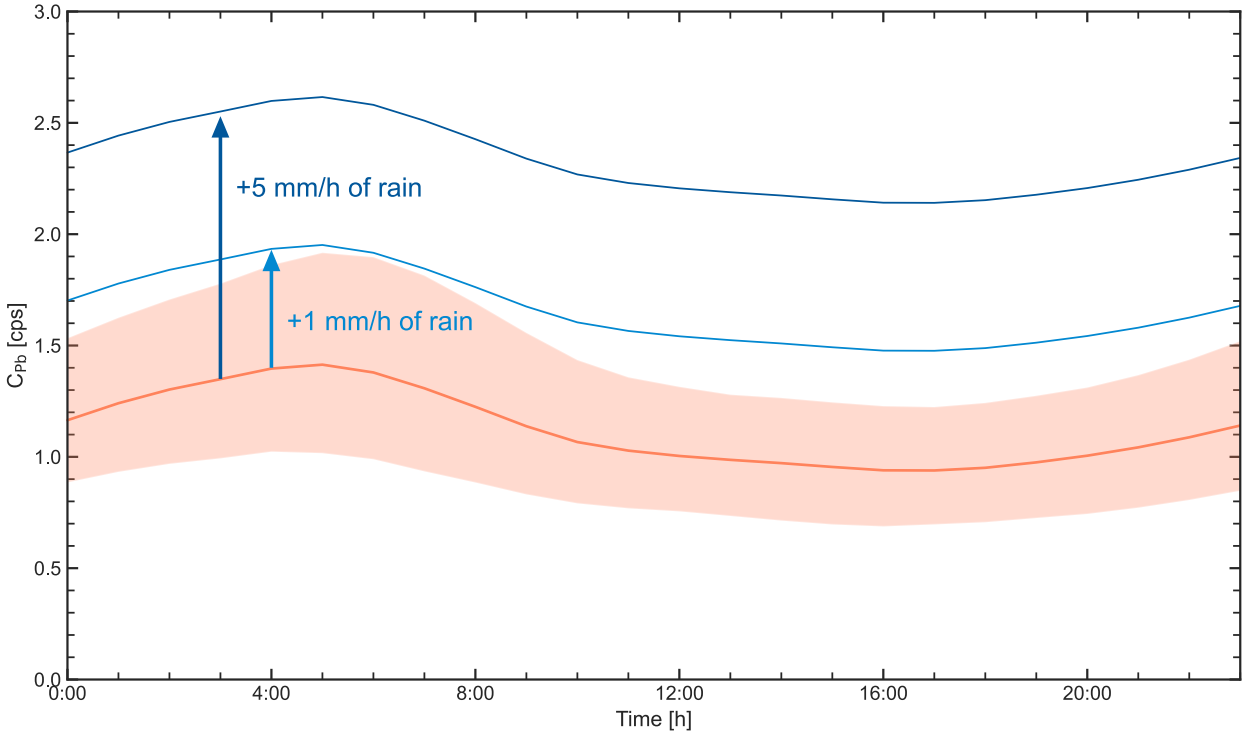

Figure 66. Diurnal oscillation of C_{Pb} as a function of the hour of the day. For each of the 268 sunny days of the two data-taking, the 15-min resolution data have been grouped in 24 1h-bins according to the time of the day in which they were acquired. The orange line shows the median C_{Pb} recorded, while the band shows its 1σ interval. The blue lines show the expected C_{Pb} during a rain of 1mm/h and 5mm/h, corresponding to an increase over the background of 0.5 cps and 1.2 cps, respectively.

3.8 Concluding remarks

This study proves the reliability of PGRS as a mature technique for proximal remote sensing applied to precision agriculture. We proved that the simultaneous observation in a gamma spectrum of a transient increase in the ^{214}Pb signal coupled with a decrease in the ^{40}K signal is an effective proxy for rainfall, while a decrease in both ^{214}Pb and ^{40}K signals is a reliable fingerprint for irrigation. A brilliant example is represented by two significant episodes when irrigation and rain happened shortly after each other (Figure 61, Figure 62). During a total of 102 rainy days and 23 irrigated days we were able to discern rain and irrigation without observing any false-positive or false-negative. Even low rain rates (~1 mm/h) were distinguishable from the gamma background at 1σ level. The rain-induced increase in the ^{214}Pb signal was clearly discernible from both environmental (diurnal oscillations) and statistical fluctuations.

After a single calibration, the PGRS station successfully measured in real time the SWC_γ at field scale level for both tomato (T2017 campaign) and maize (M2020 campaign) cultivars for a total of ~9000 hours. The station autonomously collected and processed SWC_γ, communicating the results to a remote server, making them available to any decision support platform for irrigation. Thanks to the remote-controlled data taking, the PGRS station required on-site maintenance interventions only on few occasions due to extraordinary weather events. In future perspective, PGRS stations could be implemented as supporting tools in view of satellite data calibration for quantifying SWC over large areas, bridging the gap between punctual and satellite fields of view.

The accuracy of the PGRS technique was demonstrated through validation measurements comparing SWC_γ to SWC_g estimates. The results from the two methods proved compatible within 1σ and the regression line exhibits a slope and an intercept compatible at 1σ level with 1 and 0, respectively. The accuracy extended through bare and vegetated soil conditions, showing the effectiveness of the correction adopted for the shielding effect of the BWC. Imaging a future in which this technology will be distributed in thousands of agricultural fields, the Canopy Water Content (or Vegetation Water Content) from satellite imaging could enable the estimation of the BWC without the need for disruptive measurements and model dependent evaluations. Additionally, PGR stations could be implemented as supporting tools in view of satellite data calibration, permitting to quantify SWC over large areas. Although the footprint of the PGR station is suited to be an effective ground-truth for SAR data or for soil moisture products retrieved from satellite (e.g. SMAP, SMOS, ASCAT), open questions still remain on the reliability of this approach and further investigations have to be performed in order to test the correlation among satellite and gamma ray data.

The capability to distinguish rainwater from irrigation without any meteorological support information, paired with the effectiveness in estimating the SWC_γ, makes the PGRS station a consolidated non-invasive technology in suppling crucial information for scheduling irrigations and managing resources with a view to reduce water wastage. This technique provides in real time continuous SWC_γ estimates on field scale and, simultaneously, permits to understand the origin of water precipitation, discerning rain from irrigation.

Part of the content of this chapter is based on the following publication:

A. Serafini, M. Albéri, M. Amoretti, S. Anconelli, E. Bucchi, S. Caselli, E. Chiarelli, L. Cicala, T. Colonna, M. De Cesare, S. Gentile, E. Guastaldi, T. Letterio, A. Maino, F. Mantovani, M. Montuschi, G. Penzotti, K. G. C. Raptis, F. Semenza, D. Solimando, V. Strati. "Proximal Gamma-Ray Spectroscopy: An Effective Tool to Discern Rain from Irrigation." Remote Sensing 13, no. 20 (January 2021): 4103. https://doi.org/10.3390/rs13204103.

CONCLUSION

The studies I conducted in the last 3 years allowed me to approach several scientific challenges from different points of view, exploiting the possibilities offered by decay products of ^{40}K to observe the world around us from a different perspective. I tried to engage in all-round scientific research, without locking myself in an ivory tower, studying what is far from us — the inner earth — through some of the most ephemeral particles in the universe, at the same time trying to apply my studies to what we have closest — the environment.

I had the opportunity to analyze the experimental results of the most important geoneutrino experiments ever built up to now: KamLAND and Borexino. By leaning on the shoulders of these giants and making use of the geophysical and geochemical knowledge built up by the scientific community in recent decades, I derived some considerations and constraints on the energetics of the Earth's mantle. From the combination of KamLAND and Borexino data I disentangled the mantle signal contribution by subtracting the reconstructed lithospheric component to estimate the mantle geoneutrino signal coming from U and Th. This information, combined with assumptions on the distribution of these elements in the inner Earth, permitted me to estimate a value for the radiogenic heat produced in the mantle and in turn to derive the total radiogenic heat budget of our planet, estimated to account for $20.8^{+7.3}_{-7.9}$ TW. By subtracting this value from the total heat power of the Earth, I recovered an estimate of 26 ± 8 TW for the other complementary component of heat loss, the secular cooling, providing a global vision on the heat sources which power our planet. These results can be compared to the estimations provided by the many geochemical models formulated in the last decades and, although not yet so stringent to outline a compositional model for our planet, allow us to exclude extreme scenarios and to provide information on the parameters that regulate geodynamics.

Although already posing constraints on the internal heat production of the Earth, these results are limited by our current detection capabilities. While the heat production of U and Th can be estimated by their experimentally observed geoneutrino spectra, the heat production of K is based on a model dependent relationship between K and U. The energy threshold posed by the currently employed detection method does not permit the observation of ^{40}K geoneutrinos, limiting our knowledge on the full geoneutrino spectrum and on earth's energetics. Not only have these low energy geoneutrinos not yet been

measured, but an effective experimental strategy for their detection is also still missing. For this reason, I have ventured into the search for an experimental technique that could in principle allow their detection. My proposal, based on inverse beta decay on heavy targets, relies on the double coincidence offered by the interaction of antineutrinos on ^{63}Cu nuclei. The favoured transition channel leads to an excited state of ^{63}Ni* and to the prompt emission of a positron (which readily annihilates). ^{63}Ni* in turn decays with a half-life of 1.67 μs to its ground state by emitting an 87.13 keV photon. Despite the low rate envisaged for the interaction, this double coincidence signal could be exploited to suppress all non-antineutrino backgrounds. A 240 kilotons liquid scintillator detector loaded with 50% of natural copper could enable the ^{40}K geoneutrino signal detection at 5σ level in 10 years of data taking. However, there is still a long way to go to realistically employ this technique in a real antineutrino experiment. The size of the detector, the radiopurity constraints, the difficulties posed to transparency by high loading, are all aspects that will take years and perhaps decades to overcome and make this goal realistic. I think that the paradigm shift is to have demonstrated that a technique to possibly enable ^{40}K detection exists. The scientific objectives of the future decades will then determine whether this path is worth exploring. In the meantime, new U and Th geoneutrino data are expected from the next decade, when new generation detectors SNO+, JUNO and the promising proposals Jimping and OBD will join the study of geoneutrinos. The future is bright for this subfield of neutrino physics, and I intend to take an active part in it by collaborating within the JUNO experiment.

Besides these studies, I wanted to have a positive and concrete impact in the present, which is why part of my research activities focused on the study and application of gamma spectroscopy techniques to precision agriculture. Irrigated agriculture accounts for more than 70% of global water withdrawals. Improvement of farming practices is imperative to ensure availability and sustainable management of water in the future. A concrete solution for an adequate irrigation schedule comes from the use of decision support systems based on novel technologies for a non-invasive and smart monitoring of soil water content. In this context, gamma spectroscopy can give its contribution as it is particularly sensitive to water in the soil and is not affected by systematic biases due to calibration difficulties (satellites) or spatial inhomogeneities (punctual sensors) of other alternative techniques. By placing a scintillator detector at some meters above ground and studying the temporal evolution of the ^{40}K gamma signal it is possible, after a single calibration, to estimate from the signal attenuation the water content of soil in real time. Simultaneously, the observation of the entire gamma spectrum offers the possibility to distinguish whether deposited water is due to rain or irrigation. This is possible thanks to the observation of a

transient increase in the counts of ^{214}Pb, a radon daughter enriching rainwater in clouds. The capability of automating the distinction of rainwater and irrigation, which may seem a trivial task, will become increasingly important in the context of a progressively more automated smart agriculture within the framework of the management of global water resources. I demonstrated the capabilities of such a proximal gamma spectroscopy station through the results of two data taking campaigns performed on a test agricultural field in Budrio (Italy). The combination of spectroscopic analyses, Monte Carlo simulations and experimental calibration permitted the unbiased estimation of the soil water content. The results were validated against a set of gravimetric measurements, proving the accuracy of the spectroscopic station as well as the effectiveness of the Monte Carlo estimation of the vegetation bias. Thanks to the different responses of the ^{40}K and ^{214}Pb photopeaks to rainfall and irrigation, the simultaneous time series analysis of these two distinct energy regions permitted to estimate soil water content and to discern rain from irrigation during the 368 days of acquisition.

Many other research activities and many other experiences of human value have not found a place among the written words of my thesis but represent an invaluable heritage that I will always carry with me.

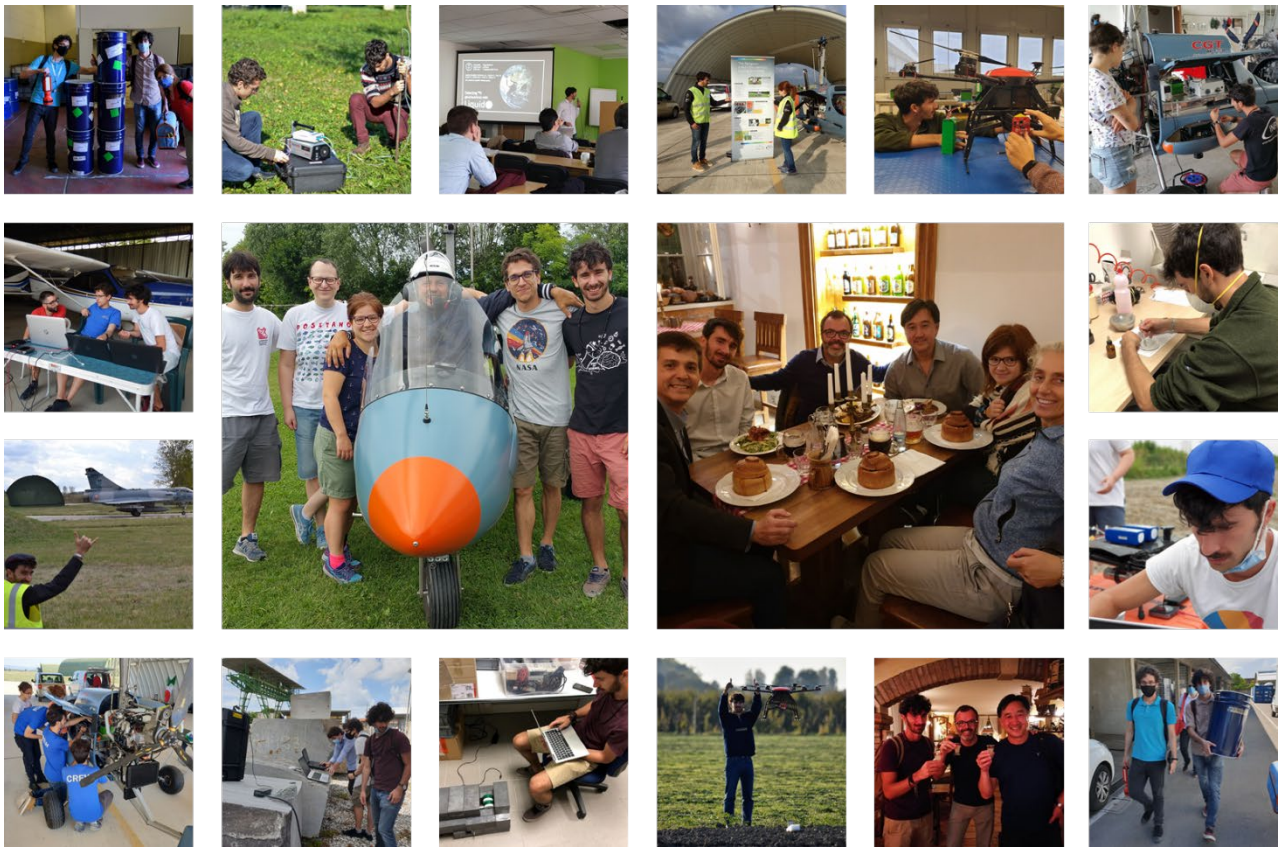

LIST OF SYMBOLS

$a(K)_X$	Abundance of Potassium in the reservoir X
$a(Th)_X$	Abundance of Uranium in the reservoir X
$a(U)_X$	Abundance of Thorium in the reservoir X
A_{CT}	Surface area - continents
A_{OC}	Surface area - oceans
A10	Arevalo, 2010
BC	Bulk Crust
BSE	Bulk Silicate Earth
BWC	Biomass water content
c_0	Velocity of light vacuum
ch	Chondrites
C	Secular cooling – Earth
C_X	Secular cooling of the reservoir X
C^{Cal}	Gamma count rate during calibration
C_K	Gamma count rate in the ^{40}K photopeak (1461 keV) energy window
C_{Pb}	Gamma count rate in the ^{214}Pb photopeak (352 keV) energy window
CC	Continental crust
CRNS	Cosmic-ray neutron sensing
CT	Central Tile (NFC of Borexino)
CMB	Core Mantle Boundary
DM	Depleted mantle
E_H	Energy of heat production
$E_{\bar{\nu}}$	Energy of antineutrino
E_{max}	Maximal energy of the emitted antineutrino
EM	Enriched Mantle
FOV	Field of View
FFC	Far Field Crust
f_C	Core-mantle differentiation factor
f_D	Enriching factor due to volatilization
h	Specific isotopic heat production
h’	Elemental specific heat production
H	Radiogenic heat – Bulk Earth
H_X	Radiogenic heat in the reservoir X
H13	Huang et al. 2013
HPE	Heat Producing Element
IBD	Inverse Beta Decay
IC	Inner Core
J10	Javoy et al., 2010
JJ13	Jackson and Jellinek, 2013
JK14	Javoy and Kaminski, 2014
JS	Japan Sea

L	Distance travelled by the antineutrino from its emission point
LAB	Lithosphere–Asthenosphere Boundary
LLSVP	Large Low Velocity Province
LC	Lower Crust
LK07	Lyubetskaya and Korenaga, 2007
LM	Lower Mantle
LNGS	Laboratori Nazionali del Gran Sasso
LS	Lithosphere
M	Mantle
M2020	PGRS data-taking campaign conducted in 2020 on maize crop
M_X	Mass of the BSE
M_C	Mass of the Core
$M(K)_X$	Mass of Potassium in the reservoir X
$M(Th)_X$	Mass of Uranium in the reservoir X
$M(U)_X$	Mass of Thorium in the reservoir X
M_V	Mass of the volatilized material
m_p	Mass of parent nuclide
m_d	Mass of daughter nuclide
MC	Middle Crust
MOHO	Mohorovicic discontinuity
MORB	Mid Ocean Ridge Basalts
MS95	McDonough and Sun, 1995
μ	Linear attenuation coefficient
N	Number of antineutrinos emitted per decay of the parent nucleus
N_p	Number of proton targets available in the detector
N_{Pb}	Number of ^{214}Pb nuclei
N_U	Number of U geoneutrino events
N_{Th}	Number of Th geoneutrino events
N_{geo}	Number of total geoneutrino events
NFC	Near Field Crust
OC	Outer Core
OV	Outer Vessel
OD	Outer Detector
OIB	Ocean Island Basalts
OP08	O'Neill and Palme, 2008
P_{ee}	Electron antineutrino survival probability
PDF	Probability Density Function
PGR	Proximal gamma ray
PGRS	Proximal gamma-ray spectroscopy
PO07	Palme and O'Neill, 2007
PO14	Palme and O'Neill, 2014
PMT	Photomultiplier Tube
Q	Integrated terrestrial surface heat power
q_{CT}	Mean heat flux - continents
q_{OC}	Mean heat flux - oceans

Q_{CT}	Heat power - continents
Q_{OCS}	Heat power - oceans
R	Rain rate
RLE	Refractory Lithophile Elements
RR	Rest of region (NFC of Borexino)
RS	Remote sensing
SED	Sedimentary layer
S_X(U+Th)	Geoneutrino signal from U and Th in the reservoir X
$Sp_i(i, E_{\bar{\nu}})$	Energy spectra of the produced geoneutrino of the i-th HPE
SWC	Soil Water Content
T	Exposure time
$T_{1/2}$	Half life
T2017	PGRS data-taking campaign conducted in 2017 on tomato crop
T_C	Condensation temperature
T02	Turcotte, 2002
T04	Turcotte, 2004
TNU	Terrestrial Neutrino Unit
U_R	Urey ratio
UC	Upper crust
ULVZ	Ultra Low Velocity Zone
UM	Upper Mantle
v_p	Seismic velocity of primary compressional waves
v_s	Seismic velocity of secondary shear waves
V_X	Seismic velocity in the reservoir X
V_G	Volume of a given raindrop
w	Gravimetric soil water content
w_γ	Soil water content measured by the gamma station
w_g	Soil water content measured via gravimetric techniques
W18	Wang et al., 2018
W20-C2	Wipperfurth et al. 2020 based on Crust 2.0
W20-C1	Wipperfurth et al. 2020 based on Crust 1.0
W20-L1	Wipperfurth et al. 2020 based on Litho 1.0
X_{iso}	Natural isotopic abundance
λ	Decay constant
$\epsilon_{\bar{\nu}}$	Antineutrino production rates for unit mass of the isotope
$\epsilon'_{\bar{\nu}}$	Antineutrino production rates for unit mass at natural isotopic abundance
Φ_i	Unoscillated geoneutrino flux of the i-th HPE
θ_{12}, θ_{13} and θ_{23}	Mixing angles between neutrinos eigenstates
δm^2 and Δm^2	Square mass differences between neutrinos eigenstates
Λ	Time-dependent count rate attenuation function accounting for biomass water content
η	Detector efficiency
Ω	Ratio between the mass attenuation coefficient of the solid portion of the soil and the one of water
σ	Cross section
ρ	Mass density
$\bar{\nu}_e$	Electron-flavoured antineutrino

BIBLIOGRAPHY

1. Chen, J., *Nuclear data sheets for A= 40*. Nuclear Data Sheets, 2017. **140**: p. 1-376.
2. Mougeot, X.J.A.R. and Isotopes, *Towards high-precision calculation of electron capture decays*. Applied Radiation and Isotopes, 2019. **154**: p. 108884.
3. Lazurik, V., V. Moskvin, and T.J.I.T.o.N.S. Tabata, *Average depths of electron penetration: use as characteristic depths of exposure*. 1998. **45**(3): p. 626-631.
4. Halperin, E.C., et al., *Perez & Brady's principles and practice of radiation oncology*. 2013: Lippincott Williams & Wilkins.
5. Plante, I. and F.A.J.N.J.o.P. Cucinotta, *Cross sections for the interactions of 1 eV–100 MeV electrons in liquid water and application to Monte-Carlo simulation of HZE radiation tracks*. 2009. **11**(6): p. 063047.
6. Hubbell, J.J.L.J.d.P.C., *Photon cross section compilation activity in the US in the range 1 keV to 100 GeV*. 1971. **32**(C4): p. C4-14-C4-20.
7. Araki, T., et al., *Experimental investigation of geologically produced antineutrinos with KamLAND*. Nature, 2005. **436**(7050): p. 499-503.
8. Bellini, G., et al., *Observation of geo-neutrinos*. Physics Letters B, 2010. **687**(4–5): p. 299-304.
9. Gando, A., et al., *Partial radiogenic heat model for Earth revealed by geoneutrino measurements*. Nature Geosci, 2011. **4**(9): p. 647-651.
10. Arevalo, R., W.F. McDonough, and M. Luong, *The K/U ratio of the silicate Earth: Insights into mantle composition, structure and thermal evolution*. Earth and Planetary Science Letters, 2009. **278**(3-4): p. 361-369.
11. Birch, F., *Elasticity and constitution of the Earth's interior*. Journal of Geophysical Research, 1952. **57**(2): p. 227-286.
12. Dziewonski, A.M. and D.L. Anderson, *Preliminary reference Earth model*. Physics of the Earth and Planetary Interiors, 1981. **25**: p. 297-356.
13. Masters, T.G. and P.M. Shearer, *Seismic models of the Earth: Elastic and anelastic*, in *Global earth physics a handbook of physical constants*, T.J. Ahrens, Editor. 1995, AGU reference shelf Series No. 1. p. 88-103.
14. Huang, Y., et al., *A reference Earth model for the heat-producing elements and associated geoneutrino flux*. Geochemistry, Geophysics, Geosystems, 2013. **14**(6): p. 2023-2029.
15. Yoder, C.F., *Astrometric and geodetic properties of Earth and the solar system*, in *Global earth physics: a handbook of physical constants*, T.J. Ahrens, Editor. 1995, AGU reference shelf Series No. 1. p. 1-31.

16. Allegre, C.J., et al., *The Chemical Composition of the Earth.* Earth and Planetary Science Letters, 1995. **134**(3-4): p. 515-526.
17. McDonough, W.F. and S. Sun, *The composition of the Earth.* Chemical Geology, 1995. **120**(3-4): p. 223-253.
18. Yoshizaki, T., et al., *Chemically defining the building blocks of the Earth.* arXiv preprint arXiv:.11717, 2018.
19. Campbell, I.H. and H. St C. O'Neill, *Evidence against a chondritic Earth.* Nature, 2012. **483**(7391): p. 553-558.
20. McDonough, W.F., *3.16 - Compositional Model for the Earth's Core*, in *Treatise on Geochemistry (Second Edition)*, H.D. Holland and K.K. Turekian, Editors. 2014, Elsevier: Oxford. p. 559-577.
21. O'Neill, H.S.C. and H. Palme, *Collisional erosion and the non-chondritic composition of the terrestrial planets.* Philosophical Transactions of the Royal Society A: Mathematical, Physical and Engineering Sciences, 2008. **366**(1883): p. 4205-4238.
22. Yoshizaki, T., W. McDonough, and R. Ash, *Ratio Variations of Refractory Lithophile Elements in Chondrites and Their Components: Implications for Planetary Compositions.* Lunar and Planetary Science Conference Proceedings, 2018(2083): p. 1436.
23. Alfè, D., M.J. Gillan, and G.D. Price, *Temperature and composition of the Earth's core.* Contemporary Physics, 2007. **48**(2): p. 63-80.
24. McDonough, W.F., *The Composition of the Lower Mantle and Core*, in *Deep Earth*. 2016. p. 143-159.
25. Watanabe, K., et al., *The abundance of potassium in the Earth's core.* Physics of the Earth and Planetary Interiors, 2014. **237**: p. 65-72.
26. Lee, K.K.M., G. Steinle-Neumann, and R. Jeanloz, *Ab-initiohigh-pressure alloying of iron and potassium: Implications for the Earth's core.* Geophysical Research Letters, 2004. **31**(11): p. n/a-n/a.
27. Murthy, V.R., W. van Westrenen, and Y. Fei, *Experimental evidence that potassium is a substantial radioactive heat source in planetary cores.* Nature, 2003. **423**(6936): p. 163-165.
28. Gessmann, C.K. and B.J. Wood, *Potassium in the Earth's core?* Earth and Planetary Science Letters, 2002. **200**(1-2): p. 63-78.
29. Humayun, M. and R.N. Clayton, *Potassium isotope cosmochemistry: Genetic implications of volatile element depletion.* Geochimica et Cosmochimica Acta, 1995. **59**(10): p. 2131-2148.
30. Corgne, A., et al., *How much potassium is in the Earth's core? New insights from partitioning experiments.* Earth and Planetary Science Letters, 2007. **256**(3-4): p. 567-576.
31. Anderson, D.L., *New theory of the Earth*. 2007: Cambridge University Press.

32. Bercovici, D., *Mantle Dynamics: An Introduction and Overview*, in *Treatise on Geophysics*. 2015. p. 1-22.
33. Fukao, Y. and M. Obayashi, *Subducted slabs stagnant above, penetrating through, and trapped below the 660 km discontinuity.* Journal of Geophysical Research: Solid Earth, 2013. **118**(11): p. 5920-5938.
34. Grand, S.P., R.D. Van der Hilst, and S. Widiyantoro, *High resolution global tomography: a snapshot of convection in the Earth.* Geological Society of America Today, 1997. **7**(4).
35. van der Hilst, R.D., S. Widiyantoro, and E.R. Engdahl, *Evidence for deep mantle circulation from global tomography.* Nature, 1997. **386**(6625): p. 578-584.
36. Williams, Q. and E.J. Garnero, *Seismic evidence for partial melt at the base of Earth's mantle.* Science, 1996. **273**(5281): p. 1528-1530.
37. Hernlund, J.W., C. Thomas, and P.J. Tackley, *A doubling of the post-perovskite phase boundary and structure of the Earth's lowermost mantle.* Nature, 2005. **434**(7035): p. 882-886.
38. Masters, G., et al., *The relative behavior of shear velocity, bulk sound speed, and compressional velocity in the mantle: Implications for chemical and thermal structure.* Earth's Deep Interior: Mineral Physics and Tomography From the Atomic to the Global Scale, Volume 117, 2000. **117**: p. 63-87.
39. Ishii, M. and J. Tromp, *Normal-mode and free-air gravity constraints on lateral variations in velocity and density of Earth's mantle.* Science, 1999. **285**(5431): p. 1231-1236.
40. Kennett, B. and A. Gorbatov, *Seismic heterogeneity in the mantle—strong shear wave signature of slabs from joint tomography.* Physics of the Earth and Planetary Interiors, 2004. **146**(1-2): p. 87-100.
41. Ni, S., et al., *Sharp sides to the African superplume.* Science, 2002. **296**(5574): p. 1850-1852.
42. Garnero, E.J. and A.K. McNamara, *Structure and dynamics of Earth's lower mantle.* Science, 2008. **320**(5876): p. 626-628.
43. Hernlund, J.W. and C. Houser, *On the statistical distribution of seismic velocities in Earth's deep mantle.* Earth and Planetary Science Letters, 2008. **265**(3-4): p. 423-437.
44. Bolton, H. and G. Masters, *Travel times of P and S from the global digital seismic networks: Implications for the relative variation of P and S velocity in the mantle.* Journal of Geophysical Research: Solid Earth, 2001. **106**(B7): p. 13527-13540.
45. Saltzer, R.L., E. Stutzmann, and R.D. van der Hilst, *Poisson's ratio in the lower mantle beneath Alaska: Evidence for compositional heterogeneity.* Journal of Geophysical Research: Solid Earth, 2004. **109**(B6).

46. Davies, D.R., et al., *Reconciling dynamic and seismic models of Earth's lower mantle: The dominant role of thermal heterogeneity.* Earth and Planetary Science Letters, 2012. **353**: p. 253-269.
47. Davaille, A., F. Girard, and M. Le Bars, *How to anchor hotspots in a convecting mantle?* Earth and Planetary Science Letters, 2002. **203**(2): p. 621-634.
48. Farnetani, C., *Excess temperature of mantle plumes: the role of chemical stratification across D ".* Geophysical Research Letters, 1997. **24**(13): p. 1583-1586.
49. Coltice, N. and Y. Ricard, *Geochemical observations and one layer mantle convection.* Earth and Planetary Science Letters, 1999. **174**(1-2): p. 125-137.
50. van Keken, P.E., E.H. Hauri, and C.J. Ballentine, *Mantle mixing: the generation, preservation, and destruction of chemical heterogeneity.* Annual Review of Earth and Planetary Sciences, 2002. **30**(1): p. 493-525.
51. Hart, S.R. and A. Zindler, *In search of a bulk-Earth composition.* Chemical Geology, 1986. **57**(3–4): p. 247-267.
52. Palme, H. and H.S.C. O'Neill, *Cosmochemical estimates of mantle composition*, in *The Mantle and Core, Vol. 2 Treatise of Geochemistry*, R.W. Carlson, Editor. 2003, Elsevier: Oxford. p. 1-38.
53. Allègre, C.J., A. Hofmann, and K. O'Nions, *The argon constraints on mantle structure.* Geophysical Research Letters, 1996. **23**(24): p. 3555-3557.
54. Anderson, D.L., *The Case for Irreversible Chemical Stratification of the Mantle.* International Geology Review, 2002. **44**(2): p. 97-116.
55. Javoy, M., et al., *The chemical composition of the Earth: Enstatite chondrite models.* Earth and Planetary Science Letters, 2010. **293**(3-4): p. 259-268.
56. Murakami, M., et al., *A perovskitic lower mantle inferred from high-pressure, high-temperature sound velocity data.* Nature, 2012. **485**(7396): p. 90-94.
57. Labrosse, S., J.W. Hernlund, and N. Coltice, *A crystallizing dense magma ocean at the base of the Earth/'s mantle.* Nature, 2007. **450**(7171): p. 866-869.
58. Lee, C.-T.A., et al., *Trace-element composition of Fe-rich residual liquids formed by fractional crystallization: Implications for the Hadean magma ocean.* Geochimica et Cosmochimica Acta, 2007. **71**(14): p. 3601-3615.
59. Boyet, M. and R.W. Carlson, *^{142}Nd evidence for early (>4.53 Ga) global differentiation of the silicate Earth.* Science, 2005. **309**(5734): p. 576-81.
60. Korenaga, J., *Urey ratio and the structure and evolution of Earth's mantle.* Reviews of Geophysics, 2008. **46**(2).

61. Jaupart, C., et al., *Temperatures, Heat, and Energy in the Mantle of the Earth*, in *Treatise on Geophysics*. 2015. p. 223-270.
62. Patočka, V., O. Šrámek, and N. Tosi, *Minimum heat flow from the core and thermal evolution of the Earth*. Physics of the Earth and Planetary Interiors, 2020. **305**.
63. Davies, J.H., *Global map of solid Earth surface heat flow*. Geochemistry, Geophysics, Geosystems, 2013. **14**(10): p. 4608-4622.
64. Mareschal, J.C., et al., *Geoneutrinos and the energy budget of the Earth*. Journal of Geodynamics, 2012. **54**: p. 43-54.
65. Lucazeau, F., *Analysis and Mapping of an Updated Terrestrial Heat Flow Data Set*. Geochemistry, Geophysics, Geosystems, 2019. **20**(8): p. 4001-4024.
66. Davies, J.H. and D.R. Davies, *Earth's surface heat flux*. Solid Earth, 2010. **1**(1): p. 5-24.
67. Hofmeister, A.M. and R.E. Criss, *Earth's heat flux revised and linked to chemistry*. Tectonophysics, 2005. **395**(3-4): p. 159-177.
68. Von Herzen, R., et al., *Comments on "Earth's heat flux revised and linked to chemistry" by A.M. Hofmeister and R.E. Criss*. Tectonophysics, 2005. **409**(1-4): p. 193-198.
69. Hofmeister, A.M. and R.E. Criss, *Reply to comments by R. Von Herzen, E.E. Davis, A.T. Fisher, C.A. Stein and H.N. Pollack on "Earth's heat flux revised and linked to chemistry"*. Tectonophysics, 2005. **409**(1-4): p. 199-203.
70. Williams, D.L. and R.P. Von Herzen, *Heat Loss from the Earth: New Estimate*. Geology, 1974. **2**(7).
71. Davies, G.F., *Thermal histories of convective Earth models and constraints on radiogenic heat production in the Earth*. Journal of Geophysical Research, 1980. **85**(B5).
72. Sclater, J.G., C. Jaupart, and D. Galson, *The heat flow through oceanic and continental crust and the heat loss of the Earth*. Reviews of Geophysics, 1980. **18**(1).
73. Pollack, H.N., S.J. Hurter, and J.R. Johnson, *Heat flow from the Earth's interior: Analysis of the global data set*. Reviews of Geophysics, 1993. **31**(3).
74. Christensen, U.R., *Thermal evolution models for the Earth*. Journal of Geophysical Research, 1985. **90**(B4).
75. Agostini, M., et al., *Comprehensive geoneutrino analysis with Borexino*. Physical Review D, 2020. **101**(1).
76. McDonough, W.F., O. Šrámek, and S.A. Wipperfurth, *Radiogenic Power and Geoneutrino Luminosity of the Earth and Other Terrestrial Bodies Through Time*. Geochemistry, Geophysics, Geosystems, 2020. **21**(7).

77. Ruedas, T., *Radioactive heat production of six geologically important nuclides*. Geochemistry, Geophysics, Geosystems, 2017. **18**(9): p. 3530-3541.
78. Fiorentini, G., M. Lissia, and F. Mantovani, *Geo-neutrinos and earth's interior*. Physics Reports, 2007. **453**(5-6): p. 117-172.
79. Van Schmus, W.R., *Natural Radioactivity of the Crust and Mantle*. Global Earth Physics: A Handbook of Physical Constants, Volume 1, 2013: p. 283-291.
80. Haenel, R., L. Rybach, and L. Stegena, *Handbook of terrestrial heat-flow density determination*. 1988.
81. Van Schmus, W., *Natural radioactivity of the crust and mantle*, in *Global earth physics: A handbook of physical constants*. 1995, Wiley Online Library. p. 283-291.
82. Dye, S.T., *Geoneutrinos and the radioactive power of the Earth*. Reviews of Geophysics, 2012. **50**(3).
83. Wohlers, A. and B.J. Wood, *Uranium, thorium and REE partitioning into sulfide liquids: Implications for reduced S-rich bodies*. Geochimica et Cosmochimica Acta, 2017. **205**: p. 226-244.
84. Wipperfurth, S.A., O. Šrámek, and W.F. McDonough, *Reference Models for Lithospheric Geoneutrino Signal*. Journal of Geophysical Research: Solid Earth, 2020. **125**(2).
85. Taylor, S.R. and S.M. McLennan, *The geochemical evolution of the continental crust*. Rev. Geophys., 1995. **33**(2): p. 241-265.
86. Rudnick, R.L. and D.M. Fountain, *Nature and composition of the continental crust: A lower crustal perspective*. Reviews of Geophysics, 1995. **33**(3): p. 267-309.
87. Wedepohl, K.H., *THE COMPOSITION OF THE CONTINENTAL-CRUST*. Geochimica Et Cosmochimica Acta, 1995. **59**(7): p. 1217-1232.
88. Mantovani, F., et al., *Antineutrinos from Earth: A reference model and its uncertainties*. Physical Review D, 2004. **69**(1).
89. McLennan, S.M., *Relationships between the trace element composition of sedimentary rocks and upper continental crust*. Geochem. Geophys. Geosyst., 2001. **2**(4).
90. Rudnick, R.L. and S. Gao, *Composition of the continental crust*, in *The Crust, Vol. 3 Treatise on Geochemistry*, R.L. Rudnick, Editor. 2003, Elsevier: Oxford. p. 1-64.
91. Stacey, F.D. and P.M. Davis, *Physics of the Earth*. 2008: Cambridge University Press.
92. Hacker, B.R., P.B. Kelemen, and M.D. Behn, *Differentiation of the continental crust by relamination*. Earth and Planetary Science Letters, 2011. **307**(3–4): p. 501-516.

93. Dye, S.T., *Geo-neutrinos and silicate earth enrichment of U and Th*. Earth and Planetary Science Letters, 2010. **297**(1-2): p. 1-9.
94. Šrámek, O., et al., *Geophysical and geochemical constraints on geoneutrino fluxes from Earth's mantle*. Earth and Planetary Science Letters, 2013. **361**: p. 356-366.
95. Labrosse, S., *Thermal evolution of the core with a high thermal conductivity*. Physics of the Earth and Planetary Interiors, 2015. **247**: p. 36-55.
96. Davies, G.F. and U. Christensen, *Dynamic Earth: Plates, Plumes and Mantle Convection*. American Journal of Physics, 2001. **69**(5): p. 620-621.
97. Buffett, B.A., *GEOPHYSICS: The Thermal State of Earth's Core*. Science, 2003. **299**(5613): p. 1675-1677.
98. Zhong, S., *Constraints on thermochemical convection of the mantle from plume heat flux, plume excess temperature, and upper mantle temperature*. Journal of Geophysical Research, 2006. **111**(B4).
99. Nolet, G., S. Karato, and R. Montelli, *Plume fluxes from seismic tomography*. Earth and Planetary Science Letters, 2006. **248**(3-4): p. 685-699.
100. Asplund, M., et al., *The Chemical Composition of the Sun*. 2009. **47**(1): p. 481-522.
101. Kozlovsky, Y.A. and N. Adrianov, *The superdeep well of the Kola Peninsula*. 1987: Springer.
102. Collerson, K.D., et al., *Rocks from the mantle transition zone: Majorite-bearing xenoliths from Malaita, Southwest Pacific*. Science, 2000. **288**(5469): p. 1215-1223.
103. Koschny, D., et al., *Interplanetary Dust, Meteoroids, Meteors and Meteorites*. Space Science Reviews, 2019. **215**(4).
104. Norton, O.R. and L. Chitwood, *Field guide to meteors and meteorites*. 2008: Springer Science & Business Media.
105. Wasson, J.T. and G.W. Kallemeyn, *Compositions of chondrites*. Philosophical Transactions of the Royal Society of London. Series A, Mathematical and Physical Sciences, 1988. **325**(1587): p. 535-544.
106. Dauphas, N., *The isotopic nature of the Earth's accreting material through time*. Nature, 2017. **541**(7638): p. 521-524.
107. Trønnes, R.G., et al., *Core formation, mantle differentiation and core-mantle interaction within Earth and the terrestrial planets*. Tectonophysics, 2019. **760**: p. 165-198.
108. Korenaga, J., *A method to estimate the composition of the bulk silicate Earth in the presence of a hidden geochemical reservoir*. Geochimica et Cosmochimica Acta, 2009. **73**(22): p. 6952-6964.

109. Warren, P.H., *Stable-isotopic anomalies and the accretionary assemblage of the Earth and Mars: A subordinate role for carbonaceous chondrites*. Earth and Planetary Science Letters, 2011. **311**(1–2): p. 93-100.
110. Burkhardt, C., et al., *A nucleosynthetic origin for the Earth's anomalous 142Nd composition*. Nature, 2016. **537**: p. 394.
111. Bouvier, A. and M. Boyet, *Primitive Solar System materials and Earth share a common initial 142Nd abundance*. Nature, 2016. **537**: p. 399.
112. Javoy, M., *The integral enstatite chondrite model of the Earth*. Geophysical Research Letters, 1995. **22**(16): p. 2219-2222.
113. Javoy, M. and E. Kaminski, *Earth's Uranium and Thorium content and geoneutrinos fluxes based on enstatite chondrites*. Earth and Planetary Science Letters, 2014. **407**: p. 1-8.
114. Drake, M.J. and K. Righter, *Determining the composition of the Earth*. Nature, 2002. **416**(6876): p. 39-44.
115. Fitoussi, C. and B. Bourdon, *Silicon Isotope Evidence Against an Enstatite Chondrite Earth*. Science, 2012. **335**(6075): p. 1477-1480.
116. Jackson, M.G. and A.M. Jellinek, *Major and trace element composition of the high 3He/4He mantle: Implications for the composition of a nonchonditic Earth*. Geochemistry, Geophysics, Geosystems, 2013. **14**(8): p. 2954-2976.
117. Lyubetskaya, T. and J. Korenaga, *Chemical composition of Earth's primitive mantle and its variance: 2. Implications for global geodynamics*. Journal of Geophysical Research: Solid Earth, 2007. **112**(B3): p. B03212.
118. Palme, H. and H.S.C. O'Neill, *3.1 - Cosmochemical Estimates of Mantle Composition*, in *Treatise on Geochemistry (Second Edition)*, H.D. Holland and K.K. Turekian, Editors. 2014, Elsevier: Oxford. p. 1-39.
119. Wipperfurth, S.A., et al., *Earth's chondritic Th/U: Negligible fractionation during accretion, core formation, and crust–mantle differentiation*. Earth and Planetary Science Letters, 2018. **498**: p. 196-202.
120. Davies, G.F., *Reconciling the geophysical and geochemical mantles: Plume flows, heterogeneities, and disequilibrium*. Geochemistry, Geophysics, Geosystems, 2009. **10**(10).
121. Turcotte, D. and G. Schubert, *Geodynamics*. 2014: Cambridge University Press.
122. Turcotte, D.L., D. Paul, and W.M. White, *Thorium-uranium systematics require layered mantle convection*. J. Geophys. Res., 2001. **106**(B3): p. 4265-4276.
123. Gamow, G., *Letter*, F. Reines, Editor. 1953.
124. Browne, E. and J.K. Tuli, *Nuclear Data Sheets for A = 238*. Nuclear Data Sheets, 2015. **127**: p. 191-332.

125. Browne, E., *Nuclear Data Sheets for A = 232*. Nuclear Data Sheets, 2006. **107**(10): p. 2579-2648.
126. McDonough, W.F., O. Šrámek, and S.A. Wipperfurth, *Radiogenic Power and Geoneutrino Luminosity of the Earth and Other Terrestrial Bodies Through Time*. Geochemistry, Geophysics, Geosystems, 2020. **21**(7): p. e2019GC008865.
127. Capozzi, F., et al., *Current unknowns in the three-neutrino framework*. Progress in Particle and Nuclear Physics, 2018.
128. Bezerra, T., et al., *High Precision Neutrino Unitarity Possible?* Proceedings of Science, 2019.
129. Wan, L., et al., *Geoneutrinos at Jinping: Flux prediction and oscillation analysis*. Physical Review D, 2017. **95**(5): p. 053001.
130. Mao, X., R. Han, and Y.-F. Li, *Non-negligible oscillation effects in the crustal geoneutrino calculations*. Physical Review D, 2019. **100**(11).
131. Fiorentini, G., et al., *Mantle geoneutrinos in KamLAND and Borexino*. Physical Review D, 2012. **86**(3).
132. Enomoto, S., *Geoneutrino Spectrum and Luminosity*. 2006.
133. Fogli, G.L., et al., *Geo-neutrinos: A systematic approach to uncertainties and correlations*. Earth, Moon, and Planets, 2006. **99**(1-4): p. 111-130.
134. Enomoto, S., et al., *Neutrino geophysics with KamLAND and future prospects*. Earth and Planetary Science Letters, 2007. **258**(1-2): p. 147-159.
135. Šrámek, O., et al., *Revealing the Earth's mantle from the tallest mountains using the Jinping Neutrino Experiment*. Scientific Reports, 2016. **6**: p. 33034.
136. Pasyanos, M.E., et al., *LITHO1.0: An updated crust and lithospheric model of the Earth*. Journal of Geophysical Research: Solid Earth, 2014. **119**(3): p. 2153-2173.
137. Baldoncini, M., et al., *Reference worldwide model for antineutrinos from reactors*. Physical Review D, 2015. **91**(6): p. 065002.
138. Mueller, T.A., et al., *Improved predictions of reactor antineutrino spectra*. Physical Review C, 2011. **83**(5): p. 054615.
139. Gando, A., et al., *Reactor on-off antineutrino measurement with KamLAND*. Physical Review D, 2013. **88**(3).
140. Watanabe, H. *KamLAND*. in *International Workshop: Neutrino Research and Thermal Evolution of the Earth*. 2016. 25 - 27 October - Sendai (Japan).
141. Watanabe, H. *Geo-neutrino Measurement with KamLAND*. in *Neutrino Geoscience 2019*. 2019. 21 - 23 October - Prague (Czech Republic).
142. Bellini, G., et al., *Measurement of geo-neutrinos from 1353 days of Borexino*. Physics Letters B, 2013. **722**(4-5): p. 295-300.

143. Agostini, M., et al., *Spectroscopy of geoneutrinos from 2056 days of Borexino data.* Physical Review D, 2015. **92**(3): p. 031101.
144. Aharmim, B., et al., *Measurement of the cosmic ray and neutrino-induced muon flux at the Sudbury neutrino observatory.* Physical Review D, 2009. **80**(1).
145. Jollet, C., *The JUNO experiment.* Il Nuovo Cimento C, 2016. **39**(4): p. 1-7.
146. Wu, Y.-C., et al., *Measurement of cosmic ray flux in the China JinPing underground laboratory.* Chinese Physics C, 2013. **37**(8).
147. Abusleme, A., et al., *JUNO Physics and Detector.* arXiv preprint arXiv:.02565, 2021.
148. Strati, V., et al., *Perceiving the Crust in 3-D: A Model Integrating Geological, Geochemical, and Geophysical Data.* Geochemistry, Geophysics, Geosystems, 2017. **18**(12): p. 4326-4341.
149. Rudnick, R.L.G., S., *Composition of the continental crust.* The Crust, of Treatise on Geochemistry, ed. R.L. Rudnick. Vol. 4. 2014: Elsevier, Oxford, 2014. 1–51.
150. Christensen, N.I. and W.D. Mooney, *Seismic velocity structure and composition of the continental crust: A global view.* Journal of Geophysical Research-Solid Earth, 1995. **100**(B6): p. 9761-9788.
151. Laske, G., et al., *CRUST1. 0: An updated global model of Earth's crust.* Geophysical Research Abstracts, 2012. **14**: p. 3743.
152. Takeuchi, N., et al., *Stochastic modeling of 3-D compositional distribution in the crust with Bayesian inference and application to geoneutrino observation in Japan.* Physics of the Earth and Planetary Interiors, 2019. **288**: p. 37-57.
153. Nataf, H.-C. and Y. Richard, *3SMAC: an a priori tomographic model of the upper mantle based on geophysical modeling.* Physics of the Earth and Planetary Interiors, 1996. **95**: p. 101-122.
154. Mooney, W.D., G. Laske, and T.G. Masters, *CRUST 5.1: A global crustal model at 5^o x 5^o.* Journal of Geophysical Research, 1998. **103**(B1): p. 727-747.
155. Laske, G., T.G. Masters, and C. Reif. *CRUST 2.0: A new global crustal model at 2 x 2 degrees.* 2001.
156. Usman, S.M., et al., *AGM2015: Antineutrino Global Map 2015.* Sci Rep, 2015. **5**: p. 13945.
157. Barna, A. and S. Dye, *Web application for modeling global antineutrinos.* arXiv preprint arXiv:.05633, 2015.
158. Plank, T., *The chemical composition of subducting sediments*, in *Treatise of Geochemistry, 2nd edition*. 2013.

159. Fiorentini, G., et al., *How much uranium is in the Earth? Predictions for geoneutrinos at KamLAND*. Physical Review D, 2005. **72**(3).
160. Coltorti, M., et al., *U and Th content in the Central Apennines continental crust: A contribution to the determination of the geo-neutrinos flux at LNGS*. Geochimica et Cosmochimica Acta, 2011. **75**(9): p. 2271-2294.
161. Blichert-Toft, J., et al., *The solar system primordial lead*. Earth and Planetary Science Letters, 2010. **300**(1-2): p. 152-163.
162. Ludhova, L. and S. Zavatarelli, *Studying the Earth with geoneutrinos*. Advances in High Energy Physics, 2013. **2013**.
163. Fogli, G.L., et al., *Combined analysis of KamLAND and Borexino neutrino signals from Th and U decays in the Earth's interior*. Physical Review D, 2010. **82**(9).
164. McDonough and Sun, *The composition of the Earth*. Chemical Geology, 1995. **120**: p. 223-253.
165. Goettel, K.A., *Models for the origin and composition of the Earth, and the hypothesis of potassium in the Earth's core*. Geophysical Surveys, 1976. **2**(4): p. 369-397.
166. Lide, D.R., *CRC handbook of chemistry and physics: a ready-reference book of chemical and physical data*. 1995: CRC press.
167. Bodnar, R.J., et al., *Whole Earth geohydrologic cycle, from the clouds to the core: The distribution of water in the dynamic Earth system*, in *The Web of Geological Sciences: Advances, Impacts, and Interactions*, M.E. Bickford, Editor. 2013, Geological Society of America.
168. Hirschmann, M.M., *WATER, MELTING, AND THE DEEP EARTH H2O CYCLE*. Annual Review of Earth and Planetary Sciences, 2006. **34**(1): p. 629-653.
169. Karato, S., *Water in the Evolution of the Earth and Other Terrestrial Planets*. Treatise of Geochemistry, 2015.
170. Nimmo, F., et al., *The influence of potassium on core and geodynamo evolution*. Geophysical Journal International, 2004. **156**(2): p. 363-376.
171. Finlay, C.C., et al., *International Geomagnetic Reference Field: the eleventh generation*. Geophysical Journal International, 2010. **183**(3): p. 1216-1230.
172. Brown, G., *The inaccessible earth: an integrated view to its structure and composition*. 2012: Springer Science & Business Media.
173. Gessmann, C., B.J.E. Wood, and P.S. Letters, *Potassium in the Earth's core?* 2002. **200**(1-2): p. 63-78.
174. Corgne, A., et al., *How much potassium is in the Earth's core? New insights from partitioning experiments*. 2007. **256**(3-4): p. 567-576.
175. Tanabashi, M., *Review of particle physics*. Phys. Rev. D, 2018. **98**: p. 030001.

176. Vogel, P. and J. Engel, *Neutrino electromagnetic form factors*. Physical Review D, 1989. **39**(11): p. 3378-3383.
177. Leyton, M., S. Dye, and J. Monroe, *Exploring the hidden interior of the Earth with directional neutrino measurements*. Nature Communications, 2017. **8**: p. 15989.
178. Grupen, C., *Astroparticle physics*. 2005: Springer Science & Business Media.
179. Wang, Z. and S. Chen, *Observing the Potassium Geoneutrinos with Liquid Scintillator Cherenkov Neutrino Detectors*. arXiv:1709.03743v3, 2017.
180. Agostini, M., et al., *Comprehensive geoneutrino analysis with Borexino*. Physical Review D, 2020. **101**(1): p. 012009.
181. Akimov, D., et al., *Observation of coherent elastic neutrino-nucleus scattering*. Science, 2017: p. eaao0990.
182. Formaggio, J.A. and G.P. Zeller, *From eV to EeV: Neutrino cross sections across energy scales*. Review of Modern Physics, 2012. **84**(3): p. 1307.
183. Raghavan, R.S., S. Pakvasa, and B.A. Brown, *New Tools for Solving the Solar-Neutrino Problem*. Physical Review Letters, 1986. **57**(14): p. 1801-1804.
184. Cabrera, A., *Reactors ν*, in *ISAAP Summer Institute 2018: Using Particle Physics to Understand and Image the Earth*. 2018: Ferrara.
185. Krane, K.S. and W.G. Lynch, *Introductory Nuclear Physics*. Physics Today, 1989. **42**: p. 78.
186. Fukugita, M. and T. Yanagida, *Physics of Neutrinos: and Application to Astrophysics*. 2013: Springer Science & Business Media.
187. Section, I.N.D., *ENSDF database* 2018.
188. Krauss, L.M., S.L. Glashow, and D.N. Schramm, *Antineutrino Astronomy and Geophysics*. Nature, 1984. **310**(5974): p. 191-198.
189. Singh, B., *Nuclear Data Sheets for A=1*. 2005. **106**(4): p. 601-618.
190. Chen, J., J. Cameron, and B. Singh, *Nuclear data sheets for A=35*. 2011. **112**(11): p. 2715-2850.
191. Cowan, C.L., et al., *Detection of the Free Neutrino: a Confirmation*. Science, 1956. **124**(3212): p. 103-104.
192. Raghavan, R.S., *New Prospects for Real-Time Spectroscopy of Low Energy Electron Neutrinos from the Sun*. Physical Review Letters, 1997. **78**(19): p. 3618.
193. Cabrera, A., et al., *Neutrino Physics with an Opaque Detector*. arXiv preprint arXiv:.02859, 2019.
194. Benziger, J., et al., *A scintillator purification system for the Borexino solar neutrino detector*. Nuclear Instruments and Methods in Physics Research Section A: Accelerators Spectrometers Detectors and Associated Equipment, 2008. **587**(2-3): p. 277-291.

195. Bityukov, S.I.J.J.o.H.E.P., *Signal significance in the presence of systematic and statistical uncertainties*. 2002. **2002**(09): p. 060.
196. Chen, M. *Potassium neutrino detection*. in *Neutrino Sciences*. 2005. Hawaii.
197. Yokoyama, M.J.a.p.a., *The hyper-Kamiokande experiment*. 2017.
198. Fiorentini, G., et al., *KamLAND, terrestrial heat sources and neutrino oscillations*. Physics Letters B, 2003. **558**(1-2): p. 15-21.
199. FAO, *The State of Food and Agriculture 2020. Overcoming water challenges in agriculture*. 2020, Rome, Italy: FAO. #210 p.
200. Nations, U., *Transforming our world: the 2030 Agenda for Sustainable Development*. New York, NY, USA, 2015.
201. Simionesei, L., et al., *IrrigaSys: A web-based irrigation decision support system based on open source data and technology*. Computers and Electronics in Agriculture, 2020. **178**: p. 105822.
202. Wang, W., et al., *Web-based decision support system for canal irrigation management*. Computers and Electronics in Agriculture, 2019. **161**: p. 312-321.
203. Dari, J., et al., *Detecting and mapping irrigated areas in a Mediterranean environment by using remote sensing soil moisture and a land surface model*. Journal of Hydrology, 2021. **596**: p. 126129.
204. Jalilvand, E., et al., *Quantification of irrigation water using remote sensing of soil moisture in a semi-arid region*. Remote Sensing of Environment, 2019. **231**: p. 111226.
205. Toková, L., D. Igaz, and E. Aydin, *Measurement of Volumetric Water Content by Gravimetric and Time Domain Reflectometry Methods at Field Experiment with Biochar and N Fertilizer*. Acta Horticulturae et Regiotecturae, 2019. **22**(2): p. 61-64.
206. Pätzold, S., M. Leenen, and T.W. Heggemann, *Proximal Mobile Gamma Spectrometry as Tool for Precision Farming and Field Experimentation*. Soil Systems, 2020. **4**(2): p. 31.
207. Strati, V., et al., *Modelling Soil Water Content in a Tomato Field: Proximal Gamma Ray Spectroscopy and Soil–Crop System Models*. Agriculture, 2018. **8**(4): p. 60.
208. Tan, X., et al., *Applicability of cosmic-ray neutron sensor for measuring soil moisture at the agricultural-pastoral ecotone in northwest China*. Science China Earth Sciences, 2020. **63**: p. 15.
209. Zhu, X., et al., *Application of cosmic-ray neutron sensing to monitor soil water content in an alpine meadow ecosystem on the northern Tibetan Plateau*. Journal of Hydrology, 2016. **536**: p. 247-254.

210. Andreasen, M., et al., *Status and perspectives on the cosmic-ray neutron method for soil moisture estimation and other environmental science applications*. Vadose Zone J., 2017. **16**(8): p. 1-11.
211. Siebert, S., et al., *A global data set of the extent of irrigated land from 1900 to 2005*. Hydrology and Earth System Sciences, 2015. **19**(3): p. 1521-1545.
212. Deines, J.M., A.D. Kendall, and D.W. Hyndman, *Annual Irrigation Dynamics in the U.S. Northern High Plains Derived from Landsat Satellite Data*. Geophysical Research Letters, 2017. **44**(18): p. 9350-9360.
213. Xie, Y. and T.J. Lark, *Mapping annual irrigation from Landsat imagery and environmental variables across the conterminous United States*. Remote Sensing of Environment, 2021. **260**: p. 112445.
214. Ozdogan, M., et al., *Remote Sensing of Irrigated Agriculture: Opportunities and Challenges*. Remote Sensing, 2010. **2**(9): p. 2274-2304.
215. Karthikeyan, L., I. Chawla, and A.K. Mishra, *A review of remote sensing applications in agriculture for food security: Crop growth and yield, irrigation, and crop losses*. Journal of Hydrology, 2020. **586**: p. 124905.
216. Salmon, J.M., et al., *Global rain-fed, irrigated, and paddy croplands: A new high resolution map derived from remote sensing, crop inventories and climate data*. International Journal of Applied Earth Observation and Geoinformation, 2015. **38**: p. 321-334.
217. Brocca, L., et al., *How much water is used for irrigation? A new approach exploiting coarse resolution satellite soil moisture products*. International Journal of Applied Earth Observation and Geoinformation, 2018. **73**: p. 752-766.
218. Patiris, D.L., et al., *Rainfall Investigation by Means of Marine In Situ Gamma-ray Spectrometry in Ligurian Sea, Mediterranean Sea, Italy*. Journal of Marine Science and Engineering, 2021. **9**(8): p. 903.
219. Tsabaris, C., et al., *Radioactivity Monitoring at North Aegean Sea Integrating In-Situ Sensor in an Ocean Observing Platform*. Journal of Marine Science and Engineering, 2021. **9**(1): p. 77.
220. Bottardi, C., et al., *Rain rate and radon daughters' activity*. Atmospheric Environment, 2020. **238**: p. 117728.
221. Grasty, R.L., *Radon emanation and soil moisture effects on airborne gamma-ray measurements*. Geophysics, 1997. **62**: p. 7.
222. Baldoncini, M., et al., *Investigating the potentialities of Monte Carlo simulation for assessing soil water content via proximal gamma-ray spectroscopy*. Journal of Environmental Radioactivity, 2018. **192**: p. 105-116.

223. Baldoncini, M., et al., *Biomass water content effect on soil moisture assessment via proximal gamma-ray spectroscopy.* Geoderma, 2019. **335**: p. 69-77.
224. Meade, K.A., M. Cooper, and W.D. Beavis, *Modeling biomass accumulation in maize kernels.* Field Crops Research, 2013. **151**: p. 92-100.
225. Stevanović, N., D. Nikezić, and A. Djordjevich, *The recoil factor of.* Journal of Aerosol Science, 2004. **35**(8): p. 1041-1050.
226. Hopke, P.K., *Use of Electrostatic Collection of 218Po for Measuring Rn.* Health Physics, 1989. **57**(1): p. 39-42.
227. Porstendörfer, J., *Properties and behaviour of radon and thoron and their decay products in the air.* Journal of Aerosol Science, 1994. **25**(2): p. 219-263.
228. Castleman, A.W., *Consideration of the chemistry of radon progeny.* Environmental Science & Technology, 1991. **25**(4): p. 730-735.
229. Mostafa, M., H. Khalaf, and M. Zhukovsky, *Radon decay products equilibrium at different aerosol concentrations.* Applied Radiation and Isotopes, 2020. **156**.
230. Greenfield, M.B., et al., *Determination of rain age via γ rays from accreted radon progeny.* Journal of Applied Physics, 2008. **104**(7): p. 074912.
231. Takeyasu, M., et al., *Concentrations and their ratio of 222Rn decay products in rainwater measured by gamma-ray spectrometry using a low-background Ge detector.* Journal of Environmental Radioactivity, 2006. **88**(1): p. 74-89.
232. Mercier, J.F., et al., *Increased environmental gamma-ray dose rate during precipitation: a strong correlation with contributing air mass.* Journal of Environmental Radioactivity, 2009. **100**(7): p. 527-533.
233. Peel, M.C., B.L. Finlayson, and T.A. McMahon, *Updated world map of the Köppen-Geiger climate classification.* Hydrology and Earth System Sciences, 2007. **11**: p. 12.
234. Strati, V., et al., *Modelling Soil Water Content in a Tomato Field: Proximal Gamma Ray Spectroscopy and Soil–Crop System Models.* Agriculture, 2018. **8**(4): p. 18.
235. Giannerini, G. and R. Genovesi. *Irrinet: IT services for farm water management, a large scale implementation in Italy.* in *EFITA 2011 Conference Proceedings*.
236. Mannini, P., R. Genovesi, and T. Letterio, *IRRINET: Large Scale DSS Application for On-farm Irrigation Scheduling.* Procedia Environmental Sciences, 2013. **19**: p. 823-829.

237. Munaretto, S. and A. Battilani, *Irrigation water governance in practice: the case of the Canale Emiliano Romagnolo district, Italy*. Water Policy, 2014. **16**(3): p. 578-594.
238. Baldoncini, M., et al., *Investigating the potentialities of Monte Carlo simulation for assessing soil water content via proximal gamma-ray spectroscopy*. J Environ Radioact, 2018. **192**: p. 105-116.
239. IAEA, N.E.D., *Guidelines for radioelement mapping using gamma ray spectrometry data*. Nuclear Fuel Materials Section, 2003. **Vienna, Austria**: p. 179.
240. Wilkening, M., *Radon in the Environment*. 1990, Amsterdam, The Netherlands: Elsevier.
241. Perrier, F. and F.J.G.J.I. Girault, *Harmonic response of soil radon-222 flux and concentration induced by barometric oscillations*. Geophys. J. Int., 2013. **195**(2): p. 945-971.
242. Greenfield, M., et al., *Variation in γ-ray count rates as a monitor of precipitation rates, radon concentrations, and tectonic activity*. J. Appl. Phys., 2002. **91**(3): p. 1628-1633.